COO-1779-76

A STUDY OF THE HELIUM-JET RECOIL-TRANSPORT METHOD

By

Kenneth Lee Kosanke

A THESIS

Submitted to
Michigan State University
in partial fulfillment of the requirements
for the degree of

DOCTOR OF PHILOSOPHY

Department of Chemistry
Program in Physical Chemistry

1973

ABSTRACT

A STUDY OF THE HELIUM-JET RECOIL-TRANSPORT METHOD

By

Kenneth Lee Kosanke

The Helium-Jet Recoil-transport (HeJRT) system has been studied for the purposes of discovering more of the detail of the mechanism of its operation and to facilitate its further development. The major portion of this thesis is a report of a series of experiments in which the operation of the HeJRT system was defined and in which the effects of varying the operating parameters of the system were recorded. This has provided an experimental basis that has allowed us to make statements on possible mechanisms of operation and the importance of certain features of the system. Of course, also included are a detailed description of our HeJRT system and sections discussing some of the extensions of HeJRT techniques that have resulted, such as those allowing the performance of on-line aqueous chemistry with the system.

The initial motivations for the construction of a HeJRT system here was its intended use as a subsystem in an on-line mass identification system to be used in conjuction with conventional nuclear counting experiments. Our present thoughts on this application are included in the introductory chapter of this thesis.

ACKNOWLEDGEMENTS

I sincerely wish to thank Dr. Wm. C. McHarris for suggesting this region of study. His guidance, encouragement, and patience during the experimental work and preparation of this thesis are greatly appreciated.

I also wish to thank Dr. W. H. Kelly of the Physics Department and Dr. F. Bernthal and Dr. R. Warner of the Chemistry Department for their help and advice. Their suggestions and advice during this project were very useful.

Dr. H. G. Blosser and Mr. H. Hilbert, assisted with the operation of the Michigan State University Sector-Focused Cyclotron.

Dr. J. Black, Mr. W. B. Chaffee, Mr. B. Jeltema, Dr. R. E. Doebler, Ms. C. Dors, Ms. J. Guile, Dr. R. E. Eppley, Mr. R. B. Firestone, Dr. R. Goles, Mr. C. Morgan, Dr. L. Samuelson, Mr. M. Slaughter and Dr. R. Todd all deserve special mention for their assistance and advice throughout the course of these experiments.

Mr. R. Au, and the cyclotron computer staff have aided greatly in the data aquisition and evaluation through the use of the XDS Sigma 7 computer.

Help has also been received from Mr. R. N. Mercer and his staff in the cyclotron machine shop, and from Mr. W. Harder and the cyclotron electronics shop.

The cyclotron drafting staff, especially Mrs. M. Blosser, have been very helpful and quick in preparing the drawings for this thesis.

Our secretaries Mrs. P. Warstler and Mrs. C. Vanneste have helped in typing this thesis.

I thank the National Science Foundation, U. S. Atomic Energy Commission, and Michigan State University for their financial support without which this study would not be possible.

Finally, I particularly wish to thank my wife, Bonnie, for her assistance in the operation of the cyclotron and in the collection of data.

TABLE OF CONTENTS

LIST OF TABLES

LIST OF FIGURES

Figure

Page

CHAPTER I

Introduction

I. a. General

There remain approximately 2000 unknown nuclides with half-lives in the range between 10^{2} and 10^{-2} seconds [BeI66a]. This includes all the remaining unknown β unstable nuclei, except some superallowed β decays which may have half-lives as short as 10^{-3} seconds, in addition to proton, neutron, and γ emitters. Figure 1 (taken from [RuG67]) is an approximate breakdown of stable or very long-lived ($t_{1/2} > 10^{9}$ years) nuclides and unknown nuclides lying between the limits of the neutron drip line and proton stability. Further, there is an indication of expected half-lives. Clearly most of these remaining unknown nuclides are expected to have half-lives of less than one second and they will outnumber the nuclides presently known. The remainder of this introduction will be devoted to a short discussion of why and how these nuclides should be investigated.

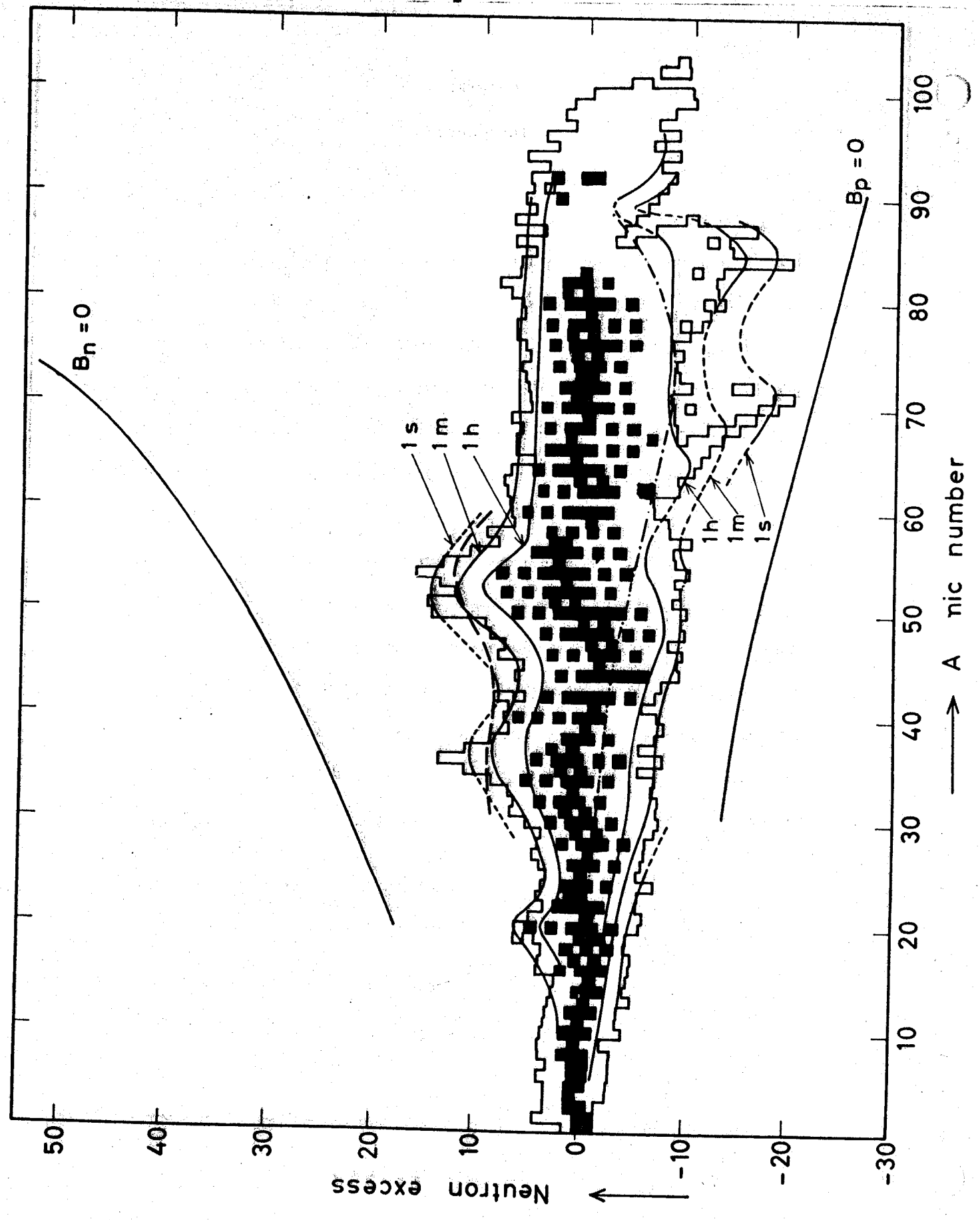

Figure 1. Approximate breakdown of nuclides lying between the neutron drip line and proton stability according to half-life. This figure is taken from [BeI66a].

I. b. Why Nuclides far from β Stability Should be Studied

β-Delayed Particle Emission

Beta-delayed particle emission occurs when as a result of β-decay the nucleus is left in an excited state, one for which the binding energy for the last neutron, proton, or α particle is negative and Coulomb barrier penetration in the case of protons or α particles competes with γ deexcitation. Cases of β-delayed particle emission have been observed for each type particle.

These decays are accessible to study using techniques designed for working with activities with half-lives greater than 10^{-2} seconds because the overall half-life for these processes is determined by the half-life of the β decay. Most of these cases found thus far are in the low-Z region where the energy available for decay and the average level spacings are large; however, now cases are being reported in the higher-Z region. Also found are regions where the binding energy for an α particle or the last proton or neutron is low, such as just above a closed shell.

The number of unknown delayed particle emitters should be quite large [BeI66a][BeD65]. Through a careful mapping of these nuclides and consideration of their particle emission energies, further refinement of the parameters in the semiempirical mass formula should be possible. Also, as far as these parameters relate to nuclear structure, further refinement there may be possible.

Particle Emission

In addition to delayed particle emission, proton and α emission begin to compete successfully as modes of decay as one proceeds further from β stability. Many of the least energetic of these decays will have half-lives in the 10^{2}-10^{-2} second range because of the difficulty of Coulomb barrier penetration. A study of these nuclides should yield information on both nuclear masses from the energetics of the decays and on nuclear wave functions from half-lives, which reflect the ability of the emitted particle to penetrate the Coulomb barrier.

New Doubly Magic Regions

It should be possible to reach the doubly magic 28-28 region using proton reactions and the 50-50 region using heavy ion reactions. Several of the nuclides only one or two nucleons removed from ^{56}Ni and most of the nuclides of the ^{100}Sn region remain unknown. A study of these nuclides one nucleon removed from doubly magic will of course involve a determination of their levels. Accordingly, these experimentally determined levels can then be used to extend calculations to the levels in nuclides further removed.

Transition Region Nuclides and New Deformed Regions

It is known in at least one case that practically spherical even-even nuclei may remain spherical as nucleon pairs are added until it

very suddenly "collapses" with the addition of another nucleon pair to a shape of stable deformation. This is evidenced by the vibrational nuclear structure suddenly changing to a rotational one with the addition of a nuclear pair. The example of this "collapse" or transition between essentially spherical and permanently deformed nuclei takes place in the beginning of the rare earth region between neutron numbers 88 and 90 [BeI66a]. (A second example of the sudden onset of deformation may be occurring at about ^{135}Nd [EkC72].) Nuclear states in the region of this sudden transition should not be amenable to either purely vibrational or rotational description. There have not been many of the nuclides of this type experimentally investigated and many more experimental studies are needed. Further, expanding decay studies to nuclides further from β stability will yield information on many more deformed nuclides including many in new deformed regions, such as the one starting in the extremely neutron deficient Xe- and Ba- isotopes [MoH65][ShR61].

Access to Highly Excited States

Because of the high energies associated with β decay far from the stability line, it will be possible to populate highly excited states in this decay. Beta decay will then complement nuclear reaction studies in examining these states. If one also considers the difficulty in obtaining suitable, i.e., stable or long-lived targets for nuclear reaction studies on nuclei far from β stability, it is probable that

β-decay studies will become the primary means of investigating these states.

Nuclear Masses from *Q*-values

The semi-empirical mass formula is in a sense a measure of a quantitative understanding of nuclei. Nested in the upwards of 40 parameters necessary to get accurate predictions are liquid drop model effects, shell model effects, and effects from other models. Accurate experimental masses measured in regions chosen to test specific parameters are thereby testing nuclear models and conceivably may lead to a more fundamental composite model. Many of the most interesting mass measurements will be made on nuclei far from β stability and can be made through determination of reaction *Q* values.

Results of Interest in Astrophysics

One of the more basic goals of astrophysics is that of developing models that will account for the relative abundances of elements in the universe. Two of the most important types of experimental information necessary to develop such a model are decay half-lives and cross-sections. Many of the more important half-lives, in particular those necessary to account for the build-up of elements above ^{209}Bi are of nuclei lying far from β stability [Bel66a].

In addition, there are many specific bits of nuclear information missing about nuclear reactions, decay energies, branching ratios, etc.,

that are necessary to check and extend current astrophysical theories. Much of this needed information is about nuclei lying far from β stability.

I. c. How Nuclides Far From β Stability Can be Studied

There are several difficulties associated with the study of nuclides far from β stability which have definitely limited their study using standard nuclear techniques. Accordingly, any serious attempt at extending nuclear investigations to regions far from β stability will have to provide new or improved techniques to overcome these difficulties. The degree of success in overcoming these difficulties will determine the profitability of any attempt at studying nuclei far from β stability. The remainder of this introduction will be devoted to a short discussion of the requirements these difficulties impose on any system to study nuclides far from β stability and how our proposed systems meet these requirements. A discussion of those techniques proposed or being implemented by other researchers studying nuclides far from β stability is beyond the scope of this thesis [MaR72b][AnG66].

The most obvious requirement of any system designed to study nuclides far from β stability is that it must provide a method of generating these nuclei in sizeable number. In a paper prepared for presentation at the International Symposium on Why And How Should We Investigate Nuclides Far Off The Stability Line [RuG67], Rudstam presents a comparison of several possible methods for producing nuclides far from β stability. The processes considered are medium energy (<50 MeV) charged particle (p,d,α) reactions like (p,xn); high energy proton reactions like $(p,2p)$,spallation $(p,2pxn)$, and proton induced fission;

heavy ion induced reactions like (HI,xn); thermal neutron fission; and (n,p) reactions with energetic (14-MeV) neutrons. The comparison between these processes is made for target material between Z=25 to 75.

While Rudstam's comparison is based on estimates of cross-sections and more or less typical beam intensities of different types of machines used to generate radionuclides, a presentation of a summary of his conclusions may be helpful. For the production of moderately neutron-deficient isotopes ($\lesssim$10 neutrons deficient) throughout the range of Z=25 to Z=75, medium energy charged particles (p,d,α) should prove to be best by far. However, as one proceeds to extremely neutron deficient isotopes, heavy-ion and spallation reactions should compete well with medium-energy proton reactions for the best production rates, with heavy-ion reaction producing better yields than spallation. For the production of neutron-rich isotopes throughout the range Z=35 to Z=55, thermal fission should prove to be best by far. However, in the region below Z=35, high-energy proton and spallation reactions are favored and in the region above Z=55 high energy proton reactions like (p,$2p$) are favored. One of Rudstam's figures (that for Z=55) has been included as Fig. 2. Rudstam's figure of merit (FM) is defined by the relation

$$FM = \int_0^d I(x)\ \sigma(x)\ \rho\ dx,$$

where I is the particle density, σ is the reaction cross-section, ρ is the target density, and d is the thickness. Rudstam assumed the following beam intensities:

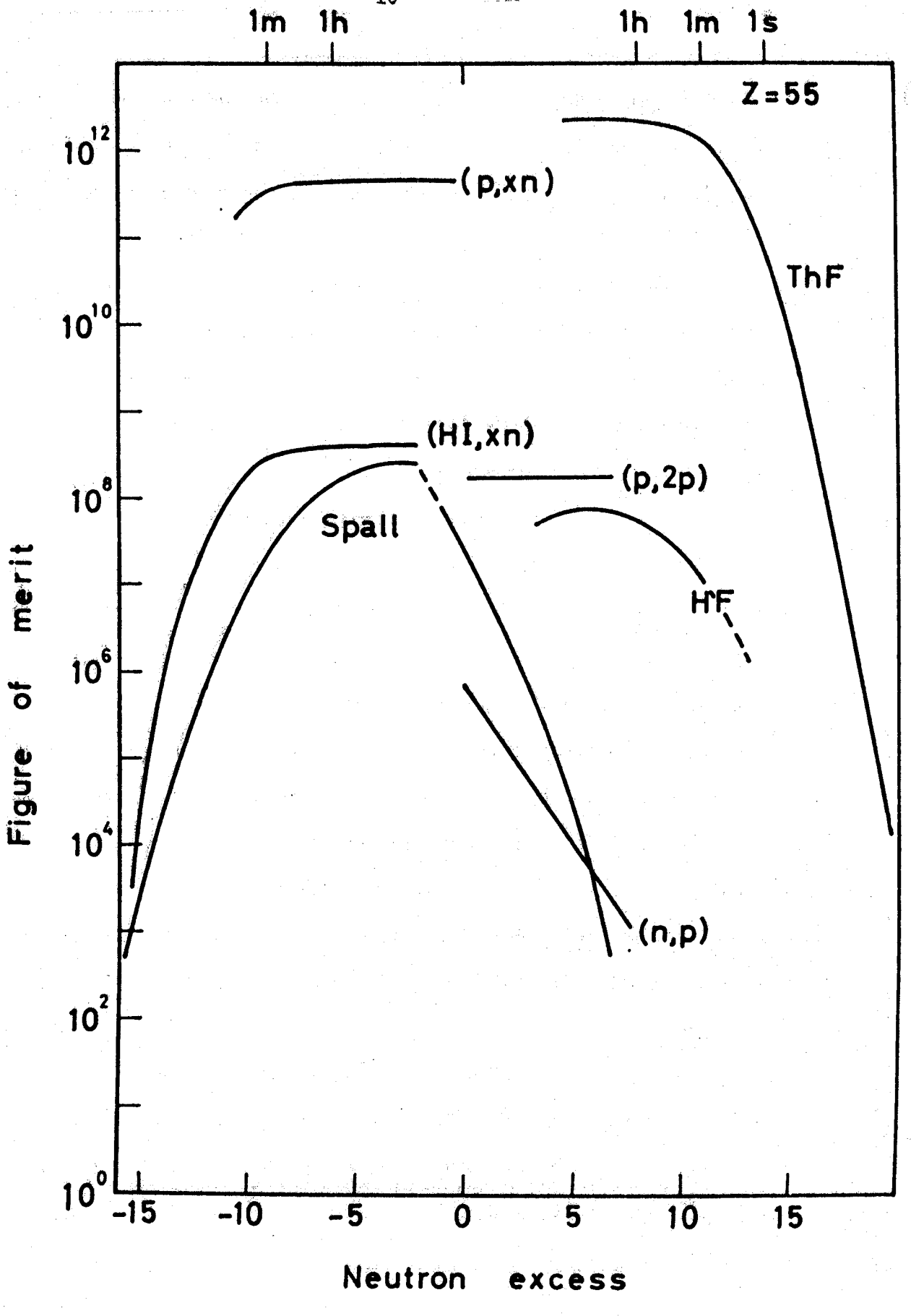

Figure 2. Graphic display of the usefulness of various techniques for generating radionuclides from targets with Z=55. This figure is taken from [RuG67].

Med. energy p or d	100 μA
High energy p	1 μA
Heavy ions	6×10^{12} HI/sec
Thermal n	10^{14} n/cm^2sec
High energy n (14-MeV)	10^{10} n/cm^2sec

In those instances where experimental cross-sections were not available, Rudstam used extrapolated or estimated values.

A second requirement for the system is that it be capable of providing the radionuclides in a form suitable for study in times approximately equal to their half-lives. If we wish to consider β unstable nuclides out to the limits of the neutron drip line and proton stability, then it is necessary to consider times as short as 10^{-2} seconds (and possibly even as short as 10^{-3} sec for a few superallowed transitions). To the extent that it is desirable not to count in beam or to use pulsed beam techniques, it is necessary to transport the activities to low background areas. In addition, for charged particle spectroscopy, it is necessary to accomplish a removal of the radionuclides from the target material in order to make a suitable source for counting, all in these short times. Further, in that daughter activities will be rapidly built up, it is necessary to provide for the continuous removal of old source material after being counted for some time interval.

For each of the possible mechanisms for generating nuclides far from β stability (proton or heavy ion induced reactions or fission), a large number of different product nuclei will result and in most

instances the interfering products will greatly out-number the desired products. Thus, an additional requirement of the system is that it provide some means of isolating or at least enriching the desired product nuclei in order to limit interfering radiations. Ideally this would be accomplished using a combination of chemical and isotopic separations.

The earlier discussion of Rudstam's paper suggests that it will be possible to produce nuclei far from β stability in good yields using proton beams with energies ≤50 MeV or ^{3}He beams with energies ≤75 MeV (with currents ≤5 μA on target) from the Michigan State University Sector Focused Isochronous Cyclotron to initiate (p,xn) or $(^{3}He,xn)$ reactions. Table 1 (in Chapter II) provides a listing of some of the reactions that are possible using these beams from the MSU Cyclotron. In most regions of the nuclear chart it should be possible to reach from one to four nuclei beyond those presently reported and several nuclei beyond those for which fairly complete data are available. In addition, it is anticipated that the MSU Cyclotron will be capable of producing heavy ion (carbon, etc.) beams before too long. It may then be possible to extend even further into the extremely neutron-deficient regions. However, the yields for these reactions will be less than those with p or ^{3}He beams.

Block and schematic drawings of one of two on-line mass separation systems presently under consideration are shown in Figure 3. At this time the system and the operation of its component parts will only be

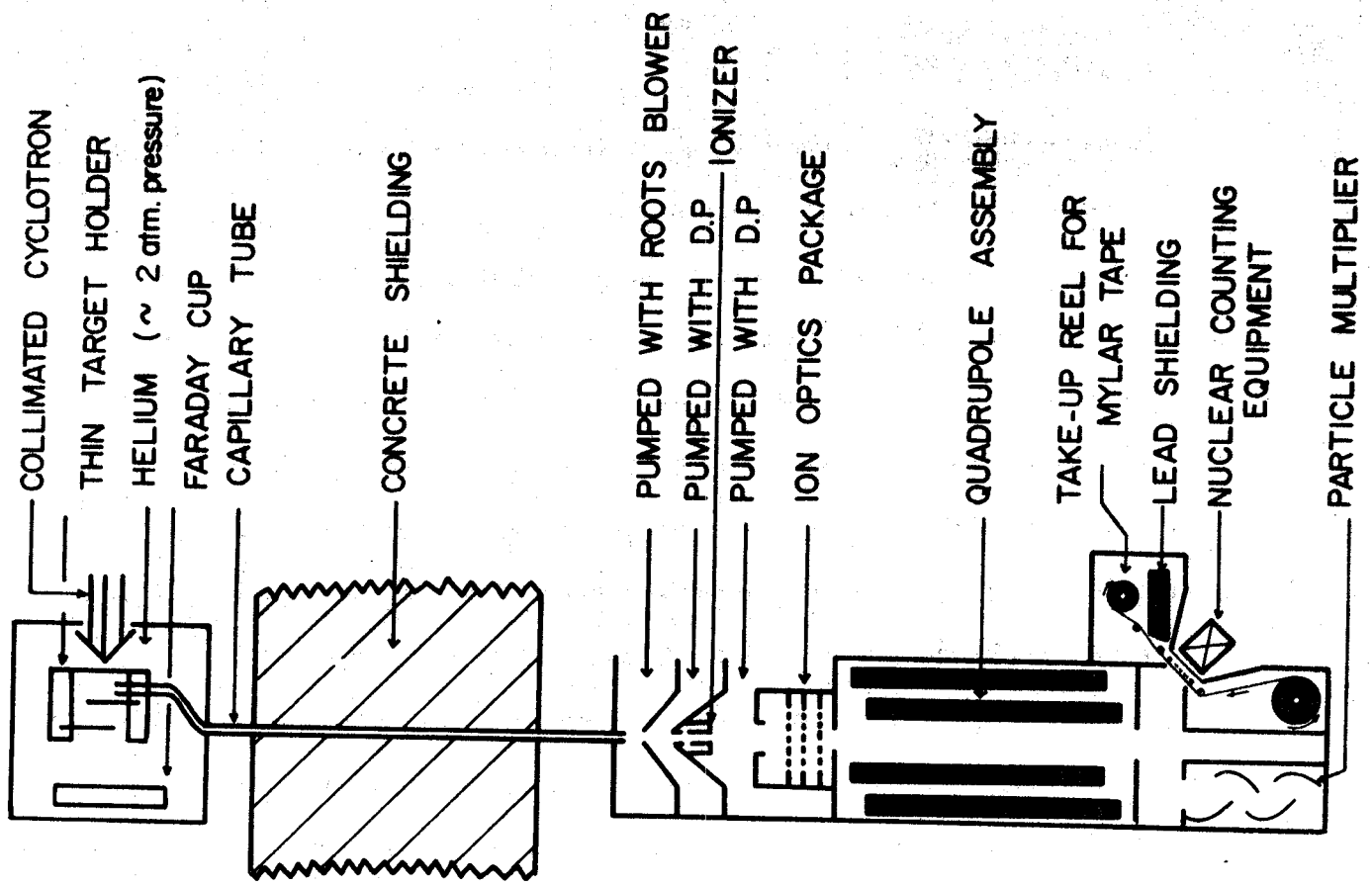

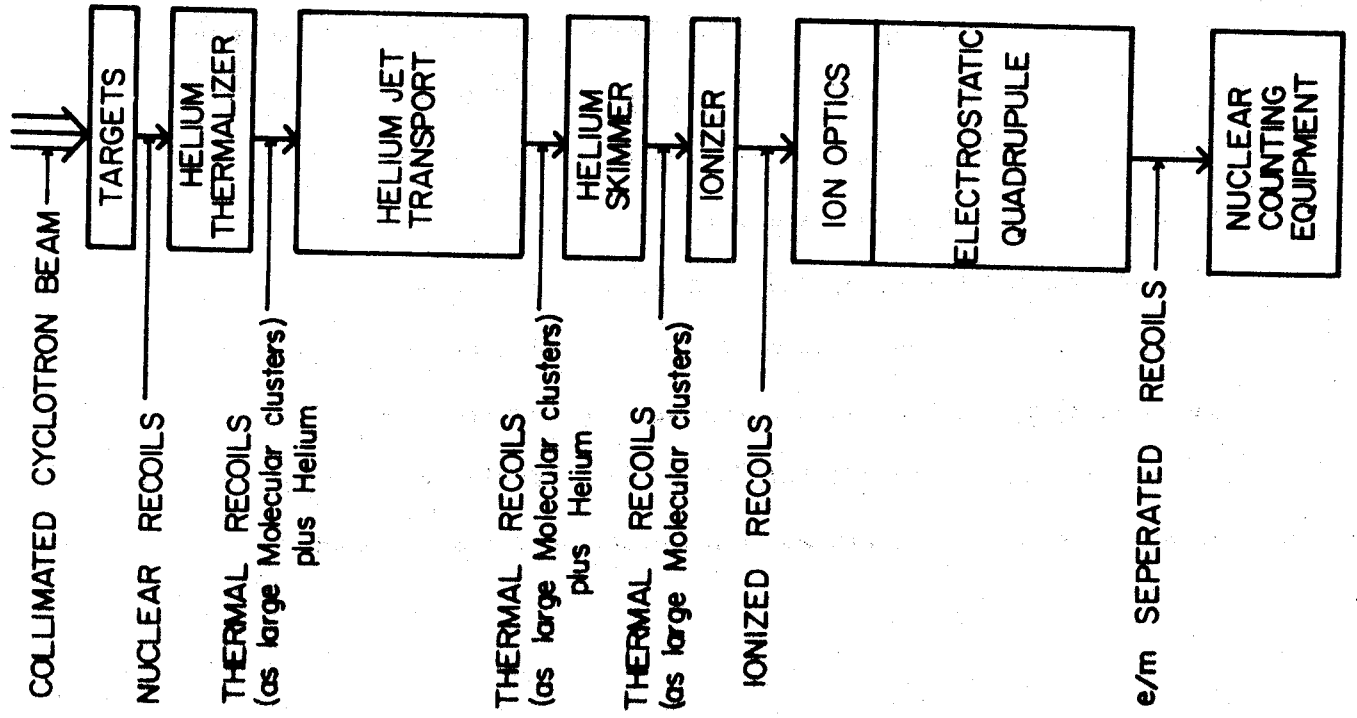

Figure 3. Sketch and block drawing of a proposed on-line system employing an electric quadrupole for mass filtering.

discussed briefly. A more detailed discussion of its construction and operation will follow in later sections.

In the Helium Jet Recoil Transport (HeJRT) portion of the system a collimated cyclotron beam enters the apparatus, striking a thin target (or a series of thin targets) in an atmosphere of helium. Those nuclei near the back of the target that interact with the beam will recoil out of the target into the helium atmosphere. Some of the characteristics of these nuclear recoils for a few representative targets and beams are listed in Table 1. The nuclear recoils are slowed to thermal energies by collisions with the helium atoms. Recent work by R. D. Macfarlane [JuH71] and in this lab suggest the next step is the attachment of the thermal recoils to large molecule clusters (with masses up to 10^8 amu). These cluster molecules are formed in the plasma generated by the cyclotron beam passing through the helium atmosphere from impurities added to the helium. The nuclear recoils are then removed from the target chamber by differentially pumping the helium containing the molecular clusters out through a polyethylene capillary. The capillary is run through concrete shielding to a low background area about 40 feet away.

At the end of the capillary most of the helium will be removed using a one or two stage skimmer. Quite efficient skimming should be possible by just directing the flow coming from the capillary at a coincal orifice [MaR72] [NiJ70]. The molecular clusters with their enormous masses are extremely well collimated (see Section II. g.

"Capillary Considerations") and will be passed quite efficiently through the orifice, whereas the helium will have a much larger angle of divergence as it leaves the capillary and will therefore largely be pumped off. If our pumping capacity is not sufficient to reduce the pressure after the first skimmer stage to the low pressures required to operate the electric quadrupole, a second skimmer stage will be used.

The molecular cluster will be broken up and the nuclear recoils ionized using a discharge set up in one of the skimmer stages, with the recoils directed into the ion optics associated with the electric quadrupole. With the quadrupole set up properly, only selective masses (e/m) will be transmitted through it [PaW58]. At the exit of the quadrupole the mass separated ions will be deflected either into an electron multiplier such that it will be possible to obtain a mass scan or onto paper or aluminized mylar tape for conventional nuclear counting.

It appears this system will be capable of providing mass-separated nuclear reaction products, separated from the target and transported to a low background area, in very short times ($\gtrsim$100 msec, Section II.g. "Capillary Considerations"), continuously, and with daughter activities removed. Thus, this system should meet all the requirements mentioned previously, with the exception of providing a chemical separation in addition to the mass separation provided by the electric quadrupole. It now seems that it may be possible to accomplish this chemical separation at the time of attachment of the nuclear recoil to the molecular cluster during thermalization (see Section II.o. "Plasma Chemistry").

A second system, and the one we will most probably construct first and patterned directly after R. D. Macfarlane's "MAGGIE" system [JuH71], is sketched in Figure 4. At this time the system and the operation of its components will be discussed only briefly. A more detailed discussion of its construction and operation will follow in later sections.

The first portion of this system as in the first system described is the Helium Jet Recoil Transport (HeJRT) subsystem; its operation was described above. Again, as in the first system described, the flow from the capillary is directed at a conical orifice (helium skimmer) to remove most of the helium from the flow and allowing most of the large molecular clusters with their nuclear recoil atoms attached to pass to the next stage of the system.

The next stage of the system is a time-of-flight spectrometer. The molecular clusters with their nuclear recoils still attached are collected on a metal plate just after the helium skimming orifice. The clusters stick to the surface on impact with it. Macfarlane has found that if the proper impurities were used to generate the molecular clusters and if the collecting surface is heated to about 200°C, the cluster molecule is broken up and driven off, leaving the nuclear recoil bound very weakly to the collecting surface. As the activities on the collecting surface β decay, the portion that decay with the proper geometry will recoil from the collecting surface. Some fraction of these β recoils will become ionized by shake-off and will be accelerated away from the collecting surface, using an accelerating grid. The

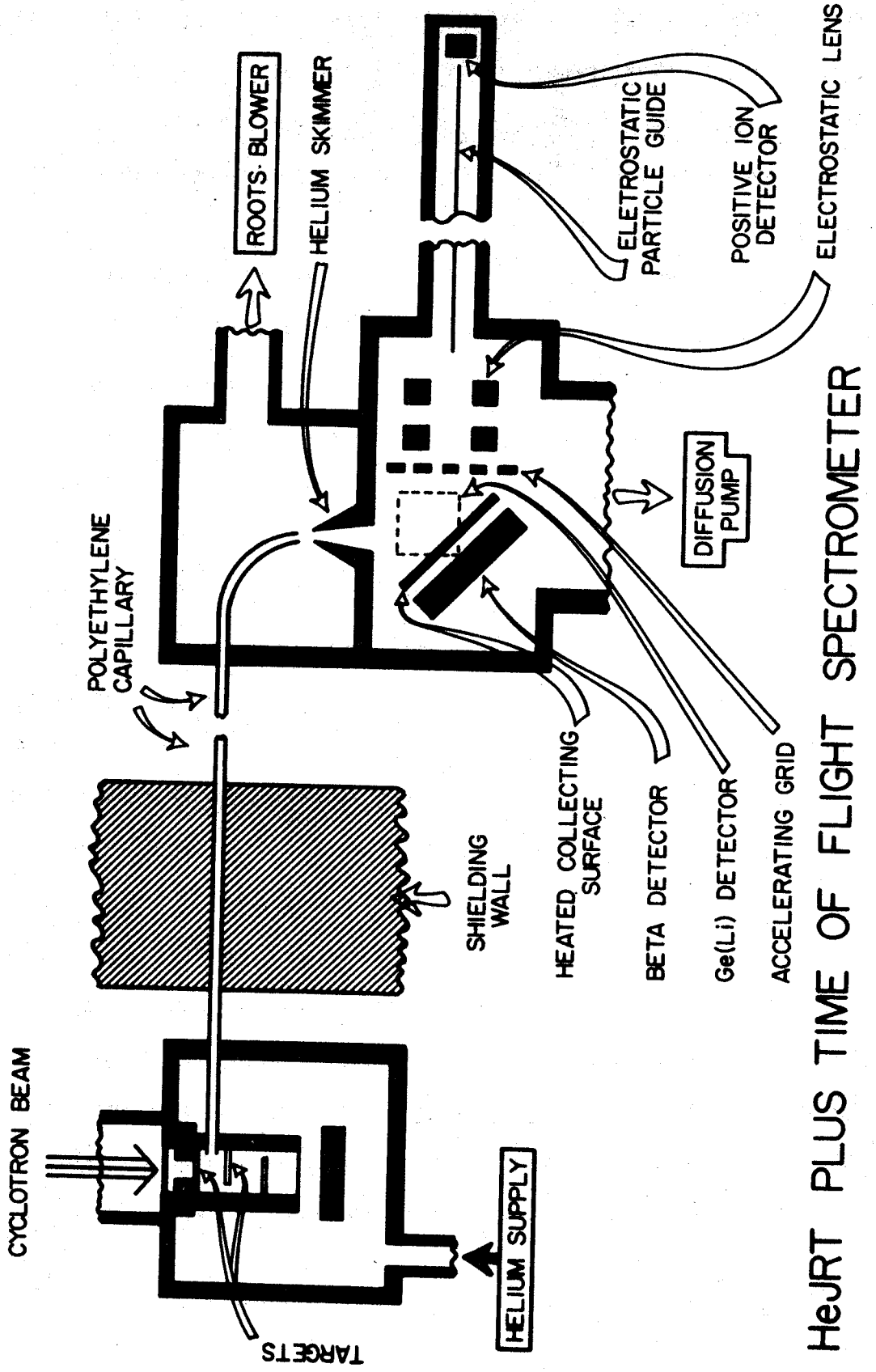

Figure 4. Sketch of a proposed on-line system employing a recoil time-of-flight spectrometer for mass identification.

accelerated β recoils are electrostatically focused and enter a particle guide which consists primarily of a charged wire running down the center of a grounded metal pipe. The β recoils follow the trajectory of a helix about the central wire. A detector for the β recoils is placed at the end of the particle guide.

If the β particle from the decay is observed in the detector behind the collecting surface, it can be used to fix the time of the decay. The time of flight of the β recoil can then be established using the output of the positive-ion detector at the end of the particle guide. Knowing the accelerating voltage and the length of the flight path, the mass of the β recoil can be determined. The outputs from the β and positive-ion detector will provide start and stop signals for a time to amplitude converter (TAC) where the output in this case will be proportional to the mass of the β recoil. Then if a γ detector is placed in the region of the collecting surface where the decay is taking place and the output of the TAC is used to route the ADC output from the γ detector into different memory locations a series of γ spectra will be recorded, each associated with a particular mass β recoil.

It appears this system will be capable of providing mass identified γ spectra in very short times (≥100 msec), continuously and without significant interference from daughter activities. As in the previously described system, it is possible to consider performing a chemical separation at the time of attachment of the nuclear recoil to the molecular cluster in the target assembly. However, this may

be a more difficult task in view of the added requirement that the cluster molecules break up on heating of the collecting surface.

CHAPTER II

HELIUM JET RECOIL TRANSPORT SYSTEM

II. a. General

Quite apart from its intended use as the first stage of the isotope separator described at the close of the introduction, the helium jet recoil transport (HeJRT) system can be used to provide sources suitable for most nuclear counting experiments. It can provide sources in which the radionuclides have been physically separated from the target and continuously transported to a low background in times <250 msec. Accordingly, the HeJRT system has been used with increasing frequency to provide α, β, and γ sources for study in this lab [Gig71], [BlJ72], [KoK72].

While in essence the operation of the HeJRT system is quite simple, much of the detail of its operation is not understood. Thus, satisfactory operation of the system is achieved more by using techniques that are better described as artful rather than scientific. As a result, when one collects the thoughts and impressions of researchers using some form of HeJRT system, one gets a collection in which much of the fine detail of its operation and many of the corresponding "best recipes" are not widely accepted. What follows in this Chapter are my thoughts and impressions on the construction, operation, and use of the HeJRT system we have constructed.

II. b. Calculation of Recoil Characteristics

Table 1 was prepared to point out possible nuclear reactions and to display some of the expected characteristics of the recoiling reaction products. The targets were chosen to approximately span the mass range of targets we expect to use in the HeJRT system. While the highest beam energies listed in the Table are not the upper limit of the MSU cyclotron, they are nearly the highest energies run routinely. Also, possible reactions and recoil characteristics for deuteron and α beams were omitted to keep the table short.

Probable (p,xn) and $(^3He,xn)$ reactions were determined solely on the basis of Q values (Q values were determined by Clare Morgan [MoC71] using the mass tables of Garvey, Grace, and Talmi or of Harvey). Where Q values were not known an estimate was made based on an extrapolarion from known Q values following systematically from other known Q values in the region. In several cases for the beam energies listed it may be possible to boil out an additional neutron. However, the yields for these reactions should be smaller than for those listed in the table. There was no attempt to account for any additional energies needed over the Q value to initiate the reaction, such as overcoming the centrifugal barrier. Also, there was no attempt made to determine the extent to which reactions involving the loss of charged particles will compete with the reactions listed. It should be expected that reactions involving the loss of charged particles will compete favorably with most of the xn reactions, particularly for those that involve

Table 1. Reactions and Recoil Characteristics Expected Using the MSU Cyclotron

Target	Energy Particle	Probable xn Reaction [a]	Reaction Product	Initial Energy of Recoils [b] (MeV)	Maximum Range of Recoils [c] In Target (mg/cm^2)	In Target (Mils)	In Helium STP (Mils)
^{24}Mg	30 MeV p	$(p,2n)$	^{23}Al	1.1	0.37	0.065	550
	45 MeV p	$(p,3n)$	^{22}Al	1.6	0.50	0.082	770
	35 MeV ^3He	$(^3He,3n)$	^{24}Si	3.4	0.69	0.124	1300
	70 MeV ^3He	$(^3He,5n)$	^{22}Si	6.4	1.19	0.188	1700
^{50}Cr	30 MeV p	$(p,2n)$	^{49}Mn	0.57	0.20[d]	0.009[d]	180[d]
	45 MeV p	$(p,3n)$	^{48}Mn	0.84	0.29	0.013	280
	35 MeV ^3He	$(^3He,3n)$	^{50}Fe	1.9	0.58	0.027	530
	70 MeV ^3He	$(^3He,5n)$	^{48}Fe	3.6	0.95	0.041	970
^{96}Ru	30 MeV p	$(p,2n)$	^{95}Rh	0.30	0.08[d]	0.002[d]	60[d]
	45 MeV p	$(p,4n)$	^{93}Rh	0.45	0.11[d]	0.003[d]	80[d]
	35 MeV ^3He	$(^3He,3n)$	^{96}Pd	1.0	0.24[d]	0.006[d]	200[d]
	70 MeV ^3He	$(^3He,6n)$	^{93}Pd	2.0	0.52	0.014	390
^{203}Tl	30 MeV p	$(p,4n)$	^{200}Pb	0.14	0.02[d]	0.001[d]	20[d]
	45 MeV p	$(p,6n)$	^{198}Pb	0.21	0.04[d]	0.001[d]	20[d]
	35 MeV ^3He	$(^3He,4n)$	^{202}Bi	0.50	0.08[d]	0.003[d]	60[d]
	70 MeV ^3He	$(^3He,8n)$	^{198}Bi	0.98	0.17[d]	0.005[d]	110[d]

[a] Probable (p,xn) or $(^3He,xn)$ reactions were determined on the basis of Q values determined using the mass tables of Garvey, Gerace and Talmi or of Harvey [MoC71]. Where Q values were not known an estimate was made. In several cases for the beam energies used in this table, it may be possible to boil out an additional neutron. However the yields for these reactions should be smaller than for the reactions listed. There was no attempt to determine the extent to which reactions involving the loss of charged particles will compete with each of the xn reactions listed. However, some of the reactions involving the loss of charged particles are expected to compete well with the xn reactions at high energies, low-Z targets, or very neutron-deficient regions.

[b] The initial recoil energies were determined on the basis of conservation of linear momentum between the particles of the beam and the compound nucleus and considering no additional sources of momentum in the breakup of the compound nucleus.

Table 1. Continued -

[c] Recoil ranges were determined using the range tables of Northcliff and Schilling [NoL70]. Corrections to the range were made to account for the mass of the recoil differing from the mass of the isotope reported in the table. The corrections assumed the primary source of energy loss to be from electronic stopping. Also,interpolation was done between the stopping media reported in the table to obtain the ranges in the targets.

[d] For particularly low values of e/m ($e/m \leq 0.0125$ MeV/amu) the ranges were obtained by extrapolating the tables. These results have particularly large uncertainties associated with them due to a large portion of their range being determined by nuclear stopping. In the case of the ranges in the targets this is further complicated by the nuclear stopping collisions occurring between approximately equal mass particles.

high beam energies, low-Z targets, and very neutron-deficient regions.

Parameters such as target thickness, target separation, and helium pressure used in setting up the target chamber for a run are based on calculations of the energy for the nuclear recoils. For several reasons these calculations were kept simple and contain many assumptions. The foremost reason was the large uncertainties associated with the range of very low energy, high mass particles, which makes precise calculation of recoil energy unrewarding. Second, in most instances it is possible to use values in setting up the experiment that are on the safe side of the calculated values by factors of 2 or 3 without seriously impairing the operation of the HeJRT system.

As a result of the medium energies of the particle beams generated by the cyclotron, the primary mechanism for the nuclear reactions involves compound nucleus formation. It is a simple matter to calculate the recoil energy of the compound nucleus by just considering linear momentum conservation (effects such as the energy transferred to the lattice holding the target nucleus are too small to be considered). The most extreme assumption made in calculating recoil energies is that there are no additional sources of momentum for the recoil associated with the breakup of the compound nucleus. This is clearly not the case and further this source of momentum can be quite large. However, in that the breakup of the compound nucleus will be roughly isotropic, the gross features of the energy distribution of recoils leaving the target will be unchanged. The exception would be the

high energy tail corresponding to recoils generated at backside of the target that have had their recoil energies altered in the break-up of the compound nucleus.

Maximum recoil ranges in the target and in He(STP) were determined using maximum recoil energies. The ranges were obtained from the range tables of Northcliffe and Schilling [NoL70]. In many instances the maximum recoil energies fall below the lowest reported in these tables. For these cases the ranges reported were extrapolated off the end of the tables. It should be expected that the uncertainties associated with recoil ranges in the target determined by extrapolation are large. Within the limits of the tables, Northcliffe and Schilling determine their ranges considering energy losses occurring through both electronic and nuclear stopping mechanisms. However, in the case of very low energy recoils (recoil velocities $<10^8$ cm/sec [HaB60]) the energy loss mechanism is primarily through nuclear stopping. In the case of the recoils traveling through the target, the mass of the recoil and the mass of nuclei in the stopping medium are essentially equal and the recoil can lose up to half its energy in a single collision. Accordingly, the ranges for these recoils will vary considerably recoil to recoil and the calculated ranges can only be considered an average effect.

II. c. Target Assemblies

A sketch of a target assembly employing a single target is included as Figure 5. Here the cyclotron beam enters from the left through a Havar window (0.001 in. in practice) separating the vacuum of the beam line from the helium atmosphere (1 to 4 atm pressure, typically run at 3 atm). See Sections II. i. "Efficiency vs. Target Assembly Pressure" and II. g. "Capillary Considerations" for discussions of the effect of He pressure on transport efficiency and on transport times, respectively. The volume between the Havar window and the target is sealed with a foam rubber gasket. This is to prevent those recoils from the window that are thermalized in this volume from entering the bulk helium supply and being swept out of the assembly along with recoils from the target.

As a result of interaction with the cyclotron beam, product nuclei recoil from the back surface of the target into the helium. Through collisions with helium atoms the recoils lose their initially high kinetic energies and are reduced to thermal energies. The approximate ranges for some typical recoils carrying a maximum energy are listed in Table 1. By pumping on the capillary, located immediately behind the target, a flow of helium down the target cylinder, mounted behind the target, and out the capillary is established. Recoils in the helium are swept with the helium from the volume behind the target and out the capillary (capillary typically used has an inside diameter of 0.055 in. and is made of polyethylene).

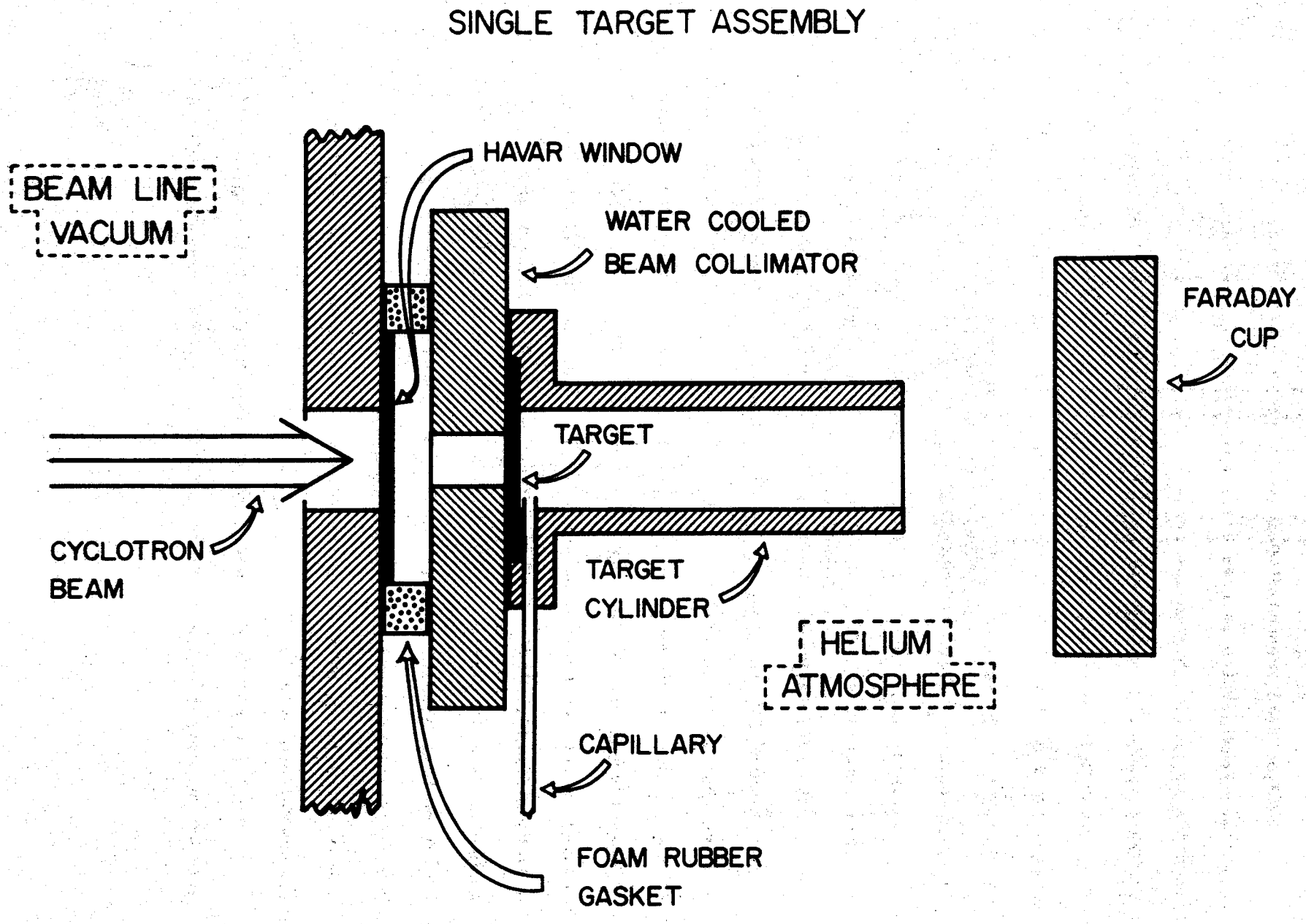

Figure 5. Single target assembly of the HeJRT system.

A major time consuming step in the process of thermalizing recoils and transporting them from the target area to low background counting areas is the time necessary to sweep the recoils from the thermalizing volume behind the target into the capillary. Accordingly, it is desirable to keep this thermalizing volume to a minimum by reducing the diameter of the target cylinder. To facilitate this, the cyclotron beam is collimated using a water cooled collimator before it is allowed to strike the target.

Initially, the target cylinder was intended to help concentrate the most recently thermalized recoils in the flow of helium leaving through the capillary and keep them from diffusing throughout the chamber containing the target assembly. However, it was subsequently learned that it is necessary to attach the recoils to large molecular clusters (cluster of masses up to 10^8 amu [JuH71]) in order to achieve efficient transport of the recoils through the 40 ft of capillary leading to the low background counting area (see Section II. f. "Cluster Molecules" [MaR72, WiK72, BoW72]). These molecular clusters are generated from impurities in the helium in the plasma provided by the cyclotron beam passing through the helium behind the target. It is presently intended that the target cylinder help concentrate the molecular clusters as well as the recoils in the flow of helium leaving through the capillary.

Figure 6 displays the result of an experiment to test the effectiveness of the target cylinder in concentrating suitable molecular clusters

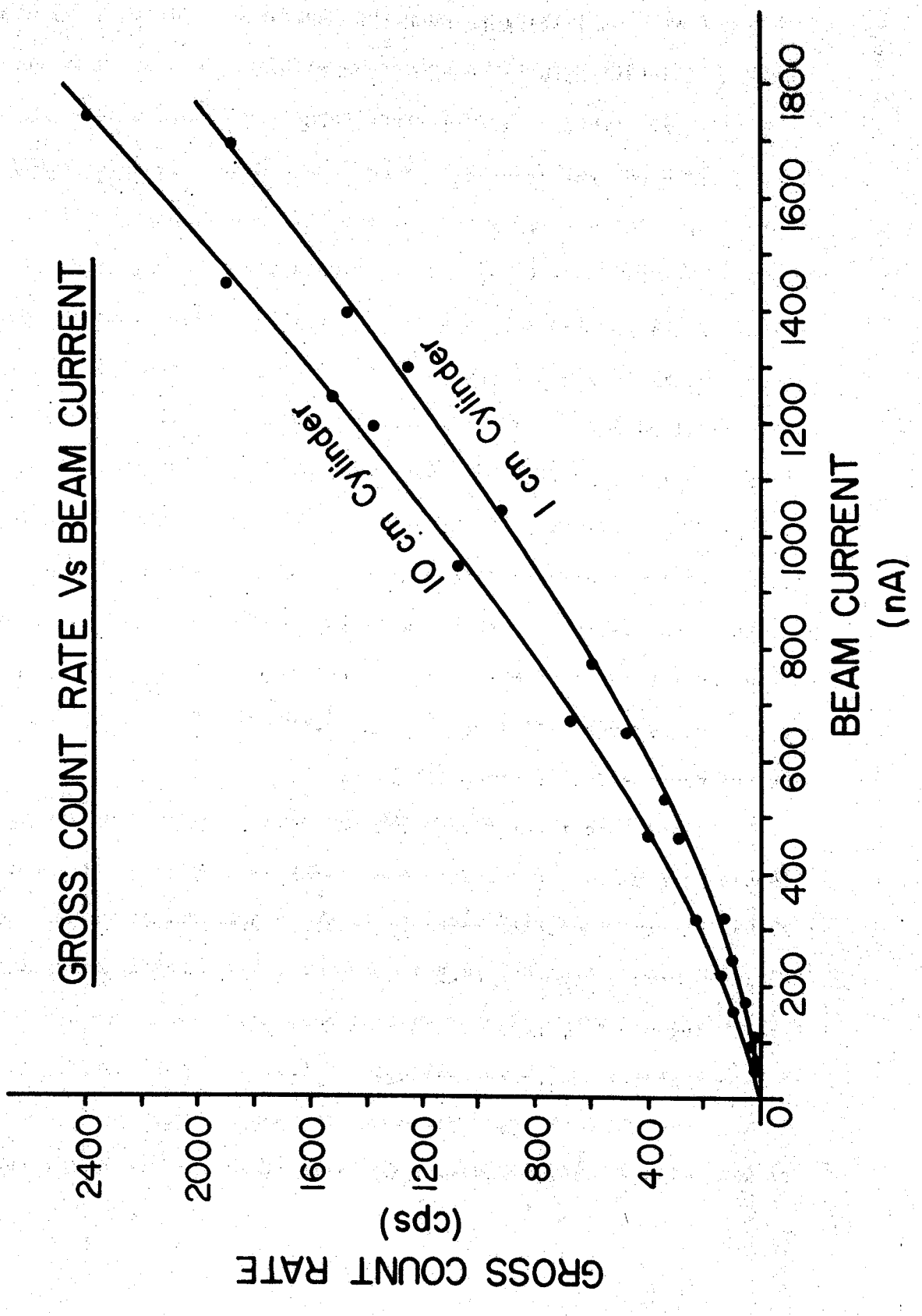

Figure 6. Gross count rate vs beam current compared for long and short target cylinders

in the helium flow leaving through the capillary. For this experiment a silicon (quartz) target was bombarded with 30-MeV protons to generate ^{28}P ($t_{1/2}$ = 280 msec). Two different target cylinders were used: one was 1 cm long and the other was 10 cm long. Both cylinders were 2 cm in diameter. The maximum range for the ^{28}P recoils, was less than 1/2 cm for 3 atm helium pressure. After considering the magnitude of the flow of helium leaving through the capillary (120 standard cm^3/second) and the maximum range for the ^{28}P recoils it is apparent that a very small number of, if any, recoils could have diffused out of either target cylinder and not have been swept with the helium into the capillary. Relative efficiencies for the system when run using each of the two cylinders were determined by just comparing the gross γ count rates observed. Spectra were recorded to make certain that peak areas for the 1.78-MeV peak of ^{28}P followed the gross γ count rate. The improved efficiency for the system when run using the long cylinder is obvious from Figure 6.

It is possible to attribute the improved efficiency of the target assembly when using the 10 cm cylinder to something other than concentrating suitable molecular clusters in the thermalizing volume. However, upon considering the increase in the relative efficiency of the system using the long cylinder as less beam current was run (at 1.6 μA the long cylinder system was 21% more efficient at transporting recoils than when the short cylinder was used, as compared with 75% more efficient at a 0.2 μA), it does seem likely that the improved transport

efficiency for the long cylinder system is related to the generation and/or concentration of suitable cluster molecules in the thermalizing volume. If the transport efficiency improvement were associated with an improvement in the flow characteristics along the long cylinder and into the capillary (which could significantly improve transport efficiency), it would be expected that the transport efficiency improvement would not be beam current dependent. A more detailed discussion of the shape of the curves presented in Figure 6 will be presented in Section II. f. "Cluster Molecules".

The capillary presently being used has an inside diameter of 0.055 in. and, with the exception of a short stainless steel end that attaches to the target cylinder, is made of polyethylene (Clay-Adams Intermedic) tubing. The coupling between the stainless steel and polyethylene capillaries is made by first cutting the polyethylene and grinding the stainless steel tubing in special jigs so that they are cut off perpendicular to their axes. The two pieces of tubing are then brought together by inserting them in a tight fitting sleeve, see Figure 7.

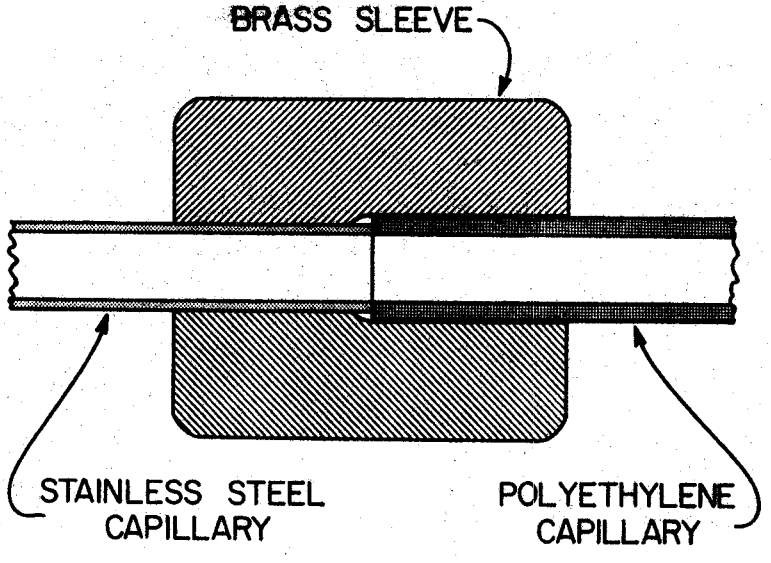

Figure 7. Stainless steel to polyethylene capillary coupling sleeve.

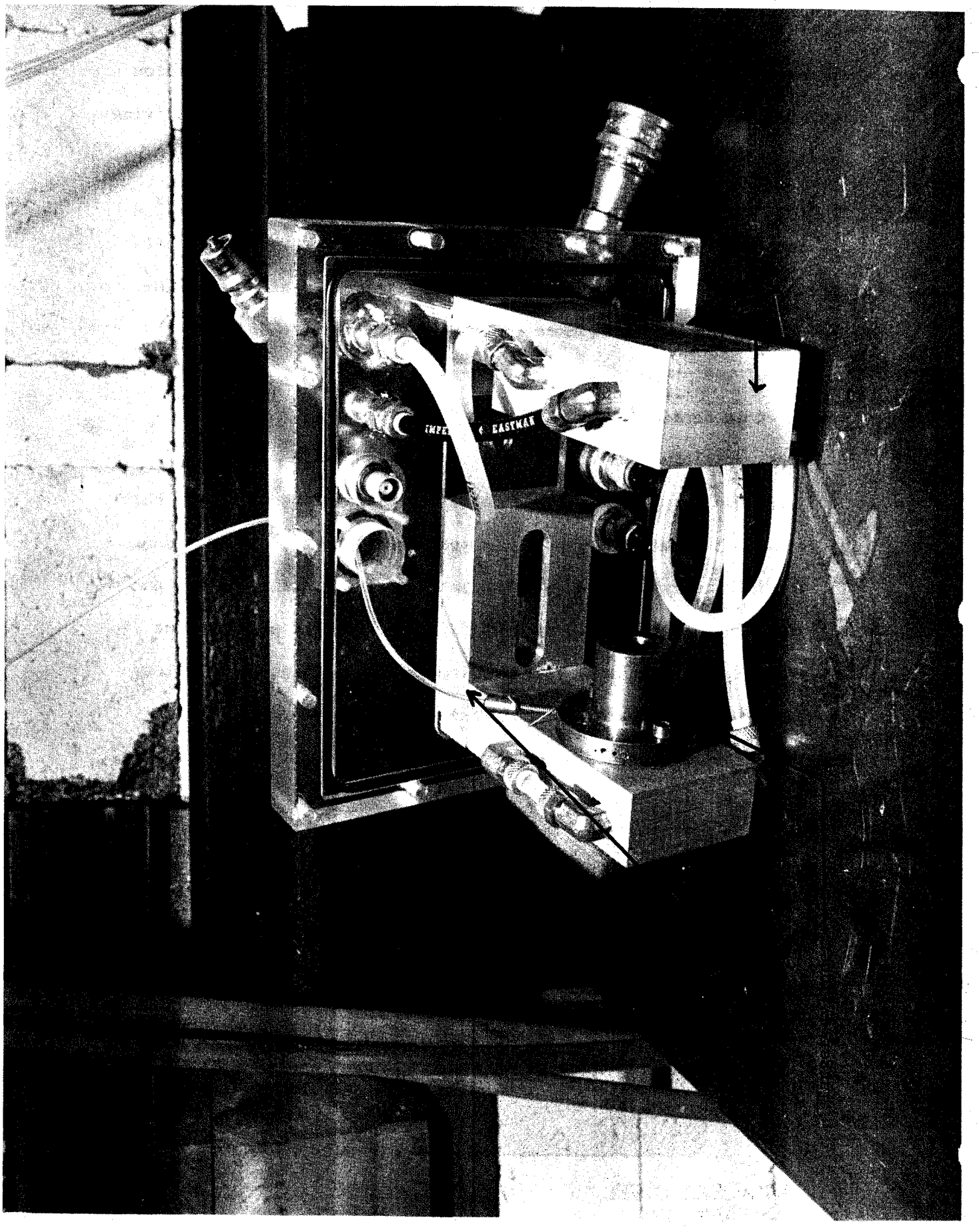

Figure 8. Target assembly components mounted on lid of target assembly chamber.

The requirements and flow considerations in the capillary are discussed in Section II. g."Capillary Considerations".

The beam is stopped and the current mointored by a water cooled Faraday cup located in the helium atmosphere. While it is not necessary to have the Faraday cup in the helium atmosphere, it was convenient and a historical carryover from earlier target configurations (discussed later in this section).

The target assembly drawn in Figure 5 is pictured in Figure 8. The components are mounted on the lid of the target assembly chamber, pictured in Figure 9, to allow easy access.

The initial target configuration used in this lab was patterned after an early configuration of R. D. Macfarlane [MaR69]. Although this configuration has not been used here for two or three years, it does represent a satisfactory target assembly with possibly very short recoil collecting times and has been used recently by other groups [BoW72] [JuH71]. The basic mechanism for generating and collecting recoils is the same as described above with the exception that recoils ejected from the target are thermalized between the target and a chrome plated aluminum hemisphere and are then swept into the capillary through an orifice in the rear of the hemisphere. The hemisphere serves double duty as recoil collector and as Faraday cup, see Figures 10 and 11. The main reason for changing to our present configuration was that it provided for an easy expansion to a multiple target assembly, which is not possible with the initial configuration.

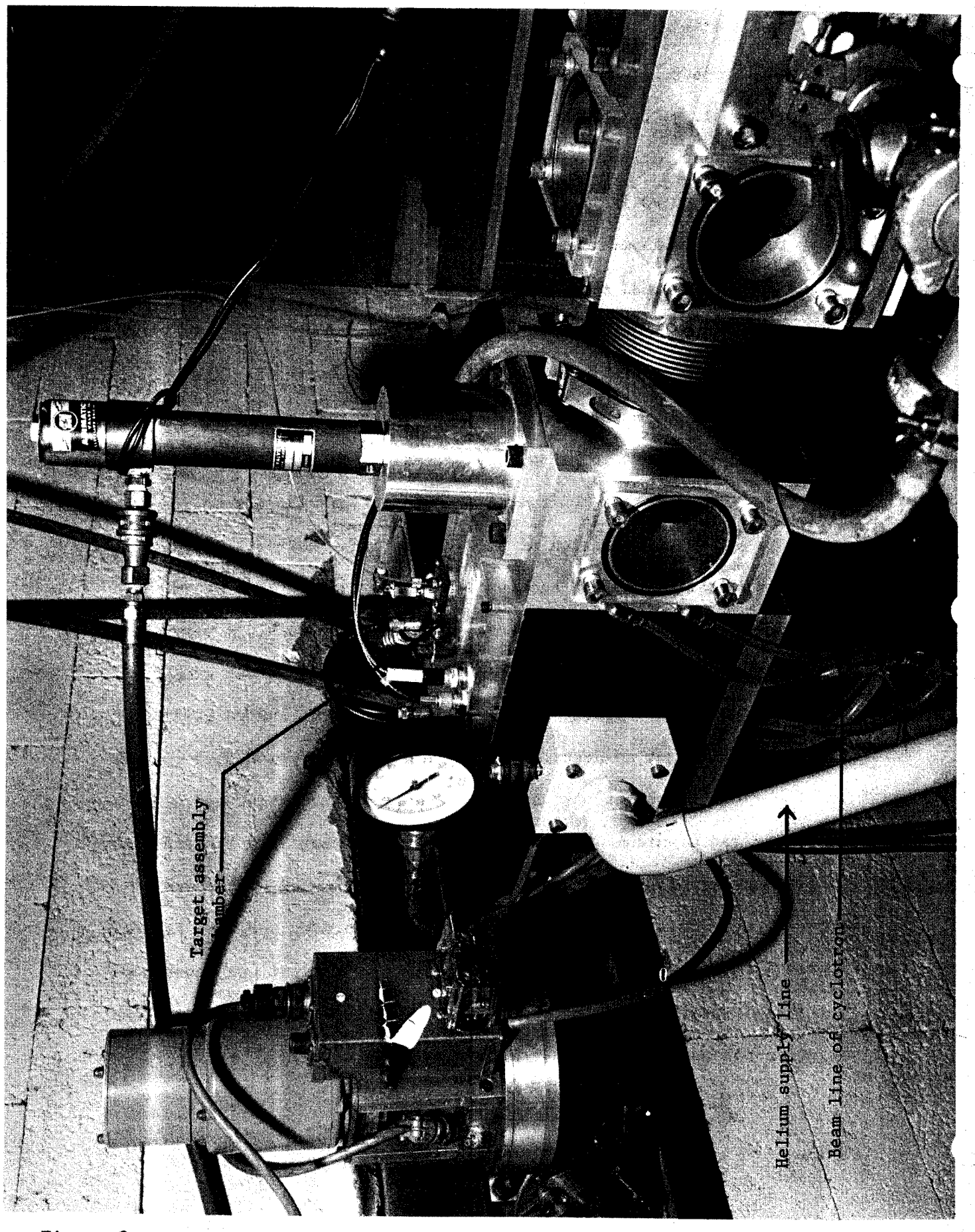

Figure 9. Target assembly chamber on cyclotron beam line.

The necessity for considering a target assembly using multiple targets is born out of the short range of recoils in thin targets. Clearly, no higher yield of recoils is to be gained by increasing the target thickness beyond the range of the most energetic recoils created by the cyclotron beam. For most cases this maximum usable target thickness is from 10^{-5} to 10^{-4} cm (see Section II. b. "Recoil Characteristics"). Even though most experiments will be possible with the HeJRT system using a single target, cases are anticipated where the number of recoils generated from a single target will be a serious limitation. This will be especially true when the HeJRT system is feeding a mass separator. Also, in general it would be wise to have a surplus of recoils generated, making it possible to tolerate larger inefficiencies in other components of an experimental set up. Accordingly, it is desirable to consider multiple target assemblies for the HeJRT system.

The simplest multiple target assembly considered is sketched in Figure 12. Here the helium exiting the target assembly first sweeps back and forth in front of each of the separate targets in sort of an S pattern. This is accomplished by simply staggering the targets and leaving small spaces, through which the helium can flow, on alternate sides of the target assembly. The thickness of the spacers between the targets must be adjusted to provide sufficient distance in order that recoils from the preceding target are thermalized within the distance to the next target. However, a major portion of the time

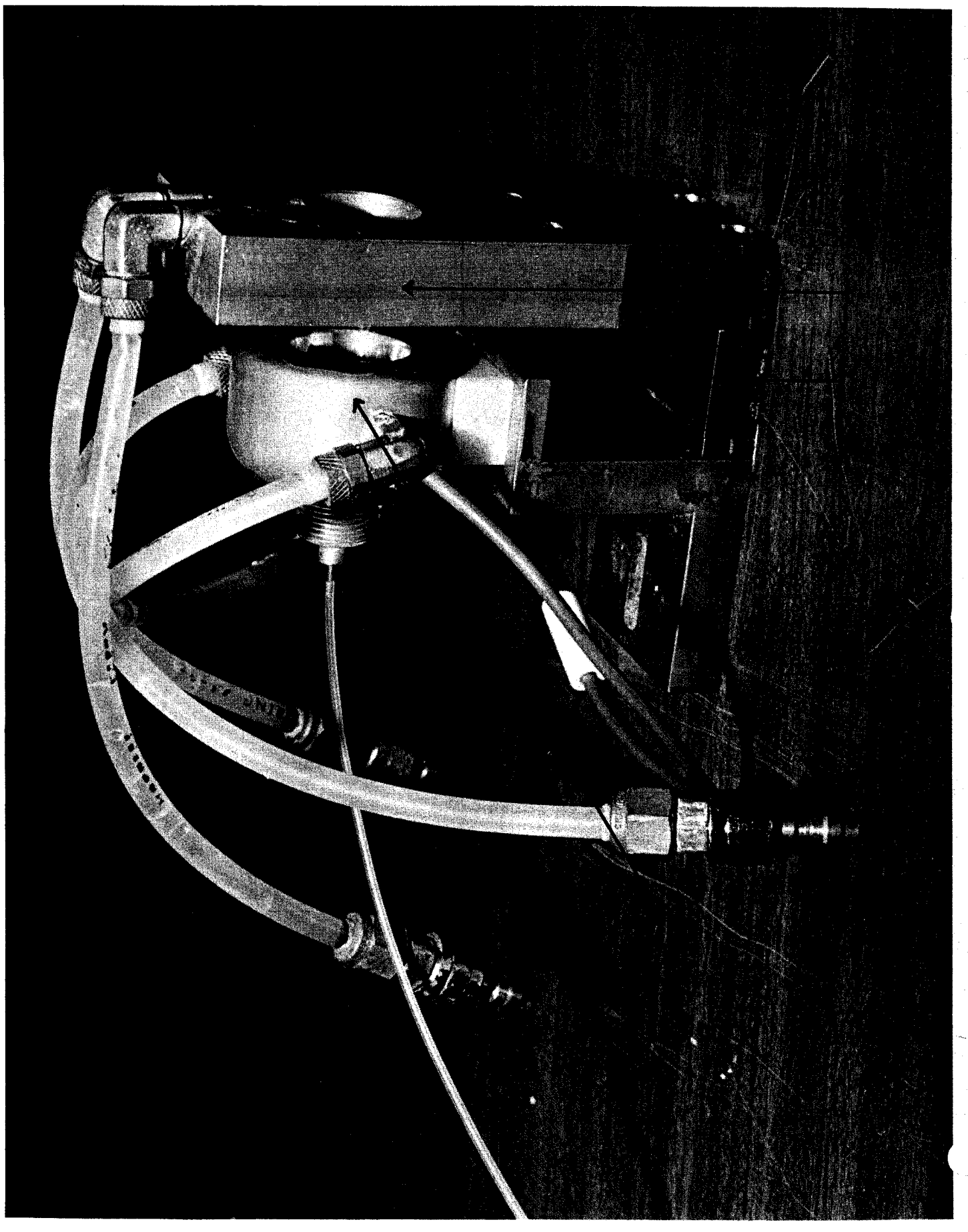

Figure 10. Original target assembly configuration.

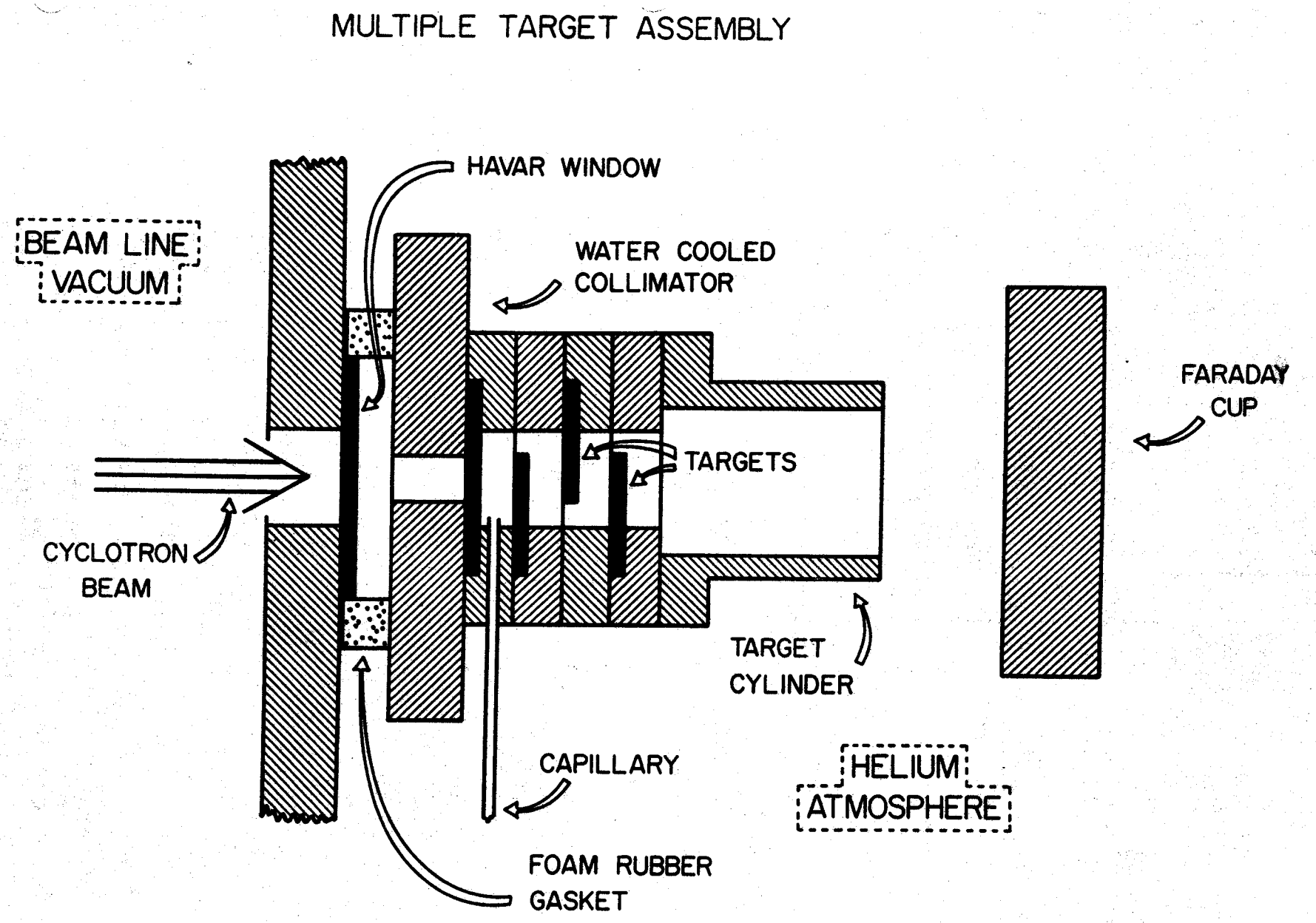

Figure 12. Multiple target assembly of the HeJRT system.

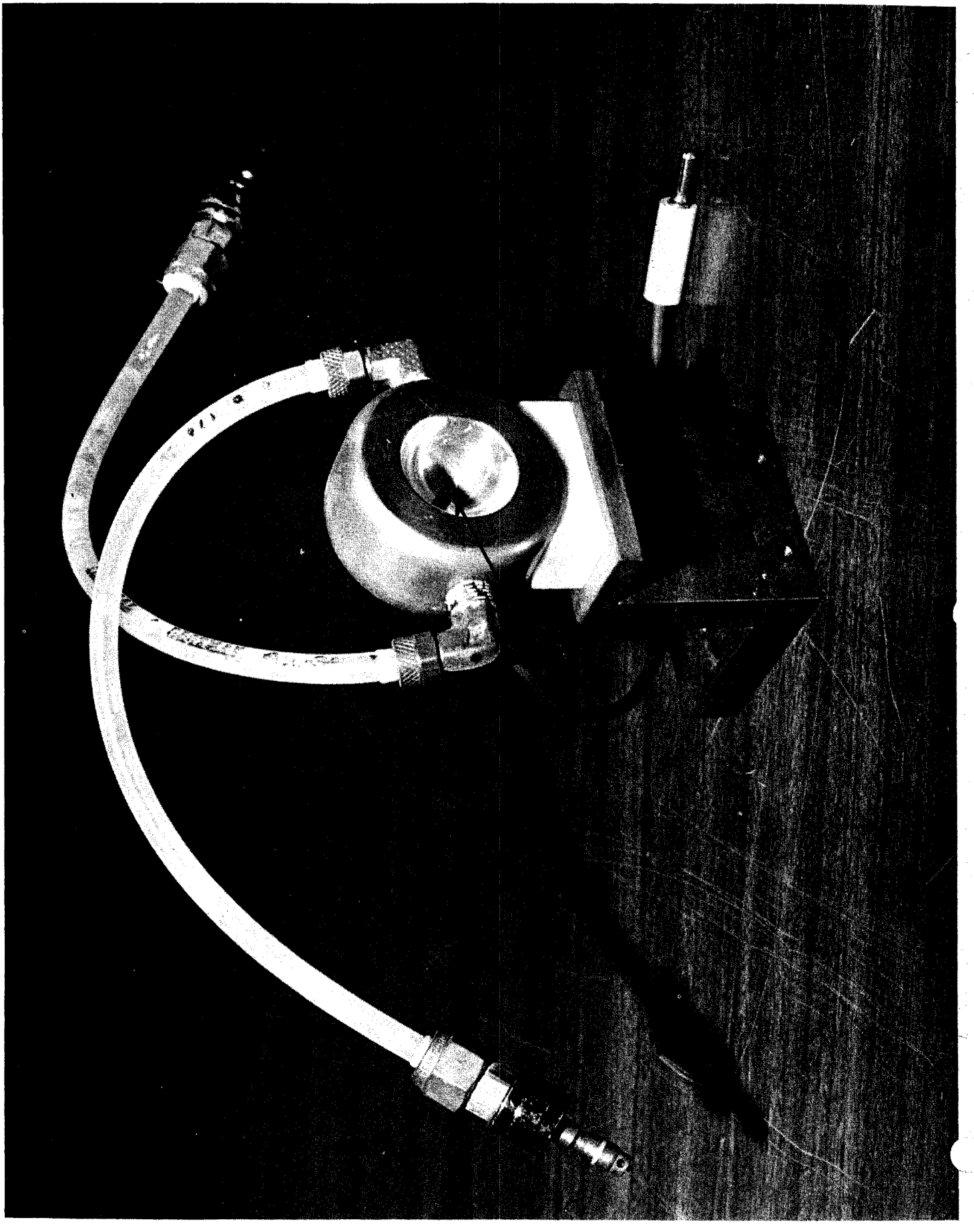

Figure 11. Recoil collecting/Faraday Cup Hemisphere.

elapsing between the generation of the recoils and having them ready for counting in the low background area is the time necessary to sweep the recoils into the capillary. (See Section II. g. "Capillary Considerations".) Thus, in an attempt to keep this time to a minimum the separation of the targets should not be any greater than necessary for the recoil to be thermalized before striking the next target.

While multiple target assemblies have been used here for some time [GiG71], a detailed study of their characteristics has not been conducted. It is known that yields from the multiple target assemblies used are up from single target assemblies; however, the exact relationship between the number or type of targets used and their yield has not been determined. It is also necessary to determine if modifications of the assembly can further improve its efficiency. The initial multiple target assembly used [GiG71] is shown in Figure 13. The one presently being used is essentially the same but looks more like the sketch in Figure 11.

The average time necessary to sweep recoils into the capillary increases with each additional target because as each target is added the total volume from which recoils must be swept is increased. If the half-life of the activity desired is of the order of the time necessary to sweep the recoils from a single target into the capillary, then adding additional targets in the manner described above may produce little increase in the total yield. Accordingly, it may be necessary to add additional capillaries as well as targets. Figure 14 is a sketch of a multiple target assembly employing as many

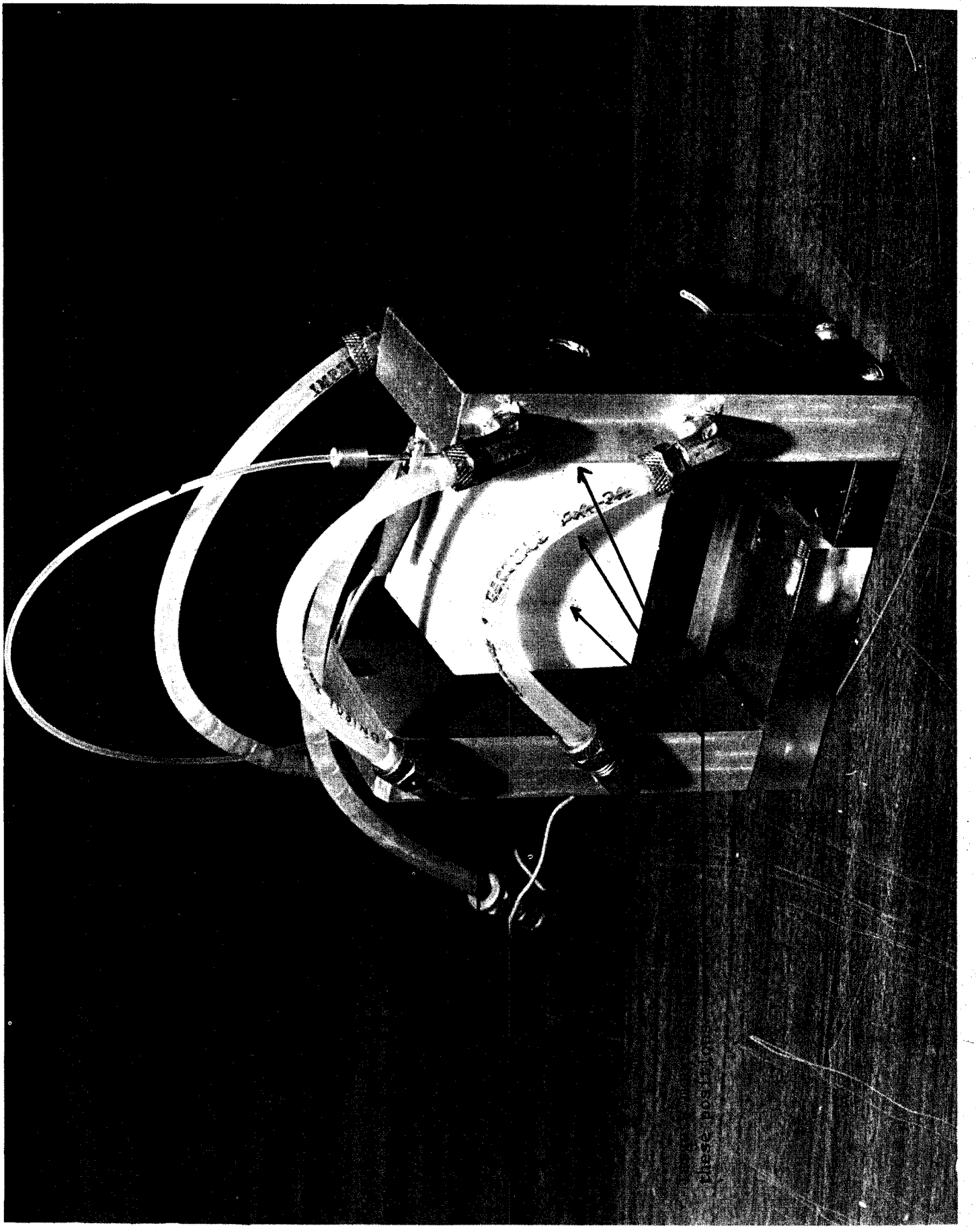

Figure 13. Picture of initial multiple target assembly using three targets.

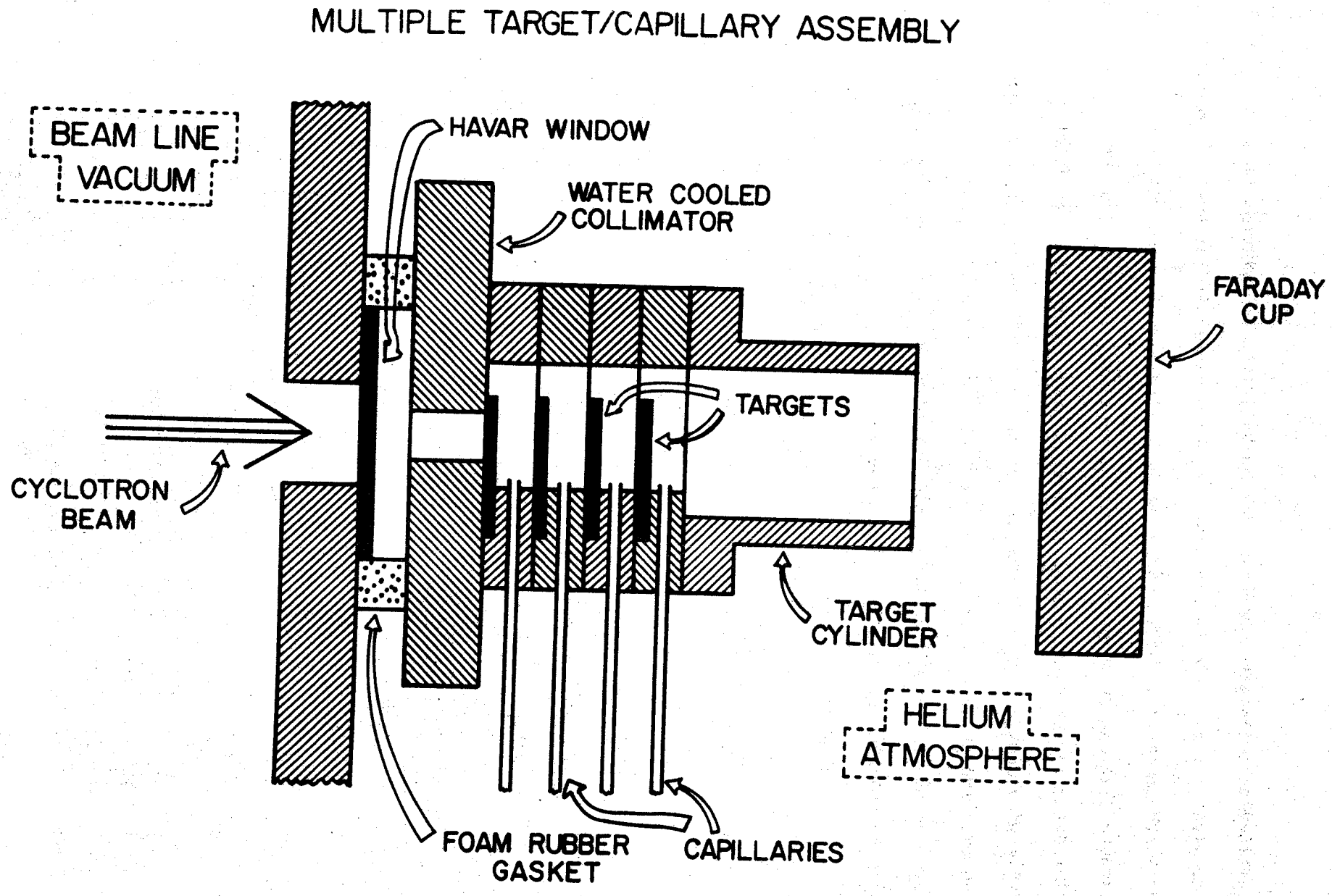

Figure 14. Multiple target/capillary assembly proposed for the HeJRT system.

capillaries as targets; however, if the half life restriction is not too severe it may only be necessary to use a capillary for every second or third target. In addition to the half life limiting the number of targets that can be swept with a single capillary there is a second limitation to the total number of targets used. This is a result of the energy degradation occurring in the targets and the helium, shifting the reaction products toward fewer neutrons boiling off. Of course, this restriction can be partially alleviated by using thinner targets, ones approaching the maximum recoil range.

II. d. Gas Supplies

Initially the helium used in the HeJRT system has a purity $\geq$99.995%; however, this is typically doped with benzene vapor to a level of 10-20 ppm. This is accomplished using the gas mixing set up shown in Figure 15. The process is a two-step procedure. First, a supply of helium is made up containing about 1 ppt benzene vapor by adding a known amount of liquid benzene into the flow of helium to a storage tank pressurized to $\gtrsim$100 psig. Initially, a compressor was used (as in Figure 15) to pressurize the tank; however, because of the uncertainties about the amount of pump oil this was adding to the helium, the compressor has been replaced with a high pressure regulator on a tank of pure helium. The second step is to take the heavily doped helium from the storage tank and dilute it with pure helium as it is fed to the target assembly. This is accomplished by taking the pressure regulated flow from the supply tank through a needle valve and flow gauge and adding it to the pressure regulated flow of pure helium, which also passes through a flow gauge. The final benzene concentration is determined and maintained using the flow gauge readings. For those runs in which the helium is doped with compressed air and water vapor, the compressed air is supplied by the compressor and is fed through the needle valve and flow gauge, while the water vapor is added by just passing the helium supplied to the detector assembly over or through a container of water.

It was originally intended that the gas mixing set-up described above be used to add target gases (e.g., Ne for a $^{20}Ne(p,n)^{20}Na$

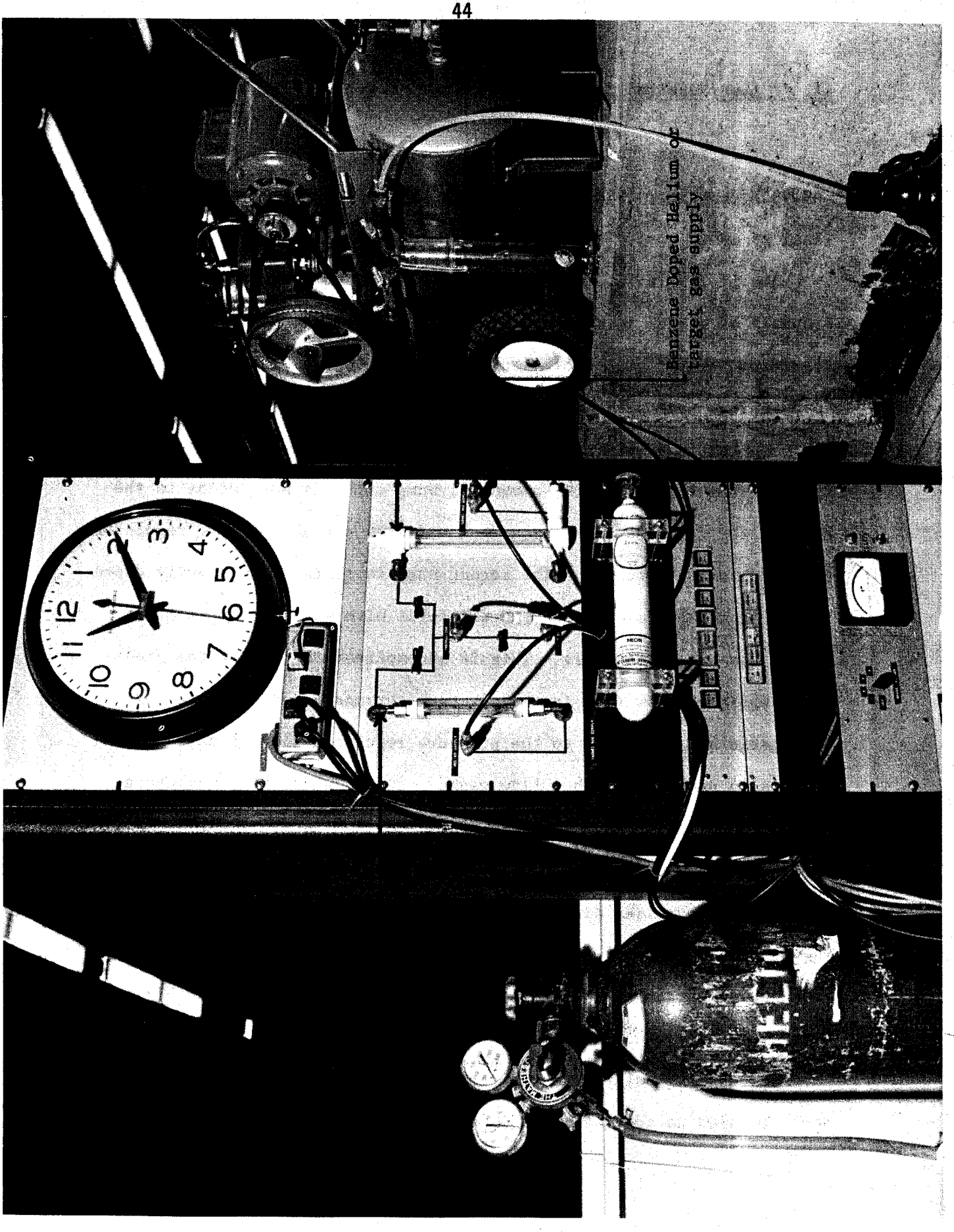

Figure 15 Target Assembly Gas Mixing Apparatus.

II. e. Detector Assembly and Tape Transport

The physical relation between the components of the HeJRT system and the detector assembly with its tape transport is shown in Figure 16. The capillary is run from the target assembly up into the detector assembly (a distance of ≈45 ft) where the flow of helium containing cluster-nuclear recoil combinations is directed at a collecting surface. The cluster molecules are accelerated as they are carried along in the helium flow to about the speed of sound in helium at room temperature (see Section II. g. "Capillary Considerations"). Because of their very large mass, up to above 10^8 amu [JuH71], this corresponds to very high kinetic energies for the cluster, ≈1.1 MeV for 10^8 amu clusters. In turn, these high kinetic energies of the clusters cause them to stick well to collecting surfaces with which they collide. The most frequently used collecting surface is 1-in. paper tape, which is fed through the detector assembly by a tape drive mechanism. Thus, it is possible to continuously expose detectors to fresh sources or to stop the system repeatedly for half life determinations, etc. The tape transport system is discussed later in this section.

Figures 17 and 18 are pictures of two of the possible set-ups for the detector assembly. The first was a set-up used in the search for β-delayed protons. The activities are collected on an aluminum wheel that is being rotated by advancing paper tape in order to expose a fresh collecting surface continuously. A detector telescope has been set up to look for the protons. The second was a set-up used in a simple γ singles experiment and is essentially the set-up used in the collection of the efficiency information in Sections II. h.

reaction) to the target assembly. This ability was lost when the necessity for adding controlled impurities became apparent. In order to regain the ability to add target gases in addition to impurities, the gas mixing apparatus is being expanded to allow the controlled addition of up to three gaseous components to the primary helium supply. An additional source of motivation for expanding the gas mixing set-up comes from the desire to try more exotic mixtures of impurities in the helium. This is necessitated by the desire to follow up the possibility of performing "Plasma Chemistry" (see Section II. o. "Plasma Chemistry").

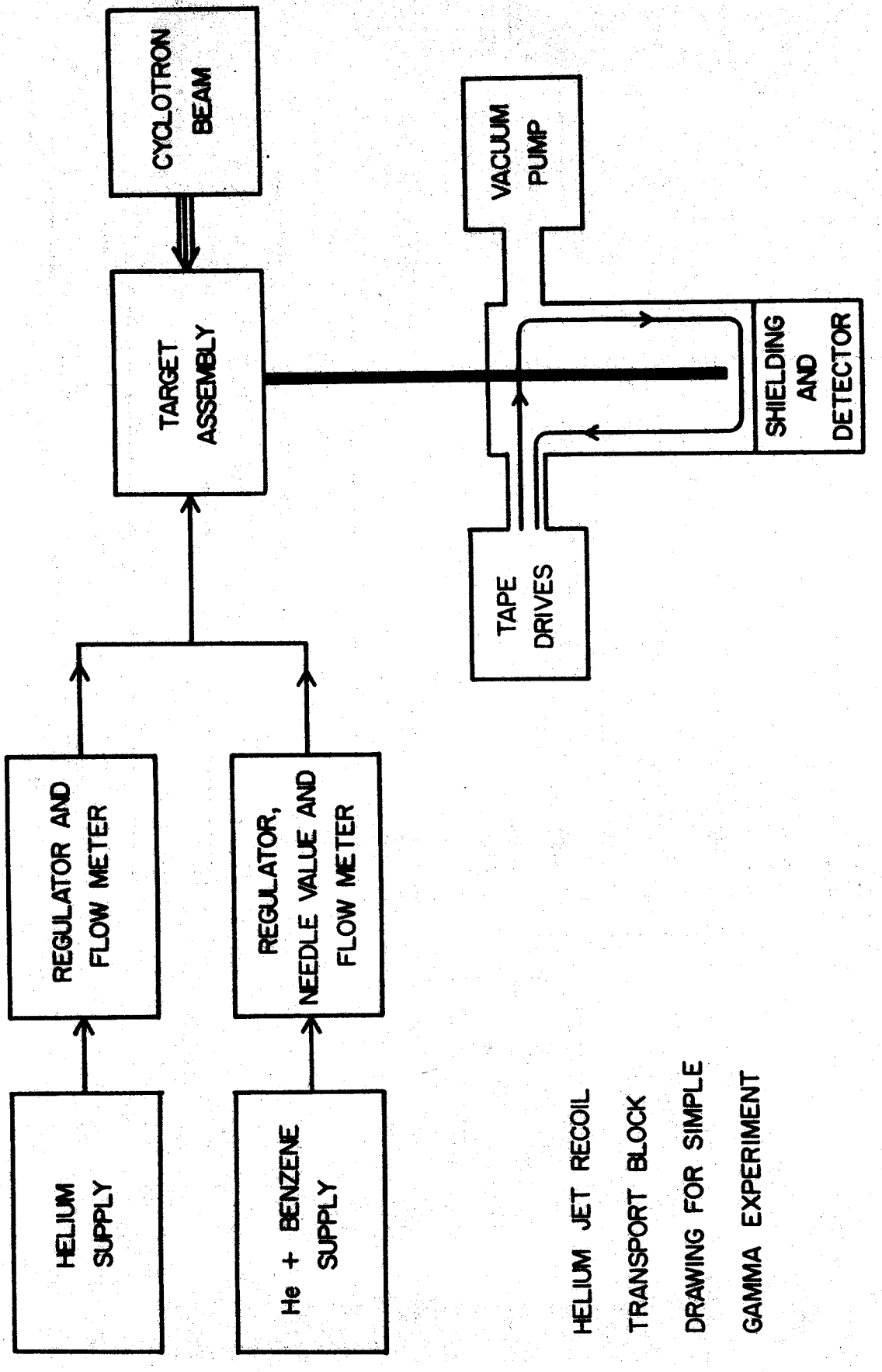

Figure 16. Block diagram of HeJRT system set-up for a simple γ experiment.

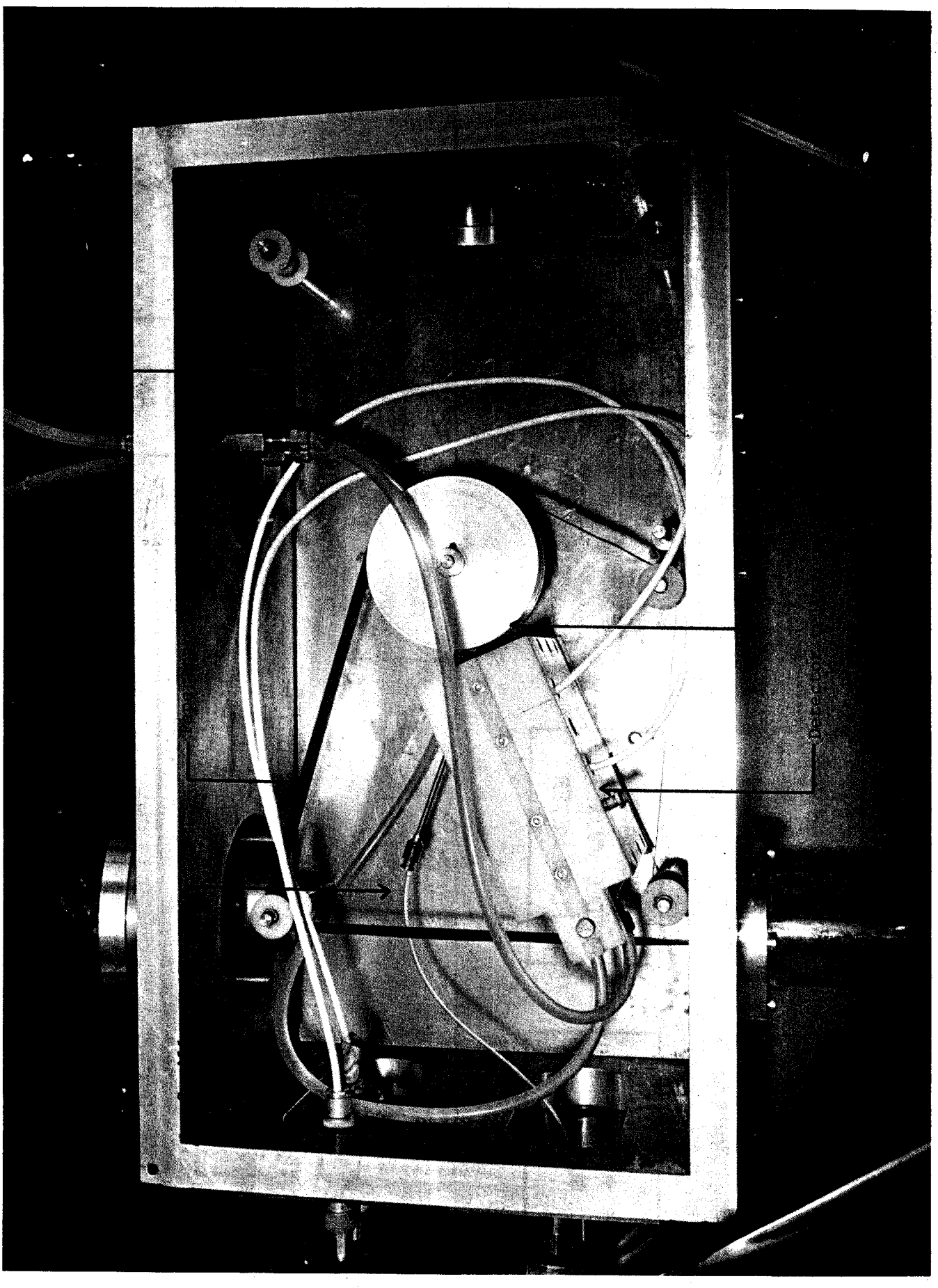

Figure 17. Detector assembly set-up in a search for β-delayed protons.

through II. 1. The activities are collected on paper tape just out of view of a collimated Ge(Li) detector located just outside the detector assembly chamber. The capillary to tape angle and distance has been adjusted so that the tip of the capillary (where activities sometimes collect) is out of view of the detector. In both figures the end of the capillary has been run through a slightly larger diameter metal tube. This has been done to hold the end of the capillary straight to facilitate aiming the capillary and to minimize the problem of activities collecting on the end of the capillary (see Section II. g. "Capillary Considerations"). An overall view of the detector assembly area is shown in Figure 19.

The tape transport system is shown in Figure 20. It is designed to handle up to 1-in. tape and has been used with paper and aluminized mylar tape. The tape is advanced using a capstan-pinch roller assembly that is driven by a stepping motor. The accuracy to which the tape speed is known is the accuracy of the pulse generator (±1%), assuming the tape does not slip or the stepping motor does not miss steps. This is a good assumption providing the proper tension is maintained on the tape and the tape speed is not excessive (≤10 inches per second). The tape transport system has the ability to move the tape in either direction at speeds up to about 15 inches per second. The recent addition of a 16-channel programmable sequencer allows for quite complex motions of the tape and can also control other functions, such as gating detectors, routing spectra, and operating other mechanical devices.

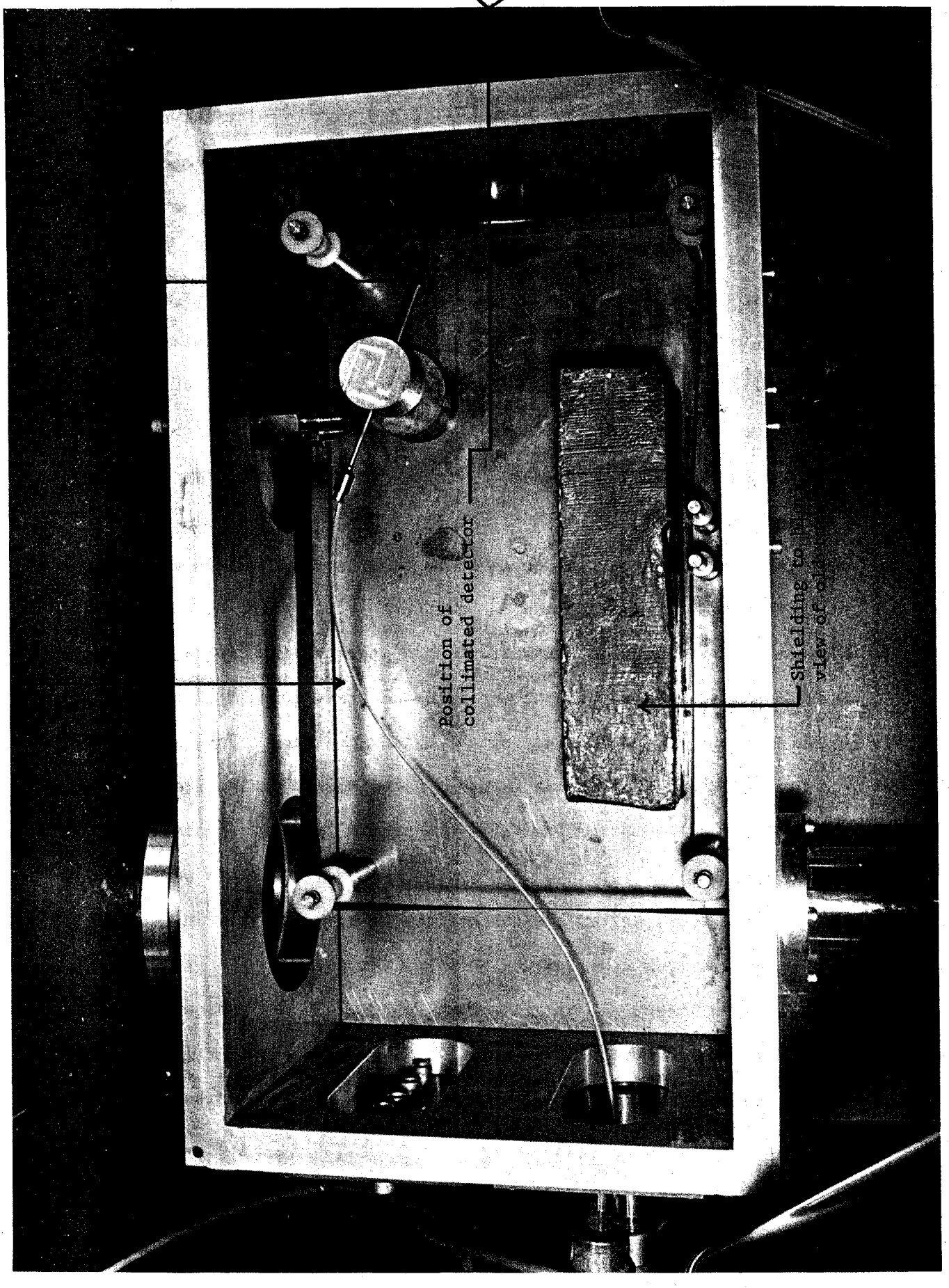

Figure 18. Detector assembly set-up in a simple γ singles run.

The pumping station for the HeJRT system is located on a platform below the detector assembly area in order to reduce the vibration of the detector assembly by the pumps. The pumping station is shown in Figure 21. The pumping system consists of an ≈300 ℓ/sec (measured capacity for helium) Roots blower backed by a 15 cfm mechanical pump. The vacuum line to the detector assembly is provided with a Chevron-style cold trap to prevent back streaming of oil from the pumps when solid state detectors are used in the detector assembly. Typically, only the 15 cfm mechanical pump is used for experiments using the HeJRT system, since the lower operating pressure offered by the Roots blower provides no increase in the total transport efficiency of the HeJRT system (see Section II. j. "Efficiency vs. Detector Assembly Pressure"). However, when the HeJRT system becomes the first stage of an on-line mass determination system, the added pumping capacity of the Roots blower will be necessary. When the HeJRT system is expanded to the on-line mass system, the additional pumps will also be placed on the HeJRT pumping station platform. Because of the possibility of the pump exhaust containing activities, all pump exhausts are ducted to a filter and pumped out of the building.

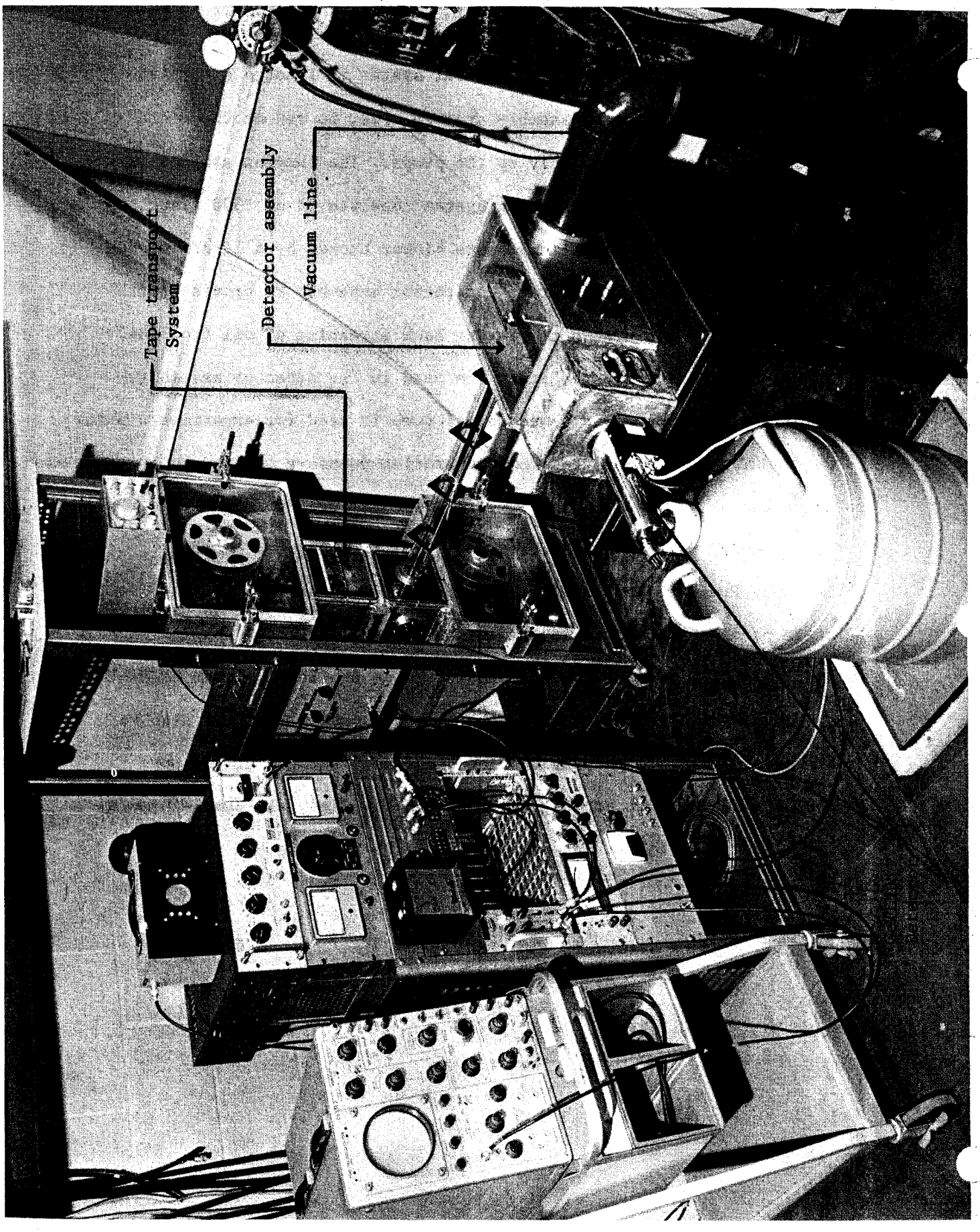

Figure 19. Overall view of detector assembly area set up for a γ singles experiment.

II. f. Cluster Molecules

Most simply stated, the role of cluster molecules in the HeJRT system is to aid in the efficient transport of recoil activities through the system and to help hold these activities on collecting surfaces. However, a good deal of detail of the mechanism is not known for certain. It can be argued the details of the mechanism are not important so long as the system works efficiently, which it does. However, we feel that when the HeJRT system is expanded to being part of an on-line mass identification system or when it is used in conjunction with aqueous chemistry and possibly plasma chemistry (see Sections II. m. "Aqueous Chemistry" and II. o. "Plasma Chemistry") this detailed information will be at least helpful if not in fact necessary. Accordingly, the program to fill in these gaps is continuing.

The possible presence of molecular cluster has been considered since Ghiorso [GhA59-69] observed that a fraction of recoils produced in heavy ion reactions on Pb targets apparently had masses as large as 10^3 amu. In 1962 Macfarlane reported results that indicated the clusters played a role in the collection of recoils when he observed that Tb recoils produced in heavy-ion reactions could be collected electrostatically as either positive or negative ions [MaR62]. Subsequently, Mikheev demonstrated that the efficiency of transport was markedly reduced when extremely pure (non-cluster generating) helium was used [MiV67]. However, the importance of the large cluster molecules was not fully realized until the HeJRT systems grew in length to their present size (capillaries with lengths in the range of 20-200 ft). In these systems the total transport efficiencies were only a few percent, and not until specific impurities were added to the helium did the efficiencies climb back toward 100%.

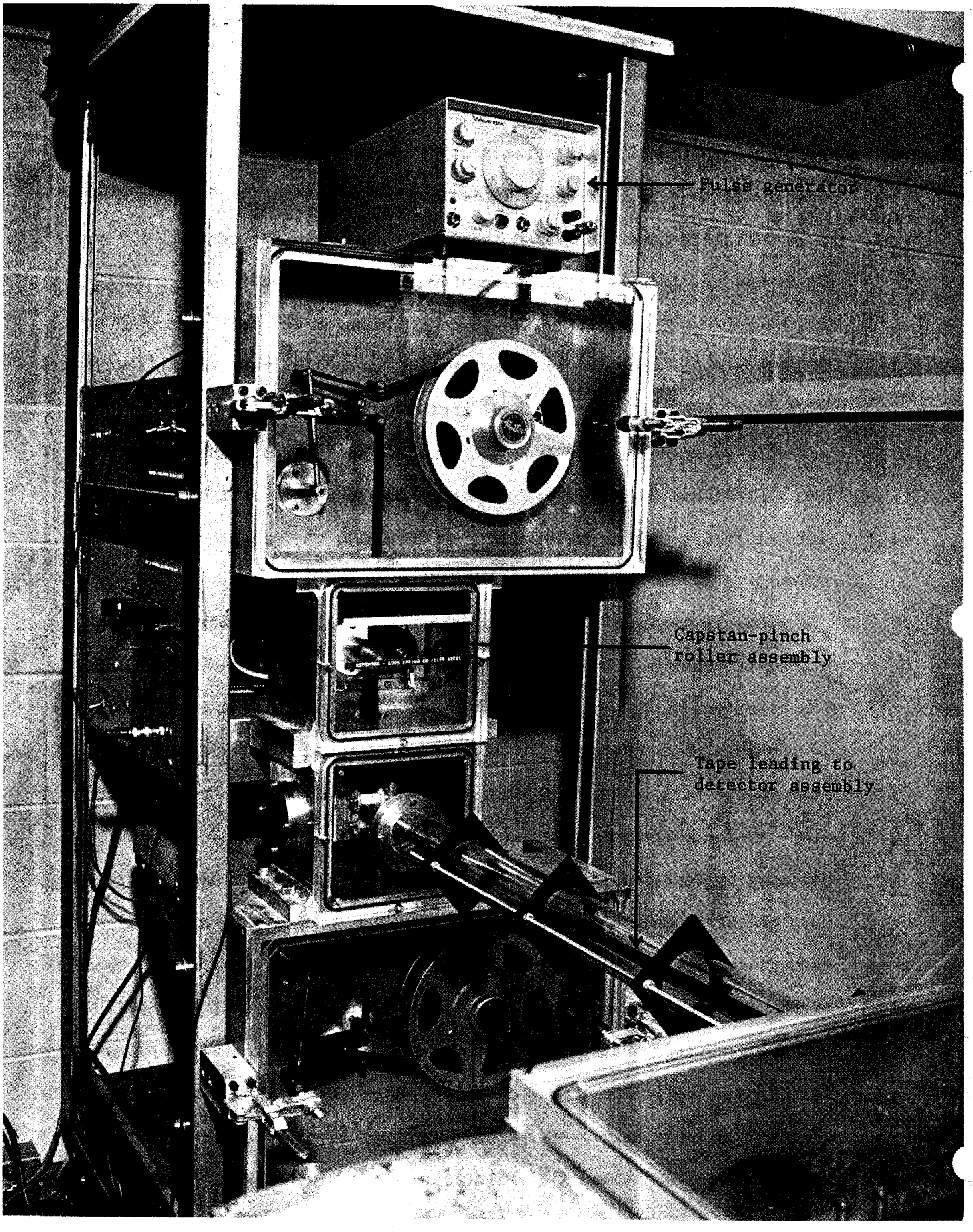

Figure 20. Tape transport system.

In our system the total transport efficiency increases by a factor of about 20 upon changing from pure helium (purity ≥99.995%) to helium containing a few parts per million benzene vapor. In addition to the dramatic increase in efficiency observed for our system we also observe the buildup of solid material (cluster molecules) at each of the points where activities are deposited. In all respects the increase in efficiency for the system is tied to the presence of cluster molecules. Those factors that foster the generation of cluster molecules increase the efficiency of the system, and the activities generated in the system "tag along" with the cluster molecules. Thus, it seems apparent that the increase in efficiency is a result of the generation of cluster molecules and the attachment of recoiling activities to these molecular clusters. Macfarlane undertook a study of the masses of the cluster molecules and found them to range upward beyond 10^8 amu [JuH71].

Once the importance of having the nuclear recoil attached to large cluster molecules was demonstrated, it was a relatively simple matter to explain why this should have been expected all along. Initially the explanation was that the large mass of the cluster molecules reduced the transverse diffusion rate in the capillary, thus reducing the chance that activity would be lost through collision with the capillary wall. Macfarlane made the additional observation that the clusters were concentrated nearer the center of the capillary [JuH71]. After some additional thought, the current concensus of people using HeJRT systems is that it is the focusing effect of laminar flow for massive objects transported in the flow that is the reason the cluster molecules drastically improve the system's efficiency. This focusing effect arises from an imbalance of forces on the large object accelerating in the flow as a result of it being acted on by laminae flowing at different speeds [CoW56]. The

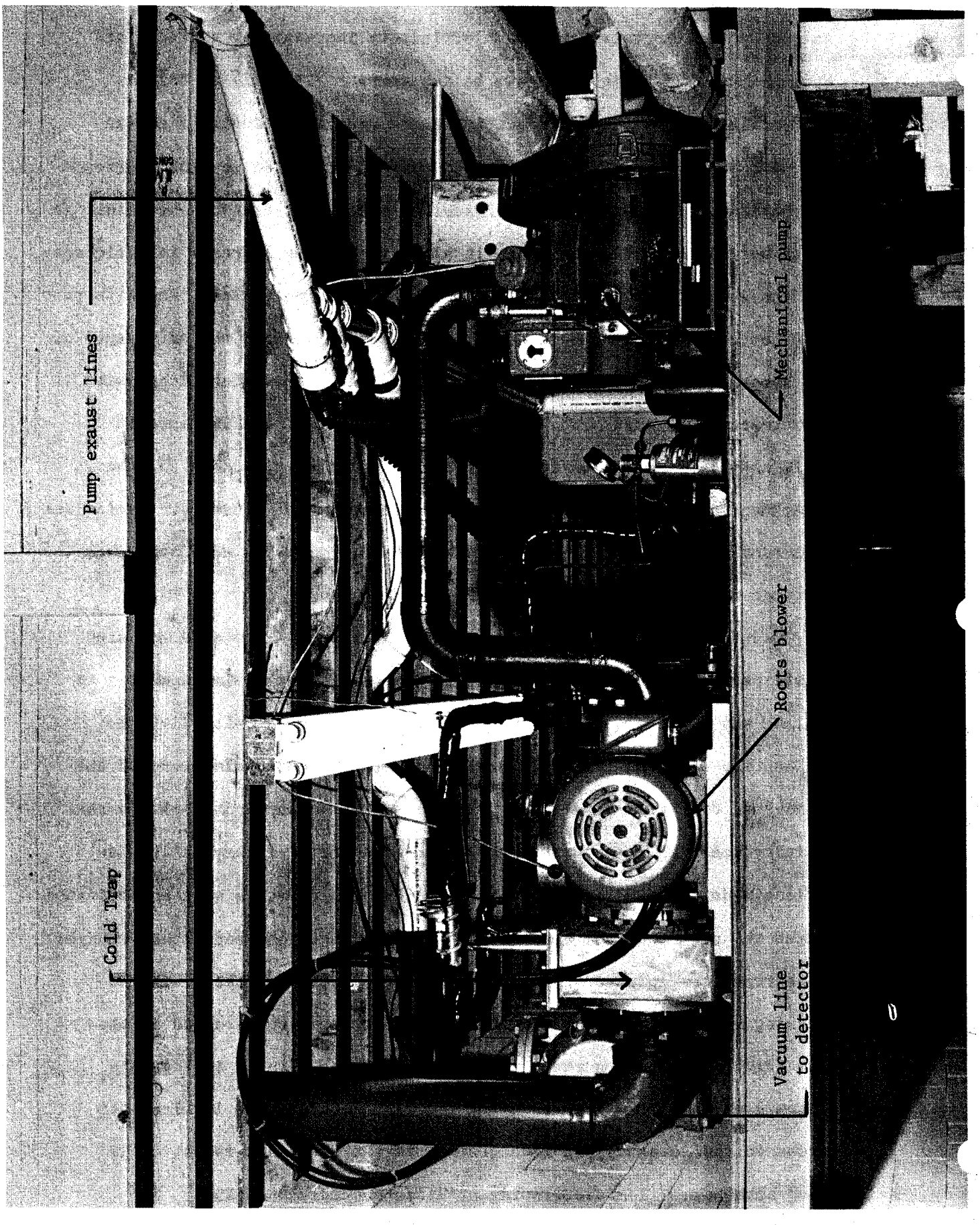

Figure 21. HeJRT pumping station on a platform located below the detector assembly area.

direction of the imbalance is toward the laminae with the higher speed, i.e., toward the center of the capillary. For the HeJRT system as it is currently set up, the Reynolds number is just between Reynolds numbers indicating laminar flow and those indicating turbulent flow (see Section II. g. "Capillary Considerations"). However, even if the flow in the center of the capillary tended toward being turbulent, the forcing effect would still be present in the laminar sublayers along the walls of the capillary.

An additional benefit resulting from the attachment of recoil activities to massive cluster molecules lies in the relative ease one has in separating clusters (and therefore activities) from the helium used to transport the cluster molecules. Owing to their enormous masses the clusters will diverge only slightly as they exit the capillary into a vacuum, whereas the helium will suffer a much greater divergence. Macfarlane has been successful in achieving good separations of recoil-carrying clusters from helium using a conical oriface (helium skimmer) with a diameter only slightly larger than the capillary diameter and at a distance of several millimeters from the end of the capillary [JuH71]. We made an attempt at determining the angle of divergence of the clusters in our system by merely observing the diameter of cluster build-ups at varying distances from the end of the capillary. For this determination the assumption was made that the clusters were not concentrated in the central regions of the capillary and that turbulence created by placing a collecting surface in the path of the flow did not affect the paths of the clusters. The result of these assumptions is the determination will yield a larger diameter than would be observed for a properly designed skimmer. The results of this determination are shown in Figure 22 which indicates an angle of divergence of $\geq 3°$ for about 90% of the clusters and an angle of

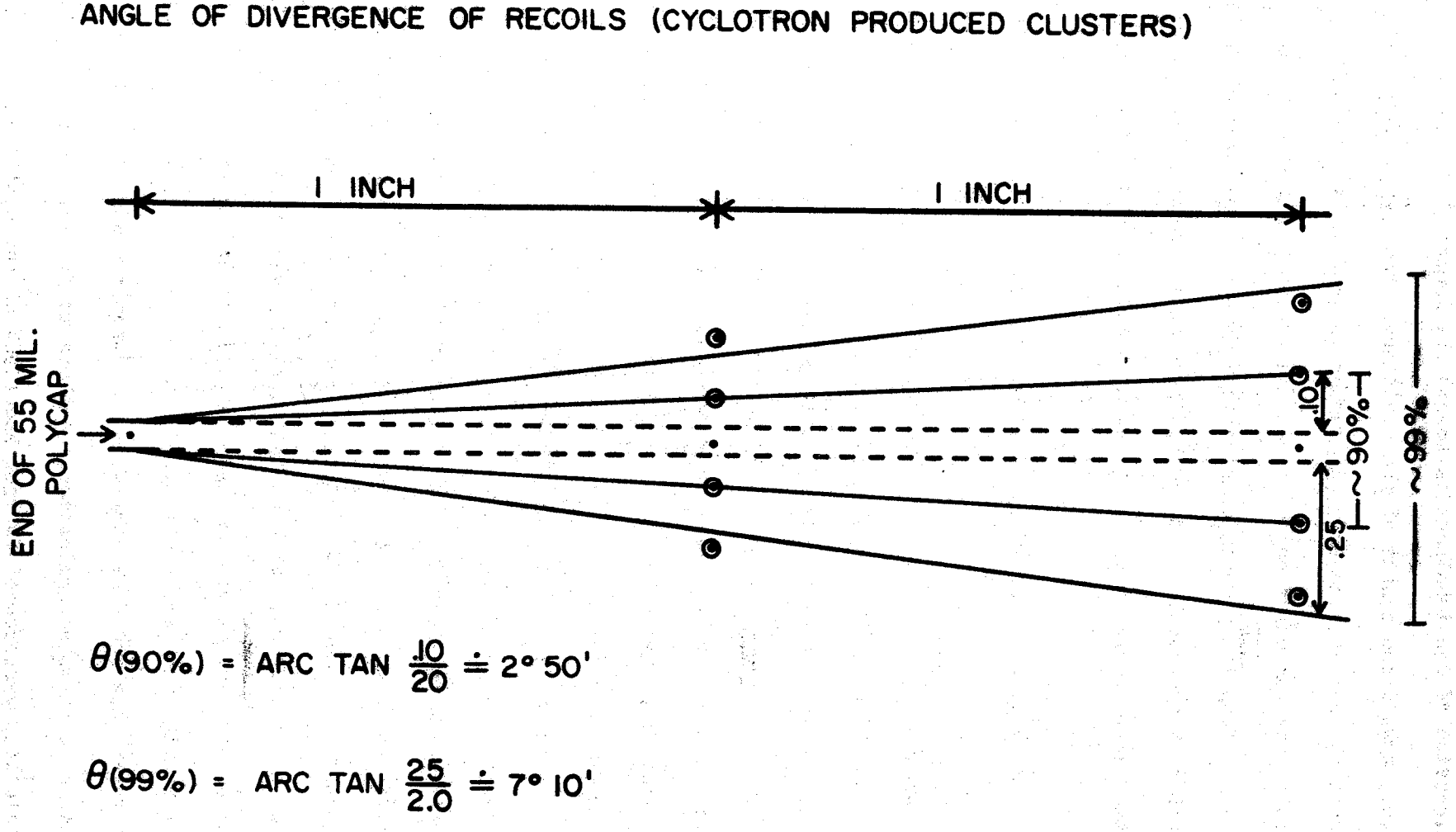

Figure 22. Approximate angle of divergence of molecular clusters leaving the HeJRT capillary.

divergence of ≥7° for 99% of the clusters.

In our case cluster molecules are generated from benzene vapor added to the HeJRT helium supply to a concentration of 10-20 ppm. Sugihara's group at Texas A & M also uses benzene vapor but at a much higher concentration. They bubble their helium through a container of benzene [BoW72] such that their benzene concentration is probably in the range of 0.1 to 1%. Macfarlane's group at Texas A & M initially used compressed air and water vapor. They added about 1% compressed air and had an open dish of water in their target assembly (private communication) (the important ingredient in the compressed air most probably was pump oil). More recently Macfarlane has been bubbling his helium through water and adding ~200 ppm CH_4 [MaR72a] or using commercial grade helium and water vapor [WiK72]. A group at Simon Fraser University used ethylene in concentrations up to 100% as their cluster generating gas [DaH73a]; however, the mechanism for generating the clusters is quite different than we are now considering. Quite obviously the cluster molecules must be primarily composed of the elements making up the impurities added to the HeJRT helium supply. Thus, the clusters would seem to be organic in nature. In addition, the improvement they bring to the total transport efficiency would not seem to depend on their exact composition. One of the things that is not known at this time is the possible importance of trace impurities in the generation of molecular clusters in providing sites for attachment of thermal recoils to the clusters.

In our case cluster growth is initiated by the passage of the cyclotron beam through the impurity-containing helium. Other researchers report the use of hard ultra-violet [WiK72] and gas discharges [WeC72] to initiate the growth of molecular clusters. Presumably cluster generation is a result of creating free radicals and/or carbonium ions and carbanions

within the plasma, formed by the beam passing through the helium from the organic impurities present. These highly reactive species then apparently react chemically to buildup the cluster molecules. Except for the necessity of the cyclotron beam (or some other source of energy input as discussed below), there is no direct information on the mechanism of cluster generation. The suggestion that it involves the formation and subsequent reaction of highly reactive organic species is made only on the basis that it seems logical. The group of Simon Fraser suggests their clusters are generated upon the expansion of ethylene gas from pressures and temperatures above the critical point [DaJ73].

Studies have been conducted to determine the relationship between beam current on target (plasma density) and system performance and between benzene concentration and system performance. In each case the HeJRT system was set up using an aluminum target, the beam was 30-MeV protons, a 45-foot long 0.055-in I.D. polyethylene capillary was used, and the activities were collected on moving paper tape such that the source material spent about 1.5 sec in view of the Ge(Li) detector. The detector assembly was pumped to ≈7 torr, and the target assembly was maintained at 2 atm. For the series of determinations seeking the relationship between beam current and transport efficiency the helium was doped with ≈50 ppm benzene vapor. For the series of determinations seeking the relationship between benzene concentration and transport efficiency the beam current was held at very nearly 1 μA. Several spectra were recorded during each series of runs to be certain the gross γ count rate followed the intensity of the 820-keV peak of ^{26}Si.

The results from the first series of runs are shown in Figure 23. It is quite apparent the amount of activity transported through the system is not linearly dependent on beam current. The production of recoils from

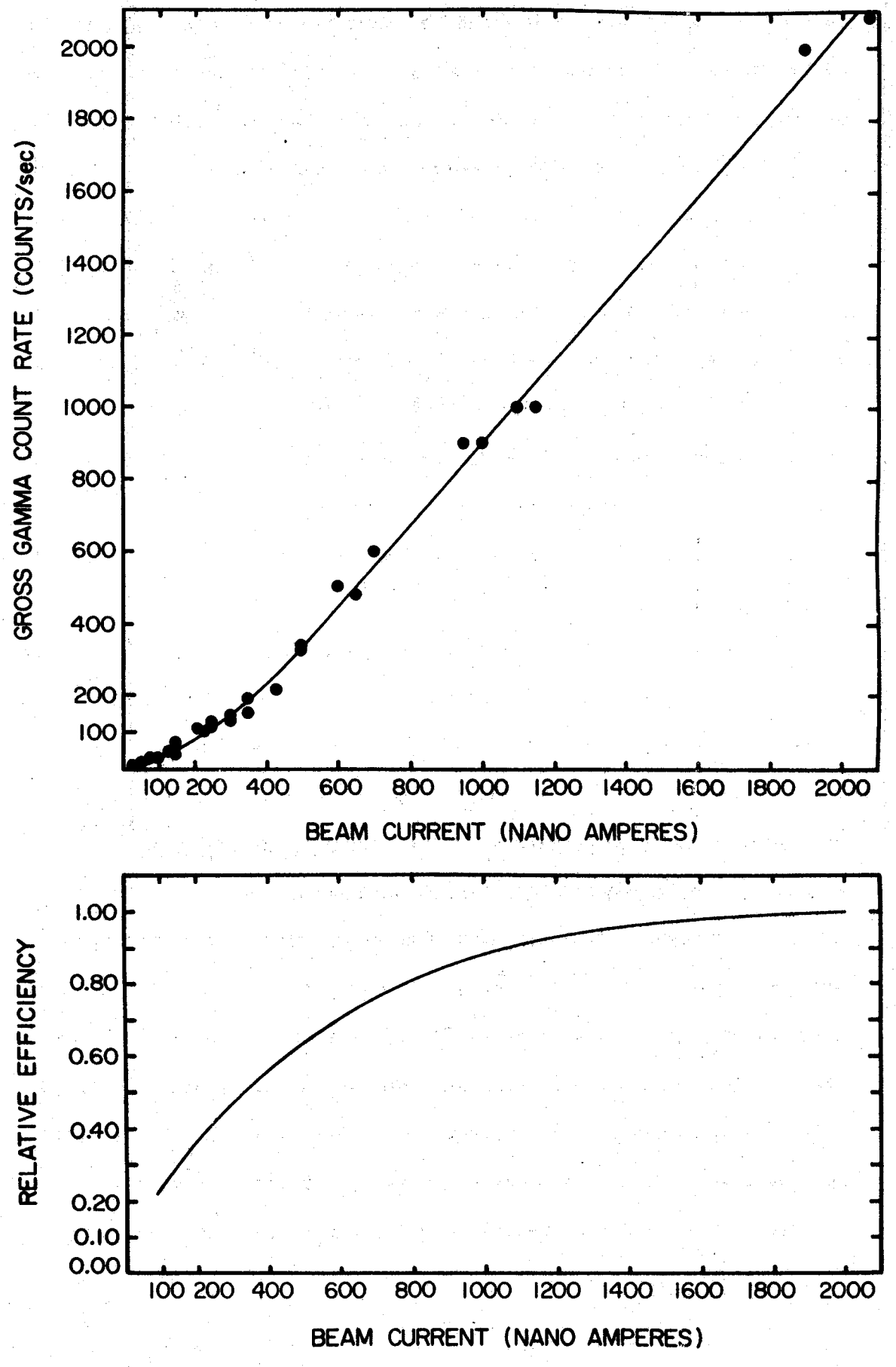

Figure 23. Relationship between beam current and relative transport efficiency.

the target must be directly proportional to beam current; therefore, it must be the efficiency with which the activity is transported through the system that is not constant. It seems most likely the drop in transport efficiency observed for low beam currents is the result of either not generating enough cluster molecules or not generating cluster molecules that are sufficiently massive. Presumably the reason for this is the drop in the number of free radicals, etc., generated because of the decreasing plasma density following the decreasing beam current. We anticipate performing an additional series of runs using a larger capillary diameter. As a result of using a larger capillary, the flow rate through the HeJRT system will be increased, thus allowing less time for suitable cluster molecules to be built up in the volume behind the target. If we are correct, we expect to see a more drastic dependence of transport efficiency on beam current.

The results from the second series of runs are shown in Figure 24. It is quite apparent that the amount of activity transported through the system is independent of the concentration of benzene between the limits shown. It is felt that the slight drop in efficiency to 98% upon going to the lowest benzene concentration may be a result of poor statistics. This is because runs in which the level of benzene in the system was more than two orders of magnitude lower still had total systems efficiencies that were quite high. It takes a couple of weeks of pumping on the HeJRT system to return the system's efficiency to the very low level observed before benzene was first added to its helium supply. Runs were also attempted in which the concentration of benzene was almost to the level of saturation, with the result of no improvement in the system's efficiency.

One of the more fundamental questions, and one of the unanswered ones,

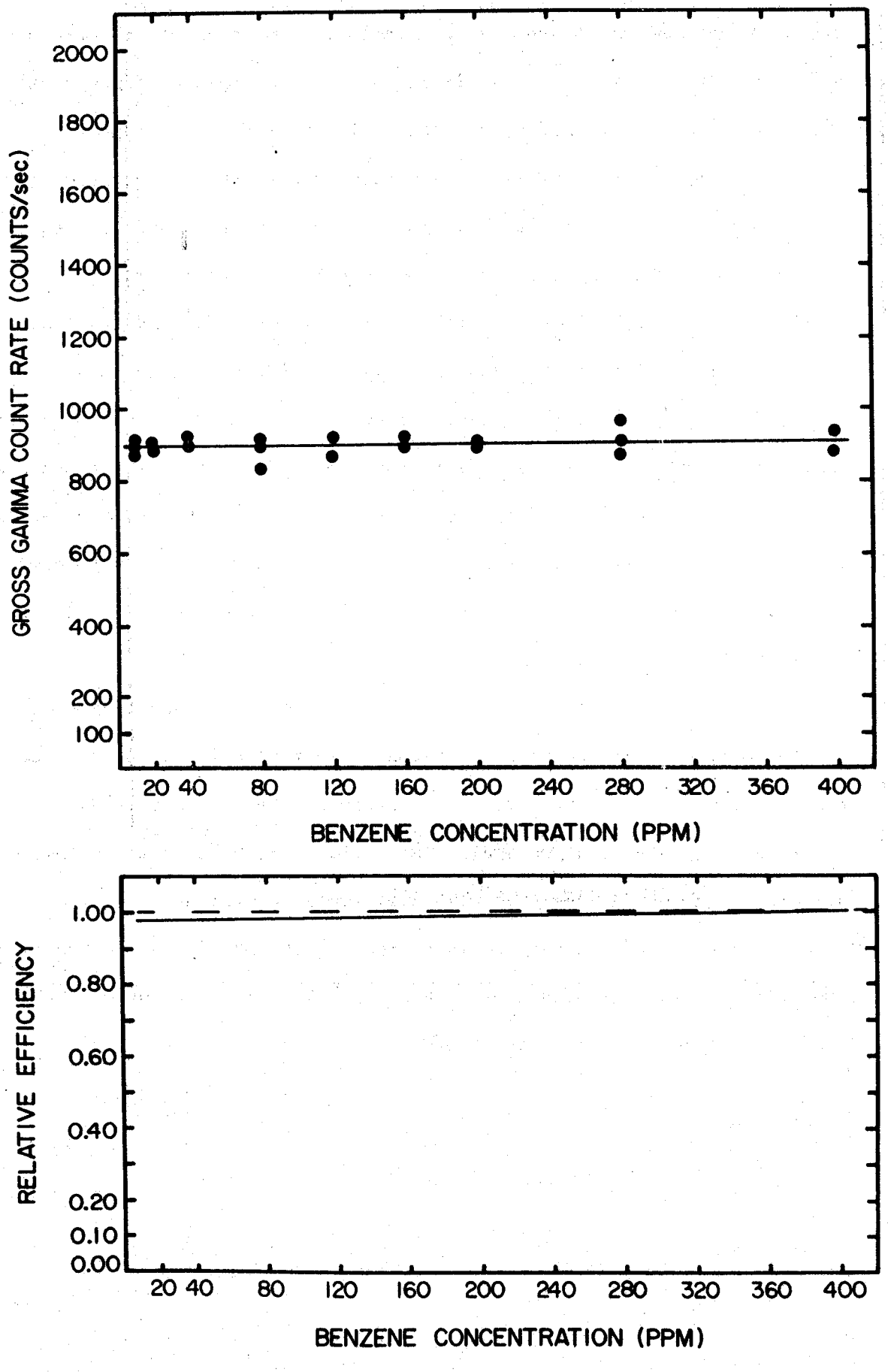

Figure 24. Relationship between benzene vapor concentration and relative transport efficiency.

about cluster molecules in the HeJRT system concerns the nature of the mechanism through which the nuclear recoil becomes bound to the cluster molecule. On the lowest level, it is possible to consider two mechanisms for this. One mechanism for the process is just one of entrapment, in which, as the bulk cluster material condenses out, the nuclear recoil becomes trapped during the process just because of its physical presence in the area. Here "condenses out" should not be taken literally but should be understood to be some form of nucleation or polymerization. A second mechanism for the process would be one in which the nuclear recoil becomes bound to the cluster at some time during the growth of the cluster. Here "bound" can be taken to be either reflecting a physical bond such as a result of van der Waals forces or an actual chemical bond. Section II. o. "Plasma Chemistry" presents some evidence supporting the mechanism involving the formation of a bond between recoils and chemically specific sites in the cluster molecule.

As could be expected, considering their probable organic nature, the cluster molecules are soluble in acetone. We routinely use acetone to remove buildups of cluster molecules within the HeJRT system. However, it was not expected that we would find build up of cluster molecules to be soluble in water. There is also some evidence (see Section II. m. "Aqueous Chemistry") that there is a break-up of the cluster molecules when added to aqueous solution, with the break-up freeing the nuclear recoil occuring in quite short times.

II. g. Capillary Considerations

Our initial experiments with the HeJRT system were run using glass capillaries that were ≈ 1 meter long. With this length of capillary we were forced to run in an inconvenient location and could not sufficiently shield the detector assembly from the neutrons (and capture γ^{15}) generated in the target assembly. When we were having difficulty obtaining longer glass capillaries and were not looking forward to splicing short ones together, an attempt was made to find a substitute capillary. A stainless steel capillary was to be ordered, but in the interim it was decided to try a polyethylene capillary supported by running it in larger glass capillary. When it was found this worked well we attempted a run in which the polyethylene capillary was strung loosely between the target and detector assemblies to determine whether the capillary could suffer slight bends without losing much transport efficiency. When the HeJRT system still performed well, a series of runs was undertaken to determine how much the capillary could be bent without a serious loss in efficiency. This series of runs culminated in the tying of the capillary in a loose square knot [KoK70] in which the bends were more severe than those expected in using the HeJRT system. The result again was no significant loss in activity transported, and as a result polyethylene capillaries were chosen for our HeJRT system.

Our initial capillaries had an inside diameter of 0.022 and 0.034 in. when the total length of the system was only a few feet. Now we typically use 0.055-in. I.D. capillary that is 40-50 feet long. If in the future we are faced with difficulties in transporting very short lived products through the system, we expect to use 0.072-in. I.D. capillary. With the present diameter capillary we often use ^{28}P($t_{1/2}$= 270 msec) to study the operation of the system and have also successfully run ^{40}Sc ($t_{1/2}$= 182 msec).

(A disucssion of the transport times for the HeJRT system is included later in this section.) The capillaries are supplied in 100 foot lengths by Clay-Adams and are their "Intermedic Tubing." The 45-ft. length of the capillary allows us to set up the detector assembly in a conveniently located low background area over the cyclotron shielding wall. While we have run with capillaries longer than 100 feet, no systematic study of the operation of the system has been made as a function of capillary length. There is, of course, the limitation of increasing transport time for longer capillaries of the same diameter.

In addition to experiments in which glass and polyethylene capillaries were used, we have also run using teflon capillaries and observed the same level of performance. In the past Ron Macfarlane at Texas A & M has run using stainless steel capillaries [MaR71]. It presently appears the operation of the HeJRT system is fairly independent of the material from which the capillary is formed. Our preference for polyethylene capillary initially was based on its flexibility, but now it is just a historical carryover.

We have observed that efficient operation of the HeJRT system requires the inside bore of the capillary to be smooth and of more or less uniform cross section. Macfarlane also reports (private communication) that localized heating or physically vibrating the capillary can greatly reduce the system's transport efficiency. Another thing to be avoided is discontinuities in the capillary. At present, our system does have one such discontinuity at the point of connection of the polyethylene capillary to the short stainless steel capillary leaving the target assembly. The capillaries are joined as described in section II. c. It has proven to be a relatively simple technique and yet has not seriously affected the transport efficiency. T. T. Sugihara's group, also at Texas A & M, has eliminated this discontinuity by eliminating the short piece of stainless steel capillary and is

running with teflon tubing entered directly into their target assembly [SuT72].

The helium flow rates for our system using a 50 ft. 0.055 in. I.D. polyethylene capillary range from 35.7 cm^3/sec (STP) to 167.8 cm^3/sec (STP) when the target assembly is pressurized from 1 atm to 3.5 atms, respectively. The relationship between target assembly pressure and flow rate is summarized in Figure 25a. This figure also includes the time necessary to sweep 1 standard cm^3 of helium into the capillary and an estimate of the time necessary for activities to traverse the length of the capillary. The sweep time is just the reciprocal of the flow rate. The decrease in sweep time does correspond to a legitimate decrease in the time necessary to get activities into the capillary in that the nuclear recoils will be stopped in the same number of standard cm^3. The estimate of the time spent traveling through the capillary is based on an equation presented by H. Dautet, et al.

$$T = \frac{L}{a} \left(\frac{2 + m_1}{3m_1}\right)$$

[DaH73], namely, where T = transit time in capillary, L = length of the capillary, a = the speed of sound in helium, and m_1 = the mach number at the entrance of the capillary. This expression assumes choked flow in the capillary (i.e. the flow reaches sonic velocity at the exit), that the flow is for an ideal gas, and that the flow is an adiabatic process. These are all reasonably good assumptions for our system. Figure 25b presents the same information for our system using a 43-ft. 0.034-in. I.D. capillary. (It should be noted the time spent in the capillary claculated from the above equation is only about one half that obtained using the graphs H. Dautet, et al., have included in their paper.)

The total transport time for a HeJRT system is just the sum of the time taken to thermalize the recoils and sweep them into the capillary

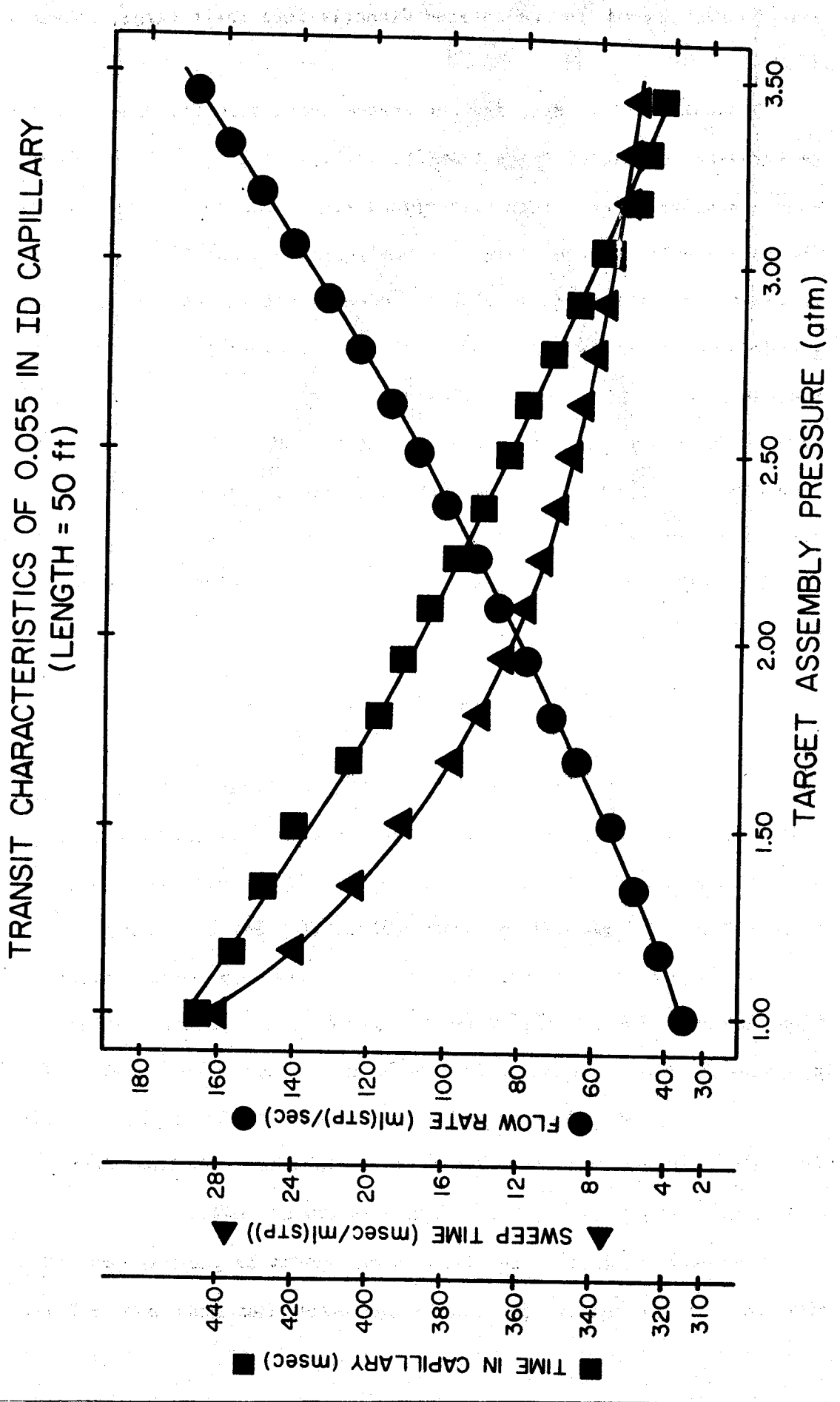

Figure 25a. Relationship between target assembly pressure and flow rate for 0.055 in. I.D. capillary. Also included are sweep times and an estimate of times in the capillary.

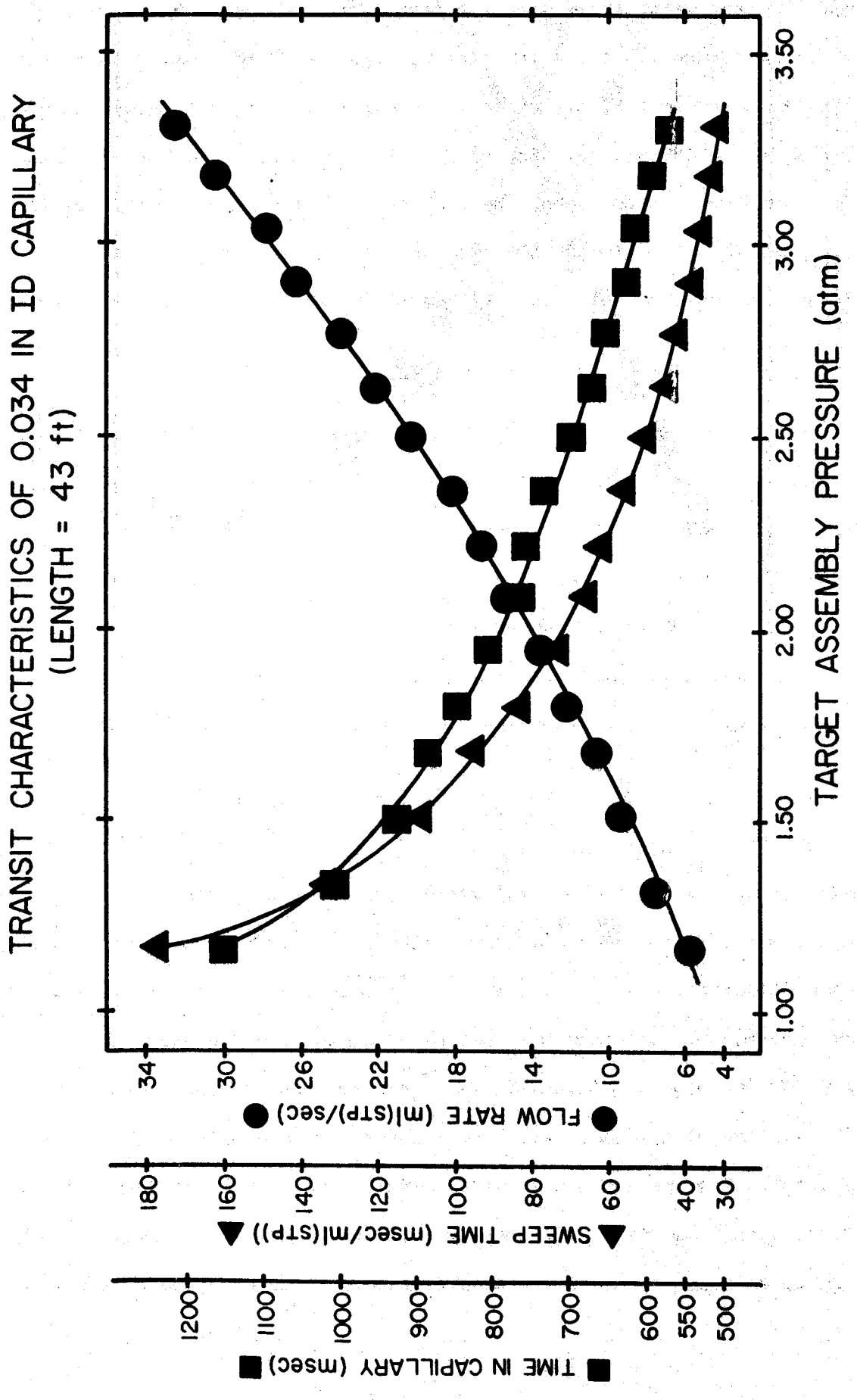

Figure 25b. Relationship between target assembly pressure and flow rate for 0.034 in. I.D. capillary. Also included are sweep times and an estimate of times in the capillary.

and the time spent traversing the capillary. Although there has been no direct measurement of transit time through our HeJRT system, there has been a measurement of the difference between the transit times for the 0.034- and 0.055-in. capillaries run at 1 atm target assembly pressure. This was accomplished using the 12.0-sec ^{23}Mg and 2.1-sec ^{26}Si activities produced with a 30-MeV proton Al. For two activities with different half-lives, the ratio of their activities (A/A') some time (t) after generation will be

$$A/A' = A_o/A'_o \, e^{-(\lambda-\lambda')t},$$

where A_o/A'_o is the ratio of initial activities and λ and λ' are the decay constants. For our purposes A_o and A'_o are functions of the beam intensity, but their ratio will be constant (with the possible exception that with large fluctuations of the current the transport mechanisms for the activities might differ, upsetting the ratio). If the same procedure is followed, allowing some different time to elapse between generation of the activities and counting, the resulting ratio of the ratios will be obtained,

$$\frac{(A/A')_{t_1}}{(A/A')_{t_2}} = e^{-(\lambda-\lambda')(t_1-t_2)}.$$

Here the ratios of the initial activities drops out, the decay constants are known, and the ratios of final activities can be measured. Thus, the time difference (t_1-t_2) can easily be determined. When this is done using our system, the agreement between the calculated and experimentally determined ratios was to within 7%. We expect to make a second determination of this time difference using the 70.5-sec ^{14}O and 0.27-sec ^{28}P activities generated from protons on a quartz target. The resulting larger difference in the decay constants will make the activity ratios more sensitive to the transport time differences. We also expect to make a direct measurement

of the transport time using a double target that will be moved through the assembly while monitoring the activities transported through the system with respect to time.

The Reynolds numbers associated with the flows near the entrance of the 45-ft capillaries range from about 40 to 250 for the 0.034-in. I.D. capillary run with target assembly pressures in the range of 1 atm to 3.5 atm and from about 300 to 1500 for the 0.055-in. I.D. capillary run with target assembly pressures in the same range. It is possible to calculate the Reynolds number at the exit of the capillary, a known Joule-Thompson coefficient, and using the detector assembly pressure (as predicted by H. Dautet et al. [DaH73] necessary to induce sonic flow at the exit of the capillary. The result of the calculations is that the Reynolds number remains essentially unchanged throughout the length of the capillary. It has generally been proven that Reynolds numbers below 2000 are associated with laminar flows [SeF70]. Accordingly, the flow through the capillary will be laminar except at any discontinuities, principally the entrance and exit of the capillary. At the entrance to the capillary there will be some distance required before the laminar boundary layer builds to the center of the capillary. The space between the boundary layer will have turbulent flow. The distance before the total flow becomes laminar is dependent on the Reynolds number of the flow and may extend several hundred diameters down the length of the capillary. When the HeJRT system is run, it is in this region where most of the activity is lost and the greatest build up of molecular clusters occurs. Presumably, this is a reflection of the flow not yet becoming completely laminar. At the exit of the capillary, as the flow suddenly expands into the larger volume and lower pressure of the detector assembly, the flow certainly becomes turbulent. However, at this point we are dealing with what could more accurately be

defined as opposed to the viscous flow associated with the higher pressures further back in the capillary, and are relying on the enormous masses of the clusters to carry them to the collecting surface. There can be activity lost in the last centimeter or two of the capillary if it is not held straight. Presumably, this is a result of the drop in pressure occurring near the exit of the capillary, with the result that there is no longer a sufficient number of interactions between the helium of the flow and the molecular clusters to cause the clusters to negotiate even a slight bend in the capillary successfully.

II. h. Total System Efficiency Determination

The overall efficiency of the helium jet transport system, including both the efficiency for the transport of activities and the efficiency for collecting these activities on paper tape has been determined for three different recoiling nuclei. The basis of the efficiency determination was a comparison of the activities generated in metal foils by conventional nuclear bombardment with the activities generated on paper tape (1" non-oiled paper computer tape) using the HeJRT system.

Copper and nickel foils were activated using the "rabbit" system described in Appendix II. The reactions of interest in the efficiency determinations were $^{65}Cu(p,3n)^{63}Zn(t_{1/2}=38.4$ min) $^{62}Ni(p,3n)^{60}Cu$ and $^{60}Ni(p,n)^{60}Cu(t_{1/2}=24$ min) and $^{58}Ni(p,\alpha n)^{54m}Co(t_{1/2}=1.5$ min). In each case a beam energy of 30 MeV was used, not because of cross-section considerations but to allow a comparison of present efficiency with previous runs in which the activities of interest were the lighter copper and zinc isotopes. The copper foils were activated with, as nearly as possible, constant currents for 30 sec, and the nickel foils for 60 sec. Five minutes after the end of each activation a 15-min count of the γ radiation from the foils were taken using a 4.6% (relative to a 3" x 3" NaI(Tl) detector at 1.33 MeV) Ge(Li) detector at standard source geometry. Photopeaks at 669, 1332, and 410 keV were used as signatures for ^{63}Zn, ^{60}Cu, and ^{54m}Co, respectively. In each case the peak areas were adjusted for integrated current on target and for ADC dead time. The dead-time correction was made using a pulser with a known repetition rate.

Following the runs made using the rabbit, the same activities were collected using the HeJRT system. Copper and nickel foils were placed

in the single target assembly (described in Section II. c. "Detector Assemblies.") The pressure in the target assembly was maintained at 1.0 atm using helium with an initial purity of >99.995% which was doped with approximately 250 PPM benzene vapor. The capillary was made of polyethylene, had an inside diameter of 0.055 in, and was just under 50 feet in length. The activities were collected on a stationary piece of paper mounted in the chamber pumped to <1000 μm pressure. As in the case of the rabbit runs, the targets were bombarded for 30 and 60 sec for the copper and nickel foils, respectively, with a nearly constant current of 30-MeV protons. After the end of the bombardment, the collection of the activities on the paper was continued for an additional minute to assure complete sweeping of activities from the target area. Five minutes after the end of the bombardment a 15-min count of the γ radiation was taken using the same detector in the same geometry. Also, as in the case of the rabbit run, the photopeak areas were corrected for integrated current and analyzer dead time.

In both the rabbit and the HeJRT runs 0.0001-in. foils were used. However, for the efficiency determination the thickness of the target used in the HeJRT system was taken to be the maximum range of the recoils, i.e., the target thickness from which recoils were able to leave the target and enter the helium atmosphere. These maximum ranges were calculated as outlined in Section II. b. "Recoil Characteristics." The efficiencies were determined to be 24% for ^{63}Zn, 49% for ^{60}Cu, and 60% for ^{54m}Co. However, it was subsequently learned that the efficiency of the HeJRT system increases as we proceed from 1 atm to 3 atm of helium pressure in the target assembly (see Section II. i. "Efficiency vs Target Assembly Pressure"). While the next section discusses this increase

using Mg and Si, the increased efficiency was confirmed for the Zn, Cu, and Co recoils. Accordingly, the efficiencies for the HeJRT system operating with 3 atm helium pressure in the target assembly are approximately 50% for Zn, 75% for Cu, and 90% for Co.

Table II. Total HeJRT System Efficiency

Isotope	Efficiency (1 atm)	(3 atm)
^{63}Zn	24%	50%
^{60}Cu	49%	75%
^{54m}Co	60%	90%

Even allowing for uncertainties of greater than 20% in the measured efficiencies relative to one another, it is clear that the HeJRT system exhibits varying efficiencies for different activities. In that the recoil represents such a small part (in the ppm range) of the cluster with which it is associated, it seems rather doubtful that these varying efficiencies are reflective of differing probabilities for the cluster-plus-recoil to stick to the tape. Similarly, it seems doubtful that these varying efficiencies are reflections of differing probabilities for the clusters-plus recoil to be transported through the system. Thus, as the final alternative it seems likely that these varying efficiencies are reflections of differing abilities of the recoil to form a "bond" with the cluster. [Additional evidence and a discussion of the recoil-cluster bond can be found in Sections II. f. "Cluster Molecules," II. k. "Efficiency vs Time," II. m. "Aqueous Chemistry," and II. o. "Plasma Chemistry." If

the recoil has a difficult time attaching to a cluster or if the attachment is weak possibly resulting in a separation of recoil and cluster as they move through the system, it is likely that some number of the recoils will be traveling through the capillary without being attached to a cluster. Accordingly, these unattached recoils will not be assisted through the system by the clusters and will have an efficiency corresponding to the efficiency of the HeJRT system using pure He, $\leq 5\%$.

II. i. Efficiency vs Target Assembly Pressure

In the initial experiments when only non-doped helium was used (and the total HeJRT system efficiency was <5% as a result), the efficiency was essentially independent of the pressure in the target assembly. Through the pressure range from 20-in. vacuum to 4-atm there was no obvious or systematic dependence of efficiency on the target assembly pressure. However, when helium doped with small admixtures of benzene is used in the HeJRT system, the effect of target assembly pressure on the overall efficiency is obvious; see Figures 26 and 27. Each point in the figures is the average of three determinations made at that pressure.

The HeJRT system was run using the single target assembly described in Section II. c. "Detector Assemblies" using approximately 40-ft polyethylene capillaries with 0.055-in. and 0.034-in. inside diameters for Fig 26 and 27, respectively. The helium was doped with benzene to a concentration of about 20 ppm. The experiment was run using as nearly as possible 1.5 μA of 30-MeV protons on an aluminum target foil, initiating for the most part the $^{27}Al(p,2n)^{26}Si$ and the $^{27}Al(p,\alpha n)^{23}Mg$ reactions. The activities were collected on paper tape moving at 0.5 in./sec past a 4.6% relative efficiency Ge(Li) detector. The activities were deposited on the tape at the edge of the detector's field of view with the capillary at a distance of 1 in. from the tape and at a 45° angle such that the tip of the capillary was out of view of the detector. The geometry was such that the activities spent 3 to 4 sec in view of the detector.

Figure 26 shows the results of runs using a 0.055-in. polyethylene capillary. Peak areas for the 820- and 439-keV transitions in ^{26}Si and ^{23}Mg, respectively, are plotted against target assembly pressures from 0 to 35 PSI gauge pressure. Peak efficiency is reached at roughly 3 atm

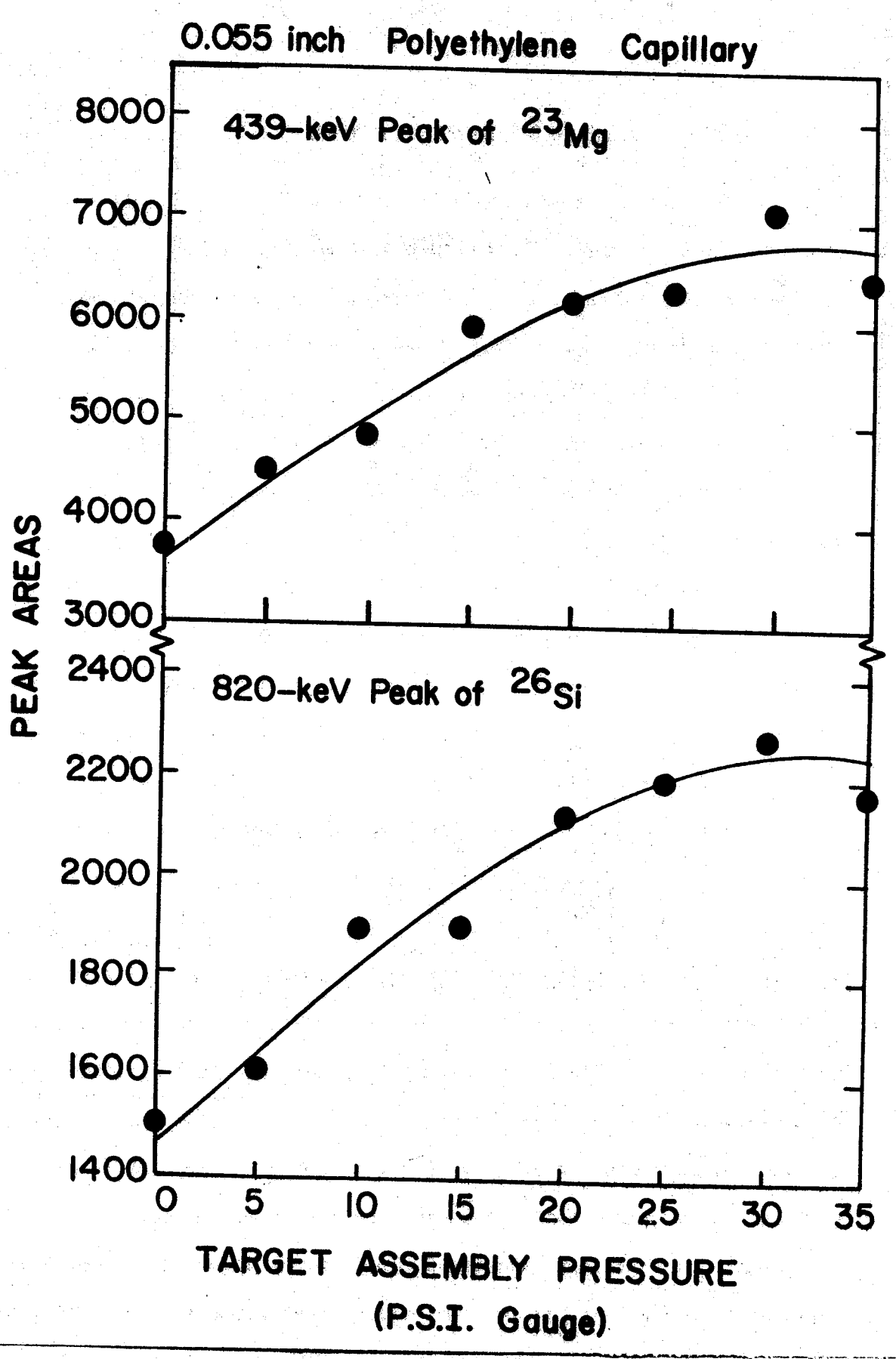

Figure 26. Peak areas for transitions in ^{23}Mg and ^{26}Si as a function of target assembly pressure, when using a 0.055 in. capillary.

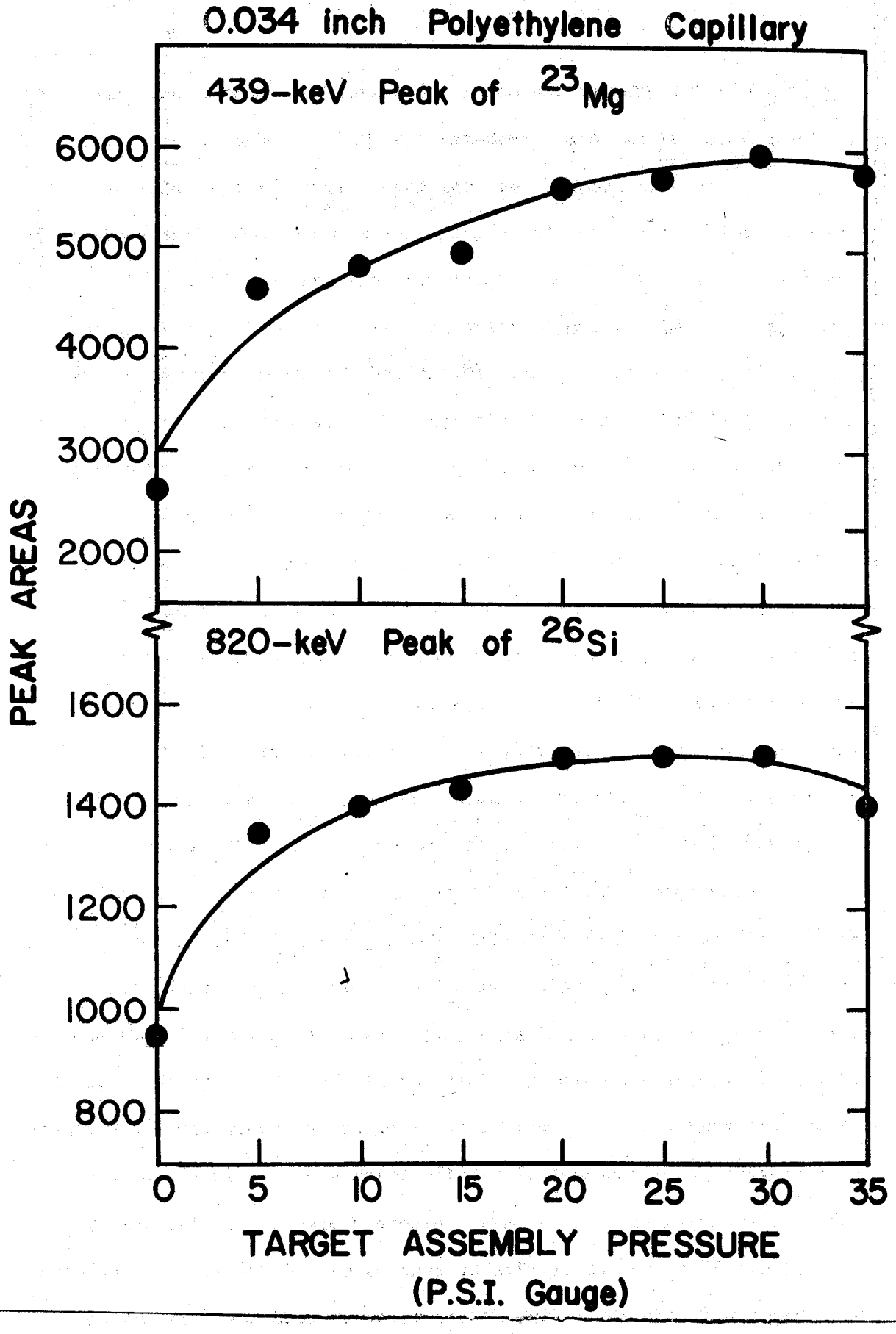

Figure 27. Peak areas for transitions in ^{23}Mg and ^{2C}Si as a function of target assembly pressure, when using a 0.034 in. I.D. capillary.

and is about 50% greater than at 1 atm. This increase in peak areas with increasing target assembly pressures has to be considered a legitimate efficiency increase and not just the reflection of a half-life effect. [The average transit time for recoils through the HeJRT system decreases for increasing target assembly pressure, see Section II. g. "Capillary Considerations."] If the increase in peak areas with increasing target assembly pressures were a half-life effect, it would be expected that the increase for the 2.1-sec ^{26}Si activity would be much more dramatic than that for the 12.1-sec ^{23}Mg activity. In that the ^{23}Si and ^{23}Mg activities were made simultaneously from the same target, it seems unlikely that this peak area increase could be attributed to anything other than an increase in system efficiency. Further, in that the final cluster-plus-recoil velocity in the capillary is not affected by the target assembly pressure, in the range 0 to 35 PSI gauge pressure under the vacuum pumping conditions used (see Sections II. g. "Capillary Considerations" and II. g. "Efficiency vs Detector Assembly Pressure), it seems unlikely that the increase in system efficiency is a result of more of the activity sticking to the collecting surface. Additional evidence supporting this is presented in Section II. c. "Collecting Surface Considerations" where a comparison is made with a collecting surface with poorer sticking ability. Accordingly, the increase in system efficiency must reflect either a decrease in the number of clusters-plus-recoils lost in their flow through the capillary or an improvement in the conditions fostering the generation of clusters or fostering the attachment of recoils to cluster, possibly a result of increasing plasma density as target assembly pressure in increased.

Figure 27 shows the results of runs using a 0.034-in. I.D. polyethylene capillary. There is some disagreement between the ^{26}Si and ^{23}Mg

curves as to where the maximum efficiency is reached and also as to the degree of the improvement at 3 atm over the efficiency at 1 atm target assembly pressure. The ^{26}Si curve reaches a maximum at roughly 2 atm and is up to about 50% over the efficiency at 1 atm, while the ^{23}Mg curve reaches a maximum at roughly 3 atm and is up to about 100% over the efficiency at 1 atm. It seems likely that this disagreement is a result of poor statistics. If it were the reflection of a half-life effect, the greater improvement in the efficiency would be observed in the shorter 2.1-sec ^{26}Si curve and not in the 12.1-sec ^{23}Mg curve.

There is a rather striking difference between the two sets of curves; the runs made using the smaller 0.034-in. I.D. capillary have a much more rapid increase in efficiency in the lower portion of the curves than for the run made using the 0.055-in. capillary. In the discussion of the runs made using the 0.055-in. I.D. capillary it was concluded that the increase in efficiency with increasing target assembly pressure resulted either because of a decrease in the number of clusters-plus-recoils lost in their flow through the capillary or an improvement in the conditions fostering the generation of clusters of the attachment of recoils to clusters. In that the increase in efficiency with increasing pressure is different for the two capillary diameters used, it seems unlikely that the increased efficiency results solely from an improvement in the conditions under which the clusters are formed or under which the recoil is attaching to the cluster. Additional evidence for this comes from the results reported in section II. f. "Molecular Clusters." Here the relative efficiency of the HeJRT system as a function of beam current is discussed. To the first order, plasma density behind the target will be directly proportional to both beam current and helium pressure. If the curves in figures 26 and 27 are corrected for the expected increase in system efficiency as a

result of increasing plasma density the major portion of the increase remains. Thus, the improvement in efficiency for the HeJRT system with increasing target assembly pressure must come primarily from an improvement in the flow of clusters plus recoils through the capillary. A possible explanation of this effect could lie in the reduction of the mean free path of the helium in the capillary as the pressure in the target assembly, and thus throughout the system, is raised. As the mean free path is reduced, the number of collisions occuring between the recoil-plus-cluster combination and Helium atoms is increased, which will tend to help concentrate the clusters in the center of the capillary. For a discussion of the focusing effects of laminar flow, see reference [Cow 56] and section II. f. "Molecular Clusters."

For each of the curves in Figures 26 and 27 it appears the curves are starting to turn downward. Ones first thought might be that this corresponded to the break down of laminar flow occuring at higher pressures in the target assembly. In section II. g. "Capillary Consideration" the Reynolds numbers of the flow were determined and while it was found that this could possibly be the case for the 0.055-in. capillary it most probably was not the case for the 0.034-in. capillary. Accordingly, it is felt that this effect is not a result of the breakdown in laminar flow in the capillary.

II. j. Efficiency vs Detector Assembly Pressure

In an attempt to determine the relationship between the total system efficiency of the HeJRT system and the pressure at which the detector assembly is held, a series of runs was made in which the system efficiency for collecting paper tape was monitored while the capillary to tape distance and angle were varied along with the pressure in the detector assembly. It was hoped that the drop in total system efficiency as the pressure in the detector assembly was raised could be identified as to the extent of it being a result of a drop in the efficiency for transporting activities through the capillary or a result of a drop in the efficiency for collecting activities on the collecting surface. It is expected the efficiencies associated with the generation of activities and cluster molecules and the attachment of activities to clusters would not be affected by varying the pressure in the detector assembly.

For these runs the helium was doped with ~10 ppm benzene vapor and the pressure across the HeJRT system was held constant at 2 atm. The capillary used was a 0.055-in. J.O. polyethylene capillary. The tape used to collect the activities transported through the system was non-oiled paper tape (computer perforation tape) and was advanced at the rate of 0.25 in.per sec. In order to eliminate any long-term effects from the cyclotron beam current varying, ^{28}P with its short half-life of 280 msec was chosen as the activity to monitor. The ^{28}P was generated using a 35-MeV 0.7-μA beam of protons on a 0.05-in. quartz target to initiate a $^{28}Si(p,n)^{28}P$ reaction. A Ge(Li) detector with a 4.6% relative efficiency was used to monitor the γ count rate. The results were corrected for any small fluctuations in the beam current and were plotted against the pressure in the detector assembly (see Figure 28). The pressure in the

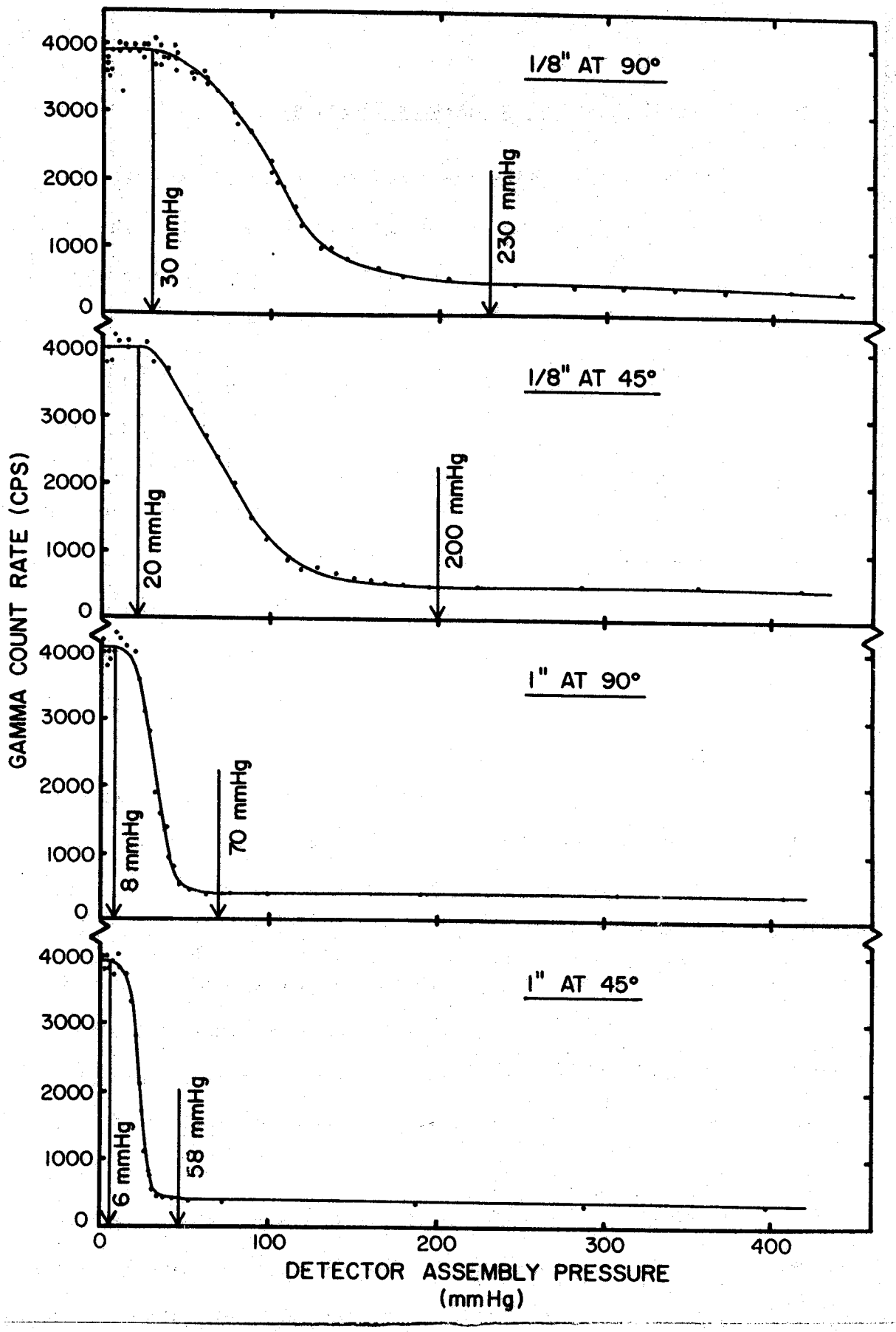

Figure 28. Curves expressing the relationship between detector assembly pressure and total system efficiency for various capillary to tape angles and distances.

detector assembly was varied by changing pumps and leaking air into the detector assembly.

In each of the cases, capillary to tape distance and angle, the initial system efficiency (P 1 torr) was essentially the same. [See Section II. L. "Collecting Surface Considerations" for a discussion of the initial efficiencies for capillary to tape distance of 1/8 and 1 in. and angles of 90° and 45°]. However, the pressure at which a reduction in the total system efficiency was first noticed was different for each of the four set-ups. A detector assembly pressure (P_a) of ≥30 torr was necessary to affect the efficiency in the 1/8"-90° set-up, P_a ≥20 torr for the 1/8"-45° set-up, P_a ≥8 torr for the 1"-90° set-up, and P_a only ≥6 torr to affect the efficiency of the 1"-45° set-up. In each of the cases, as the pressure was further increased the observed count rates fell to a constant minimum value, which corresponded to none of the activity collecting on the tape and was just the result of decay occuring as the helium containing the activities was being pumped from the detector assembly. This was confirmed by the ovservation of an increase in the count rates when the vacuum pump was turned off (thus allowing a build up of helium containing activities in the detector chamber) followed by an appropriate reduction when the pump was turned on again.

If the observed drops in total system efficiency with increasing detector assembly pressure are the result of drops in the collecting efficiency as a consequence of collecting through a more dense atmosphere, it would be expected that the drops in efficiency would occur at lower pressures and be more severe as the capillary to tape distance was increased, allowing a greater opportunity for the beam of activities to interact with the atmosphere. Similarly, it would be expected that the drops in

efficiency would occur at lower pressures as the capillary to tape angle was made more oblique, allowing a greater opportunity for the beam of activities to be deflected from the collecting surface. Both effects are seen in the results reported in Figure 28. If the observed drops in total system efficiency with increasing detector assembly pressure were the result of drops in the transport efficiency as a consequence of changing flow considerations in the capillary, it would be expected that the efficiency would hold constant until the pressure in the detector assembly was raised beyond the point at which flow of Mach 1 could no longer be achieved, at which time the efficiency would start to drop off and continue to drop off with increasing pressure. Note, the pressure experienced at the exit of the capillary at Mach 1 is no longer achieved in the helium flow will be independent of capillary to tape distance and angle. From H. Dautet's paper [DaH73] this should occur at detector assembly pressures of ≥35 torr for our system operating as described above. While in each case the total system efficiency did seem to hold constant before starting its drop, the pressure at which the drop started and the severity of the drop was very much dependent on the capillary to tape distance and angle. It is of course necessary to consider that the pressure recorded for the detector assembly is then the pressure experienced at the exit of the capillary. However, it would be expected this error would be largest for the 1"-90° case, and this is the case for which the pressure corresponding to the initial drop in efficiency is the highest. Accordingly, it seems the primary factor acting in the drop in total system efficiency with increasing detector assembly pressure is a drop in collecting efficiency. This conclusion is reinforced upon considering the total system efficiencies of 50-75% reported in Section II. m. "Aqueous Chemistry" for collecting

activities in aqueous solution under atmospheric pressure.

From the results discussed above it is quite apparent that the requirements of the pumping system for a HeJRT system used alone are minimal. It is only necessary to maintain pressures of 20-30 torr in the low pressure end of the system without loss of efficiency. Only when the HeJRT is used to supply activities to equipment requiring low pressures is it necessary to consider large pumping capacities and helium skimming.

II. k. Efficiency vs Time

When considering the total HeJRT system efficiency vs time, it is necessary to consider two time scales. The first, measured in seconds, is the short-term efficiency building up when the cyclotron beam is first turned on. This is related to effects such as the time required to build up suitable cluster molecules. The second, measured in hours, is the long-term efficiency falling off as the system is used for long runs. This is related to effects such as cluster molecules collecting in the capillary. Occasionally it seems as if there is a third time scale, measured in minutes, over which the efficiency tends to build up after the cyclotron beam is first turned on. However, this time vs efficiency effect has not been documented. It is felt that this effect may be the result of moisture or oil leaving the target surface when it heats up from the beam striking it.

A series of runs was made to characterize the short-term efficiency build-up when the cyclotron beam is first turned on. In these runs 280-msec ^{28}P was the primary activity monitored. The ^{28}P was generated using 30-MeV protons on a 0.05-in. quartz target through the $^{28}Si(p,n)^{28}P$ reaction. The helium was doped with ~50 ppm benzene vapor and the pressure of the target assembly was maintained at 3 atm. The pressure in the detector assembly was maintained at ≥1 torr. The capillary was used 0.055-in. polyethylene. The activities were collected on paper tape which was advanced only between runs to supply a fresh surface for the next run. Also, between each run the target assembly was pumped out several times to remove cluster molecules remaining from the previous run. Each run consisted of making an x-y plot of gross γ count rate time (using a time base) as the cyclotron beam was turned on and off (see Figure 29). During the cyclotron on time the beam current was held as nearly constant as possible

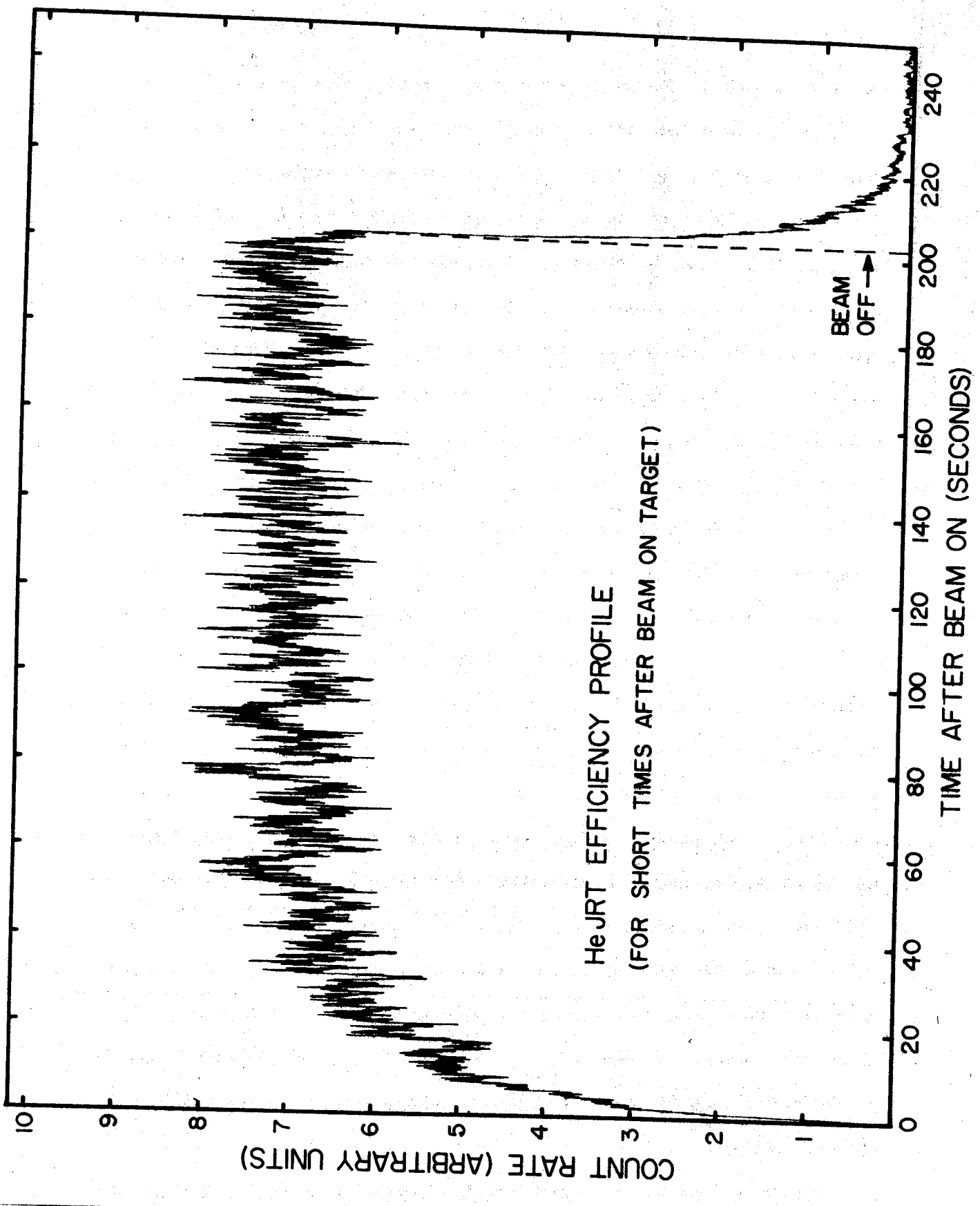

Figure 29. An example of the plots recorded as the cyclotron beam was turned on and off in an attempt to discover the short term efficiency build-up in the first moments after the beam is turned on.

usually ±3% and data from only the most constant runs were saved. The beam was turned on and off by raising and lowering a scintillator in the beam line near the cyclotron. The beam passing through the scintillator diverged and was of the wrong energy to be transported through the beam optics. This method of turning on and off the beam was chosen because it was faster than the vacuum valves in the beam line (about 0.2 sec as opposed to more than 1.0 sec for the valve). The count rate signal was taken from an ORTEC rate meter (#441) set for 10% standard deviation (shortest time constant). The output was plotted using a relatively fast Esterline Angus x-y recorder with a maximum slewing speed of 55 in./sec.

By comparing the curve recorded as the beam was turned on with the inverted curve recorded as the beam was turned off it should be possible to ovserve the build up of the total HeJRT system efficiency in the early moments after the cyclotron beam is first turned on. This should be possible because the time constants of the rate meter and the x-y recorder will be the same for increasing or decreasing count rates and the growth and decay curves for the activities generated will just be inversions of one another. Accordingly, the present difference in these two curves will correspond to the efficiency of the system. Figure 30 displays composite "beam-on" and "beam-off" curves taken from a collection of count rate curves like the one in Figure 29. Also shown in Figure 30 is the short term efficiency curve generated from the percent difference between the "beam-on" and "beam-off" curves. It can be seen that the efficiency rises very rapidly to about 70%, then rises rather slowly, taking almost a minute to reach full efficiency.

For these runs the standard target cylinder (see Section II. c. "Target Assemblies"), which is about 4-cm long, had been replaced with one 10-cm long, such that it came to within 2 mm of the Faraday cup. This was

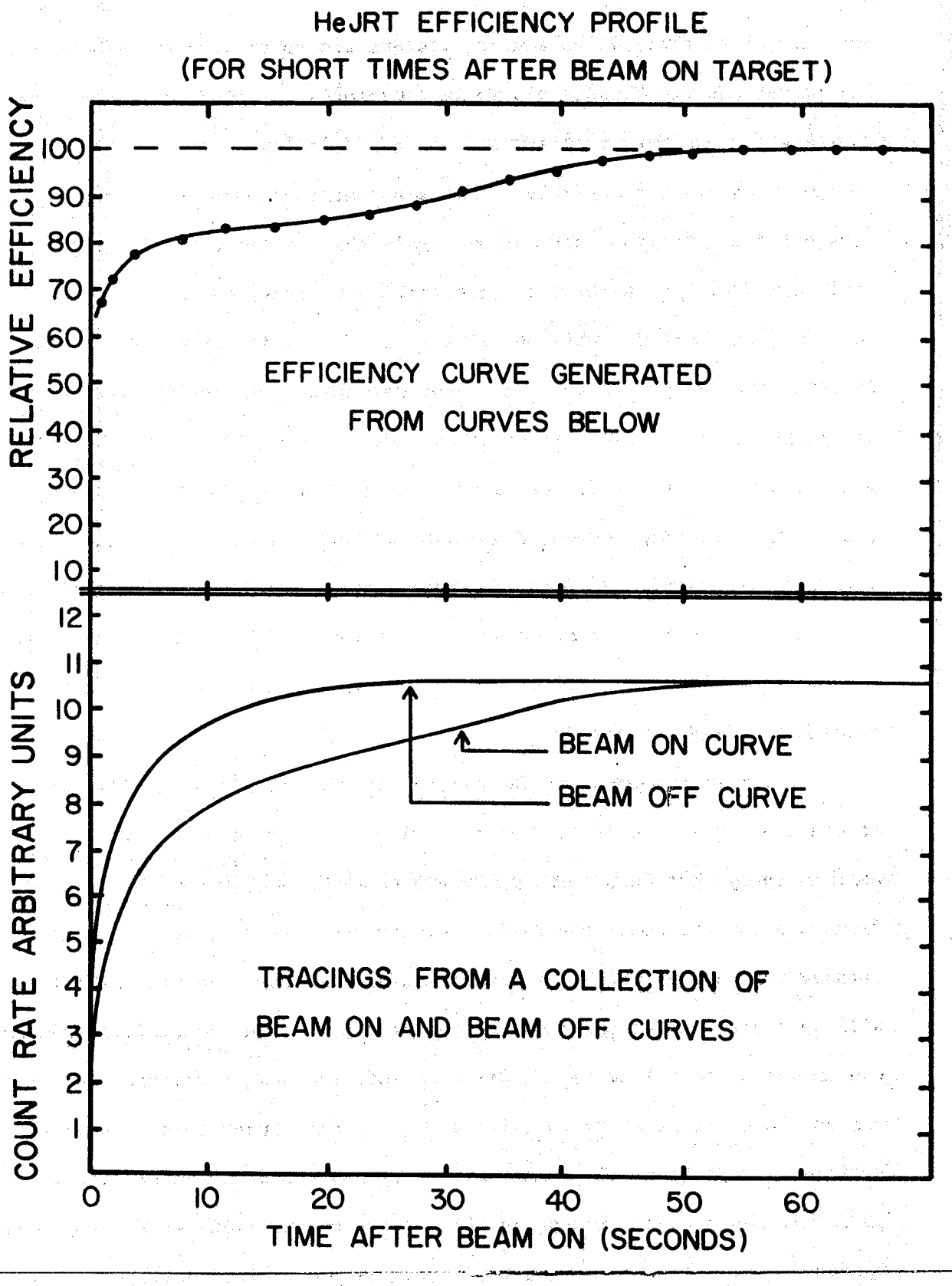

Figure 30. Composit beam-on and beam-off curves, and the relative efficiency for the HeJRT system in the first few moments after beam is first turned on.

done to insure that all molecular clusters generated in the volume between the target and the Faraday cup would immediately proceed toward entering the flow through the capillary and would not diffuse out into the bulk helium in the target assembly. This was important because if many of the clusters did enter the bulk helium supply the efficiency of the HeJRT system would not stabilize until the concentration of clusters in the bulk helium supply equilibriated. With the flow rate of 7500 standard cc-min, the rate at which the target cylinder was swept was about once every 1-1/2 sec. Accordingly, any increase in efficiency due to the generation of cluster molecules should be manifested within times of a few seconds (allowing for some mixing occuring between the helium in the cylinder and fresh helium entering the cylinder). Thus, it seems likely that the initial rapid rise in efficiency during the first seconds corresponds to the build up of the cluster molecules necessary for the efficient transport of activities through the HeJRT system.

The longer component of the efficiency rise is not so easily explainable. It could be explained if cluster molecules were diffusing out into the bulk helium supply, but this seems extremely unlikely in view of the large helium flow rate and the small separation between the target cylinder and the Faraday cup through which the clusters could diffuse. This possibility will be checked after the construction of a new target assembly is completed, one in which the helium is fed directly into the target cylinder and which has no place for clusters to diffuse to. If the longer component of the efficiency rise is still present with this new target cylinder, other possibilities such as adsorption of clusters on the cylinder walls or dead spaces occuring in the flow in the target assembly will be looked into.

As the HeJRT system is used the efficiency of its operation tends to

decrease; however, it is difficult to characterize this effect quantitatively. In early runs the drop in total system efficiency typically would manifest itself in a manner of hours of running time. Presently the drop in system efficiency does not manifest itself until many days of running time have elapsed. In fact, the capillary is now typically replaced after a week or so of running time not because of a drop in efficiency for the system but to prevent such a drop from occuring at an inconvenient time in an experiment. Thus, it is difficult to place a high efficiency time limit on the capillaries used in the system as operated today. It is, however, possible to make some empirical and/or qualitative statements concerning this efficiency drop and to present some thoughts on the subject which are not supported by hard experimental evidence.

The first concerns the nature of the efficiency drop. The efficiency will hold fairly constant, then after some time will start to drop. Then it will drop quite rapidly to about 10-20% of its initial efficiency, after which the drop is much more gradual. If the system is then rejuvinated as described below, the efficiency will return to essentially its initial value; however, as the system's use is continued the efficiency will again fall and the drop will occur after a shorter period of running than did the initial drop.

The reason for the efficiency drop is related to a build-up of material in the capillary and on the target which is usually quite visable. The effect of the build-up in the capillary presumably is to introduce additional turbulence in the helium flow and thereby to decrease transport efficiency. It seems logical that this turbulence would cause a further build-up, causing the more rapid drop in transport efficiency. The build-up in the capillary is soluble in acetone. Accordingly, by flushing the capillary

with acetone it is possible to rejuvinate the capillary. Presumably the build-up on the targets is from the same source; however, it is heated by the cyclotron beam and resembles more a carbon deposit, which is not soluble in acetone.

In early runs when benzene was first added to the helium supply to increase the efficiency of the HeJRT system, quite large amounts of benzene were used (higher than 0.1% in some cases). In an effort to reduce the build-up of material in the capillary and on the targets, the concentration of benzene in the system was gradually cut back to the 10-20 ppm used at present. While this may have helped slightly in the case of the build-up on the target it did not seem to bring about a major improvement in the case of the build-up in the capillary.

It seems the rate of decay of the system efficiency is related to air in the system. It was observed that the problem of build-up of material in the capillary was particularly bad in those runs in which the target assembly was opened frequently and those runs in which the operation of the HeJRT system using benzene in the helium supply was compared with using air plus water vapor in the helium supply. In both cases, if the pump-out of the target assembly were not complete, air would remain in the system. In general, little care was taken in these early runs to get a complete pump-out of the target assembly, relying on the flow of helium to purge the system. Since that time care has been taken to get more complete pump-outs, and the target assembly is filled with helium and pumped out 3 or 4 times before bringing the beam into the assembly. This, possibly combined with the low benzene concentrations used at present, have essentially solved the problems of build-up in the capillary and have greatly reduced the problem of build-up on the targets. Accordingly, the problem of the total transport efficiency dropping with time has been essentially eliminated.

II. 1. Collecting Surface Considerations

In the earliest runs of the HeJRT system in this laboratory the standard collecting surface was the sticky side of masking tape. For the past couple of years, since the addition of the tape transport, the standard collecting surface has become paper tape (1" non-oiled computer perforation tape, Singer P/n 200 1218 tape). The reason for the change to paper tape was for the obvious experimental simplification and has had no effect on the collection efficiency. On those occasions when cooled solid state detectors are exposed to the vacuum of the detector assembly, aluminized mylar tape is used to eliminate the problem of the small amount of moisture in the paper tape from entering the vacuum and condensing on the detector. Other groups have used such things as old computer magnetic tape (T. T. Sugihara, Texas A & M University, private communication), metal surfaces, and surfaces smeared with vacuum grease. All things considered, it does not seem to make very much difference what is used as a collecting surface when molecular clusters are used to carry activities through the system. However, a comparison of the collection efficiency of paper tape and aluminized mylar tape indicates the aluminized mylar tape to be a little less efficient. Figure 31 shows the results of the comparison made at a series of different target assembly pressures while looking at the 439-keV peak of ^{23}Mg. Each of the points in the figure is the average of three determinations made at that pressure. The two curves have the same essential shape, but the curve for aluminized mylar is from 9 to 12% below that for paper tape. In each case the detector assembly was pumped to below 10 torr and the capillary to tape distance and angle were 1/2 in. and 90°, respectively. At this time it is felt there is not enough known to present an explanation of the differing collection efficiencies, other

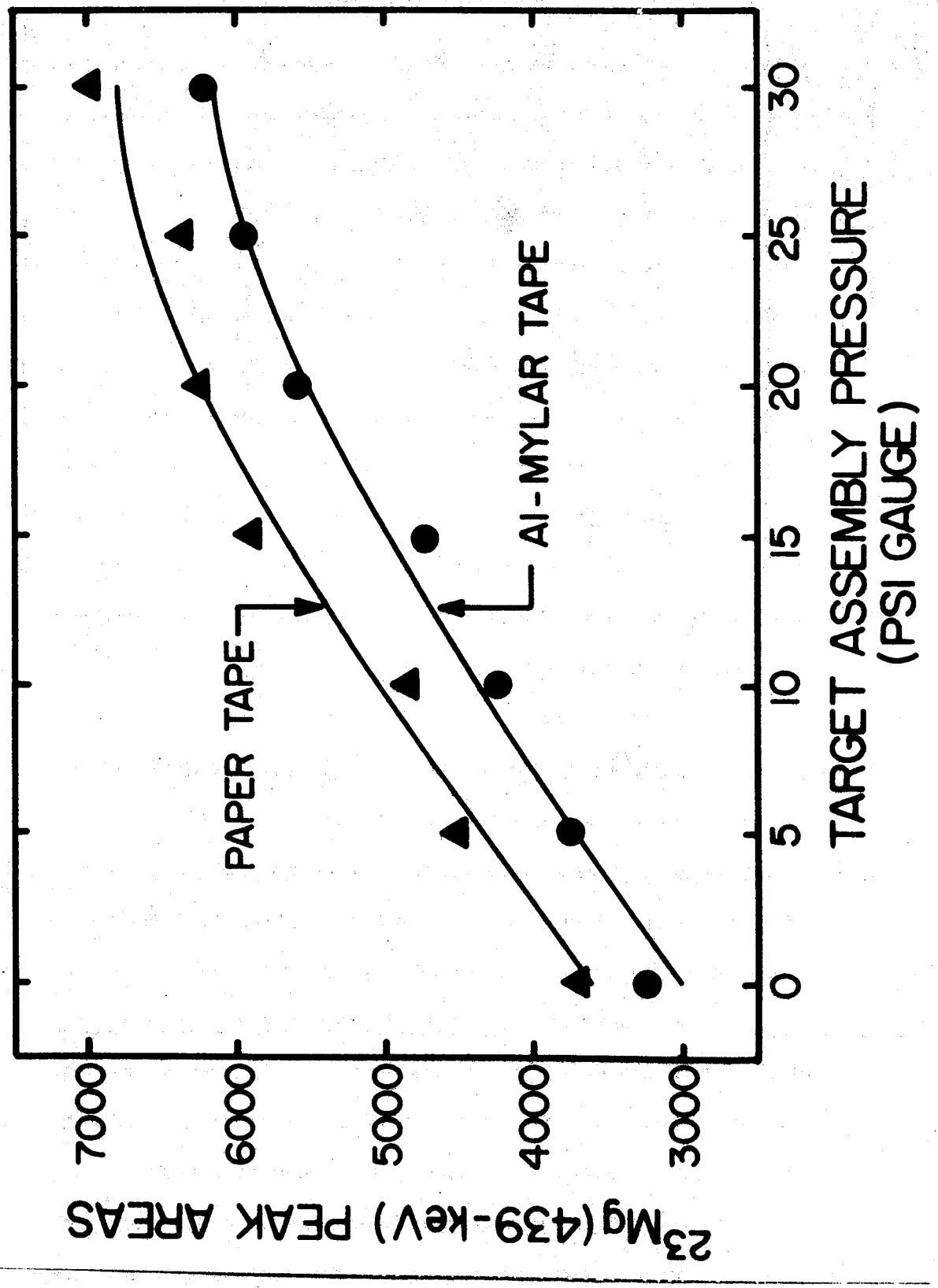

Figure 31. A comparison of the effectivness of paper tape and aluminized mylar tape as a collecting surface.

than to suggest the possibility that it is related to the rougher textured surface presented by the paper tape.

A preliminary study has been conducted to determine the effect of varying the tape to capillary distance and the angle on collection efficiency. The collection efficiency was followed by monitoring the gross γ count rate of activities produced with 30-MeV protons on aluminum. The two principal components of the activity were ^{23}Mg and ^{26}Si. For these determinations a 0.055-in. polyethylene capillary was used and the helium flow was doped with 10 ppm benzene vapor. The results are summarized below for paper tape.

Tape to Capillary Angle	-- Distance	Collecting Efficiency
90°	1/8 inch	≡100%
90°	1 inch	97.5 ± 5.%
45°	1/8 inch	98.5 ± 5.%
45°	1 inch	97.5 ± 5.%

Accordingly, within the limits of the uncertainty of the measurements the collecting efficiency for paper tape is unaffected by changes in capillary to tape angles up to 45° or distances up to 1 in. Since the drops in efficiency upon changing the angle and distance are so small, if they do exist, none of the in-between values were checked. The capillary to tape angle and distance of 45° and 1 in. are what is typically used in γ singles experiments in order to keep the tip of the capillary (where activities will often build up) out of the view of a collimated detector. Activities have been collected on paper tape at distances up to 6 in. with fairly good yields; however, at this distance it is necessary to take into consideration the divergence of the cluster molecules leaving the capillary. Approximately 90% of the clusters diverge with an angle of less than 3°

(see Section II. F. "Cluster Molecules"). As yet this study has not been extended to the aluminized mylar tape we occasionally use. However, by private communication, the members of R. D. Macfarlane's group at Texas A & M report the efficiency for collecting on mylar tape drops to about 50% on changing the capillary to tape angle from 90° to 45°

When the HeJRT system is operated using molecular clusters to increase transmission efficiency, it is necessary to consider a couple of side effects. The first is a desirable effect; when the desired product of the nuclear reaction is volatile or is naturally a gas, it is not necessary to go to any additional effort (like using a LN_2 cooled collecting surface) to hold the activity after transport through the system. This is evidenced by the presence of the 2311-keV line from 71-sec ^{14}O in all γ spectra recorded when using an oxide target in the HeJRT system. The line is present in good yields in runs using both paper tape and aluminized mylar tape, both at room temperature. The second effect is not desirable when performing charged particle spectroscopy; the build-up of cluster molecules on the collecting surface, through which the emitted charged particles must pass will degrade the energy of the particles. The effect on β particles is small except when the build-up of clusters occurs over a long period of time as is the case for long-lived activities. However, the effect on the energy of emitted α particles is much more serious even when the build-up of clusters is only limited to a few minutes. It is hoped a heated collecting surface can be used in these cases to break up the cluster molecules as they are deposited on the collecting surface, such as R. D. Macfarlane uses in his recoil time-of-flight spectrometer [MaR73].

II. m. Aqueous Chemistry On-Line

The hope that "wet" chemistry could be performed on-line with the HeJRT system arose from the observation that the efficiency of the HeJRT system when depositing activities on paper tape did not start to fall off until the pressure in the detector chamber (box where activities transported through the system are deposited on some collecting surface and counted) was raised to above 20-30 torr (see Section II.n. "Detector Assembly Pressure vs. Efficiency". This was important because the vapor pressure of water at 20°C is 17.5 torr. Accordingly, it would be possible to do aqueous chemistry under these conditions (collecting chamber pressure $\gtrsim$20 torr) and not have the solutions boiling off.

The first attempt at chemistry was an on-line attempt in the search for ^{64}Ge. The apparatus for this run is shown in Figure 32. The activities were generated using a ^{3}He beam on a natural Zn foil and were transported through a polyethylene capillary to the detector chamber. The detector chamber was pumped so as to maintain a pressure $\gtrsim$20 torr. The exit of the capillary was directed at an orifice in a sealed container partially filled with concentrated HCl. It was hoped that the activities attached to molecular clusters would enter the HCl container through the orifice and become trapped in the acid solution. There the Ge activities would form the volatile chloride $GeCl_4$ and be pumped off to a cold trap, where they could be counted. This first attempt was unsuccessful primarily because of inefficiencies remaining in the HeJRT system at that time, poor alignment between the capillary and orifice to the acid container,

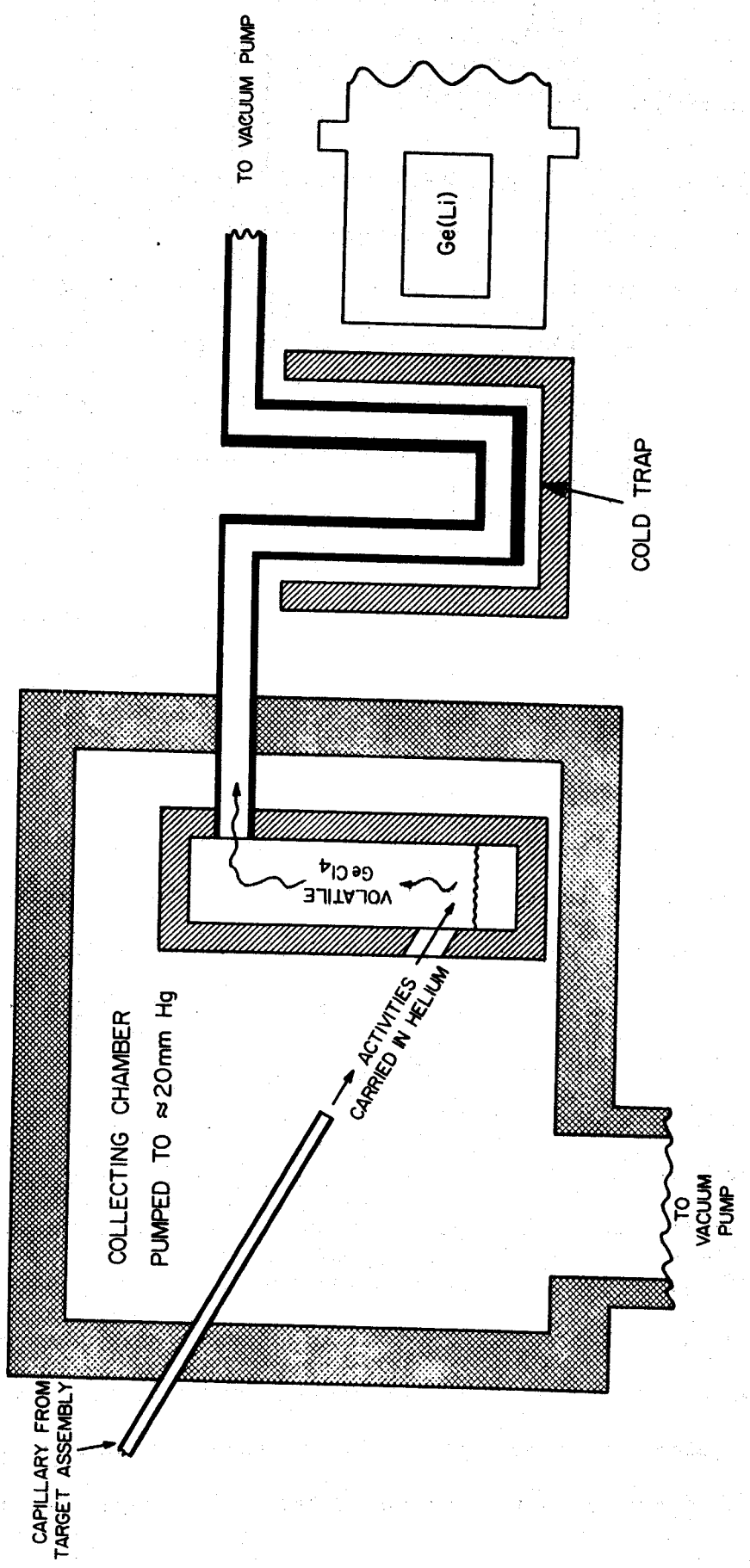

Figure 32. Sketch of the experimental set-up for our first attempt at performing aqueous chemistry with the HeJRT system.

and a very small effective target thickness. The ^{64}Ge search was subsequently successfully carried out [RoR72] using essentially this chemistry, but a pneumatic target system [KoK73] ("rabbit") system was employed instead of the HeJRT system.

The first successful chemistry followed the discovery that not only is it possible to trap activities flowing up the capillary in aqueous solution by merely bubbling the helium flow from the capillary through the solution, but also that the yields remained essentially as good even if the "low pressure" end of the capillary and the aqueous solution were at atmospheric pressure. In a series of runs comparing the amounts of activity trapped in solution under various pressures to that collected on paper tape under $\leq$1 torr pressure it was observed that between 1/2 and 2/3 of the activity could be collected in the aqueous solutions. The amount of activity trapped was largely independent of the pressure over the solution (the pressure gradient across the total system was held constant at about 2 atm). The amount of activity trapped was also found to be independent of the acid concentration of the trapping solution (important if chemistry is to be performed). We also felt that much of the activity lost might have been retained by generating smaller bubbles (with correspondingly higher surface to volume ratios) to provide for more contact between the gas contained in the bubbles and the solution.

If one accepts the role of clusters to be that described in Section II.f."Cluster Molecules", then it does not necessarily follow

that if one can trap activities in solution it will be possible to perform conventional chemistry with these activities. If the thermalized recoils become a part of the cluster molecules at some point during the transport process, then it would not be possible to perform chemistry characteristic of the recoil unless the recoil is successfully freed of the cluster molecule. The reason for this is simply that the recoil is present only as a very small component (about a part per million) in the recoil-cluster combination. Accordingly if the recoil remains attached to the cluster after they are trapped in a solution one would expect the combination to follow chemistry characteristic of the cluster and not of the recoil. It is observed that cluster molecule deposits are soluble in water; however, it still does not necessarily follow that it will be possible to successfully perform chemistry with the recoils. If the recoil is deeply imbedded in the cluster molecule and if the individual cluster molecules maintain their integrity in dissolving, then the recoil would not be freed from the cluster in the dissolution process.

The first attempt at performing chemistry on activities transported by the HeJRT system and trapped in aqueous solution at atmospheric pressure was successful. This was the separation of Cu and Zn activities using ion-exchange techniques. A natural Zn target was bombarded with 30-MeV protons. The principal activities generated were (33 sec) ^{63}Ga and (24 min) ^{60}Cu, from the $(p,2n)$ and $(p,\alpha n)$ reactions on ^{64}Zn. The activities were transported through the HeJRT

system and trapped in a 2*N* HCl solution by simply letting the helium flow from the capillary bubble through a small beaker of acid under atmospheric pressure. Activities were collected for about 25 min. During the 25 min collecting time and a short additional time before the activities were loaded on the ion-exchange column, essentially all the ^{63}Ga decayed to (38 min) ^{63}Zn. The column was loaded with Dowex 1-x8 in the chloride form. The column was subsequently eluted with an additional small amount of 2*N* HCl, then the column and the eluant were each counted for about 10 min using a 4.6% Ge(Li) detector. The spectra recorded are shown in Figure 33. It appears the separation was rather clean in that there is no evidence of either Zn line appearing in the spectrum of the eluted sample and only a small amount of Cu was not completely eluted from the column as evidenced by the weak appearance of the 1333-keV line in the spectrum from the column.

The observation that straightforward chemistry characteristic of the recoil is successful with activities transported with the HeJRT system suggests that somehow the recoil has been freed from the recoil-cluster combination. A discussion of possible mechanisms for freeing the recoil from the cluster molecule would not be profitable at this time as more information is needed from experiments not yet performed. Also unknown at this point was the time required for the process of freeing the recoils from the clusters. This time was obviously less than the 5 to 10 minutes that elapsed between the end of the collection of activities in the experiment described above and

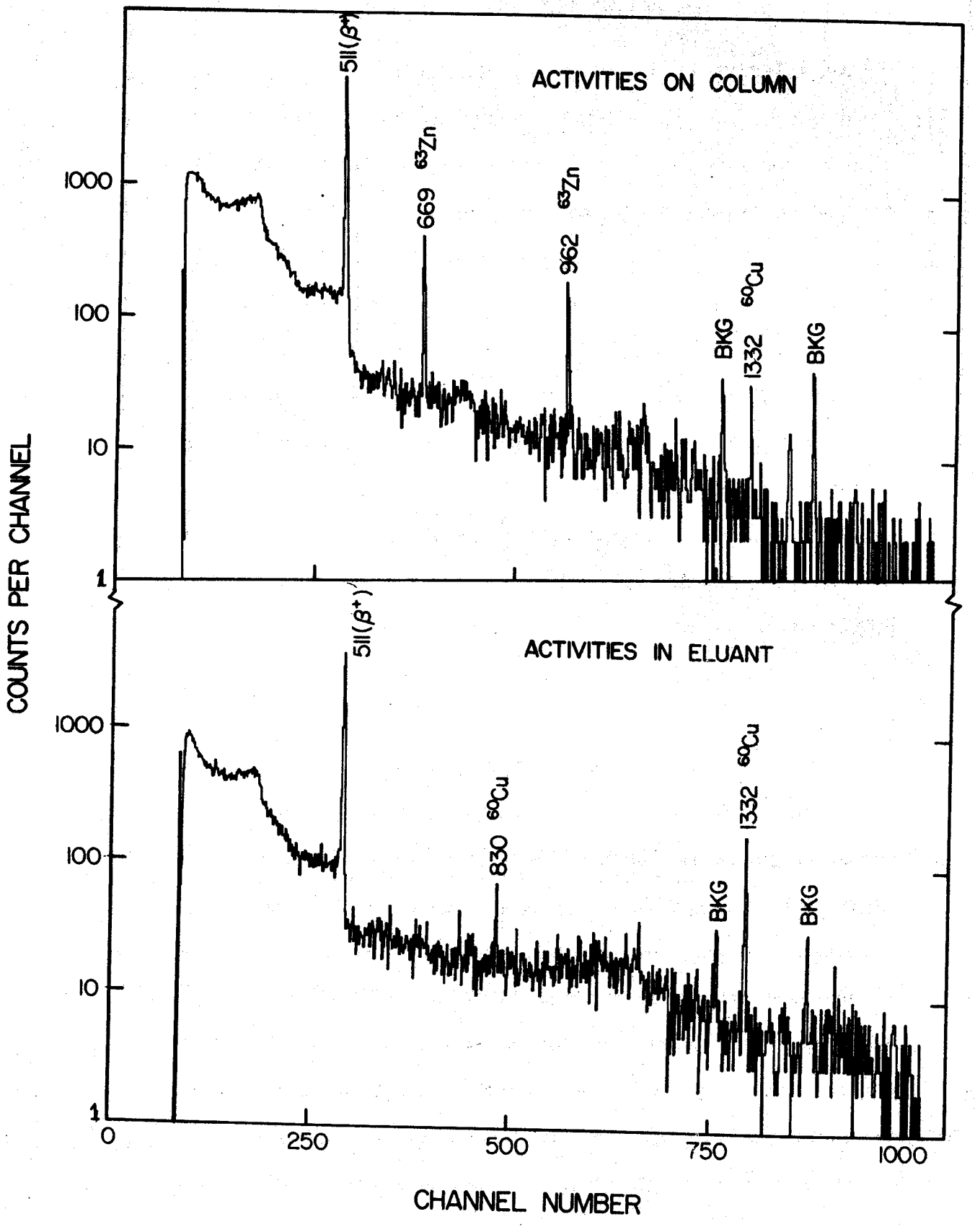

Figure 33. Spectra recorded in our first successful attempt at performing aqueous chemistry with the HeJRT system.

the passage of these activities through the ion-exchange column. If it were much longer than this it would not have been possible to have so clean a chemical separation. Zinc activities still trapped in cluster molecules would have passed through the column, resulting in Zn lines being present in the spectrum of the eluted sample.

The next attempt at performing chemistry on activities transported by the HeJRT system was an attempt at performing chemistry on-line with the HeJRT system. It was a separation of Ga from both Cu and Zn activities using ion-exchange techniques. As in the previous attempt, a natural zinc target was bombarded with 30-MeV protons, producing primarily the same (33 sec) ^{63}Ga and (24 min) ^{60}Cu activities. Also present was some ^{63}Zn from the partial decay of ^{63}Ga and from a (p,pn) reaction on ^{64}Zn. However, time was not allowed in this run for the ^{63}Ga to decay appreciably to ^{63}Zn. The flow from the capillary of the HeJRT target assembly entered directly into the chemical system (see Figure 34), and was mixed with a flow of 8*N* HCl (with carrier) pumped from a container of acid. The mixing took place in a small chamber and was quite turbulent because of the large volume of helium flowing from the target assembly ($\sim$40 standard cm^3/sec). The mixture of helium and acid moved rapidly to the top of an ion-exchange column, again because of the large volume of helium flowing. Here the acid solution was allowed to enter the column while the escaping helium, presumably still carrying some activities, was pumped away. The ion-exchange column was loaded with Dowex 1-×8 in the chloride form; a

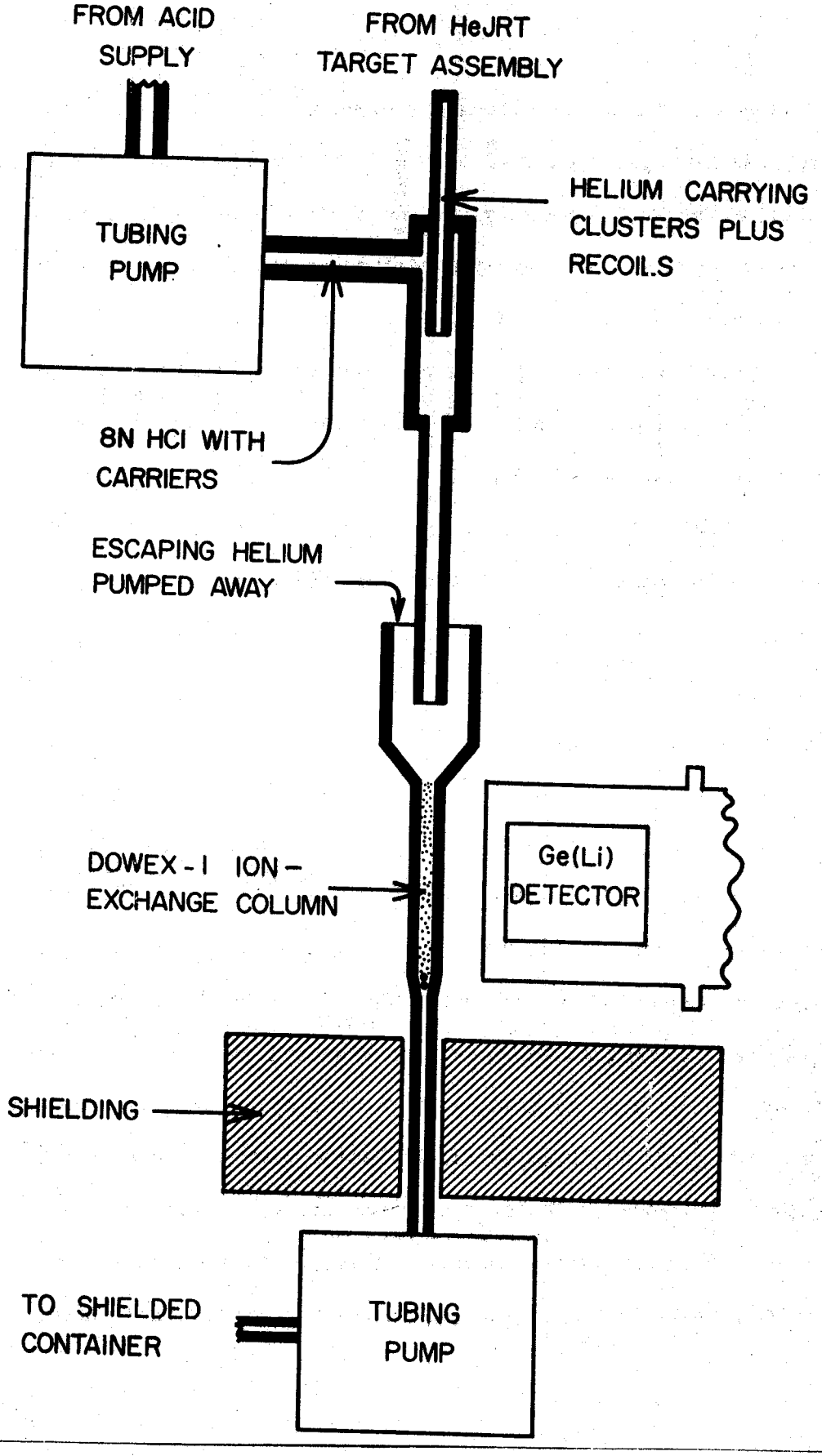

Figure 34. Sketch of the experimental set-up for on-line aqueous chemistry used in our third attempt at performing chemistry with the HeJRT system.

rather large mesh (50-100) was used to decrease the hold-up time of the column. The acid solution was drawn through the column and pumped to a shielded container, and a 4.6% Ge(Li) detector was used to record the γ-ray spectra of activities on the column.

To serve as a comparison a run was made where the activities were collected on moving paper tape under vacuum. The tape speed was such that the activities on the tape spent about 1 min before the Ge(Li) detector. Two short sections of the spectra recorded in this experiment are shown in Figure 35 along with a comparison of the results. Further comparisons with a previous run made by G. C. Giesler [GiC71] using the "rabbit" system are also included in the figure. The relative intensity of the ^{60}Cu to the ^{63}Ga peaks in the chemistry run are down by a factor of 6 over those in the published rabbit run and by a factor of 5 over those in the paper tape run. The ^{63}Zn relative to the ^{63}Ga peaks in the chemistry run are down by a factor of more than 2 over those in the rabbit run. Further, the data acquisition rate was up by a factor of about 2 for the chemistry run over the rabbit run. The possibility that the improvement in the ^{63}Ga to ^{60}Cu and ^{63}Zn ratios was just a half-life effect is eliminated by the increased presence of (2.6 min) ^{64}Ga and (15 min) ^{65}Ga peaks at 1387- and 1354-keV, respectively, in the chemistry spectrum.

This experiment provides an improved upper limit of the time necessary to free recoils from molecular clusters in aqueous solution. The time elapsing between the mixing of the helium and acid flow, and

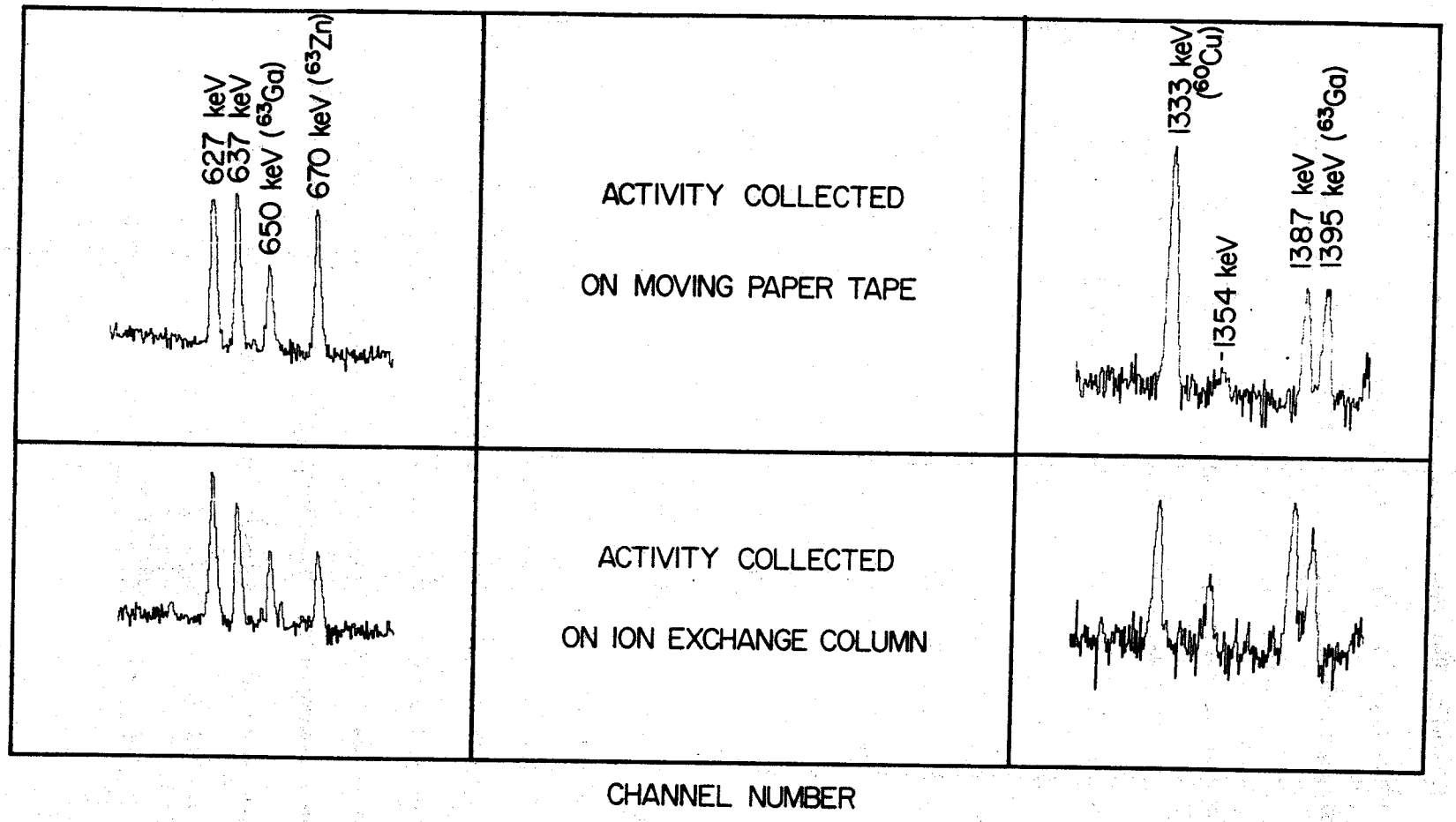

RATIO ^{63}Ga(650)/ ^{63}Zn(670)

RABBIT RUN ⟶ 0.42

COLLECTING ON TAPE ⟶ 0.62

COLLECTING ON COLUMN ⟶ 0.98

RATIO ^{63}Ga(1395)/ ^{60}Cu(1333)

RABBIT RUN ⟶ 0.11

COLLECTING ON TAPE ⟶ 0.15

COLLECTING ON COLUMN ⟶ 0.72

Figure 35. Portions of the spectra recorded using our experimental set-up for on-line aqueous chemistry and comparison with the results from previous runs.

the acid solution leaving the ion-exchange column was of the order of 1 second. Accordingly, the upper limit on the time necessary to separate recoil and cluster should be set at about 1 second in this case. A check of the eluant from the column should have been made to see if any Ga activities were present; if no Ga activities were present the upper time limit of 1 second would be definite. However, from the data rate observed it is certain that at least a large fraction of the recoils had been separated from clusters in this 1 second elapsed time.

We are currently preparing to perform a series of experiments that will attempt to set a definite upper limit on the time necessary to separate recoils from clusters and also to demonstrate further the usefulness of this technique by performing separations on successively shorter-lived activities. There is some hope this series will culminate in the separation of (182 msec) ^{40}Sc from other products.

It is clear that much of the detail of the mechanism allowing conventional chemistry with HeJRT transported activities is not presently understood. The point of the preceding discussion is just that it is possible to do this type of chemistry with the HeJRT system. It might be further pointed out that there may be additional applications, beyond just rapid nuclear chemical separations, resulting from the observation that relatively simple "wet" chemistry, on-line with the HeJRT system, is possible. One additional application of this technique could be to supply chemically active radioisotopes, in times $\lesssim$1 second, that are carrier and parent free, for use in studying biological or other chemical systems.

II. n. Gas Phase Separations

To date there has been no attempt to use this HeJRT system for separations involving the selective generation of gaseous products for the purpose of achieving separations of reaction products in differing physical states. There are two projects presently under consideration that would make use of this technique in this laboratory. They are the search for ^{54}Ni and measuring the β end points of ^{55}Ni and ^{64}Ge. It is hoped these projects can be accomplished by generating the activities as nickel carbonyl and as monogermane, by replacing the helium with carbon monoxide and hydrogen, respectively. In general, the method of separation would be to run the jet system in such a manner that its transport efficiency is very low for non-gaseous products. This is in contrast with the normal operation of the jet system, in which non-gaseous (as well as gaseous) recoils are bound to clusters to achieve high efficiencies for their transport through the system. The jet system would be run without using cluster generating impurities in the gas supplies and possibly sources of turbulence could also be placed in the capillary. Since these actions do not decrease the efficiency for transporting products normally in the gaseous state, a separation of gaseous and non-gaseous products would be achieved. If the desired activity is the only one forming a gaseous product under the conditions being used, the separation should be complete. If more than one gaseous product is formed it would be necessary to use some other property such as boiling point or decom-

position point to separate the activities further after they exit the capillary. For a further discussion of this type of separation, see K. Bachmann's article in Proceedings of the International Conference on Electromagnetic Isotope Separations and the Techniques of Their Applications (1970), p. 126 [BMBW-FB 70-28].

II. o. Plasma Chemistry

For the purposes of this discussion plasma chemistry is taken to mean chemistry occurring between thermalized recoils and cluster molecules in the plasma in the target assembly for the purpose of achieving chemical separations. There is some evidence separations of this nature can be accomplished. If this does become a reality, it will extend the realm of ultra-fast chemistry beyond those elements that easily form gaseous products in the HeJRT system. The difficulty of collecting or trapping gaseous products would be eliminated, since virtually any surface could be used for collecting the activities. This type of chemical separation would also be fully compatible with either method of on-line mass separation (identification) discussed in this thesis.

The possibility of being able to perform plasma chemistry arises from a consideration of the mechanism through which the recoil becomes a part of the cluster molecule. It seems likely that the cluster molecules are formed as impurities present in the helium condense out of the plasma in the target assembly (where "condense out" is not clearly defined and can be taken to be polymerization, nucleation, etc; see Section II c "Cluster Molecules"). If during the process of condensation, the thermal recoil, because of its physical presence in the region of condensation, becomes trapped in the cluster molecule, then plasma chemistry will not be possible. If on the other hand, the thermal recoil becomes bound to some chemically active site on the

cluster molecule during or after the condensation process, the possibility of controlling the nature of these chemically active sites and thereby possibly achieving a separation of chemically differing recoils can be considered. That is to say, if it is possible to control the types of recoils that become attached to clusters, a separation of the recoils will be accomplished as a result of the very poor transport efficiency of the HeJRT system for those recoils not attached to clusters.

The "chemically active site" hypothesis is supported by the results of two experiments. The first supporting experiment was the series of total efficiency runs made for the HeJRT system. Efficiencies were determined for Zn, Cu, and Co recoils and were found to be 50%, 75%, and 90%, respectively (see Section II.h. "Total System Efficiency Determination" for the details of this determination). Physically these three recoils are quite similar to one another (atomic radius, polarizability, ionization potentials, etc.). Thus, it is difficult to explain the different efficiencies observed unless somehow their chemical natures are also considered, and this implies some sort of chemical bonding between recoil and clusters. The second supporting experiment was a series of runs in which the impurities fed into the helium were changed and the transport efficiencies for a pair of activities provided from the same target were monitored. In this experiment a natural aluminum target (100% ^{27}Al) was bombarded with 30-MeV protons to produce (2.1 sec) ^{26}Si and (12 sec) ^{23}Mg from

$(p,2n)$ and $(p,\alpha n)$ reactions, respectively. Spectra of the products were recorded when the primary impurity in the helium was 1) benzene vapor, 2) compressed air and water vapor, and 3) when the level of impurities was very low. The concentration of benzene vapor used was roughly 0.01% to 0.1%. The concentration of compressed air used was roughly 5% and the water vapor was added by passing the helium through a gas washing bottle. Each time an impurity change was made the target assembly was pumped out and refilled two or three times with helium doped with a different impurity. However, when the main component of the impurities was changed from run to run it should be presumed that a small (and possibily significant) amount of the impurities from the previous run remained in the target assembly. This was particularly true in the runs where pure helium was used; here the transport efficiency did not drop nearly so much as it would have if no impurities had remained. The results of this experiment are shown in Figure 36. It is quite apparent that the absolute efficiencies of the HeJRT system for transporting different activities is dependent on the type of impurities in the helium. Magnesium is transported best when benzene vapor is used, while silicon is transported best when compressed air plus water vapor is used (the ratio of Si to Mg activities transported changes by nearly 40% on changing these types of impurities used to produce cluster molecules). An attempt to somehow explain away the change in efficiency for Si (by assuming the formation of a silane preferentially when one type of impurity is used) does nothing to explain away the change in efficiency for Mg. Since the activities were made at the same

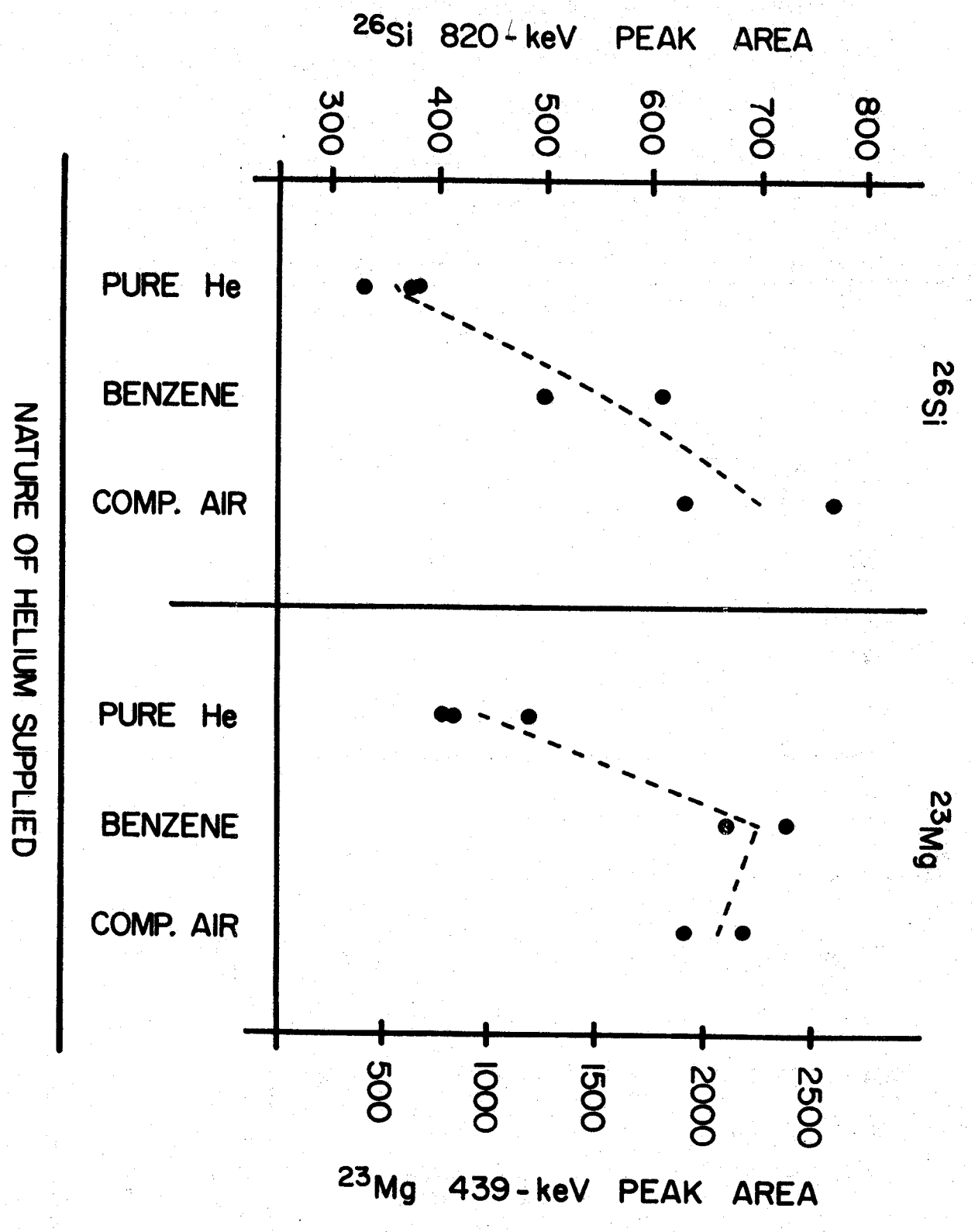

Figure 36. Results supporting the possibility that chemical separations will be possible using "plasma chemistry".

time, under the same conditions, from the same target, the efficiency changes cannot be explained away as a half-life effect or as a reflection of any changes (other than the source of cluster generating components) in the HeJRT system during the experiment.

Accordingly, from the observation that total transport efficiencies are dependent on both the chemical nature of the recoil and the source of impurities for the cluster molecule (i.e., the chemical nature of the cluster molecule), it seems likely that plasma chemistry (as defined at the start of this section) can be achieved. There remains one last consideration that may help to make clean plasma chemistry a reality. That is the possibility of generating cluster molecules off-line and feeding those molecular clusters into a system using pure helium (see Section II. f. "Cluster Molecules"). This may help because it may allow generation of more exotic molecular cluster out of components (impurities) or under conditions that would be detrimental to the successful operation of the HeJRT system.

REFERENCES

[AnG 66] G. Anderson, Ark. Fys. 36, 61 (1966).

[BeD 65] D. R. Bes, Nucl. Inst. and Methods 38, 277 (1965).

[BeI 66a] I. Bergström, Nucl. Inst. and Methods 43, 116 (1966).

[BlJ 72] J. N. Black, Ph.D. Thesis, Michigan State University, 1972.

[BoW 72] W. W. Bowman, T. T. Sugihara, and R. D. Macfarlane, Nucl. Inst. and Methods 103, 61 (1972).

[CoW 56] Wm. H. Corcoran, J. B. Opfell, and B. H. Sage, Momentum Transfer in Fluids, Academic Press (1956), New York.

[DaH 73] H. Dautet, S. Gujrathi, W. J. Wiesehahn, J. M. D'Auria, and B. D. Pate, Nucl. Inst. and Methods 107, 49 (1973).

[EkC 72] C. Ekström, S. Ingelman, M. Olsmats, B. Wannberg, G. Anderson, and A. Rosen, Nuc. Phys. A196, 178 (1972).

[GhA 59-69] A. Ghiorso, unpublished results (1959-1969) Reference taken from [MaR 69].

[GiG 71] G. C. Giesler, Ph.D. Thesis, Michigan State University, 1971.

[HaB 60] B. G. Harvey, Annual Reviews of Nuclear Science 10, 235 (1960).

[JuH 71a] H. Jungclas, R. D. Macfarlane and Y. Fares, Radiochimica Acta 16, 141 (1971).

[JuH 71b] H. Jungclas, R. D. Macfarlane, and Y. Fares, Phys. Rev. Letters 27, 556 (1971).

[KoK 70a] K. L. Kosanke and G. C. Giesler, MSU Nuclear Chemistry Annual Report 1970, COO-1779-49, 247 (1970).

[KoK 70b] K. L. Kosanke, Michigan State University, Nuclear Chemistry Annual Report 1970, COO-1779-49, 251 (1970).

[KoK 72] K. L. Kosanke and R. B. Firestone, Michigan State University Cyclotron Annual Report, 1972, p. 28 and p. 97.

[MaR 62] R. D. Macfarlane, Phys. Rev. 126, 274 (1962).

[MaR 69] R. D. Macfarlane, R. A. Gouch, N. S. Oakey, and D. F. Torgerson, ORO3820-2 (1969); Nucl. Inst. and Methods 73, 285 (1969).

[MaR 71] R. D. Macfarlane, Texas A & M University, Private Communication.

[MaR 72] R. D. Macfarlane and Wm. C. McHarris, For publication in "Nuclear Reactions and Spectroscopy," ed. by J. Cerny, Academic Press, 1972.

[MiV 67] Private Communication to R. D. Macfarlane reported in [MaR 72].

[MoR 65] H. Moringa and N. L. Lark, Nucl. Physics 67, 315 (1965).

[NiJ 70] J. M. Nitschke, Proceedings of the Leysin Conference, 1970.

[NoL 70] L. C. Northcliffe and R. F. Schilling, Nuclear Data Tables, Vol. 7 No. 3-4, 233 (1970).

[OwJ 64] J. A. Owczarek, Fundamentals of Gas Dynamics Int. Textbook Co., (1964) Scranton, Pa.

[PaW 58] W. Paul, H. P. Reinhard, and U. vanZahn, Z. Phys. 152, 143 (1958).

[RoR 72] R. G. H. Robertson and Sam M. Austin, Phys. Rev. Letters 29, 130 (1972).

[RuG 67] Gosta Rudstam, Ark. Fys. 36, 9 (1967).

[SeF 70] F. W. Sears and M. W. Zemansky, University Physics, 4th Ed., Addison-Wesley (1970), Reading Mass.

[ShR 61] R. K. Sheline, T. Sikkeland, and R. N. Chaands, Phys. Rev. Letters 1, 446 (1961).

[SuT 72] T. T. Sugihara, Texas A & M University, Private Communication.

[WeC 72] Conrad Weiffenbach, Foster Radiation Lab., Private Communication.

[WiK 72] K. Wien, Y. Fares, and R. D. Macfarlane, Nucl. Inst. and Methods 103, 181 (1972).

APPENDIX I

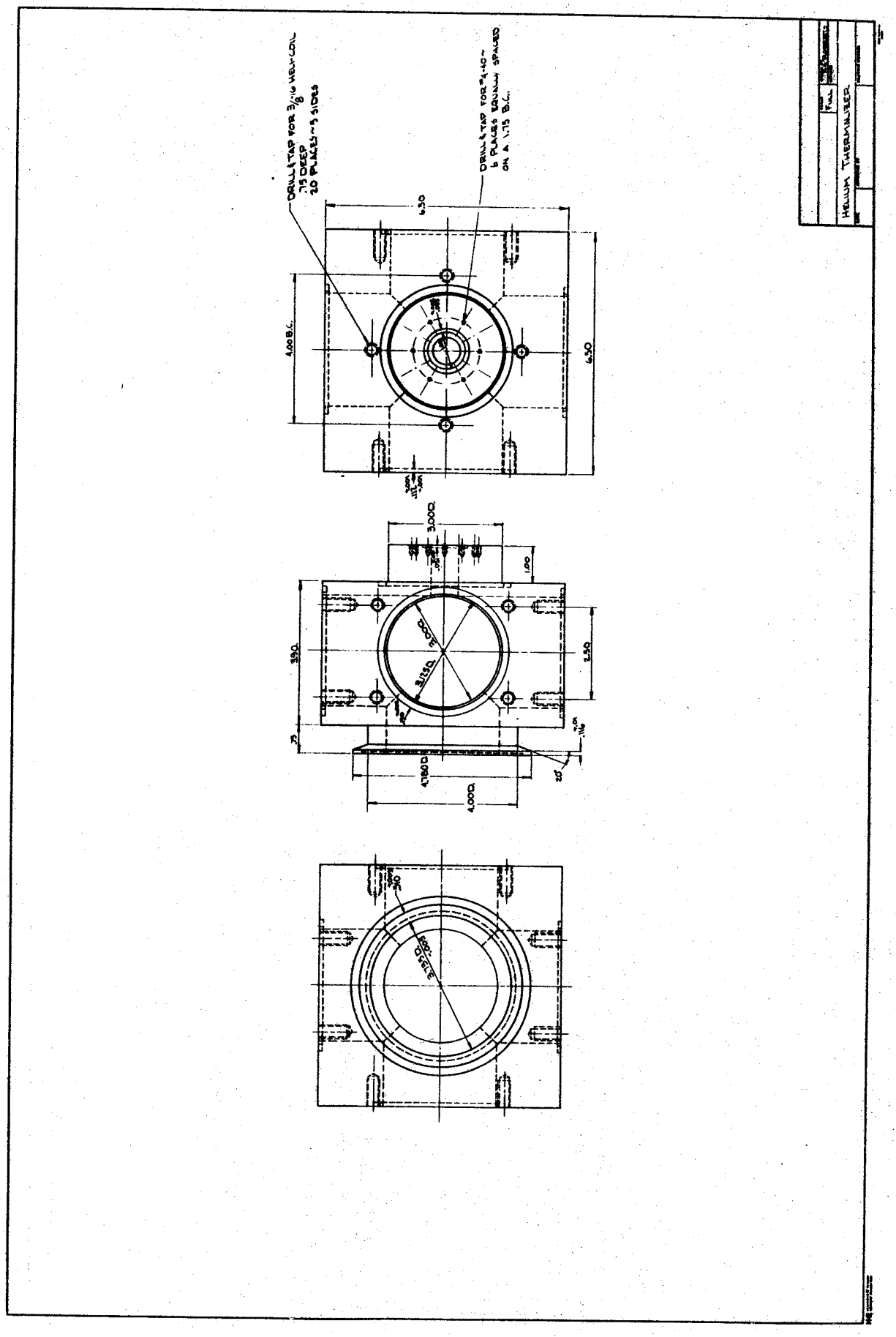

Figure 37a. Detail Drawing of Target Assembly Box, Viewing Port.

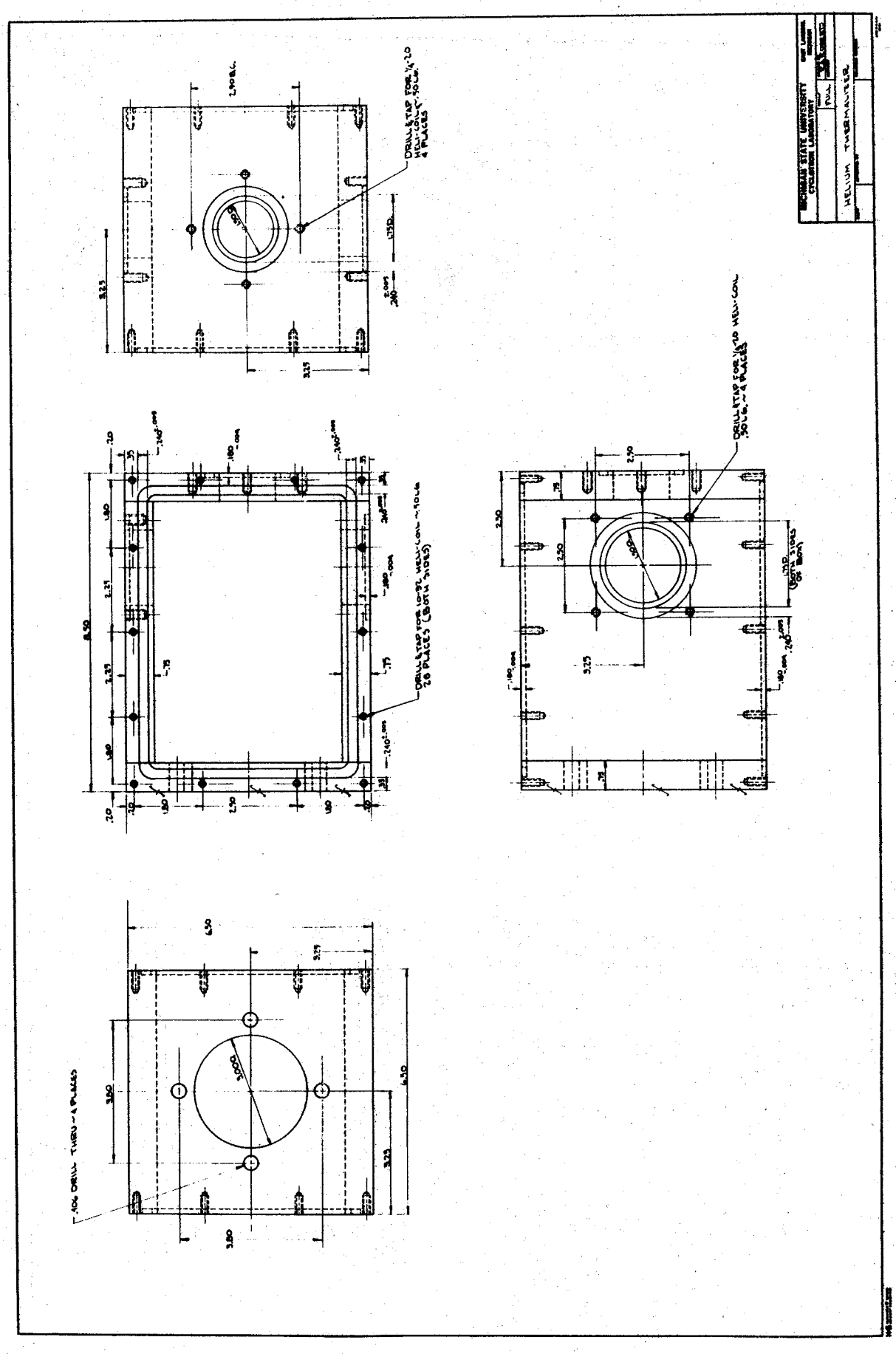

Figure 37b. Detail Drawing of Target Assembly Box, Helium Chamber.

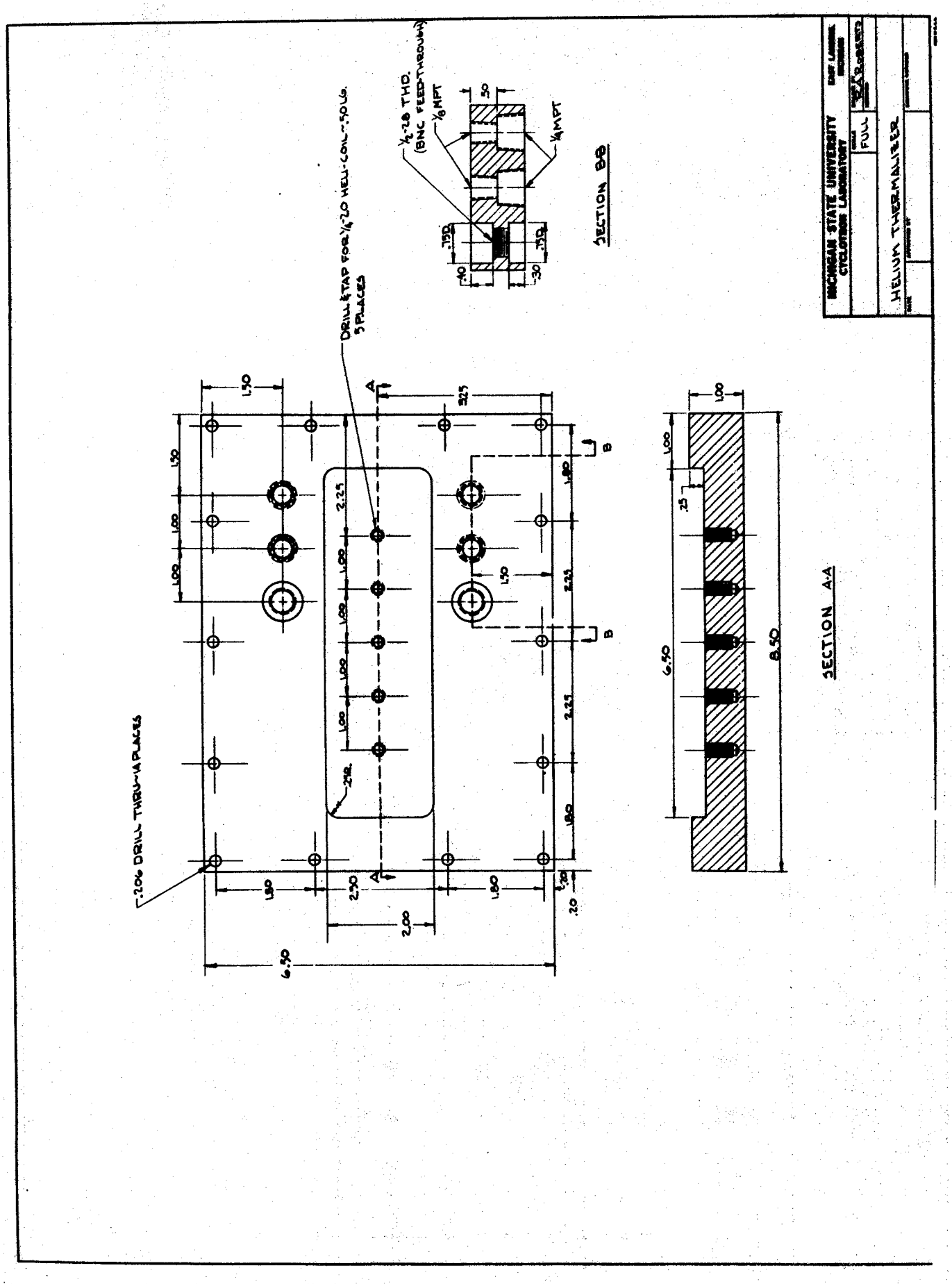

Figure 37c. Detail Drawing of Target Assembly Box, Bottom Plate.

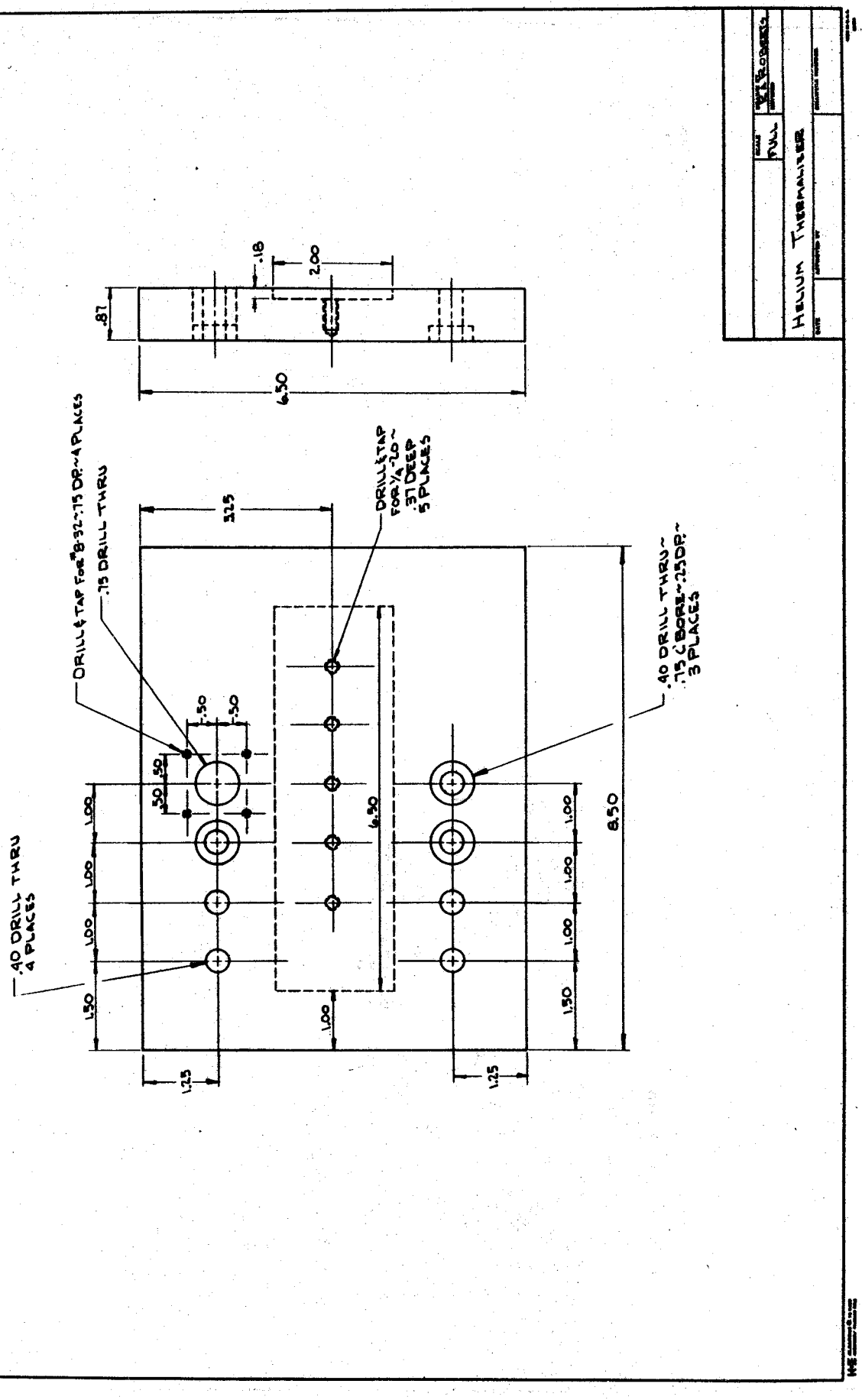

Figure 37d. Detail Drawing of Target Assembly Box, Top Plate.

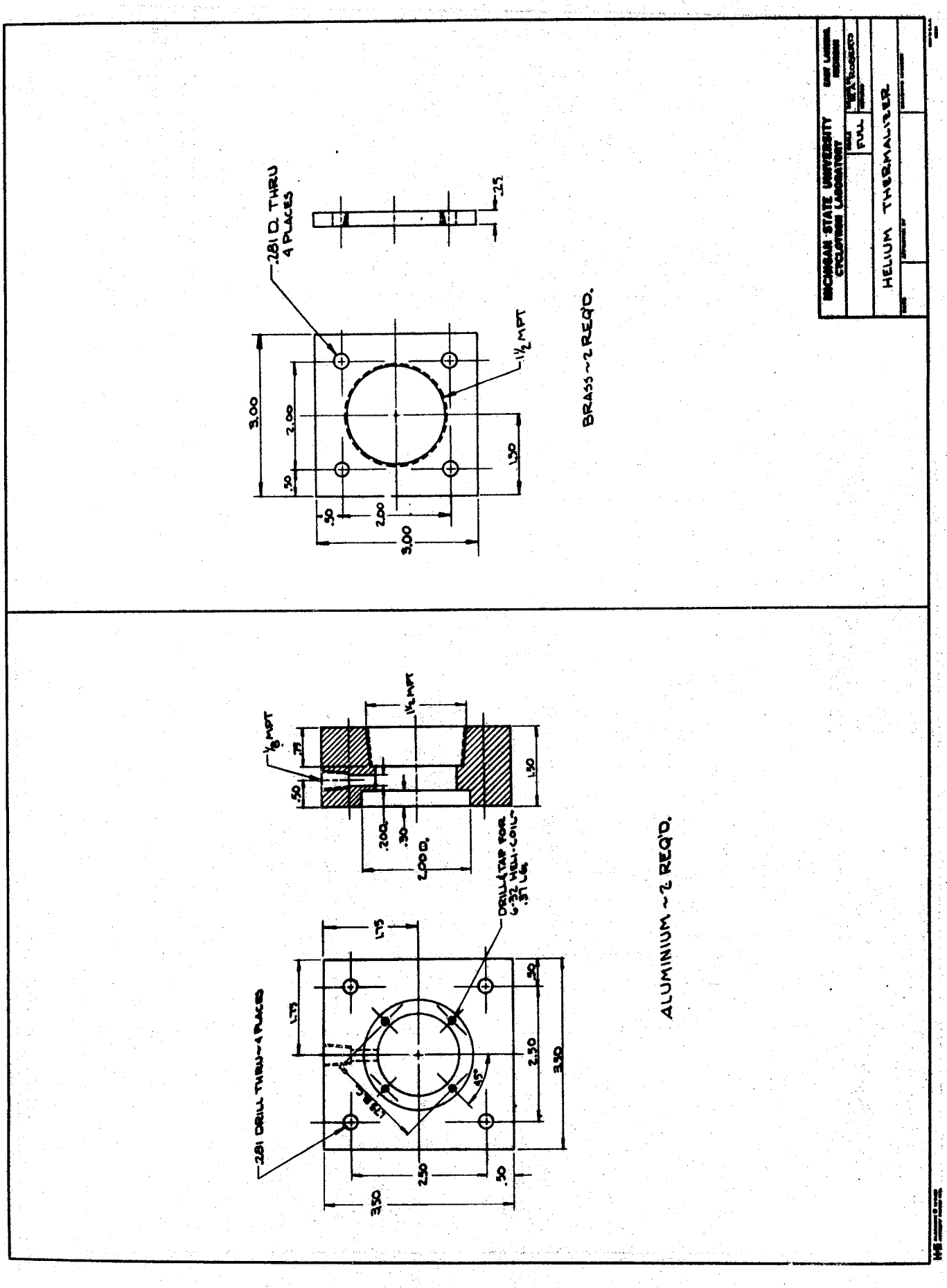

Figure 37e. Detail Drawing of Target Assembly bcv, Flanges.

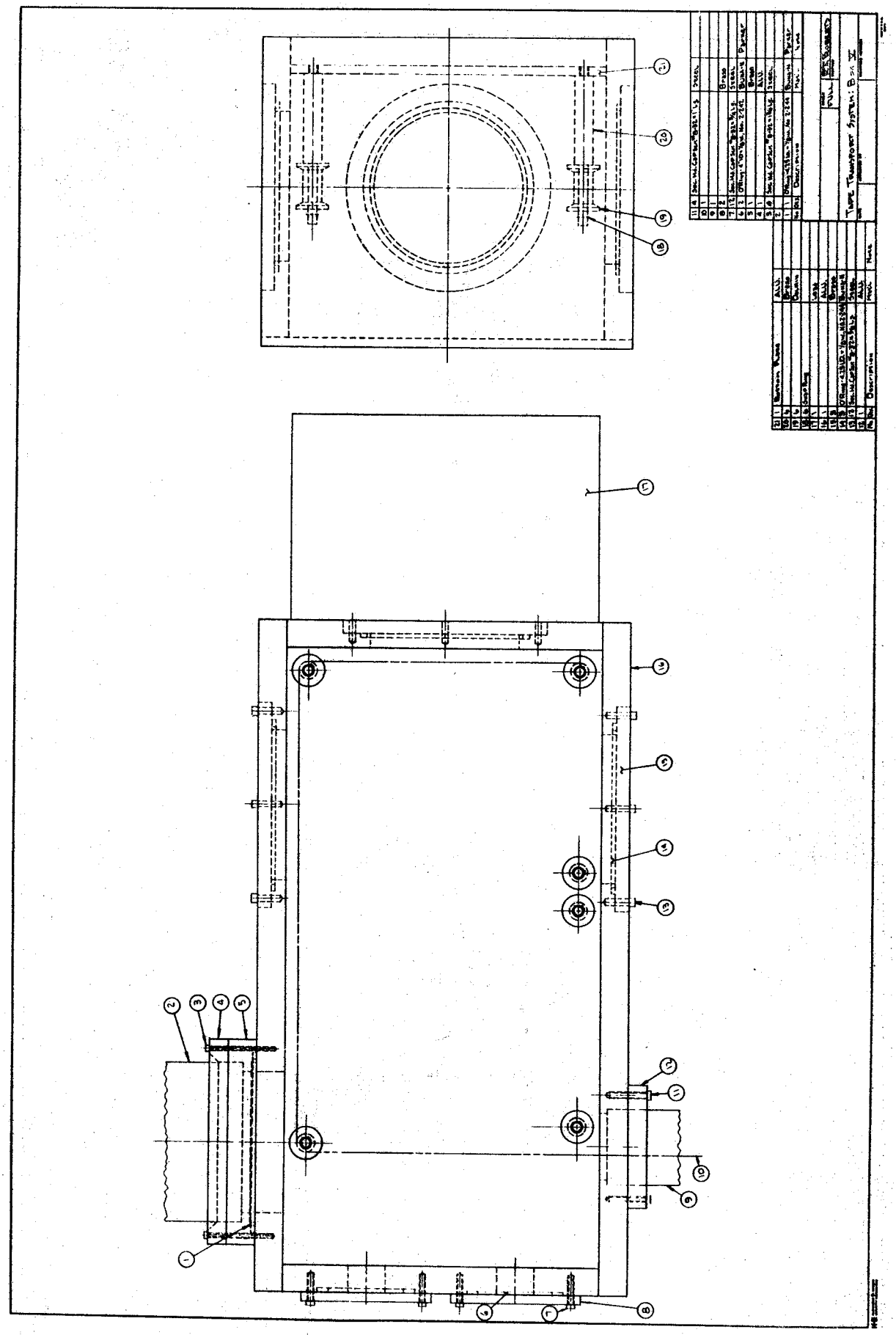

Figure 38a. Assembly Drawing of Detector Assembly Box.

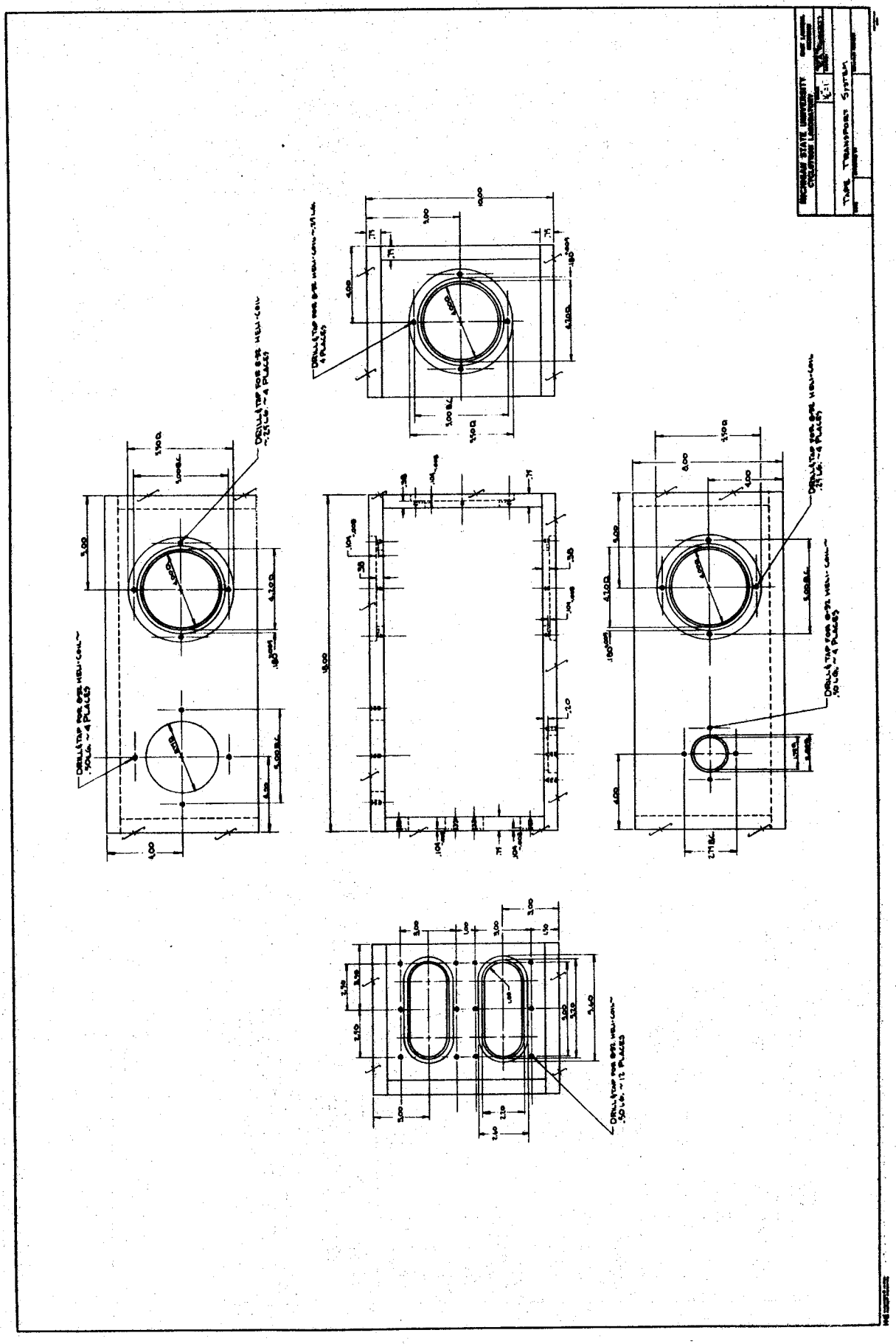

Figure 38b. Detail Drawing of Detector Assembly Box, Vacuum Chamber.

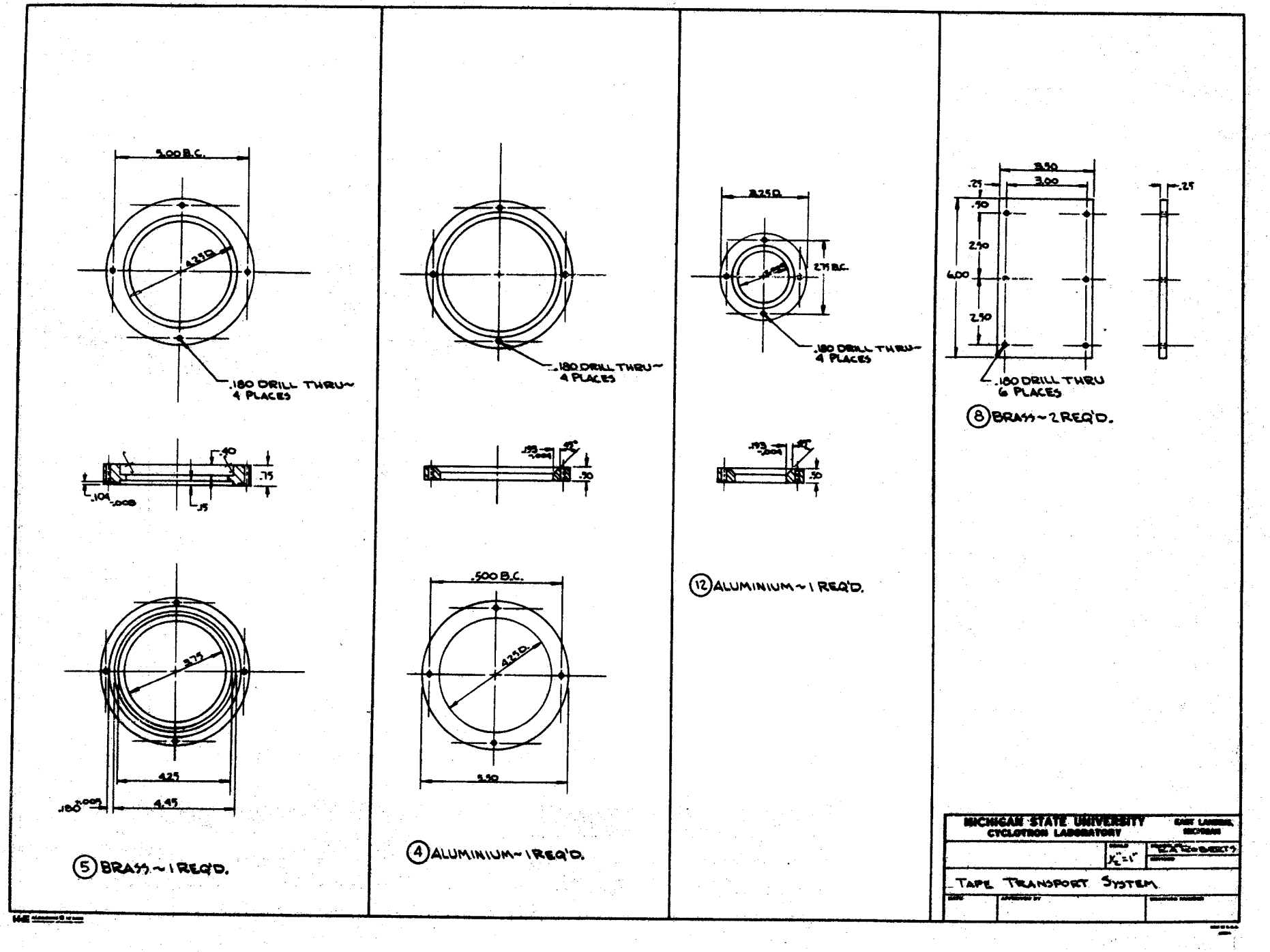

Figure 38c. Detail Drawing of Detector Assembly Box, Flanges.

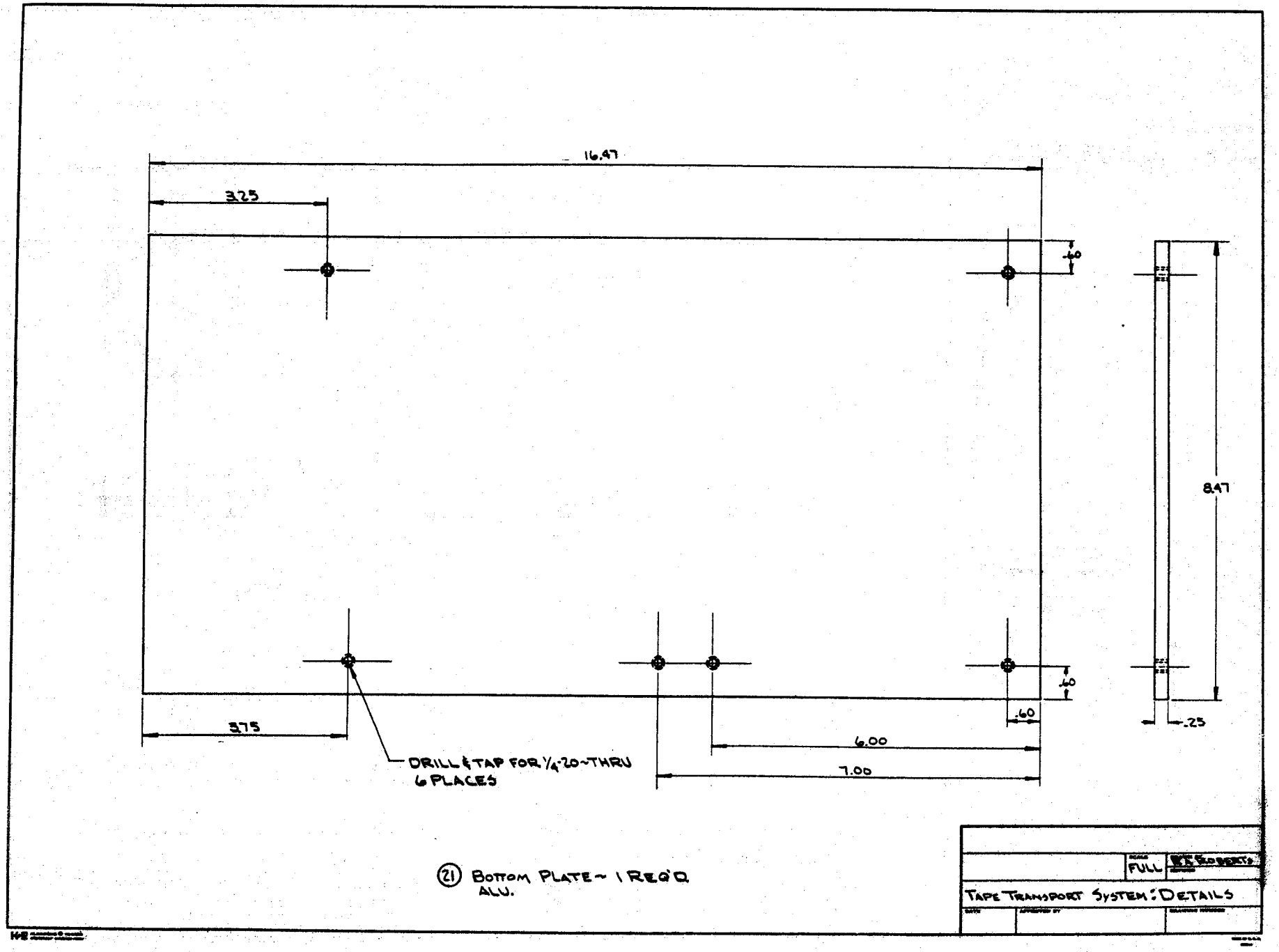

Figure 38d. Detail Drawing of Detector Assembly Box, Spindel Plate.

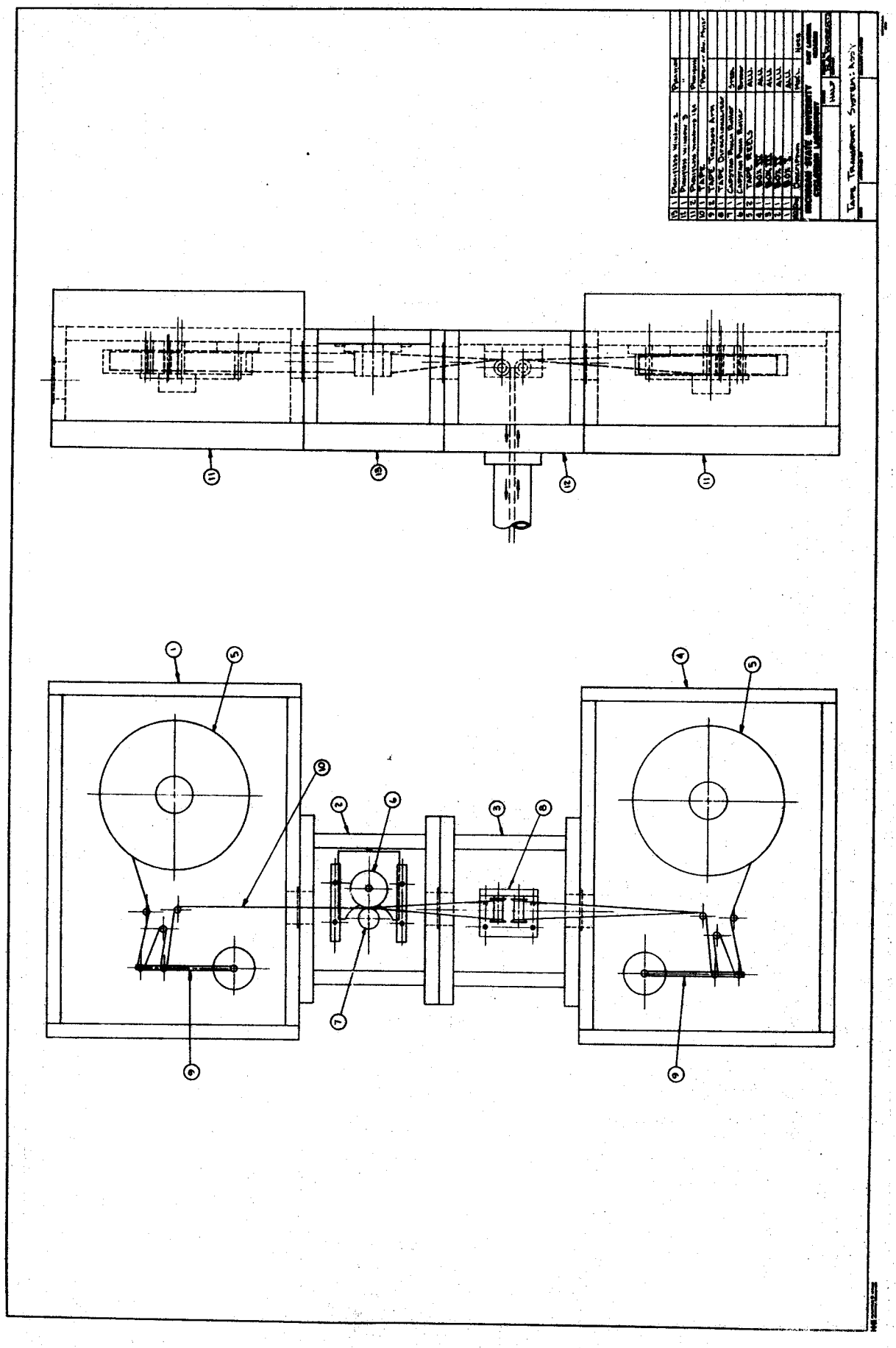

Figure 39a. Assembly Drawing of Tape Transport System.

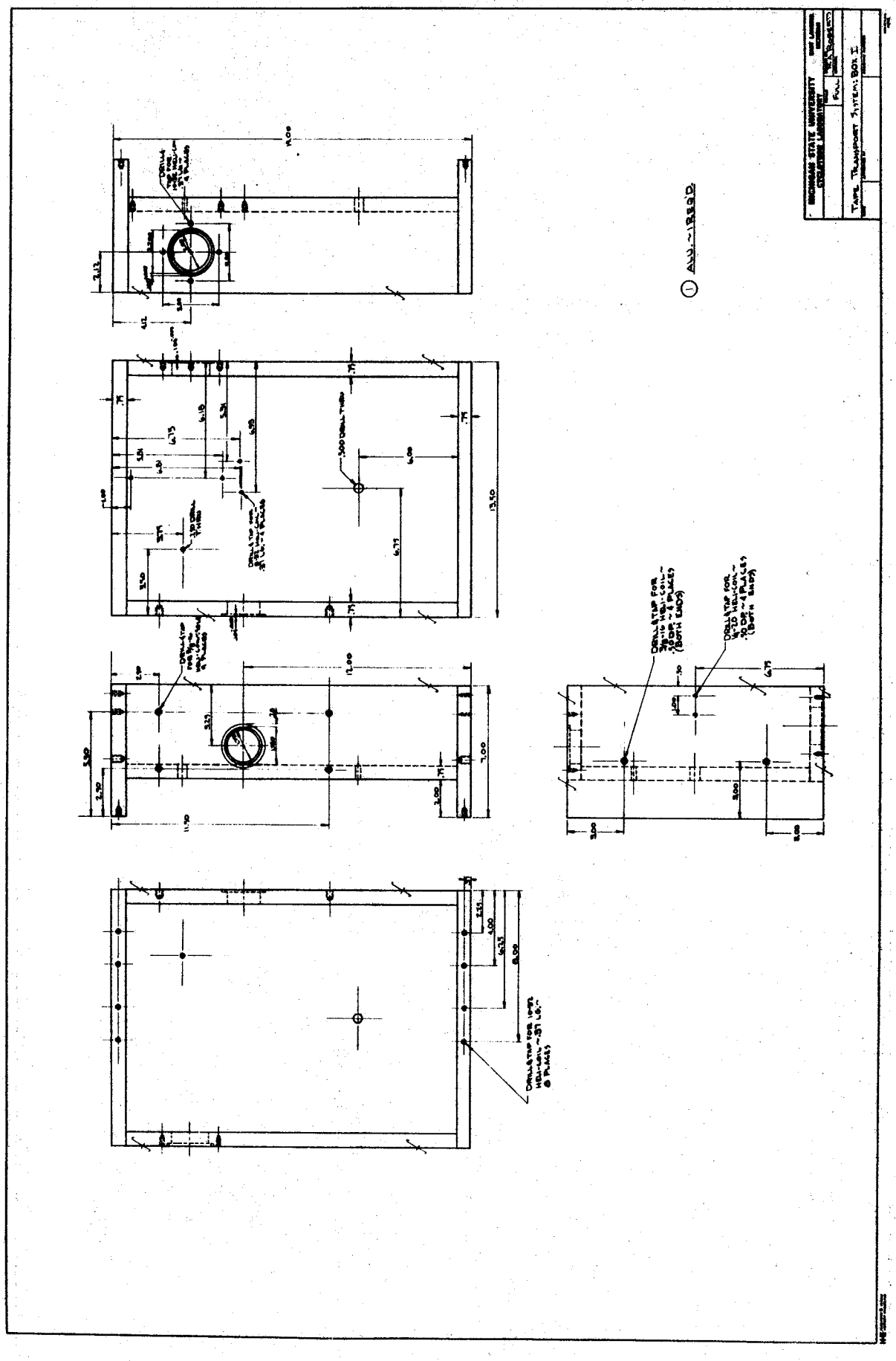

Figure 39b. Detail Drawing of Tape Transport System, Box I.

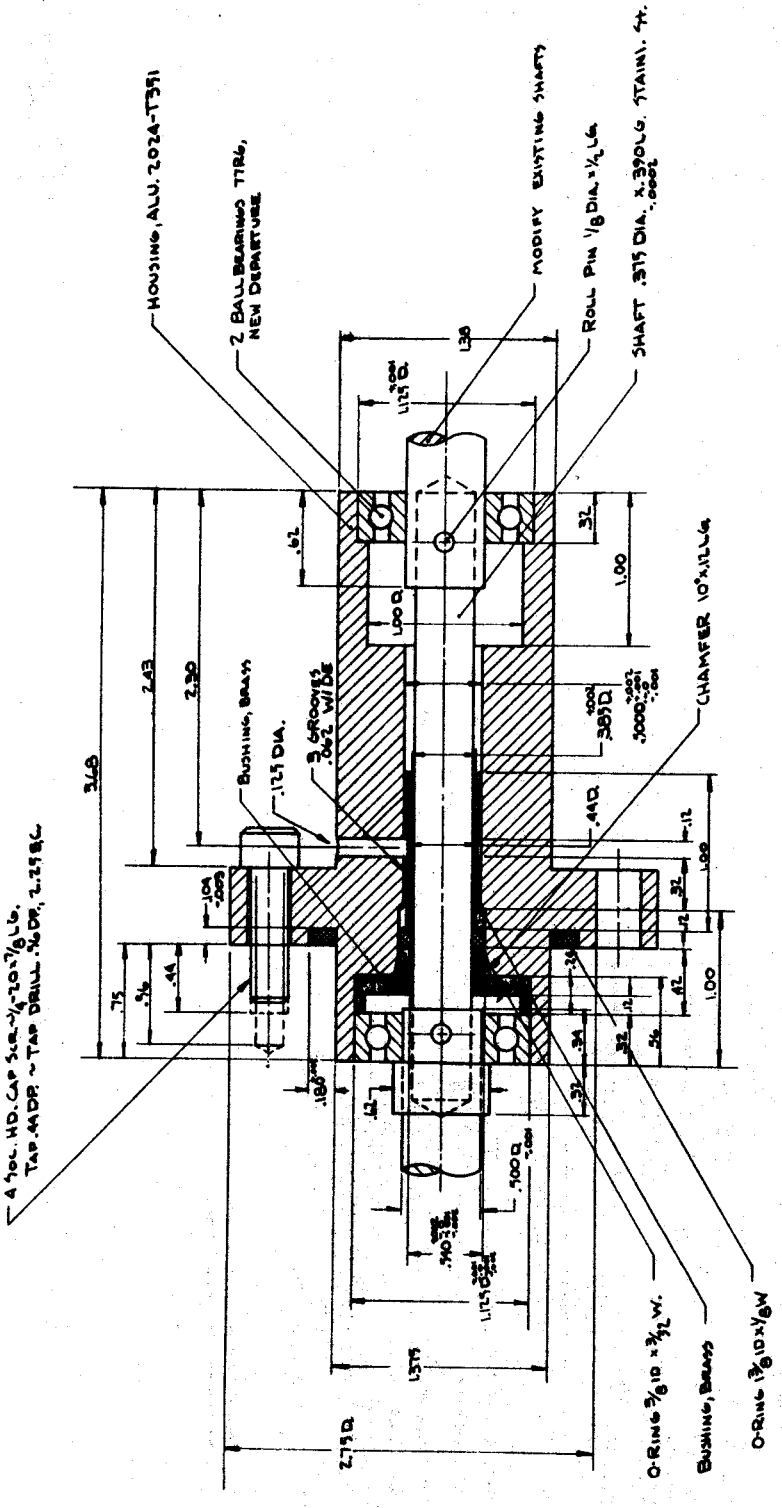

Figure 39c. Detail Drawing of Tape Transport System Box I & IV Vacuum Feedthrough.

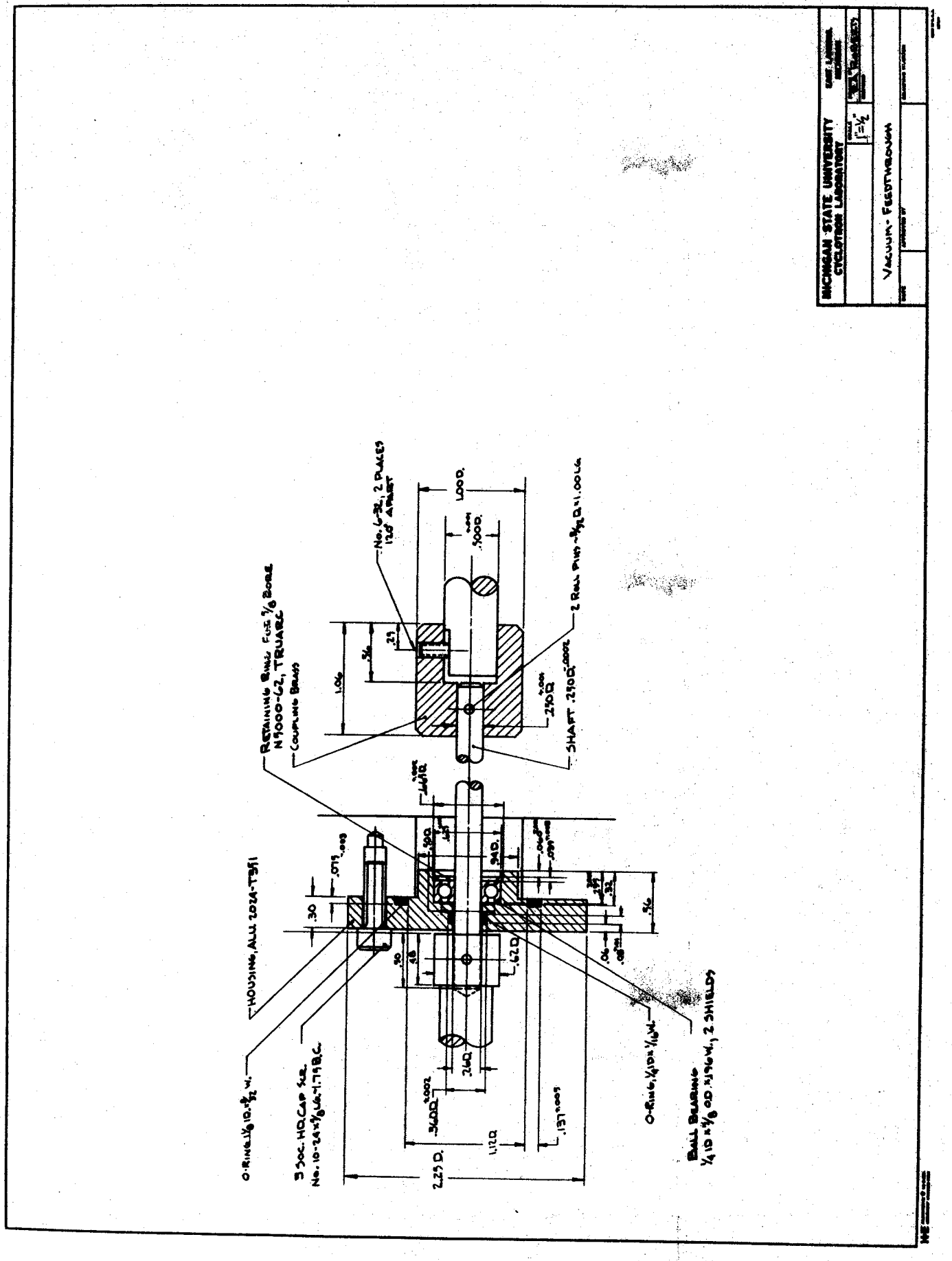

Figure 39d. Detail Drawing of Tape Transport Sy m, Box I & IV Vacuum Feedthrough.

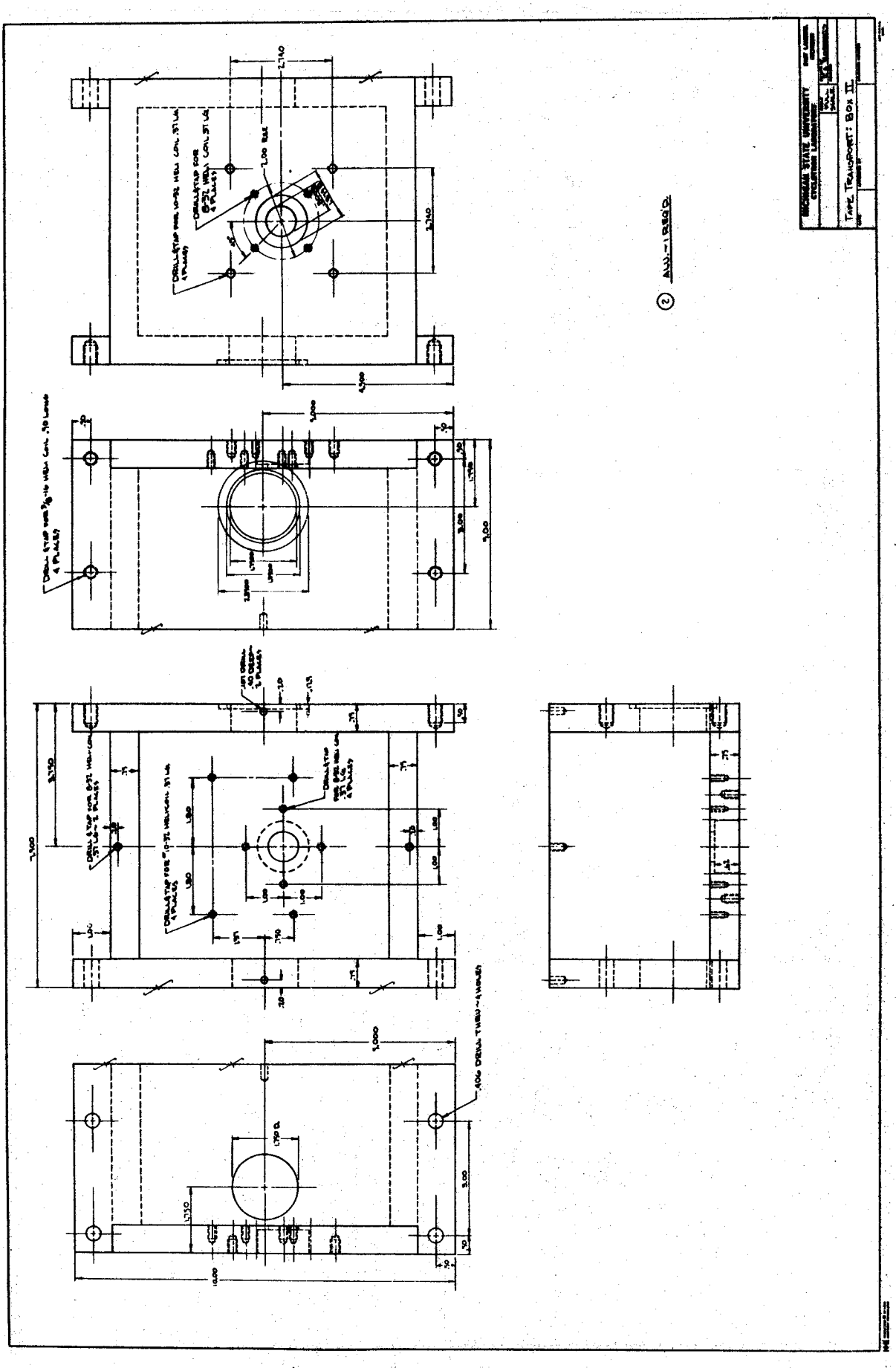

Figure 39e. Detail Drawing of Tape Transport System, Box II.

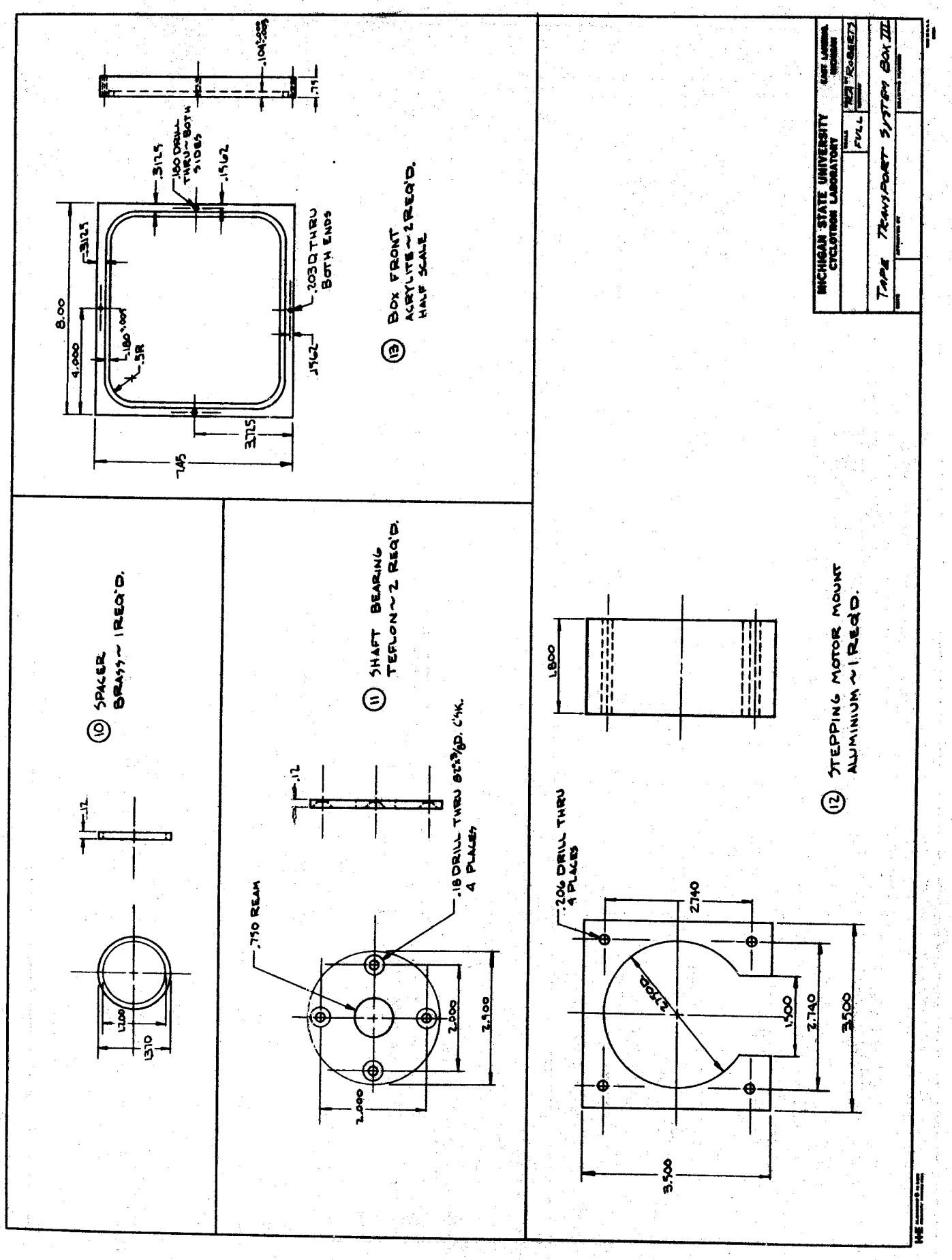

Figure 39f. Detail Drawing of Tape Transport System, Box II Components.

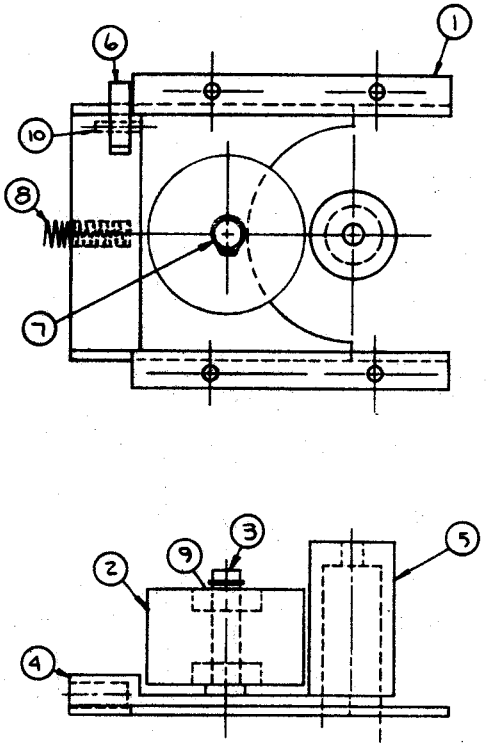

No	Qty	Description	Mat'l	Note
10	1	PIN 1/8 DIA. x 1 1/2 LG.	STL.	
9	2	BEARING C6DD	STL.	NICE
8	1	5/16 OD. SPRING	STL.	
7	1	RETAINER RING 5100-37	STL.	TRUARC
6	1	SLIDE LOCK	STEEL	
5	1	CAPSTAN	STL. STL.	
4	1	IDLER PLATE	STEEL	
3	1	SHAFT	STEEL	
2	1	IDLER WHEEL	RUBBER	
1	2	SLIDE	STEEL	

MICHIGAN STATE UNIVERSITY
CYCLOTRON LABORATORY
EAST LANSING, MICHIGAN

SCALE: FULL

TAPE TRANSPORT: CAPSTAN/IDLER WHEEL ASSY

DATE | APPROVED BY | DRAWING NUMBER

Figure 39g. Assembly Drawing of Tape Transport System, Box II Capstan/Idler Wheel Assembly.

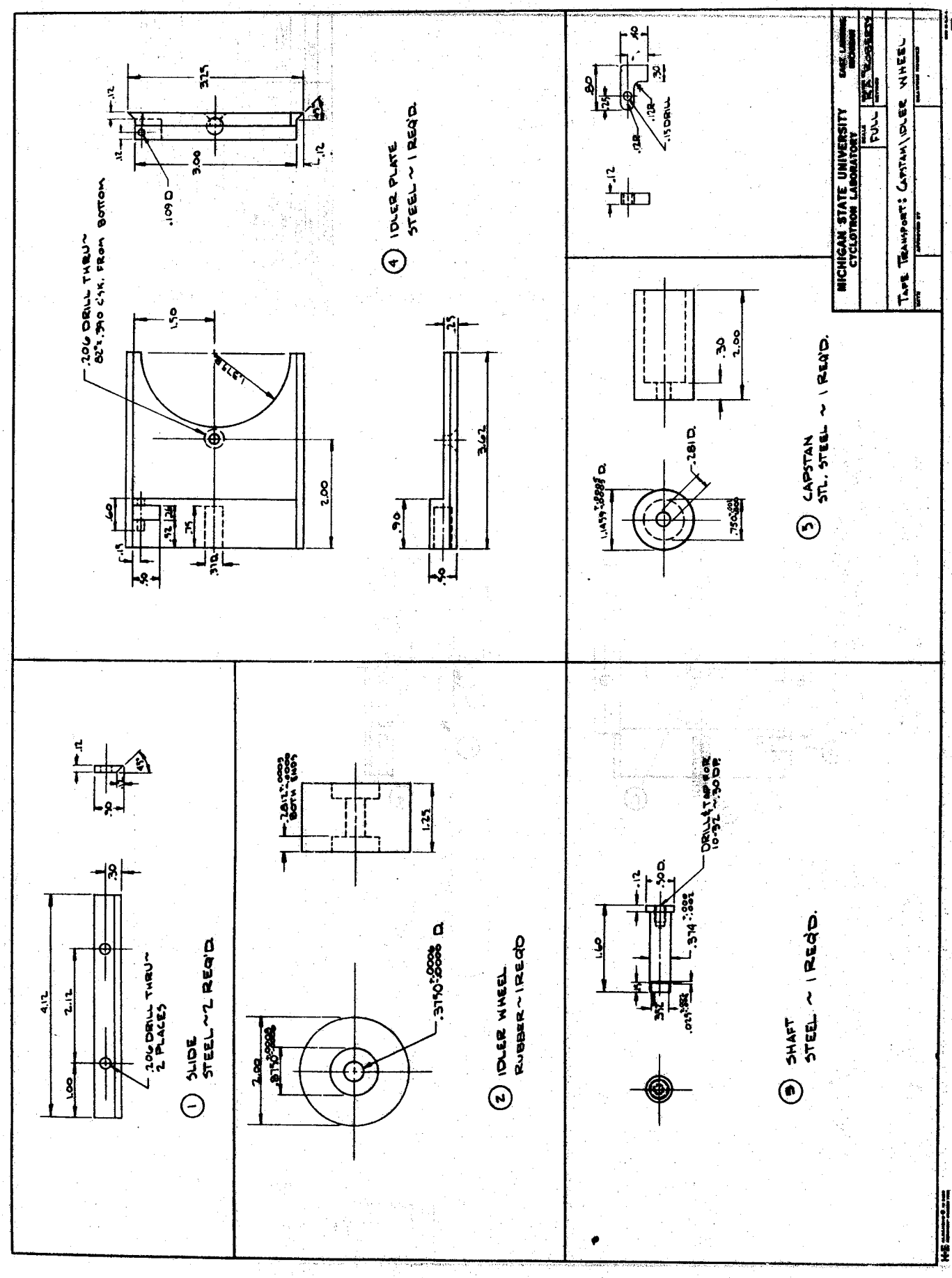

Figure 39h. Detail Drawing of Tape Transport System, Box II Capstan/Idler Wheel Assembly.

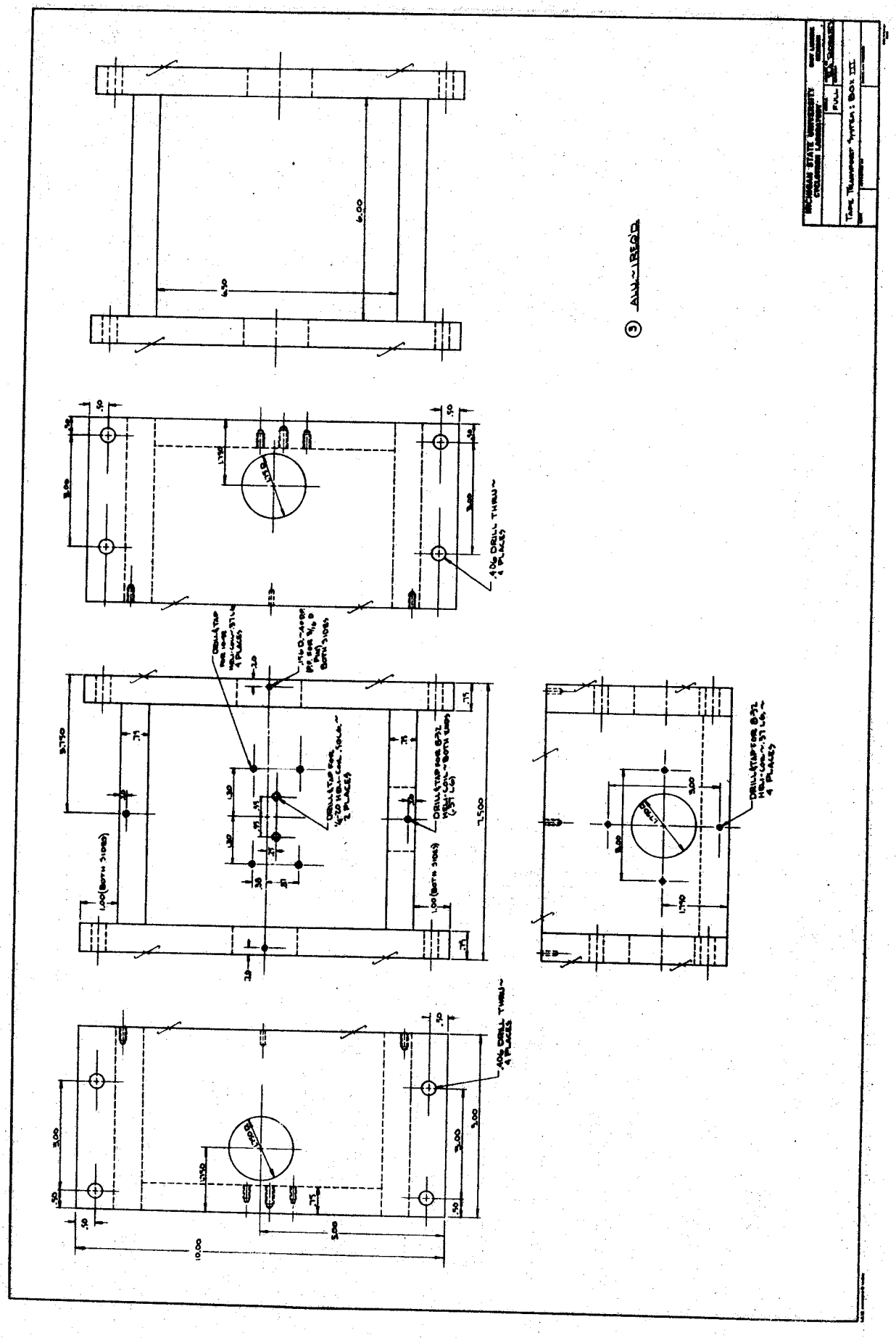

Figure 391. Detail Drawing of Tape Transport System, Box III.

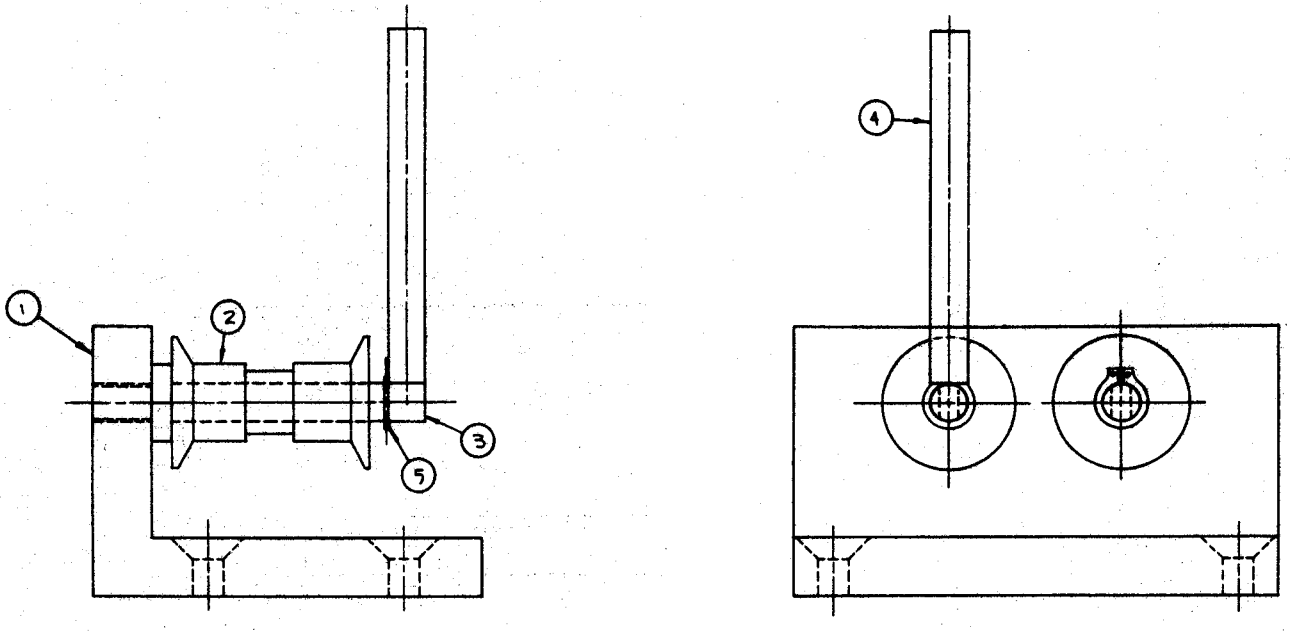

No	Qty	Description	Mat'l	Note
5	2	RETAINING RING 5100-24	STEEL	TRUARC
4	1	SHAFT HANDLE	STEEL	
3	2	SHAFT	STEEL	
2	10	SPINDLE	DELRIN	
1	1	FRAME	ALUMINUM	

MICHIGAN STATE UNIVERSITY CYCLOTRON LABORATORY EAST LANSING, MICHIGAN

SCALE 1"=1/2" SIZE B

TAPE TRANSPORT: DIRECTIONALIZER

DATE | APPROVED BY | DRAWING NUMBER

Figure 39j. Assembly Drawing of Tape Transport System, Box III Directionalizer.

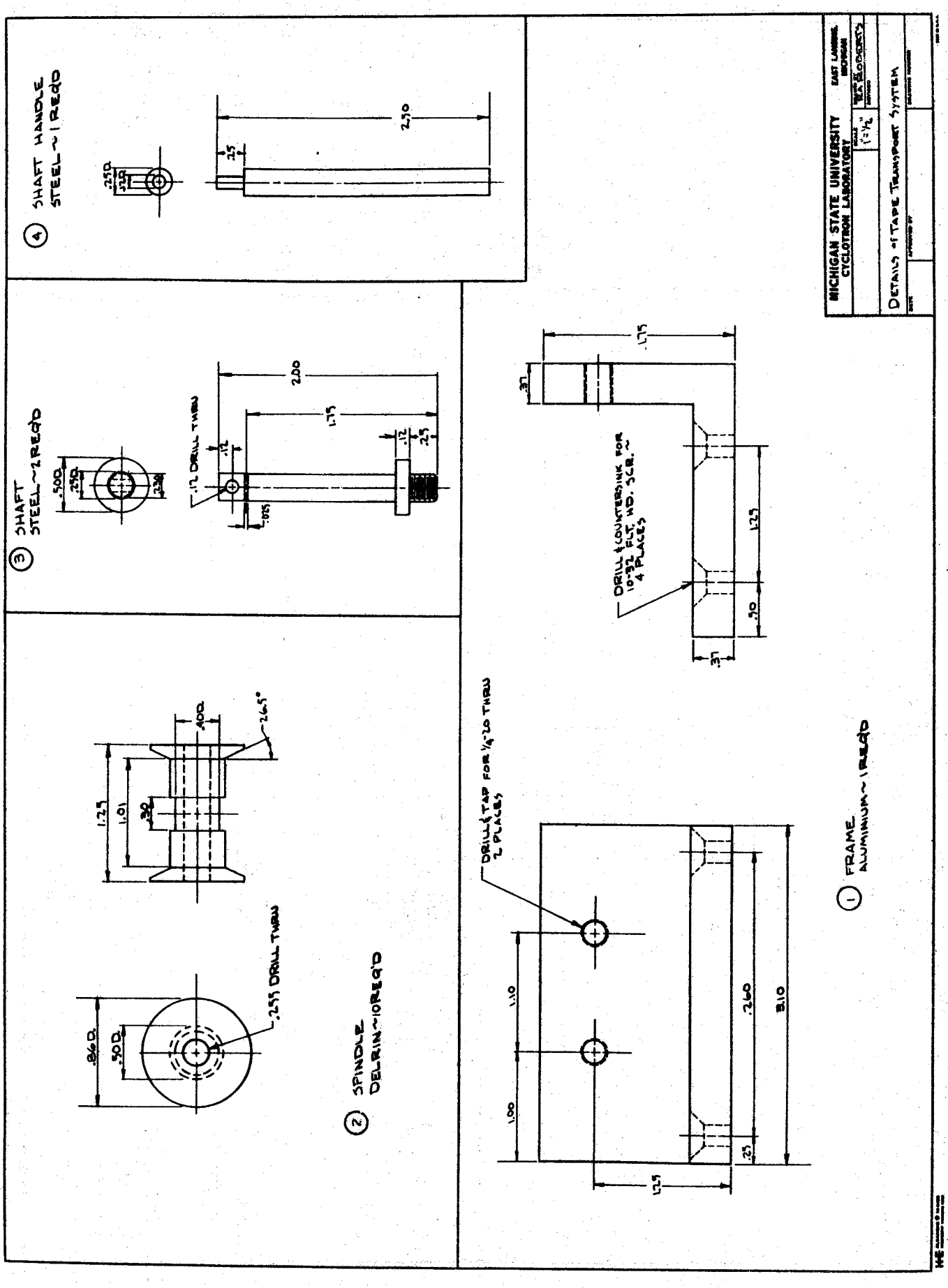

Figure 39k. Detail Drawing of Tape Transport System, Box III Directionalizer.

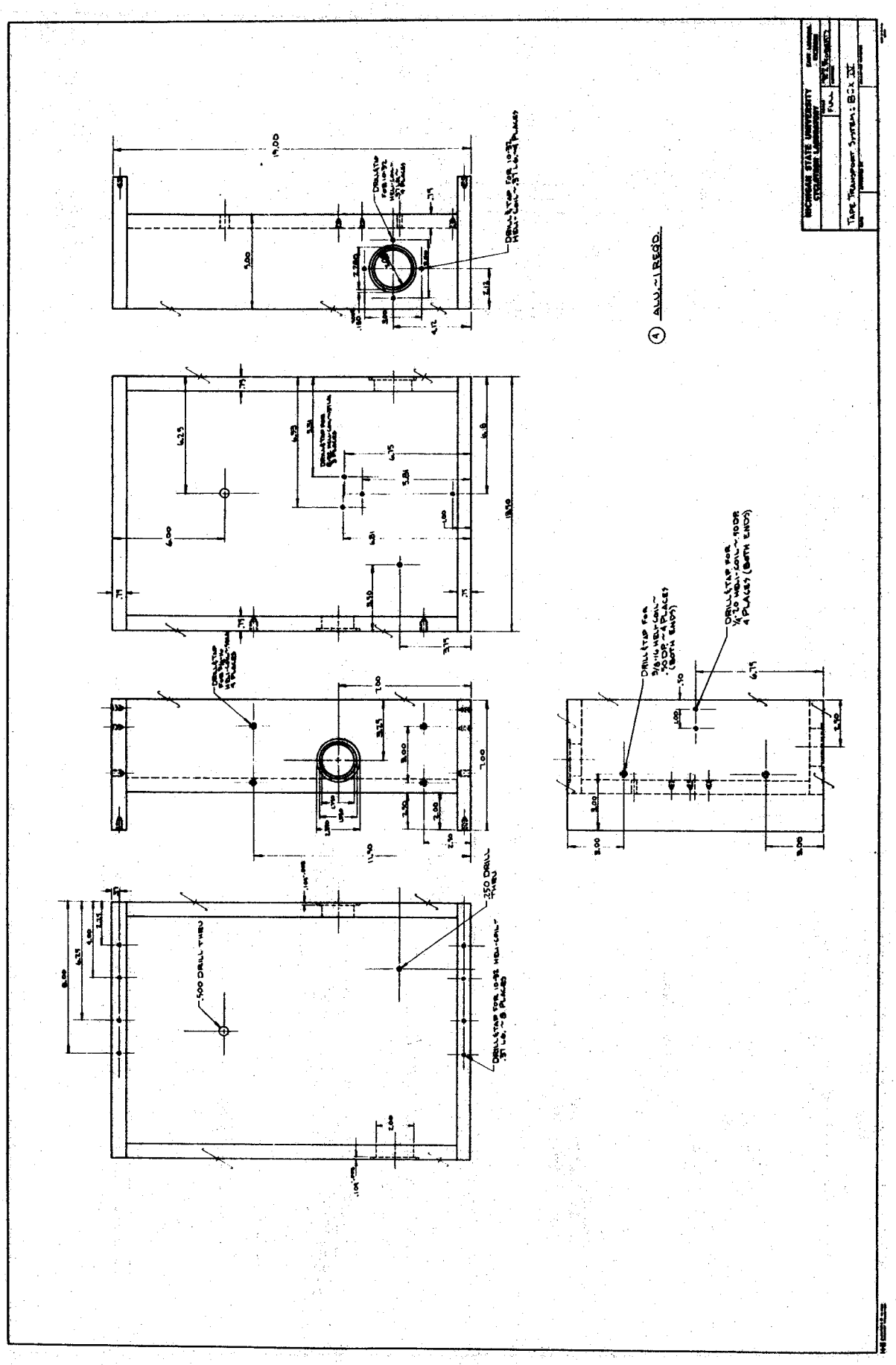

Figure 391. Detail Drawing of Tape Transport System, Box IV.

APPENDIX II

Rabbit: Pneumatic Target Transport System

The pneumatic target transport system was developed to aid in the study of moderately short-lived radioisotopes ($t_{1/2} \gtrsim 1$ sec) and to make generally more efficient use of Cyclotron time. The system provides rapid transit of targets from a low background area into the cyclotron beam for irradiation. The target carrier ("rabbit") is stopped at the ends of its path with an air cushion and can be oriented with respect to the cyclotron beam at the *in* terminal or with respect to external detectors at the *out* terminal. During irradiations the rabbit is cooled by conduction and by an air flow directed over the target. The initial system provided rabbit transport over a distance of about 100 ft in 2 seconds. However, with increased use of in-beam or pulsed-beam techniques[1] and the He-Thermalizer-jet transport system[2] to study short-lived species, it was no longer necessary to have rabbit transit times this short. Accordingly, the rabbit *out* terminal was moved to a more convenient location and the rabbit transit line was increased slightly. The present system covers a distance of about 200 ft in 5 sec. The system is illustrated in Fig. I.

The rabbit (shown in Fig. II) is propelled through thin walled cellulose acetate or polyvinyl chloride tubing by about 3 psi gauge pressure on one side and a partial vacuum created with a commercial vacuum cleaner on the other side. This is quite sufficient to propel

---

[1] See Michigan State University Nuclear Chemistry Annual Report, 1970, COO-1779-49, p. 257 and p. 264. Also J. N. Black's Ph.D. Thesis, Michigan State University (1971).

[2] See K. L. Kosanke's Ph.D. Thesis, Michigan State University (1972) for discussion of He-thermalizer jet-transport technique or Michigan State University Nuclear Chemistry Annual Report, 1970, COO-1779-49, p. 247.

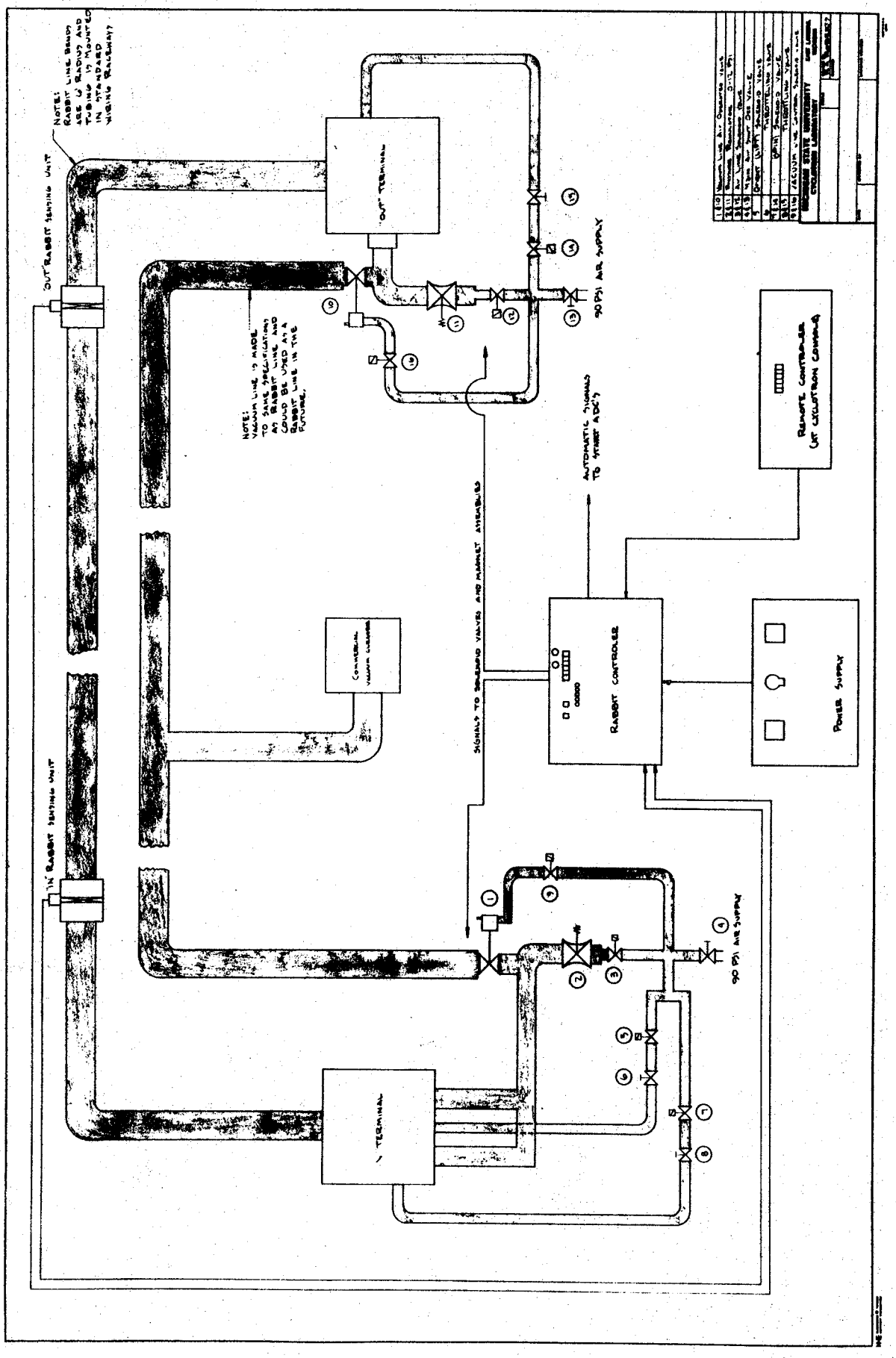

Figure I Schematic of rabbit system.

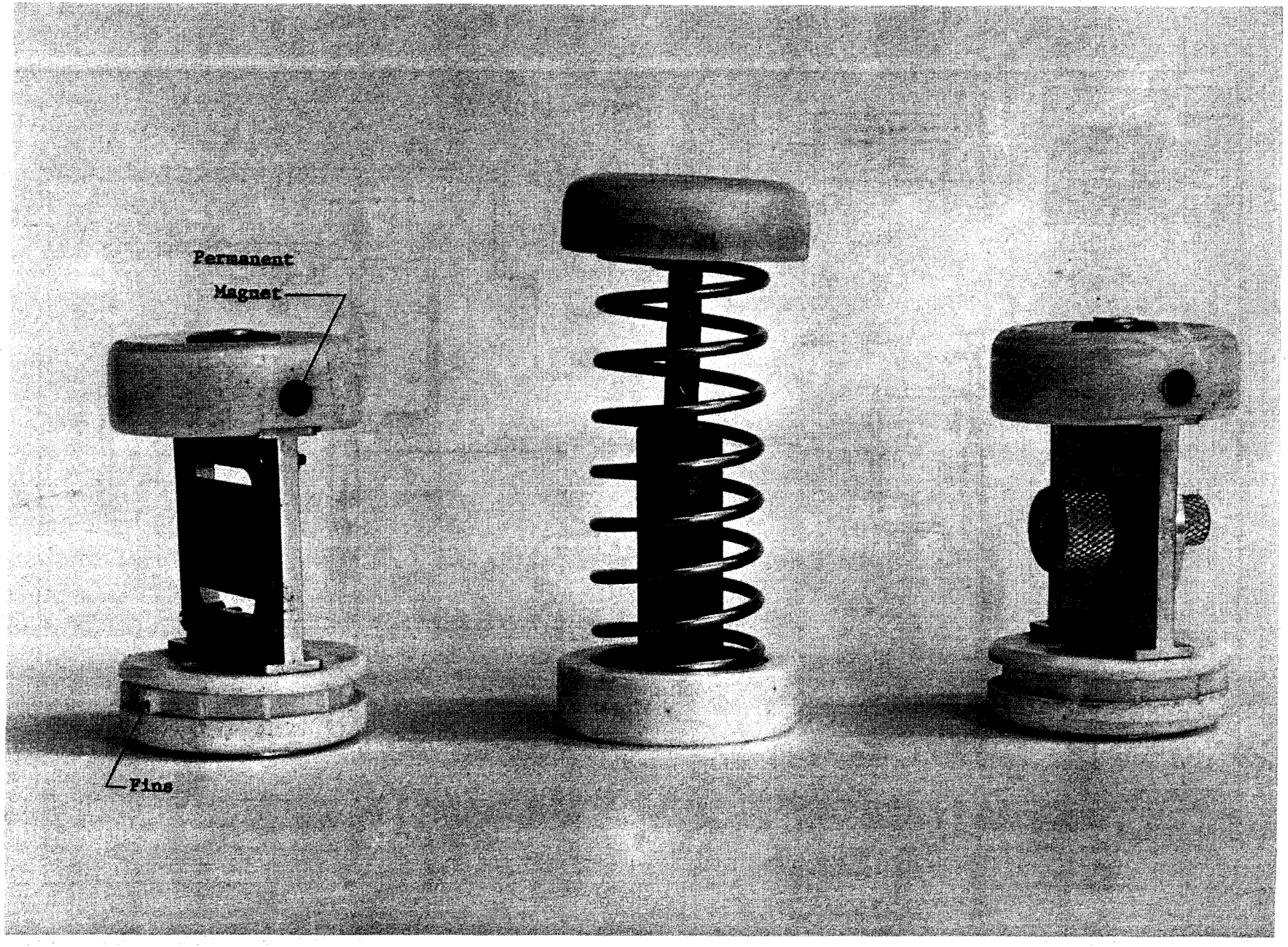

Figure 2 A,B,C (from left to right) A) Standard rabbit with target mounted on frame. B) Test rabbit used when initially setting up of system. C) Special rabbit used for small targets.

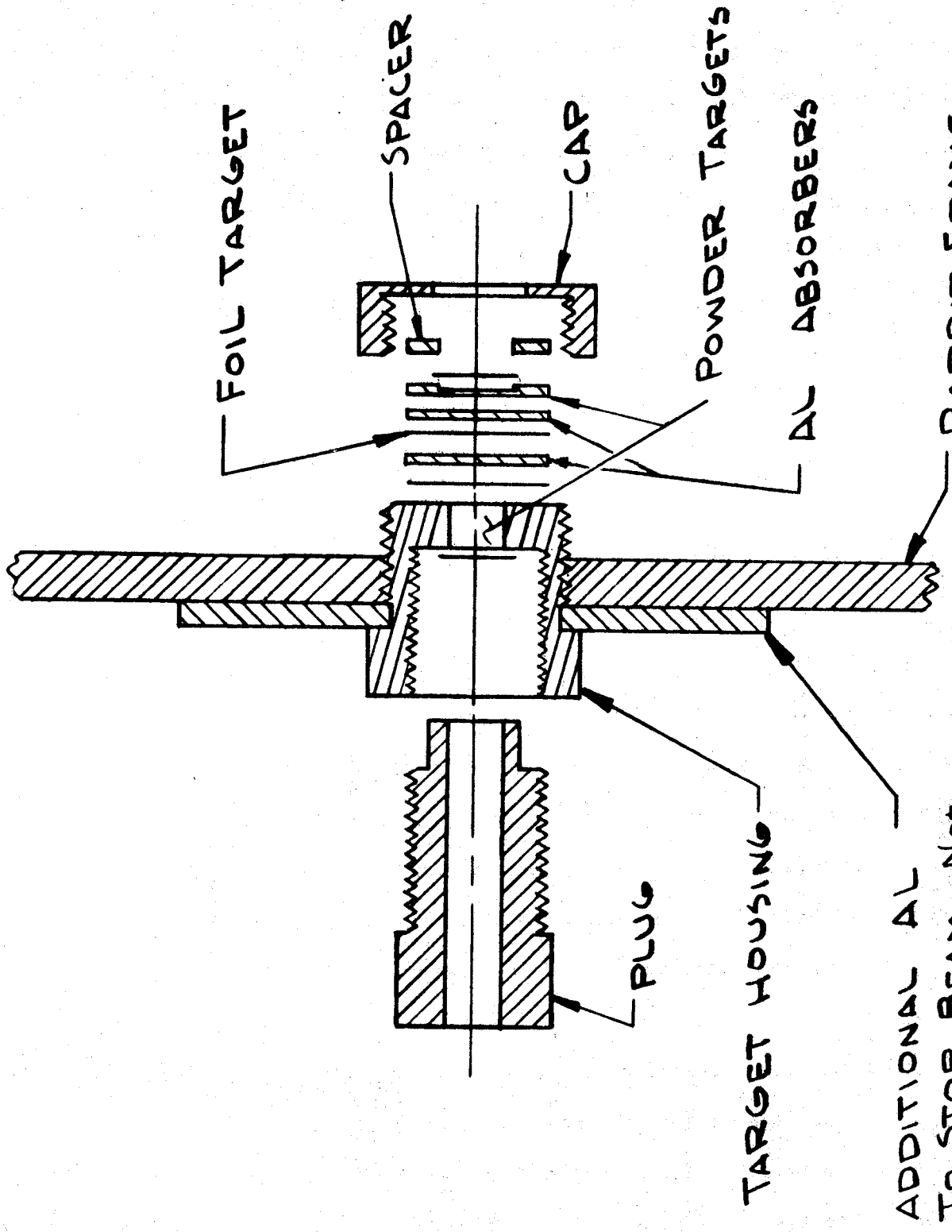

Figure 2-D Special rabbit target holder in exploded view.

even heavily loaded rabbits through the system. The rabbit system is essentially a closed system, so that any lost radioactive material is transported through the system and will end up in the vacuum cleaner. Wherever possible, cellulose acetate tubing was used in constructing the transport line because it is transparent and this aids in the location of lost materials in the line (broken rabbits, nuts and bolts, improperly attached targets and absorbers). Those places were cellulose acetate tubing was not used are in the curved sections of the line. Here it was found that polyvinyl chloride was necessary to make satisfactory bends. The best bends were made by heating the PVC tubing in a large oven (≈100°C for 5-10 min.) while applying a slight gas pressure internally to keep the tubing from collapsing. The hot tubing was then bent around a form of the proper curvature. We found that bends ≤1 ft radius could be made in this way; however, most of the bends used in the system are of a 6' radius. The tubing was mounted in standard 9" electrical wire race-way (Fig. III). Each major section was joined with unions that allow easy removal of the section should that become necessary. The line supplying vacuum to the *in* and *out* terminals of the rabbit system was made to the same specifications as the rabbit line, so that it could be used as a second rabbit line with only slight modification if an expansion of the system is ever desired.

The mechanism for orienting and cooling the rabbit is illustrated in Fig. IV. The orientation process is started using two jets of air directed at the rabbit. The first, directed up from the bottom, lifts the rabbit slightly from the surface on which it is resting. The second

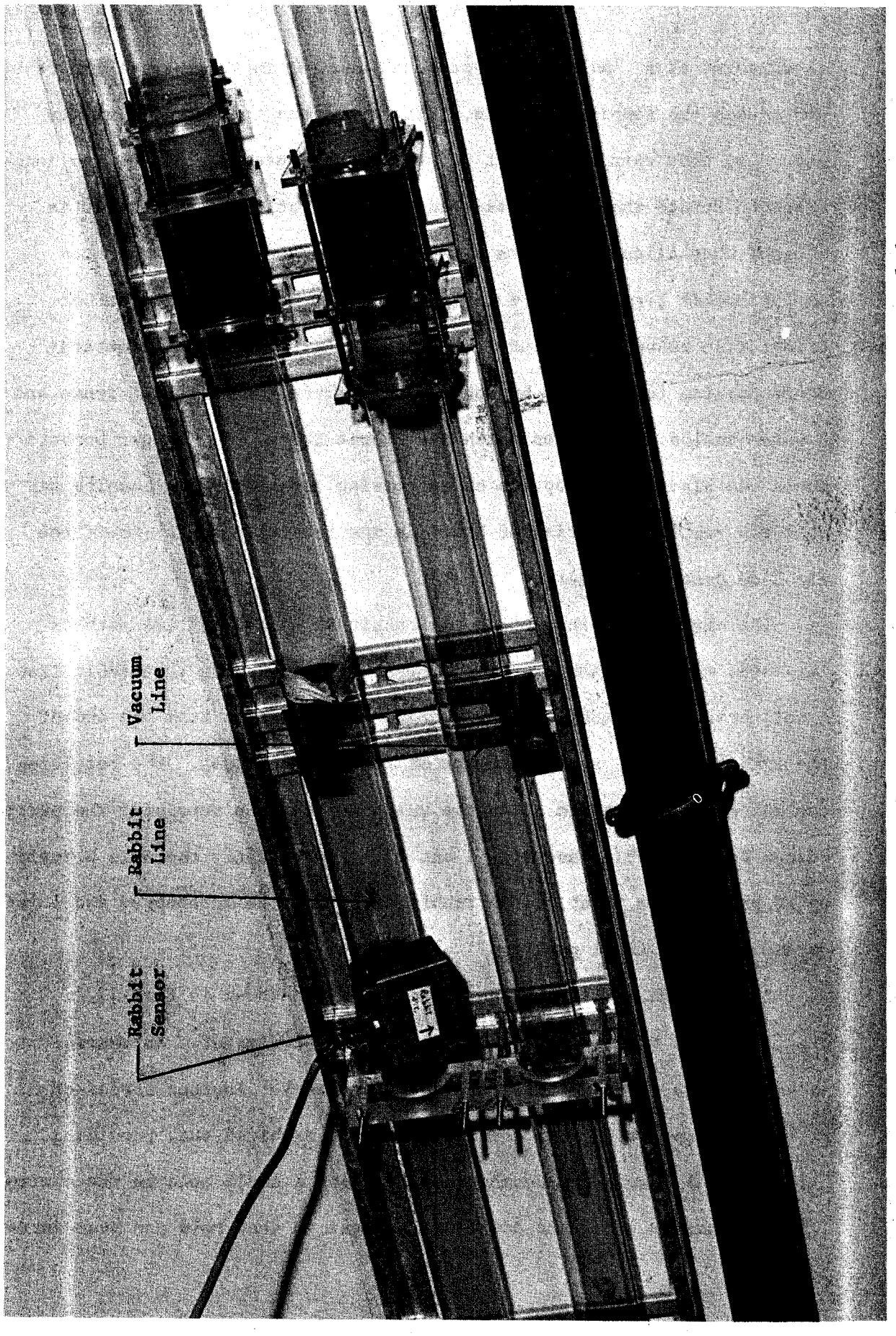

Figure 3 Rabbit line is mounted in electrical raceway. The pipe sections are coupled with unions to facilitate disassembly of the line should a rabbit or target become lost. Also shown is the electronic sensor that detects the passage of the magnet mounted in the rabbit.

is directed at a "pelton" type wheel mounted in the base of the rabbit and causes the rabbit to rotate. [The wheel has teeth only part way around so that when the rabbit is properly oriented the air jet no longer tends to rotate the rabbit (see Fig. II)]. Rotation of the rabbit is stopped when alignment occurs between a fixed electromagnet mounted in the rabbit terminal and a permanent magnet mounted in the rabbit. Orientation is usually accurate to within 5°. During short bombardments cooling is achieved by conduction between the Al rabbit frame and a water cooled Al plate on which the rabbit rests. For longer bombardments one also has the option of increasing the cooling by passing air over the rabbit. A series of holes in the rabbit tends to direct the air flow over the target.

The air cushion that stops the rabbit at the end of its path is initiated when the rabbit passes a sensor mounted along the rabbit line. A coil around the rabbit pipe is located about 8 feet from the end of the rabbit line and senses passage of the rabbit magnet. The resulting current pulse is used to close the valve on the line supplying the partial vacuum to the rabbit (see Fig. I and VI. Accordingly there is a build-up of pressure in front of the rabbit causing it to be stopped and lowered gently into its final position.

Some of the rabbit configurations used are shown in Fig. II. Fig. IIa shows the standard rabbit loaded with a target. An absorber package can be added to this rabbit if necessary. Another series of rabbits was made with the central region not machined out, providing .150 in of Al absorber. Further, by drilling a small hole in the central .150 in Aluminum plate and mounting a target in that hole the beam current

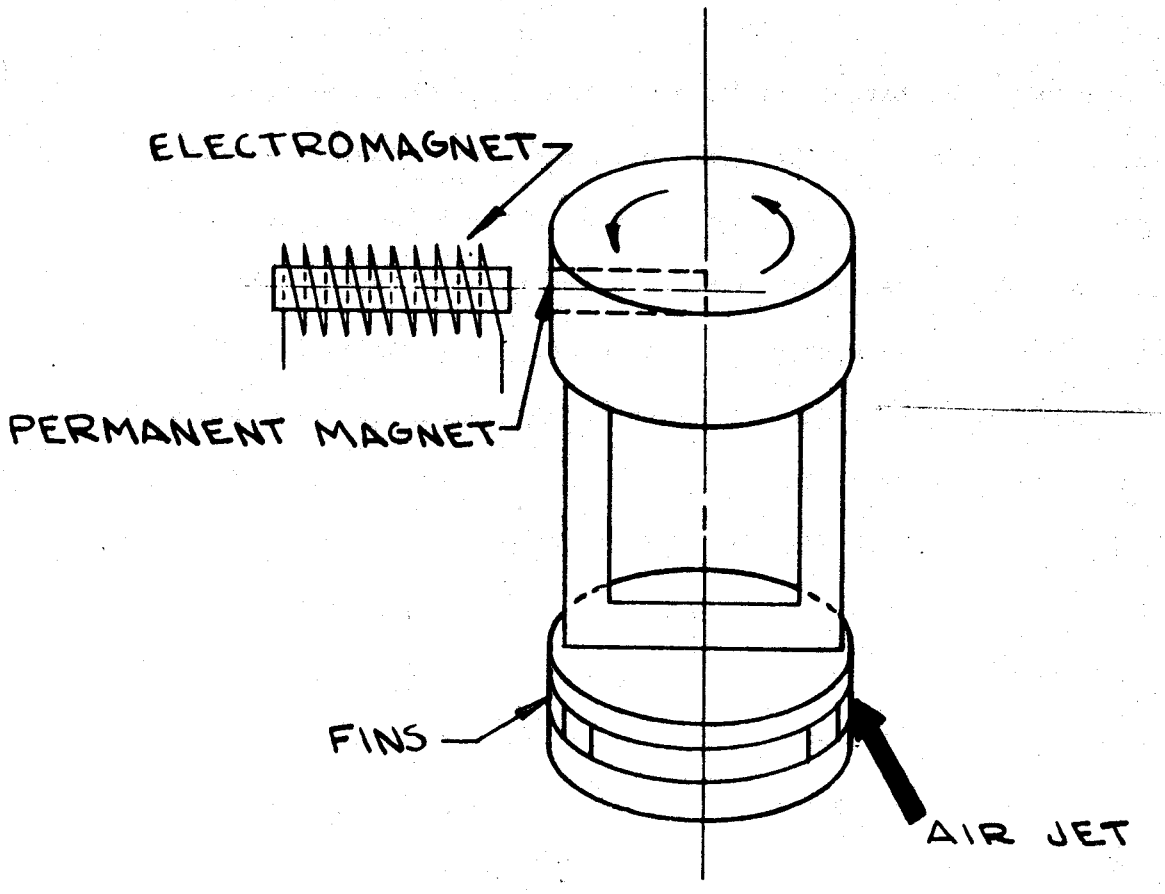

Figure 4-A Rabbit orientation mechanism.

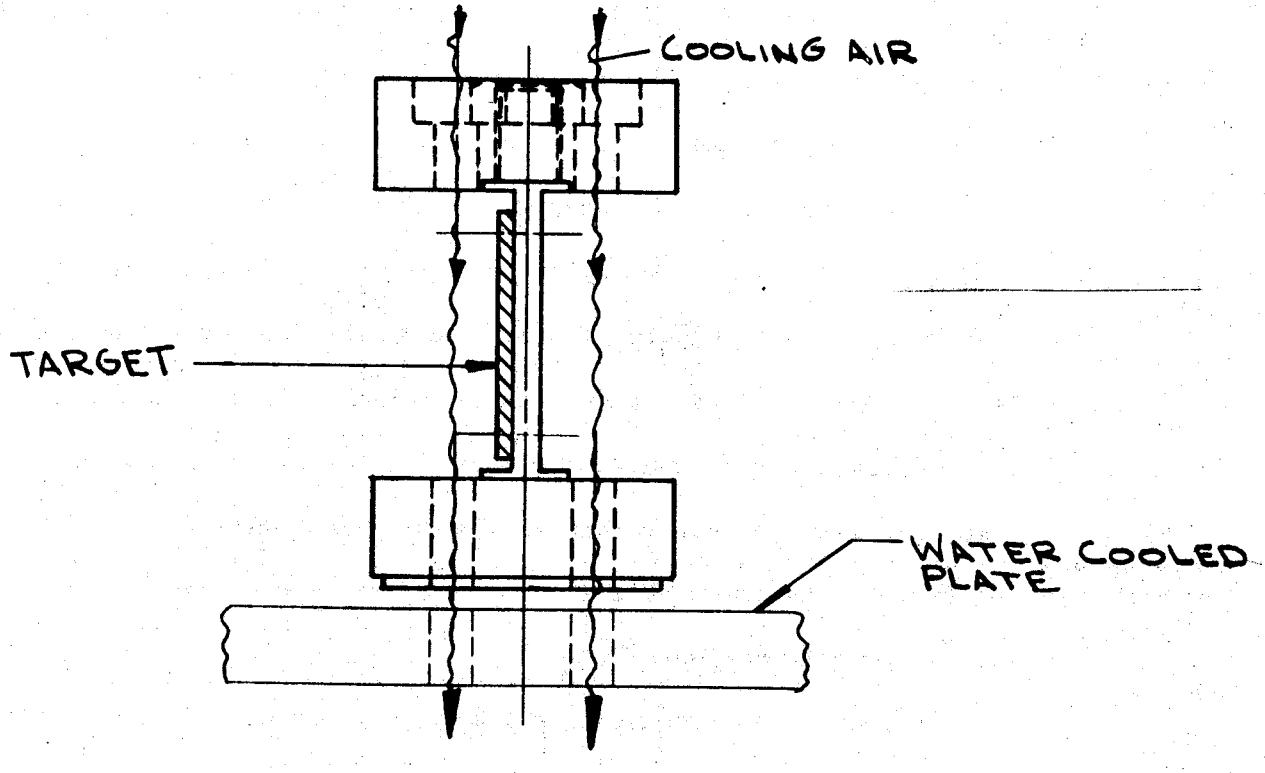

Figure 4-B Target cooling mechanism. Consisting of direct air cooling and cooling through contact of rabbit frame with a cooled plate.

passing through the target can be monitored (in some cases it was necessary to increase the thickness of the central plate to insure the stoppage of the cyclotron beam not passing through the target. Also these rabbits have been used to provide mounting for special target holders. One of these special target holders is shown in Fig. IIc and in exploded view in Fig. IId. This one was principally used to prepare targets of powdered separated isotope materials. On several occasions foil targets were mounted in front of the separated isotope target. In one instance a collection of three different foil targets of appropriate thickness were irradiated simultaneously with a powdered separated isotope target. More recently, a similar unit with O-ring seals was used to prepare ^{13}N without the ^{13}N being carried off with thermal decomposition products of the carbonate target. Also shown in Fig. IIb is the spring loaded rabbit used to test the system.

Fig. V shows the *in* and *out* rabbit terminals. Separation of the rabbit system and the cyclotron vacuum is provided by a 0.001 in Havar window. A remotely controlled absorber system was designed to be placed between the Havar window and the rabbit, but was never constructed. To aid in the study of short-lived activities, the *out* terminal was equipped with a .050 in plastic window to allow counting of targets without removing the rabbit from the terminal. In conjunction with this mode of operation the "rabbit controler" has a built-in sequencer that automatically brings the rabbit to the *out* terminal after the beam is shut off, orients the rabbit in the terminal, and subsequently routes data into as many as four ADC's.

A collection of schematics and machine drawings is provided in

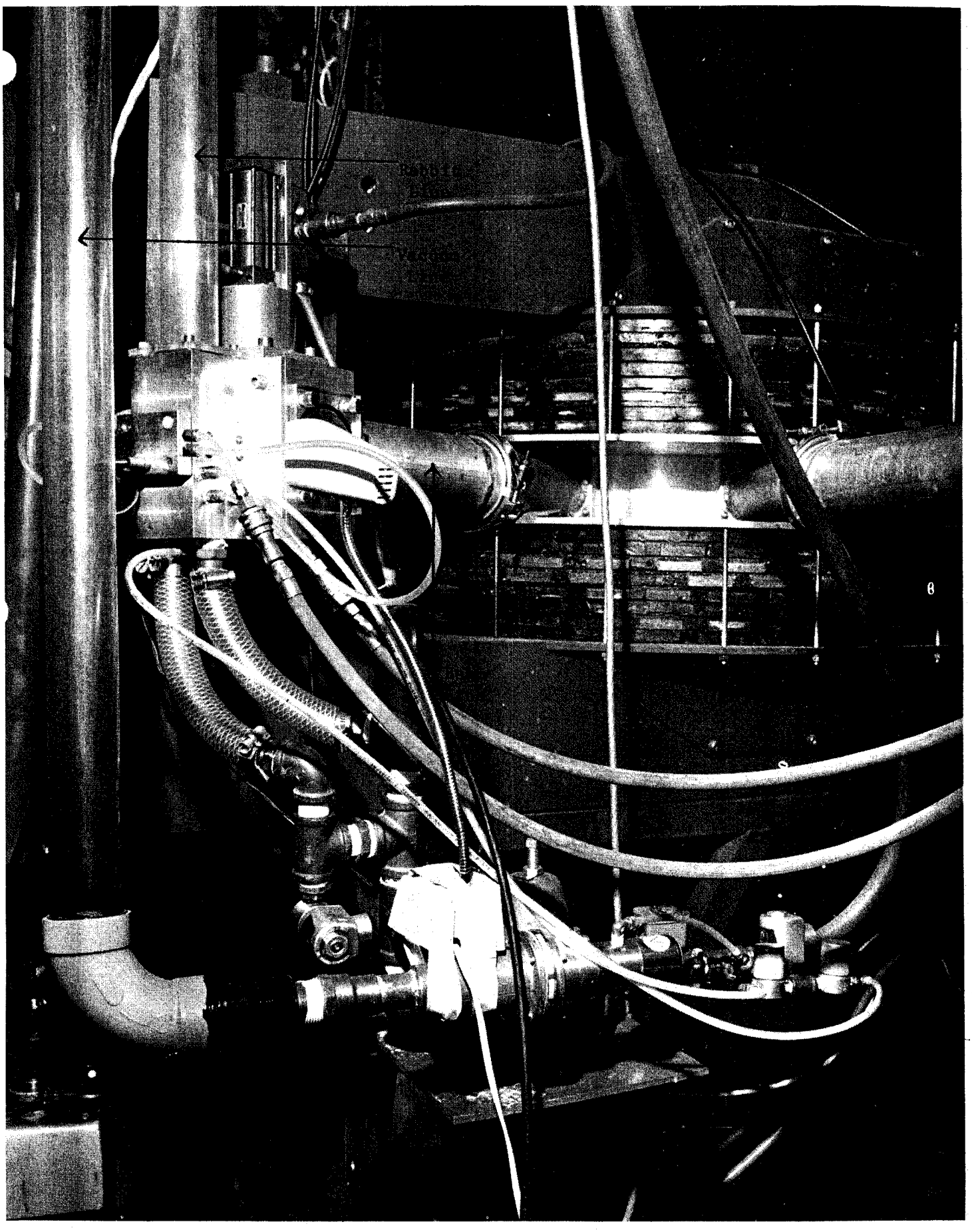

Figure 5-A Rabbit *"in"* terminal located in the cyclotron beam line.

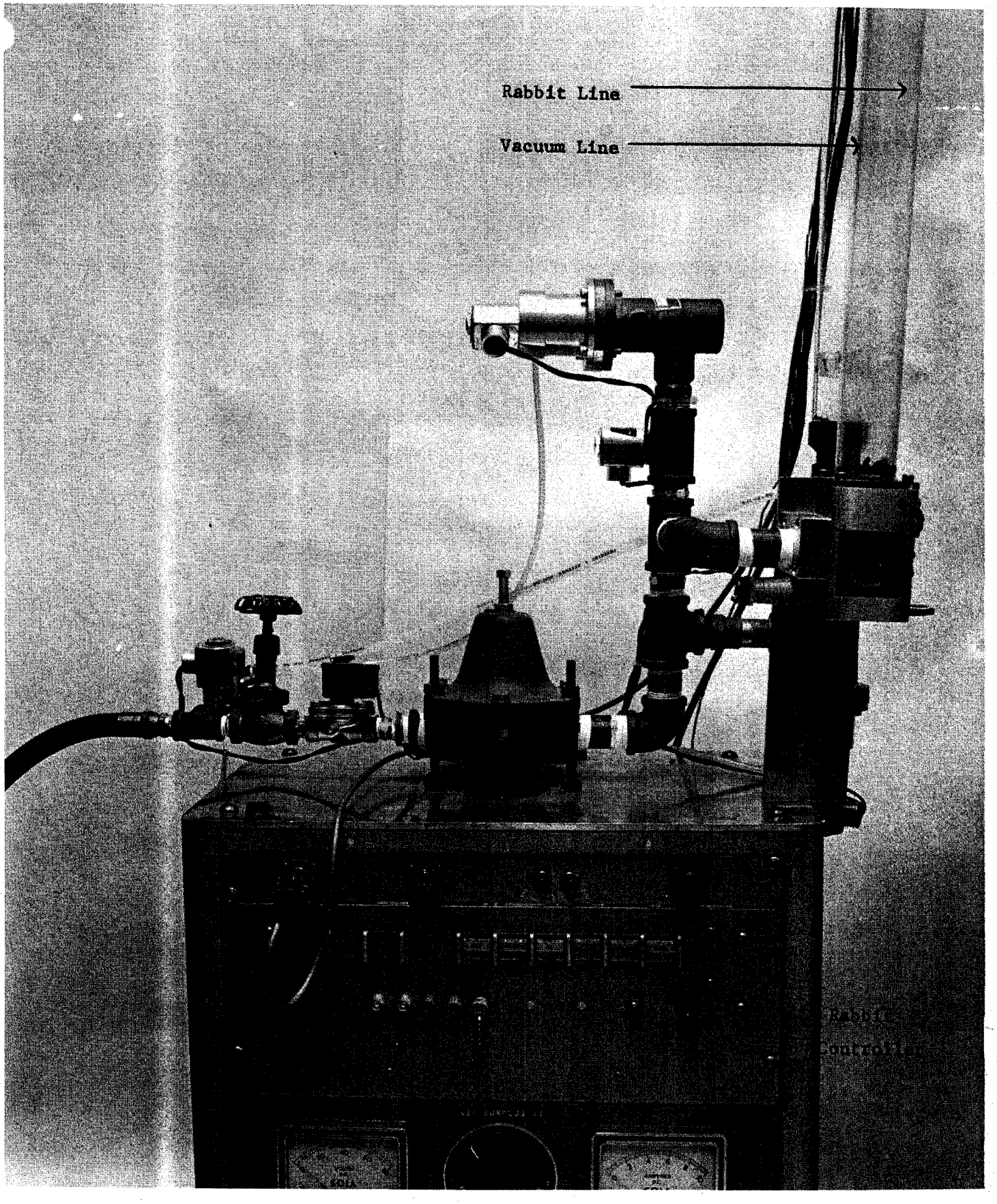

Figure 5-B Rabbit *"out"* terminal located in a low background area about 200 feet from the *"in"* terminal.

Fig. VI.

The utility of the system is perhaps best demonstrated by the fact that from the time of its completion, all targets prepared for off-line study in this lab have been prepared using the rabbit system.

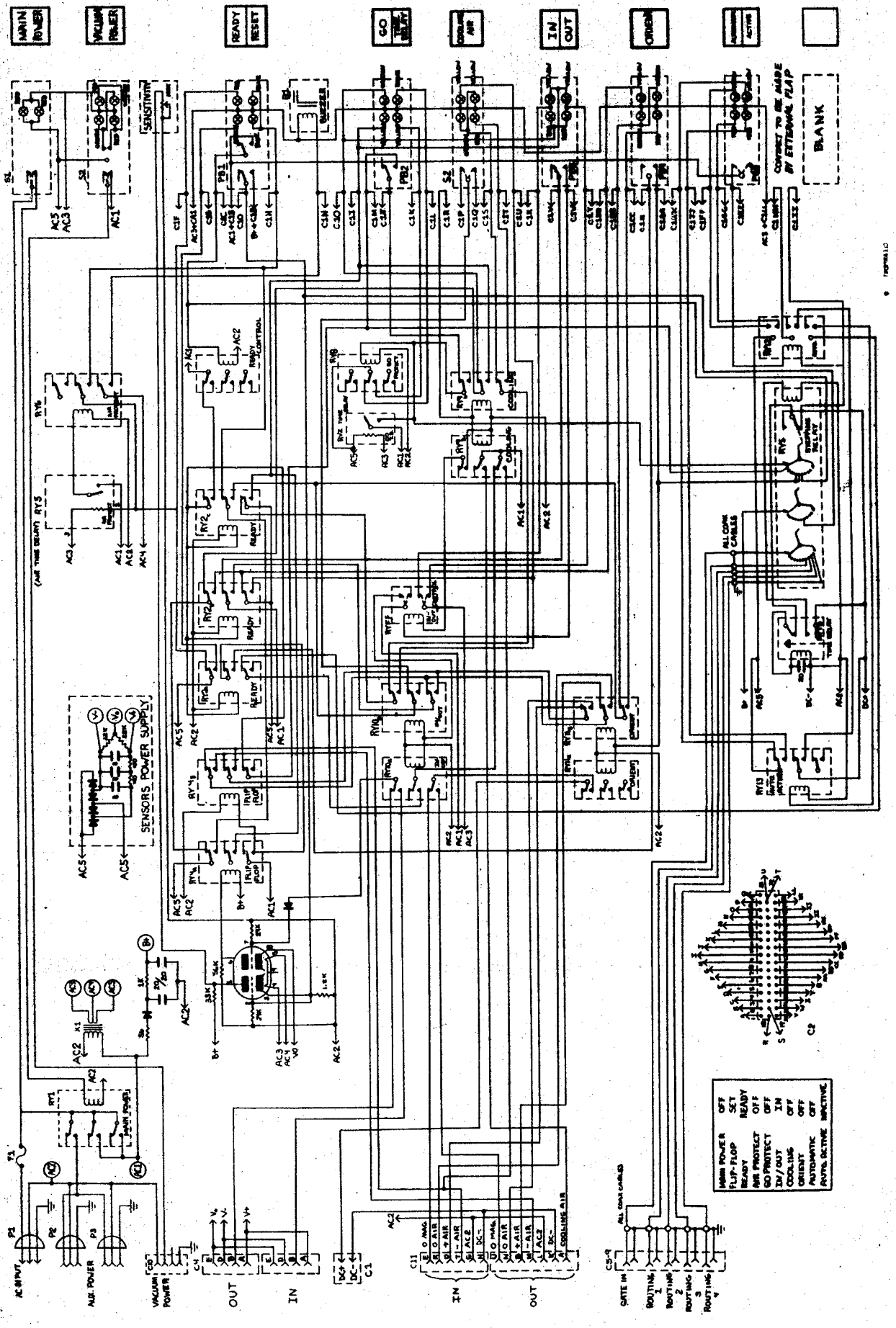

Figure 6-A Schematic of the master rabbit controller located at "*out*" terminal in low background area.

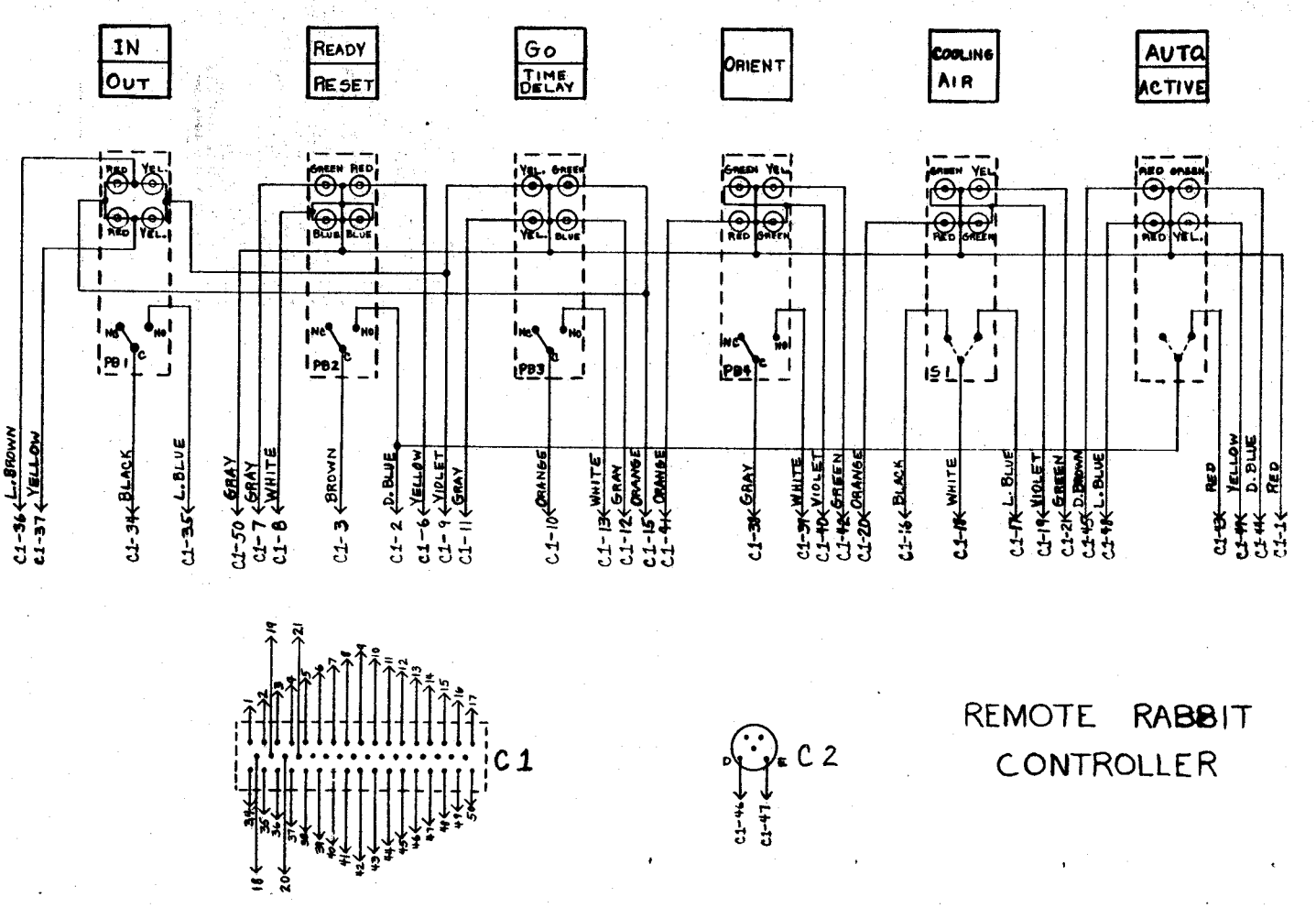

REMOTE RABBIT CONTROLLER

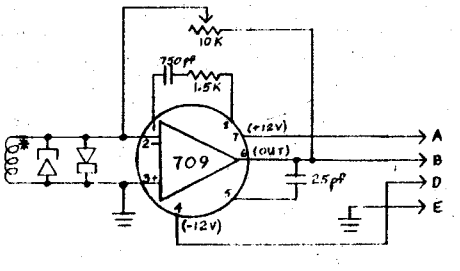

RABBIT SENSOR

* SEVERAL HUNDRED TURNS OF #36 WIRE ON A 2" ID 20" FORM MOUNTED IN A RABBIT PIPE.

Figure 6-B Schematic of the remote rabbit controller and rabbit sensor.

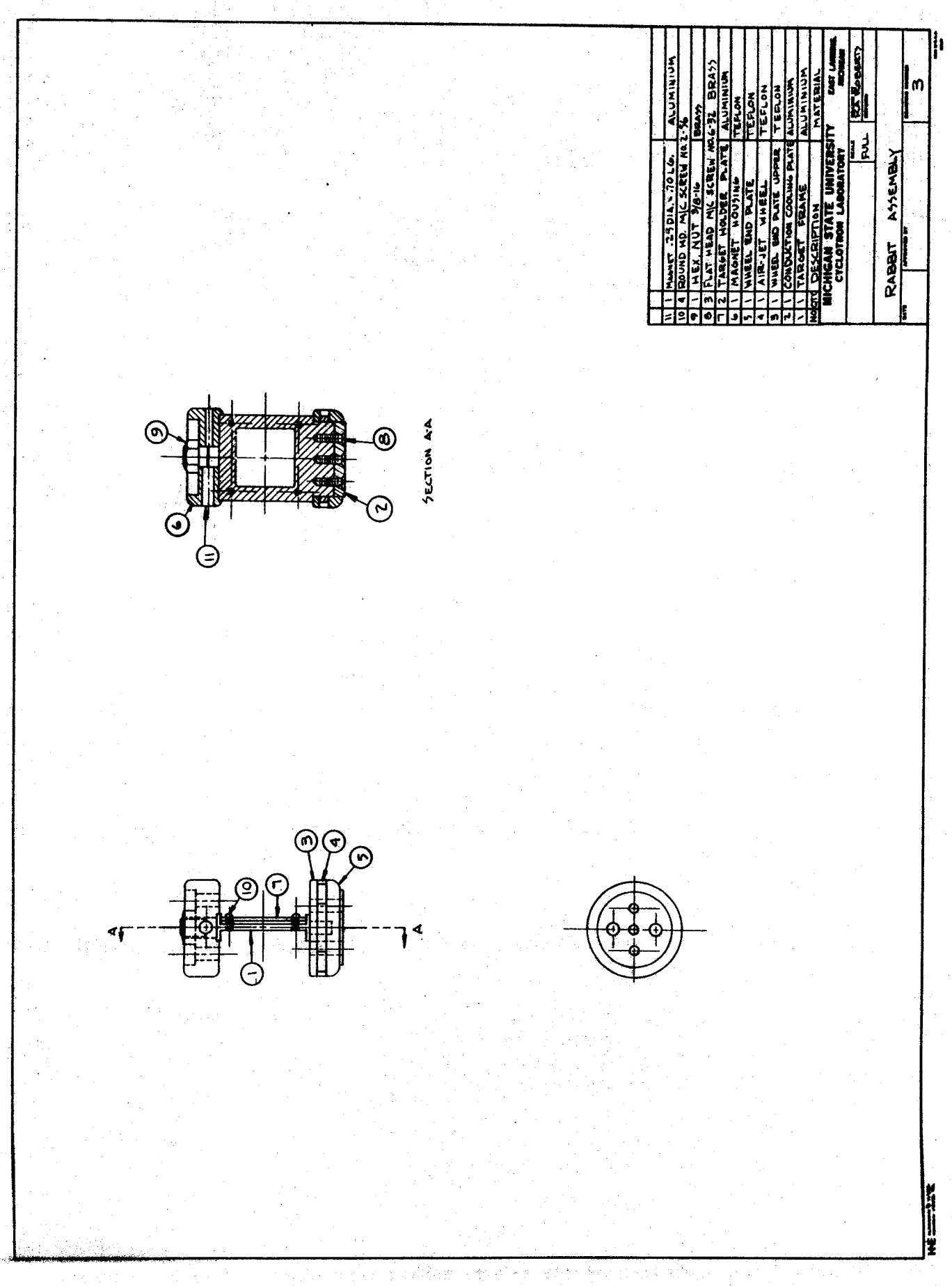

Figure 6-C Assembly drawing of standard rabbit.

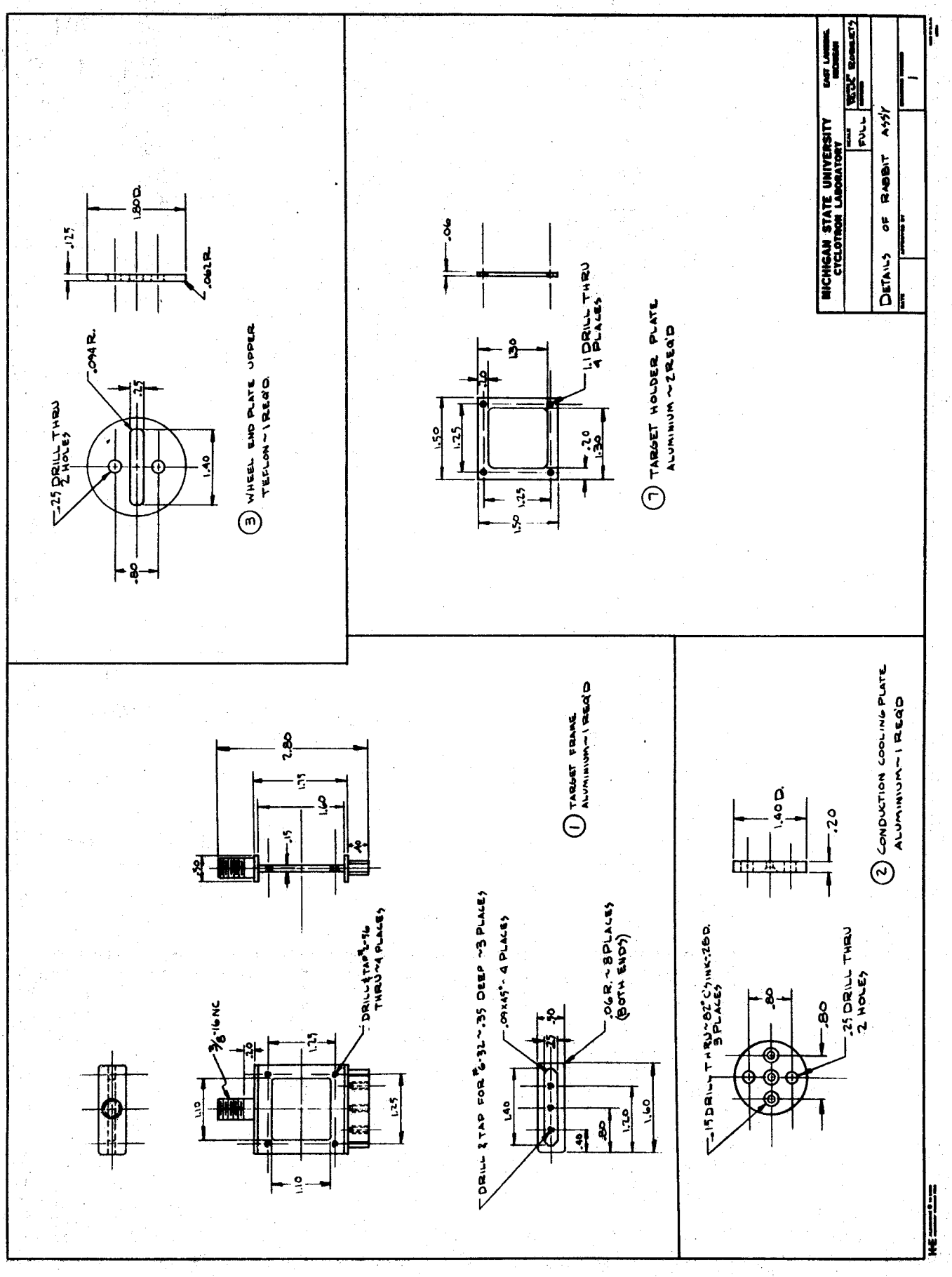

Figure 6-D Detail drawing of standard rabbit.

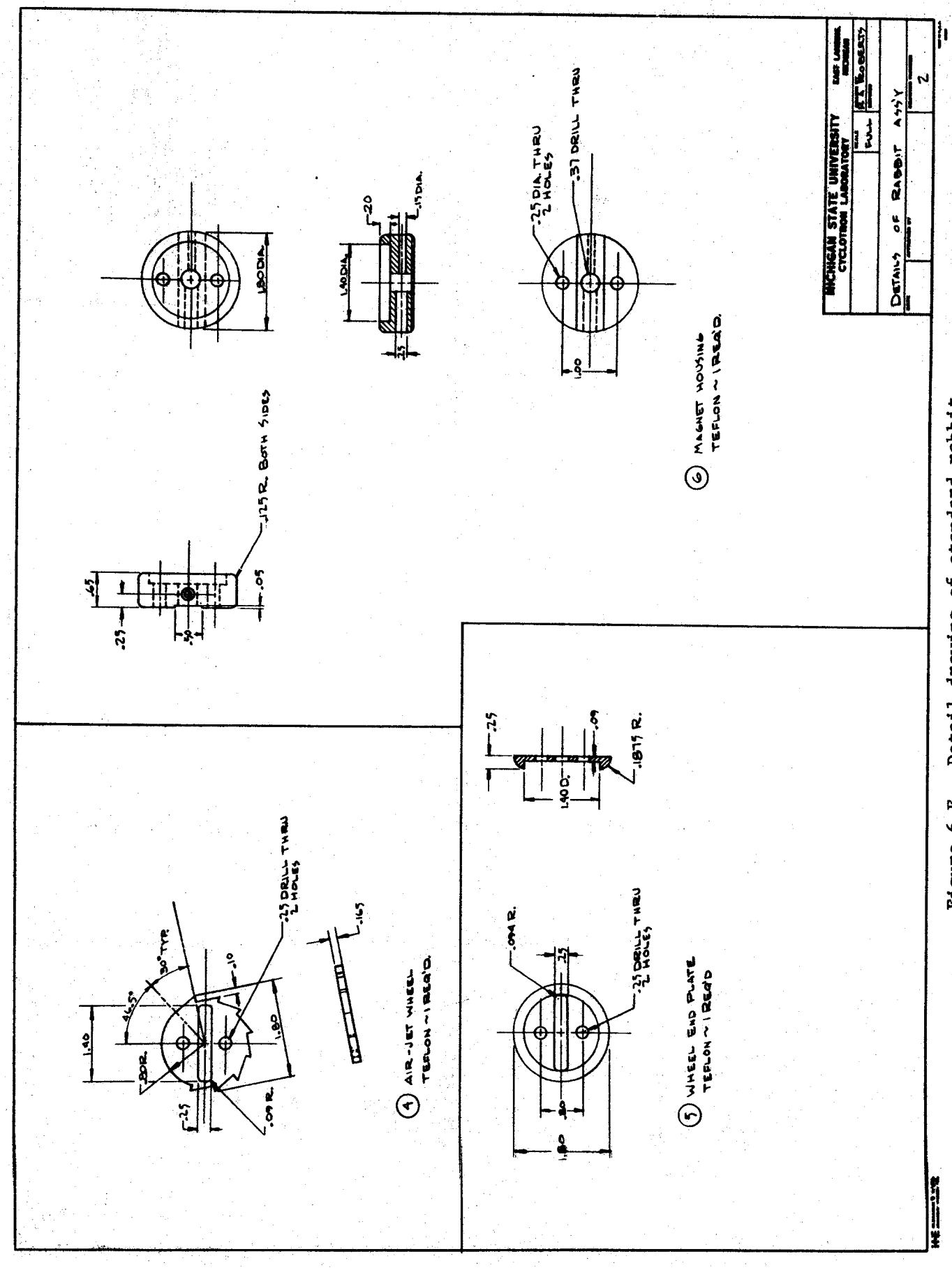

Figure 6-E Detail drawing of standard rabbit.

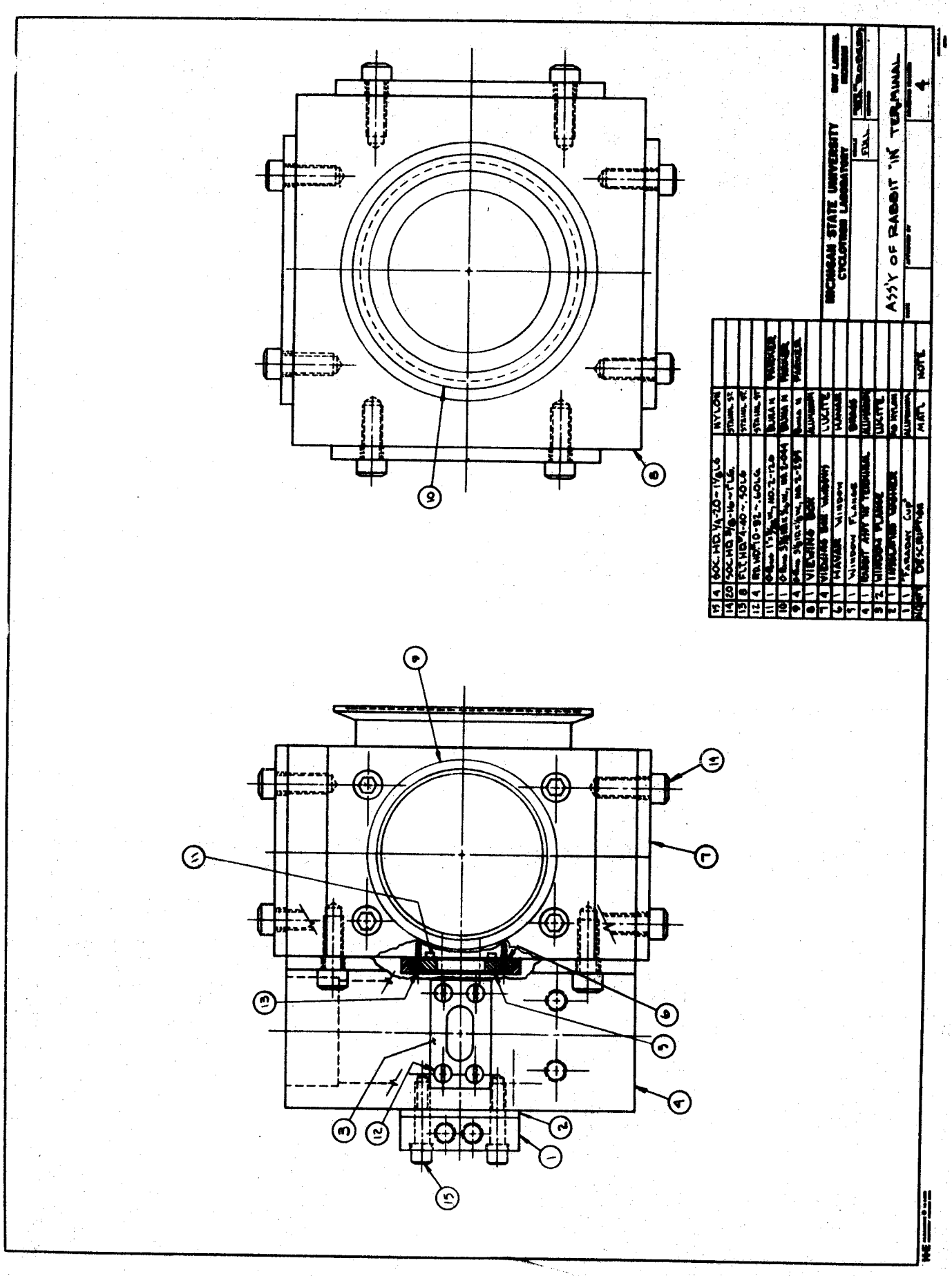

Figure 6-F Assembly drawing of rabbit "in" terminal located in the cyclotron's vault. Cyclotron beam enters the drawing from the right.

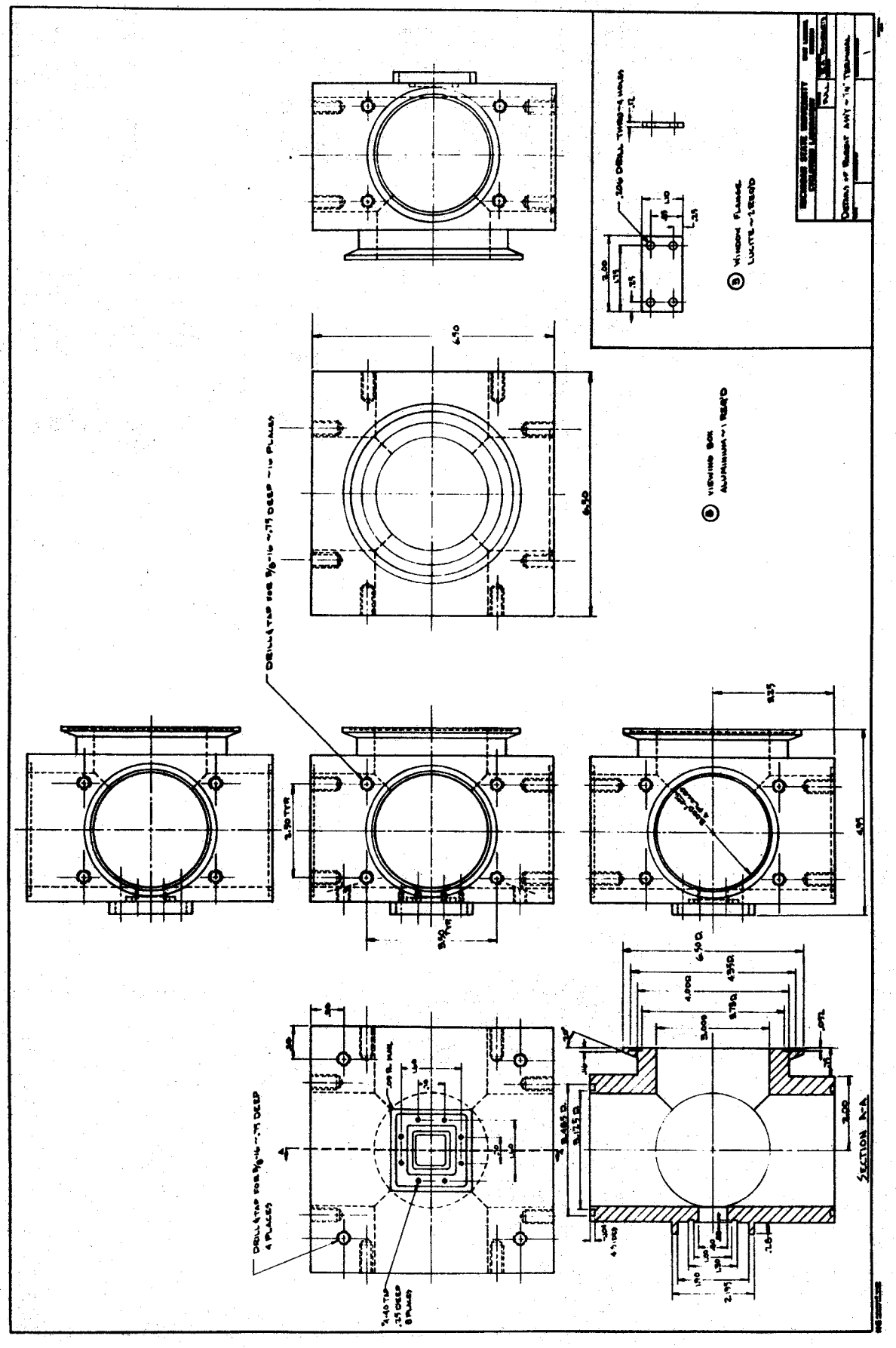

Figure 6-G Detail drawing of rabbit "in" terminal.

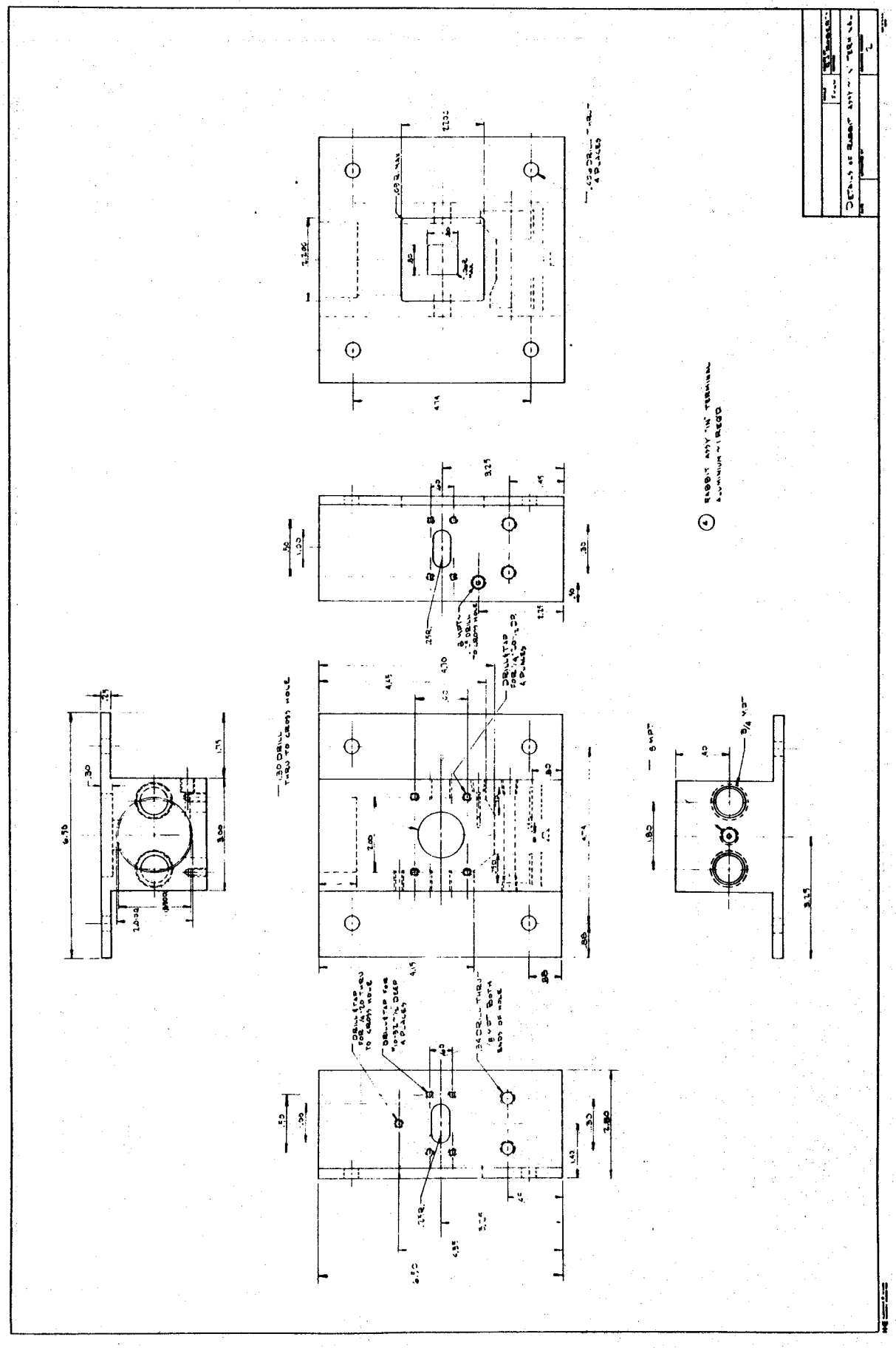

Figure 6-H Detail drawing of rabbit "in" terminal.

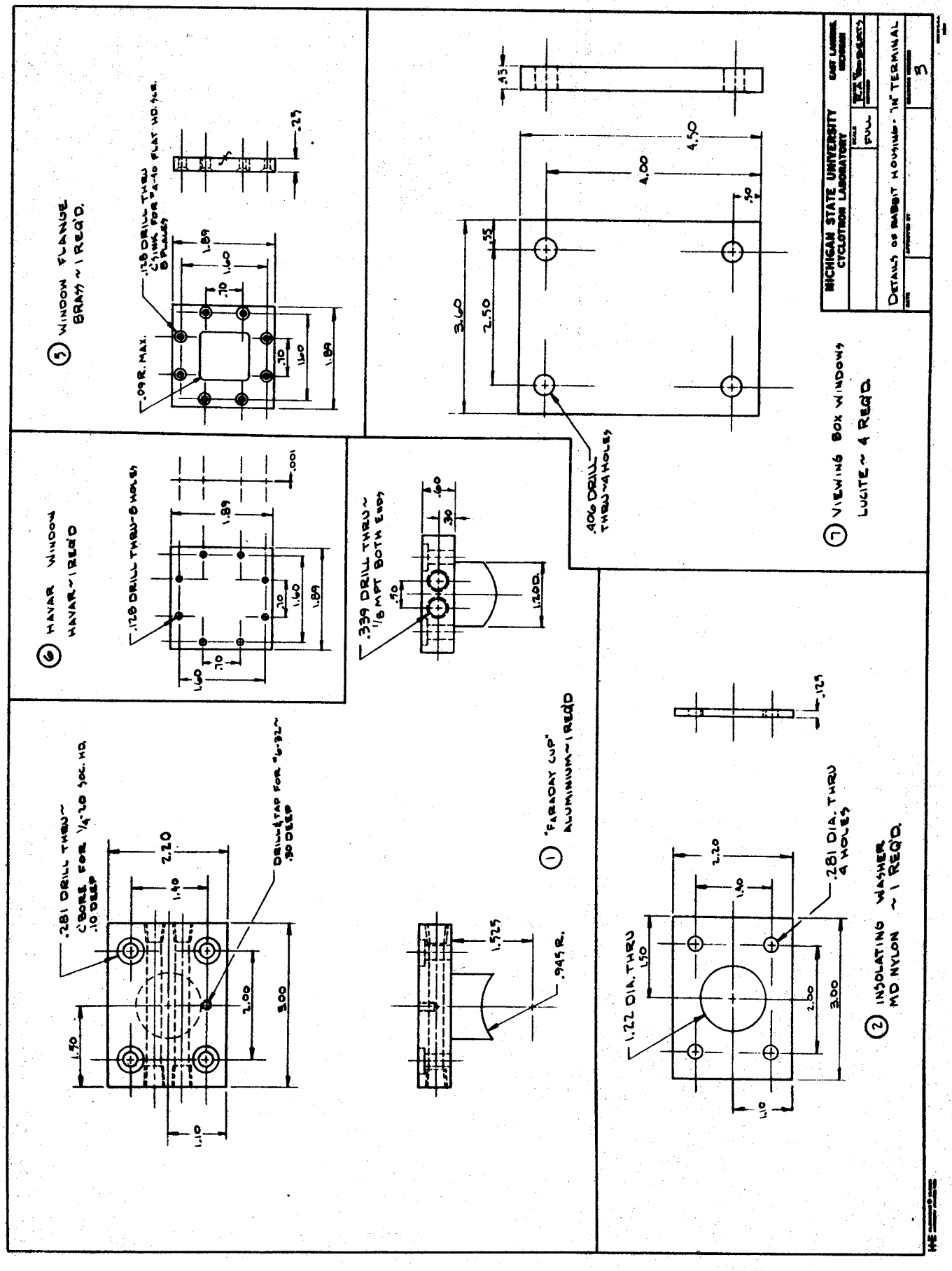

Figure 6-I Detail drawing of rabbit "in" terminal.

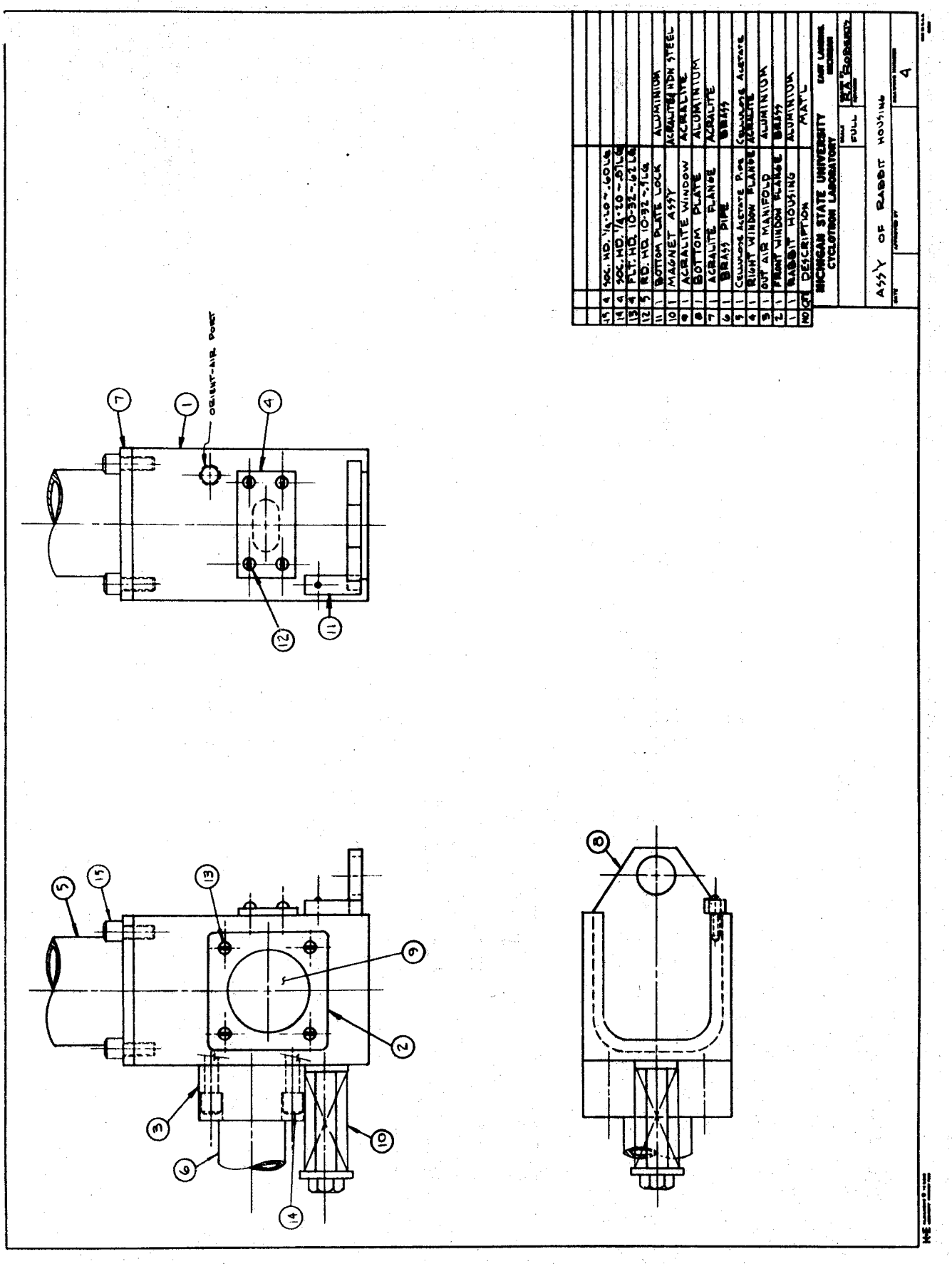

Figure 6-J Assembly drawing of rabbit "out" terminal located in low background area.

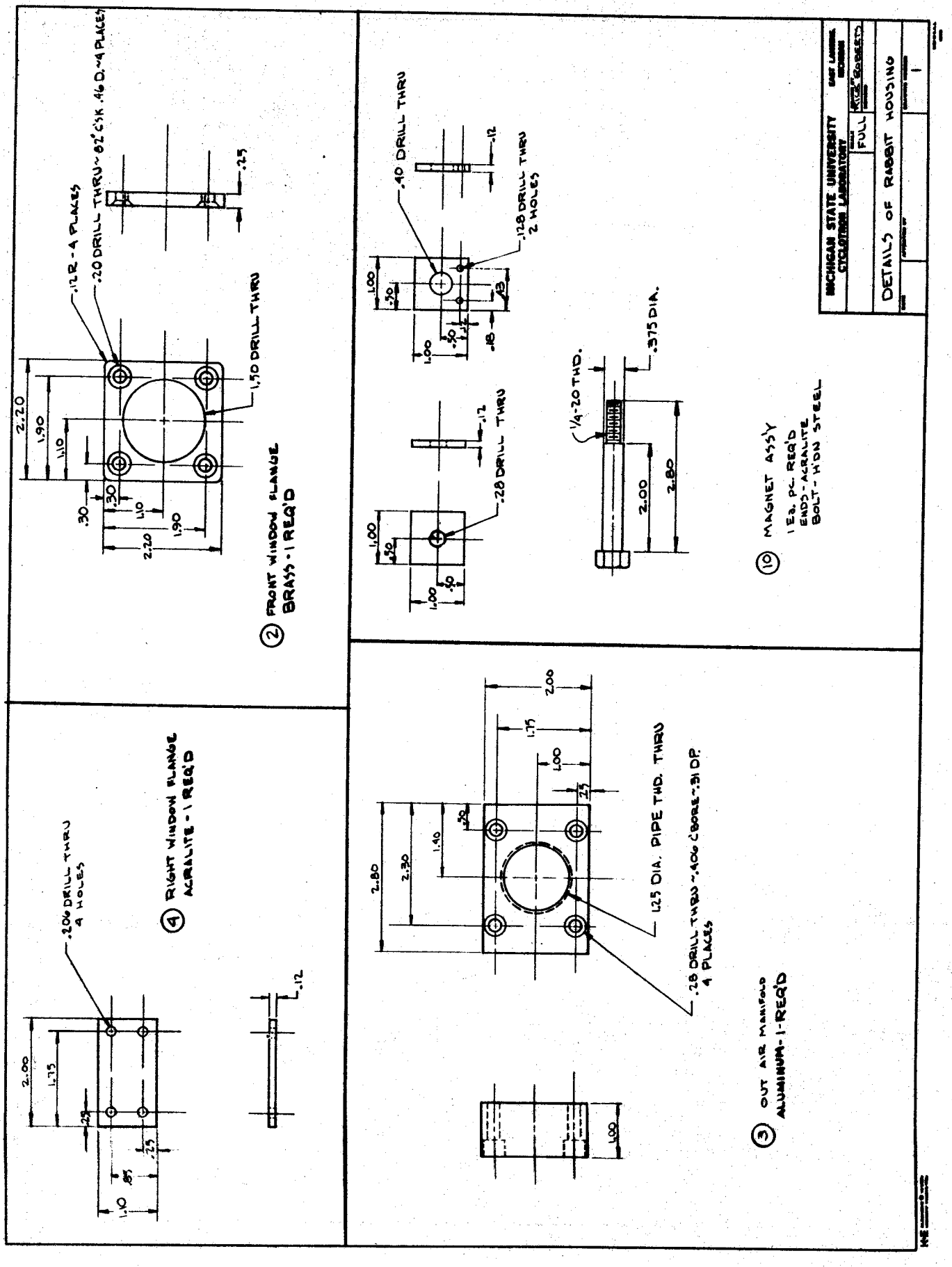

Figure 6-K Detail drawing of rabbit "*out*" terminal.

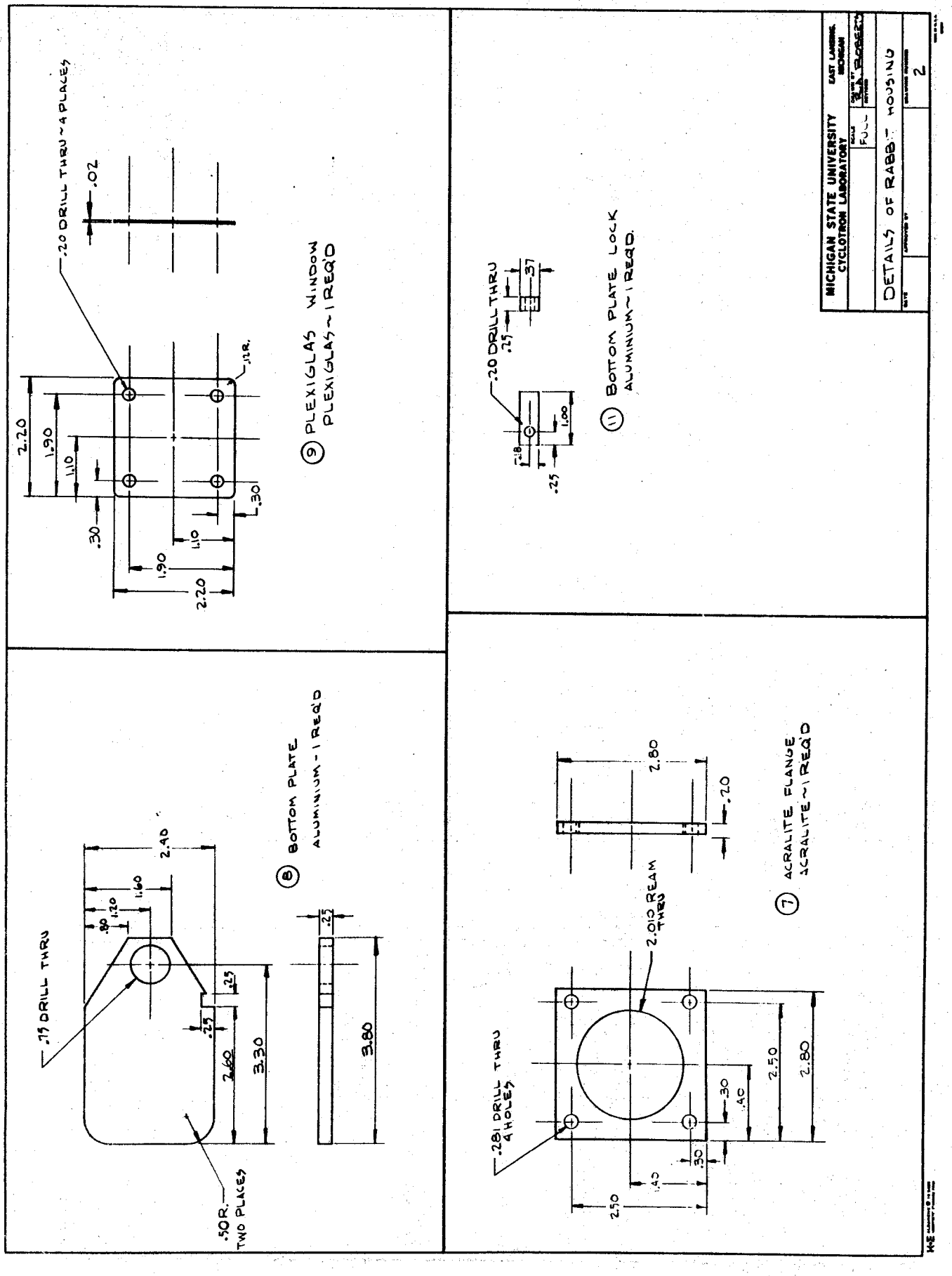

Figure 6-L Detail drawing of rabbit "out" terminal.

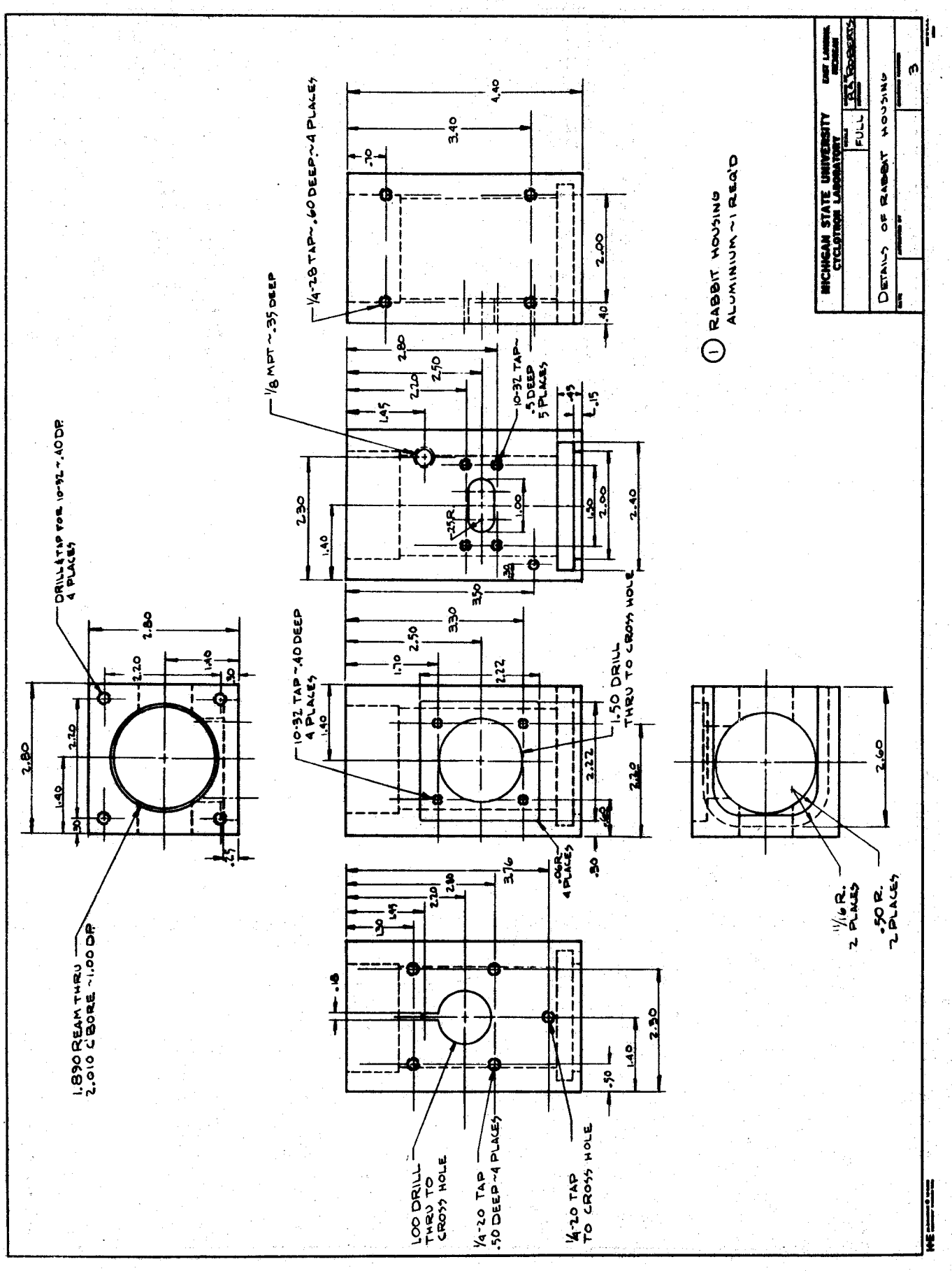

Figure 6-M Detail drawing of rabbit "*out*" terminal.

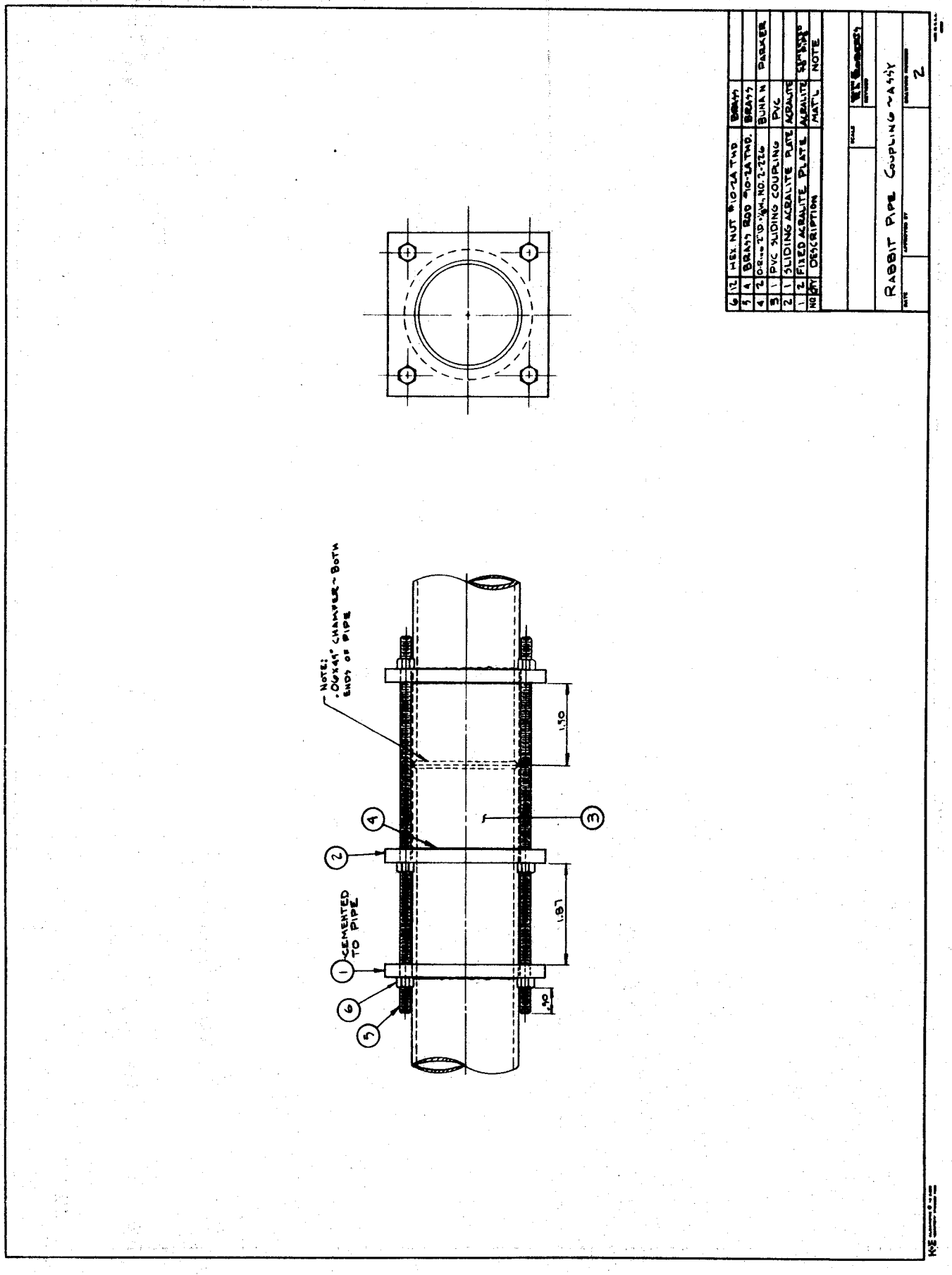

Figure 6-N Assembly drawing of rabbit line coupling. (Note: this is a coupling and not a union).

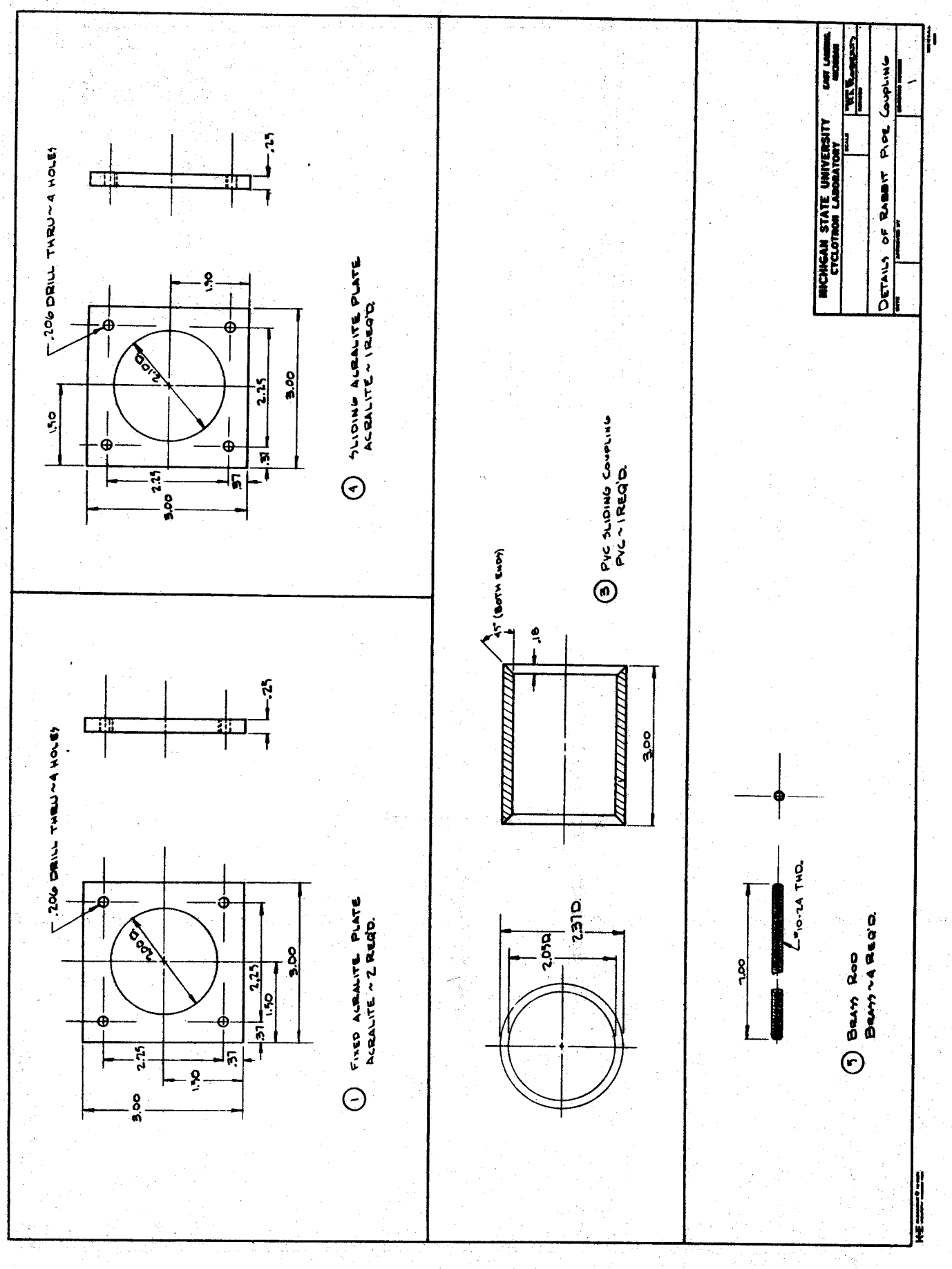

Figure 6-0 Detail drawing of rabbit union.

APPENDIX III

The Decay of ^{205}Bi

I. Preamble

As a part of a continuing study of neutron-deficient nuclei in the Pb region, results are presented on the states in the $^{205}_{82}Pb_{123}$ nucleus as populated by the primarily electron capture (ε) decay of 15.3-d $^{205}_{83}Bi_{122}$. Our group became interested in looking at the neutron-deficient Pb region in detail [DoR70, CrJ68, GuJ70, JoW73] when some anomalies were noticed for nuclei in the region. With these nuclei lying so close to the doubly-magic $^{208}_{82}Pb_{126}$ nucleus they should be spherical, and collective modes of excitation should occur at higher energies than in most nuclei. Accordingly, the low-lying states should be directly amenable to single-particle or few-particle shell model calculations. However, by the time ^{205}Pb is reached these simple calculations for the low-lying levels yield less than satisfactory results. Further, the collective effects, as evidenced by the location of the first 2^+ state corresponding to a quadrupole vibration in the even-even light lead isotopes, are somewhat less than straightford. It would be expected that the quadrupole vibration in ^{208}Pb would occur quite high and then drop down as one proceeds to lighter nuclei that are less rigid. However, the position of this state in ^{206}Pb, ^{204}Pb, and ^{202}Pb deviates from the predicted trend and are at 0.80-, 0.90-, and 0.96 MeV, respectively. Thus it was felt that improved experimental results for this entire region could be a great help in improving the nuclear theory of this and similar regions.

While the decay of ^{205}Bi had been studied extensively in this past [ScM56, FrA58, StR58, AlD60, StR60, VeS60, PeC61, HeC61,VeS64, BeK64 MiA67, RuT71, AlC71] it was felt that this study was justified considering

the improvement in experimental techniques employed as well as the depth to which this study was conducted.

II. Source Preparation

A. Sources:

Initial ^{205}Bi sources were prepared by bombarding natural Pb foils (1.5% ^{204}Pb, 23.6% ^{206}Pb, 22.6% ^{207}Pb, 52.3% ^{208}Pb) with 36.-MeV protons from the Michigan state University Sector-Focused Cyclotron to induce the ^{208}Pb $(p,4n)^{205}$Bi reaction. Initial activities of the target foils ranged up to 200 R/h. The targets were aged from 6 to 10 weeks to optimize the 15.3 d ^{205}Bi with respect to the 11.2 h ^{204}Bi, the 6.2 d ^{206}Bi, and the 30 y ^{207}Bi. Before counting, the ^{205}Bi activity was chemically separated from the targets using more or less standard chemistry [VeS63]. The targets were dissolved in a minimal amount of 6*N* HNO_3 and the bulk of the Pb precipitated as a chloride. After addition of ferric ion to the decanted supernate, the Bi activity was coprecipitated several times by the addition of first a minimal amount of 6*N* HCl and then an excess of 6*N* NaOH. The precipitate was then washed with water and taken up in 9*N* HCl. The ferric ion was extracted with isopropyl ether, leaving the Bi activity in the aqueous phase which was then taken to dryness. The Bi activity was taken up with 8*N* HCl and loaded on a column of Dowex 1×8 anion exchange resin where it was washed with 8*N* HCl and 0.1*N* HCl. The Bi activity was either counted while adhered to the column or was eluted from the column using 0.5*N* HNO_3.

Other ^{205}Bi sources were prepared by bombarding mass-separated ^{206}Pb (97.22% ^{206}Pb obtained from Oak Ridge National Laboratory) with 19-MeV protons to induce the ^{206}Pb$(p,2n)^{205}$Bi reaction. Also, one ^{205}Bi source was prepared by bombarding natural Tl as $TlNO_3$ (29.5% ^{203}Tl and 70.5% ^{205}Tl) with 37-MeV alphas to induce the ^{205}Tl$(\alpha,4n)^{205}$Bi reaction. These sources were aged several days before study and were reexamined after several weeks.

B. e^- Sources

"Mass-free" sources were prepared for study of the *N* and *O* conversion of a 2.3-keV transition in the decay of ^{205}Bi. Needless to say, the sources necessary to make this study profitable had to be of superior quality. In addition to the ^{205}Bi sources, ^{206}Bi sources were also prepared for a comparison of the general Auger background for the conversion.

While some sources were prepared using material from bombardment of natural lead foils, our best ^{205}Bi and ^{206}Bi sources were prepared using separated isotope targets. 19-MeV protons were used to induce the ^{206}Pb$(p,2n)^{205}$Bi reaction and 25-MeV protons were used to induce the ^{205}Pb$(p,3n)^{206}$Bi reaction. The activity of the separated isotope targets were usually from 3 to 10 R/h on contact.

The chemistry used in retrieving source material from the cyclotron targets was ordinary but required extraordinary cleanliness and purity of reagents. In the case of the separated isotope targets, the raw source material was dissolved in a minimum of 6*N* HNO_3, then the bulk of the lead was precipitated by addition of red fuming HNO_3. The decantate was dried then taken up in 8*N* HCl. This was loaded on a column of 50-100 mesh Dowex 1×8 anion-exchange resin. Large mesh resin was used in order that a small quartz tear-shaped plug could be used in place of glass wool to hold the resin in the column without loss of resin. The column was previously washed at all concentrations of each acid to be used. The column was then eluted using 0.1*N* HCl and 0.01*N* HNO_3. The bismuth activity was eluted from the column using 0.5*N* HNO_3. Only that fraction of the eluant with the highest specific activity was collected. Typically we could get 20 to 25% of the activity in ≤1 ml plus a second sample containing 20 to

30% of the activity in ≤ 2 ml.

All glassware, or more accurately "quartzware", had been previously washed in a solution of:

60% distilled water,

35% HNO_3 (analytical grade),

5% HF (analytical grade), and

0.2% alconox.

Following the washing, the quartzware was leached for several days in conductivity water (deionized, distilled, doubly deionised, distilled water). All acids used were "Ultrex" grade supplied in borosilicate ampoules under an atmosphere of argon. "Ultrex" grade acids were supplied by J. T. Baker Chemical Co., Phillipsburg, N.J. We found the quality of these acids to surpass that which could readily be made in our lab. The 8*N* HCl was prepared by a dilution of the Ultrex HCl with conductivity water, then passing it through a quartz ion-exchange column of washed Dowex 1×8 resin. The 0.1*N* HCl was prepared by dilution of the "columned" 8*N* HCl, then passing it again through a column washed at 8*N* and 0.1*N*. In the preparation of the dilute solutions of HNO_3, we found it advantageous to clean up the conductivity water further by passing it through the ion-exchange column when in the chloride form.

Spectrometer sources, 0.5 mm by 12 mm on 0.5-mil aluminum, were prepared by vacuum evaporation. Liquid source material was loaded and dryed on a tungsten boat that had been flashed for several seconds in vacuum.

Initial attempts using carbon and tantalum boats were unsuccessful in preparing high quality sources (carbon boat, resulted in production of thick sources; tantalum boat, essentially all the source material hung up on the boat). A tantalum boat lined with platinum did seem to work

satisfactorily. After bringing the boat up to a temperature just below the point where significant amounts of bismuth activity would start to come off, a series of sources was prepared. As many as five sources were prepared from one loading of the boat, collecting fractions of activity coming off from one loading of the boat, collecting fractions of activity coming off at slightly higher temperatures for longer times. Of the order of 90% of the source material was removed from the boat, with 25 to 40% passing through the mask. We generally found that the second or third source gave us the most favorable combination of activity and resolution. In an attempt to improve the background due partly to backscattering of higher energy electrons we made some sources on 150 $\mu g/cm^2$ aluminum leaf. The improvement was minimal and thought not to be worth the effort.

III. Experimental Results

A. γ-Ray Singles Spectra

Energies and intensities of the ^{205}Bi γ rays were determined using several different detector systems. Initial work employed a 7-cc five-sided trapezoidal Ge(Li) detector. Figure 1 shows a γ spectrum collected with this detector in 90 hours and has a resolution of 2.7 keV for the 703 keV transition. More recent γ spectra concentrating on smaller portions of the spectrum have been collected with two five-sided trapezoidal Ge(Li) detectors having photopeak efficiencies of 2.5% and 3.6% relative to a 3X3-in NaI(Tl) detector at 1.332 MeV. Typical resolutions for these detectors were 2.3- and 2.1-keV FWHM at 1.332 MeV. Detector systems employed room-temperature FET preamplifiers, low noise *RC* linear amplifiers with pole zero compensation coupled to a Nuclear Data 2200 analyzer or to Northern ADC's interfaced to a PDP-9 or a Sigma-7 Computer.

Energies of the prominent γ rays were measured in a series of runs by counting the ^{205}Bi sources simultaneously with collections of energy standards listed in Table I chosen to bracket the ^{205}Bi transition being looked at. The centroids of the photopeaks were determined with a live-display computer program which used the upper two-thirds of the photopeak after subtracting out the background. The background was determined for each peak by making a least-squares fit of selected points on both sides of the photopeak to an nth-degree (up to $n = 5$) polynomial. The centroids of the calibration peaks were used to define a quadratic calibration curve from which the energies of the prominent ^{205}Bi peaks were calculated. The energies of the weaker ^{205}Bi γ rays were then determined in a similar fashion by using the energies of the prominent γ rays as secondary standards. However, in many instances it was necessary to strip multiplet peaks.

Figure 1. Gamma Ray Singles Spectrum of ^{205}Bi

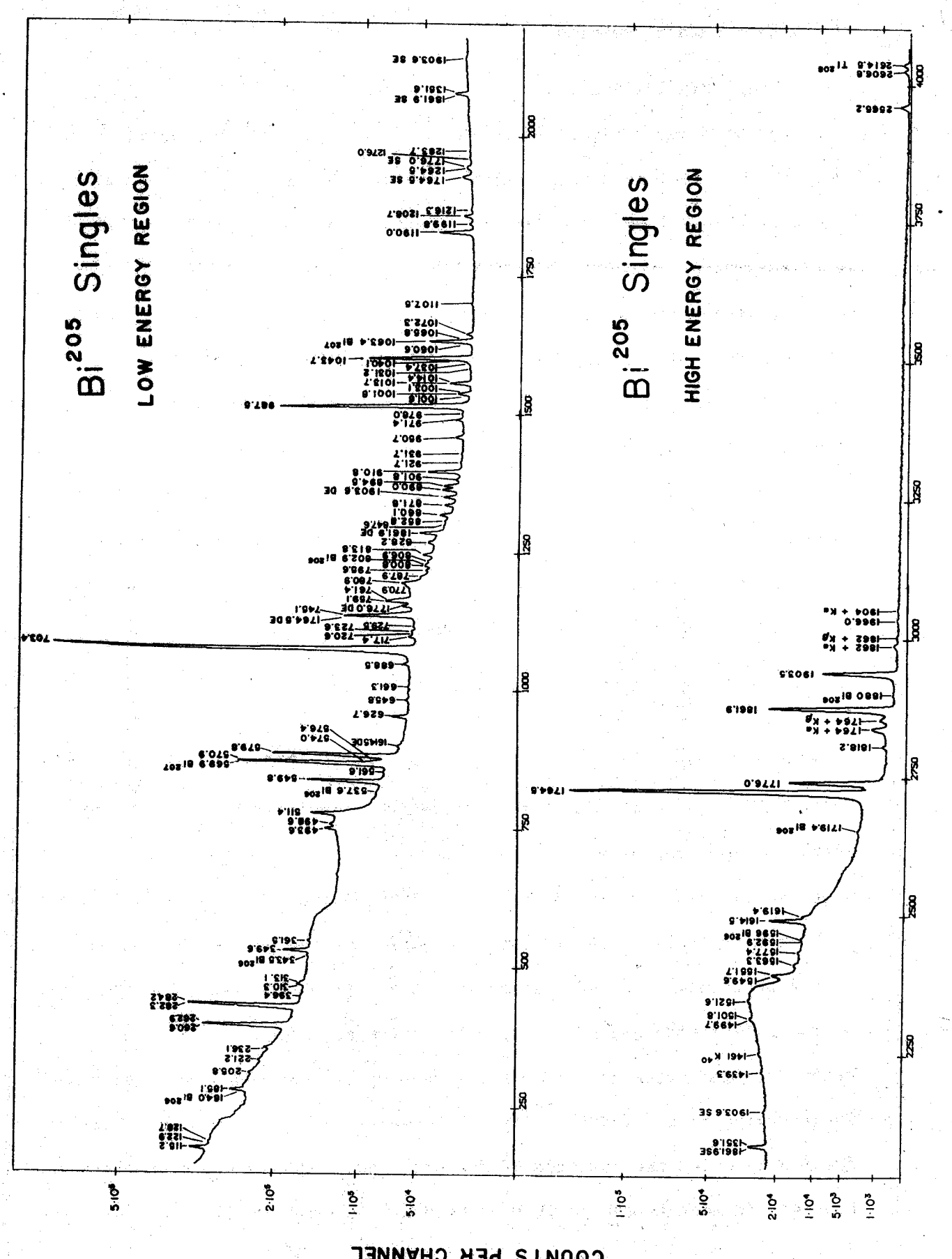

TABLE I

Bi^{205} Primary Energy Calibration

Primary Standards			Secondary Standards (in Bi^{205})
Isotope	Energy	Ref.	Energy
Ta^{182}	100.104±.002	(a,b)*	
			115.178±.05
Co^{57}	121.97 ±.05	c	
Co^{57}	136.33 ±.04	c	
Ta^{182}	152.435±.003	(a,b)	
Ta^{182}	156.387±.003	a	
Ce^{139}	165.852±.010	d	
Ta^{182}	179.393±.004	(a,b)	
Ta^{182}	229.322±.008	(a,b)	
			261.045±.02†
Hg^{203}	279.191±.008	d	
			283.840±.02†
Ir^{192}	295.938±.009	d	
Ir^{192}	308.429±.010	d	
Ir^{192}	316.486±.010	d	
			349.557±.03
Au^{198}	411.795±.009	e	
			549.834±.04
			579.801±.05
Tl^{208}(ThC'')	583.139±.023	f	
Cs^{137}	661.61 ±.04	(f,g)	
			703.402±.06
Co^{56}	846.78 ±.06	(g,k,l)	
Y^{88}	898.03 ±.04	(g,h,i,j)	
			910.823±.07
			987.545±.06
Co^{60}	1173.23 ±0.4	f	
			1189.962±.08
Co^{56}	1238.30 ±.05	(g,k,l)	
Na^{22}	1274.55 ±.04	(h,i,j,m)	
Co^{60}	1332.50 ±.03	g	
			1351.56 ±.22
Co^{56}	1360.25 ±.05	(g,k,l)	
			1614.515±.16
Y^{88}	1836.13 ±.04	(g,h,i,j)	
			1861.908±.12
			1903.455±.10
Co^{56}	2015.37 ±.06	(g,k,l)	
Co^{56}	2034.93 ±.06	(g,k,l)	
			2565.192±.12
Co^{56}	2598.58 ±.06	(g,k,l)	
			2606.754±.14
Tl^{208}(Thc'')	2614.47 ±.10	f	

† A composite peak of 260.56 and 262.89 or of 282.26 and 284.22.

* ( ) Corresponds to the average of the values reported in references.

a. Average of U. Gruber, R. Koch, B. P. Maier, and O. W. B. Schult, Z. Naturforsch. 20a, 929 (1965).

b. E. J. Seppi, H. Henrikson, F. Boehm and J. W. M. Dumond, Nucl. Instr. Methods 16, 17 (1962).

c. J. B. Marion, Gamma-Ray Calibration Standards, Univ. of Maryland Tech. Report 653 (1957).

d. J. B. Marion, Gamma-Ray Calibration Energies, Univ. of Maryland Tech. Report 656 (1968).

e. G. Murray, R. T. Graham, and J. S. Geiger, Nucl. Phys. 45, 177 (1963).

f. G. Murray, R. T. Graham, and J. S. Geiger, Nucl. Phys. 63, 353 (1965).

g. R. Gunnink, R. A. Meyer, J. B. Niday and R. P. Anderson, Nucl. Instr. Methods 65, 26 (1968).

h. W. W. Black and R. L. Heath, Nucl. Phys. A90, 650 (1967).

i. A. V. Ramayya, J. H. Hamilton, S. M. Brahmavar and J. J. Pinajian, Physics Letters 24B, 49 (1967).

j. J. Legrand, J. P. Boulanger and J. P. Brethon, Nucl. Phys. A107, 177 (1968).

k. M. E. Phelps, D. G. Sarantites and W. G. Winn, Nucl. Phys. to be published.

l. R. A. Meyer and D. Camp, private communication, Lawrence Radiation Laboratory, Livermore, California (1970).

m. D. H. White and D. J. Groves, Nucl. Phys. A91, 453 (1967).

Initially this stripping was done by hand using composites of known singlet peaks lying close to the peaks in question. More recently this stripping has been computer assisted [RoJ69], fitting with Gaussin peaks with exponential tails generated by characterizing near by singlet peaks.

Gamma intensities were determined using experimentally determined efficiency curves for each detector. The efficiency curves were determined using sources that emit several γ rays whose relative intensities have been well established. The points so obtained were then fitted to an equation of the form, log (efficiency) = $A + B\log E + C(\log E)^2 + D(\log E)^3$, where A, B, C, and D are empirical constants and E is the energy in keV [DoR70]

Energy and intensity results as well as a survey of the results reported by other investigators are listed in Table II. Uncertainties listed for the γ energies are based on the uncertainties in the primary and secondary energy standards, the heights of the peaks above backgrounds, in some instances the necessity of peak stripping, and the reproducibility of the calculated energies from many spectra. In general these reported uncertainties are quite generous. Uncertainties listed for our γ intensities are the larger of either 10% of intensity or the maximum deviation of measurement; for particularly weak peaks or peaks that have been stripped, considerably larger uncertainties are listed and represent our confidence in the data.

Several of the γ's require additional comment in that the centroids of several multiplet peaks were too close to be stripped accurately. Energies for the 1001.6-, 1001.8, 1003.1-keV triplet and the 1013.7-, 1014.4-keV doublet were determined from their positions in the decay scheme. Their intensities were determined using a combination of first estimating the relative contributions necessary to reproduce the energy of the multiplet,

TABLE II

Comparative Gamma Energies and Intensities

Gamma Energy			Gamma Intensity		
This work[a]	Ref RuT71	Ref.VeS63[b]	This work[c]	Ref.RuT71	RefVeS63
2.328±.007[h]					
		26.22±.01			
		45.43±.08			
		90.03±.02			
115.18±.05	115.16±.13	115.14±.03	0.24±.03	0.23±.04	
[122.9][d]	(122.47±.08)[e]	122.86±.11	0.02±.01	0.05±.01	
[128.7]	(129.74±.13)	128.69±.19	0.03±.01	0.03±.01	
[147.8]	(147.32±.09)		0.01±.01	0.08±.01	
[149.6]	(149.51±.24)		0.01±.01	0.02±.01	
[154.6]	(157.27±.22)	157.28±.03[f]	0.01±.01	0.04±.01	
[164.8]	(165.11±.20)		0.03±.01	0.05±.02	
185.11±.15	185.27±.12	185.09±.04	0.29±.03	0.28±.05	~.7
205.85±.20	205.84±.27	205.79±.04	0.09±.02	0.10±.02	
221.17±.20	221.02±.13	221.16±.05	0.08±.02	0.09±.02	
236.07±.10	236.00±.05	236.02±.03	0.18±.05	0.17±.05	
		237.16±.05	< 0.03		
		248.91±.28	< 0.02		
260.56±.04	260.51±.05	260.53±.03	3.41±.55	3.10±.46	5.7±1.5
262.89±.08	262.82±.07	262.86±.03	1.16±.12	1.19±.21	
282.26±.08	282.26±.10	282.30±.03	1.34±.35	1.15±.12	6.0±1.0
284.22±.04	284.12±.10	284.23±.03	4.94±.55	4.80±.15	
[296.4]		297.17±.32	0.02±.01		
310.37±.10	310.37±.07	310.43±.03	0.26±.08[g]	0.27±.05	
313.06±.15	313.05±.09	313.00±.06	0.18±.05[g]	0.18±.03	
[313.6][g]			------- [g]		
349.56±.03	349.55±.05	349.63±.04	1.55±.16	1.48±.17	2.7±0.7
	354.60±.06		<0.05	0.08±.01	
361.50±.08	361.60±.11	361.56±.05	0.16±.03	0.18±.04	
		421.83±.06	< 0.05		.35±0.2
[476.4][g]			< 0.05		
[488.2]	(488.35±.18)		0.08±.05	0.19±.06	
493.65±.08	493.70±.04	493.83±.05	1.12±.11	0.98±.14	3.5±1.
498.64±.10	(498.84±.15)	498.82±.08	0.53±.10	0.55±.13	
511.39±.18	511.43±.07	511.70±.05	3.30±.33	3.24±.34	6.3±1.5
549.83±.04	549.86±.03	550.09±.09	8.78±.87	8.88±.92	
[553.6]	(553.72±.28)		0.6±0.3	0.39±.11	
561.64±.12	(561.26±.20)	561.74±.19	0.12±.03	0.20±.06	
570.93±.08	570.58±.04	570.73±.05	12.92±1.3	13.2±1.5	39.0±5.
574.01±.18	573.87±.04	574.09±.08	1.87±.25	1.73±.37	
576.37±.18	576.21±.15	576.29±.17	0.73±.20	1.08±.13	
579.80±.05	579.78±.03	580.02±.05	16.67±1.7	16.78±1.7	

609.0[g]	(609.78±.20)				
626.71±.08	626.72±.04	626.96±.09	0.11±.05	0.36±.09	
		634.39±.22	1.81±.18	1.78±.20	6.0±8.
645.76±.10	646.07±.07		<0.1		
661.30±.15[g]			0.25±.04	0.20±.04	
688.53±.10	688.60±.11	688.71±.10	0.10±.05		
703.40±.06	703.40±.04	703.36±.04	0.64±.06	0.63±.09	
		710.76±.06	≡100.00	≡100.00	≡100.00
[712.7]		712.65±.49	<0.5		
717.41±.10	717.35±.11	717.49±.12	0.09±.05		
720.55±.15	720.75±.23	720.53±.16	0.91±.15	0.77±.17	
723.55±.12	723.67±.12	723.50±.18	0.33±.10	0.37±.10	
729.46±.15	729.68±.23	729.46±.14	0.52±.10	0.53±.11	
745.06±.12	744.88±.08	744.97±.13	0.17±.06	0.26±.19	
759.07±.12	759.12±.06	759.02±.07	2.03±.25	2.33±.28	13.0±3.
761.37±.12	761.47±.10	761.23±.09	3.81±.40	3.73±.42	
770.93±.15			2.21±.40	2.17±.32	
	772.10±.32		0.15±.03		
780.90±.15	780.84±.09	780.79±.08		0.11±.03	
787.89±.12	787.76±.13		1.77±.18	1.56±.31	
795.59±.10	795.69±.08	795.59±.08	0.32±.10	0.36±.06	
800.81±.15	(800.92±.14)		0.36±.05	0.43±.14	
806.92±.12	806.43±.05	806.12±.20	0.62±.10	0.42±.08	
813.84±.10	813.81±.06	813.78±.09	0.55±.10	0.53±.16	
828.19±.12	828.21±.13	828.10±.10	1.52±.15	1.49±.25	
[831.1]			0.98±.15	0.96±.14	
847.57±.20			0.12±.05		
852.78±.15	852.78±.26		0.04±.02		
860.10±.10	860.10±.10	859.93±.14	0.16±.05	0.23±.05	
871.78±.10	871.86±.10	871.96±.06	1.40±.15	1.40±.31	5.5±2.
[874.4]			1.30±.13	1.32±.19	
890.04±.10	890.09±.04	889.95±.05	0.07±.04		
894.50±.10	894.65±.04	894.88±.08	2.22±.22	2.06±.24	
901.84±.12	901.78±.15		1.79±.18	2.70±.35	
910.82±.07	910.84±.05	910.93±.08	0.45±.05	0.42±.08	
		913.36±.61	5.47±.55	5.25±.57	10.6±2.
921.74±.15	(922.03±.17)		< .25		
931.67±.15	931.25±.69		0.19±.03	0.20±.04	
950.70±.10	950.76±.08		0.15±.04	0.18±.02	
971.35±.10	971.49±.15	971.90±.07	1.21±.12	1.28±.15	
978.03±.12	978.51±.35		0.90±.09	0.91±.19	
987.54±.06	987.56±.04	987.75±.07	0.23±.06	0.12±.03	
1001.6[g]			54.61±5.5	53.35±5.5	63. ±3.
1001.8[g]	1001.90±.05	1002.36±.09	0.83±.20[g]		
1003.1[g]			0.70±.25[g]	1.79±.26	
1013.7[g]		1013.8	0.50±.15[g]		
1014.4[g]	1014.22±.07	1014.25±.09	0.23±.20		
			3.31±.50	3.10 .42	

1031.18±.25	(1031.72±.28)		0.16±.04	0.13±.03	
1037.4 ±.5			0.49±.20		
1040.1 ±.5			0.97±.30		
1043.68±.08	1043.66±.06	1043.69±.07	25.30±2.5	23.87±2.7	28.0±5.
		1048.24±.20	<0.5		
	(1051.61±.75)		<0.3	0.15±.02	
1060.65±.25		1062.71±.11	0.24±.03		
1065.81±.25	1065.95±.11		0.34±.04	0.34±.05	
1072.30±.10	1072.21±.09	1072.35±.05	1.00±.10	1.00±.16	
1107.50±.20	1107.54±.11		0.33±.03	0.37±.09	
		1128.08±.08	<.15		
1189.96±.08	1189.94±.05	1190.00±.10	7.97±.79	7.34±.81	7.8±1.5
1199.76±.12	1199.81±.21	1199.76±.09	0.65±.06	0.63±.17	
1208.66±.10	1208.57±.08	1208.32±.40	1.82±.18	1.65±.21	
1216.34±.20	(1216.29±.28)		0.29±.04	0.23±.05	
1264.51±.25	1264.42±.31	1264.74±.16	0.86±.09	0.84±.13	
1275.96±.25			0.18±.04		
1283.68±.25			0.12±.05		
1351.56±.22	1351.47±.11	1351.73±.10	3.50±.35	3.52±.52	≈3.
1439.27±.25	(1438.61±.24)		0.44±.10	0.34±.07	
1499.71±.40			0.56±.14		
1501.79±.35	1500.22±.61	1499.96±.40	0.75±.20	0.95±.35	
1521.60±.25	1522.12±1.1		0.73±.07	0.64±.16	4.5±1.
1549.60±.35			1.05±.11		
1551.71±.25	1550.81±.24	1552.18±.10	3.02±.30	2.54±.70	
1563.29±.25	1563.11±.14		0.72±.12	0.73±.16	
1577.35±.25	1577.40±.28		0.50±.05	0.51±.19	
1592.9±1.0	1594.47±2.0		0.41±.10	0.33±.16	
1614.52±.16	1614.34±.06	1615.41±.07	7.92±.79	6.36±.77	7.5±2.
1619.38±.20	1619.06±.21		1.05±.11	0.76±.10	
[1633.5][g]			<0.10		
		1721.00±.40	<0.20		
1764.46±.16	1764.27±.08	1766.14±.09	121.2±12.	93.05±10.	
		1768.94±.40	<10.		115.±10
1775.96±.16	1775.80±.06	1777.67±.16	14.24±1.4	11.09±1.3	
1818.22±.20	1818.27±.40		0.20±.02	0.17±.04	
	1844.76±.40		<.05	0.07±.01	
1861.91±.12	1861.69±.05	1863.91±.15	23.44±2.3	17.45±2.0	
1903.46±.10	1903.35±.07	1905.88±.29	9.30±.93	6.71±.75	36.5±5.
		1925.06±.40	<.02		
1966.01±.35	1965.95±.56		0.04±.01	0.05±.02	
2565.19±.12	2565.47±.85		0.18±.04	0.16±.06	
2606.75±.14	2606.78±.42		0.10±.02	0.07±.02	

[a] Uncertainties in energies were assigned on the basis of uncertainties in measuring ^{205}Bi secondary standard peaks (see Table I) with consideration to the complexity of the spectral region and intensity of the peak being looked at, and in general are quite generous.

[b] Ref. VeS63 - these are electron energies.

[c] Uncertainty in intensities are the larger of either 10% of intensity or maximum deviation of measurement; for particularly weak peaks or peaks in a complex spectral region considerably larger uncertainties are used and represent the confidence we have in the data.

[d] [ ] represents possible ^{205}Bi transitions included for completeness of table.

[e] ( ) represents peaks seen only once in ref. VeS63.

[f] Listed with unassigned possible ^{205}Bi transitions in ref. VeS63.

[g] See text for explanation.

[h] See section III.E. of this report.

then comparing this proposed multiplet shape with the experimental shape. On the basis of the coincidence and sum-coincidence (see Section III.B.) study of the multiplet at ~311 keV it has not been possible to determine conclusively whether it is a doublet or a triplet containing an additional weak transition at 313.6 keV. It has been reported as a 310.37-, 313.06-keV doublet; if it is indeed a triplet there would need to be a slight change in the reported energy and intensity for the 313.06-keV transition. The energy of the 609.0-keV transition could not be determined accurately because of an interfering lab background; however, coincidence work definitely confirm its belonging to the decay of ^{205}Bi. Similarly, the 661.30-keV transition, initially thought to be ^{137}Cs in the lab background, has been shown to be a transition from ^{205}Bi by coincidence studies. The 476.4- and 1633.5-keV transitions were identified only from coincidence work and only possible maxima for the intensities are reported.

B. Coincidence Spectra

In that the more prominent γ's have already been rather definitely assigned by previous investigators, this investigation of ^{205}Bi did not begin with anti- and integral coincidence experiments in an attempt to identify transitions to the ground state. However, we do include our results for these experiments at the end of this section as a confirmation for some of the assignments in our proposed decay scheme.

The primary thrust of our coincidence study has been the collecting of two sets of "megachannel" Ge(Li)-Ge(Li) [DoR68] coincidence data. With the megachannel system 4096-channel X 4096-channel 2-dimensional coincidence spectra were recorded by computer on magnetic tape as individual coincidence events. The run collecting the most coincidence events (>3.5 million events collected over a period of three days) with the best resolution was made using the 3.6% and 2.5% detectors placed ≈75° to each other. A graded lead absorber was placed between the detectors to prevent Compton cross-talk between the detectors. The source material was placed off the end of the absorber in such a way that the count rates of the two detectors were equal. The resolving time was 50 nsec.

Subsequent to collecting the coincidence events, the tapes were played back having set groups of gates to be scanned on each pass. In addition to generating spectra by setting gates on peaks, backgrounds adjacent to peaks and normalized peak to background difference spectra could be generated. Accordingly, by using these three different types of coincidence spectra it was readily possible to make coincidence assignments. Further in that the coincidence information was easily retrieved numerous gates could be set on different portions of multiplet peaks to establish specific coincidences. More than 300 different gates were set on 95 areas of

interest. These areas are indicated in Figure 2 of the x and y integral coincidence displays. The areas are identified by their approximate energy (usually the energy of a transition) and a code to indicate which of the three types of spectra were generated. However, the number of each type generated with slightly different parameters is not indicated. A rather complete collection of the spectra generated are shown in Figure 3 and are discussed in Sections IV and V. A summary of the coincidence data is listed in Table III.

As a bonus from having our coincidence experiments recorded on magnetic tape as individual event pairs we were able to use a sum-coincidence technique[GeG71] to help resolve some remaining ambiguities and add confirmation of some aspects of the proposed decay scheme. These sum coincidence spectra were generated by having the computer add the addresses of the event pair (with the requirement that either $y>x$ or $x>y$, this being necessary because the gains of the detector systems were not matched) then outputting only these events falling in sum gates previously set. The any-sum spectrum for $y>x$ and some of the more interesting gated sum spectra are shown in Figure 4. Before discussing the application of these spectra to determine our decay scheme in Section IV there are a couple of things to be noted about them. First, it is possible to create false peaks generated from the underlying Compton background, but these are distinguishable from true sum peaks by their broadness and generally poor shapes. The width of these false peaks is a function of the width of the gate set in the sum-coincidence spectrum. Secondly, even though few distinct peaks are evident in the any-sum spectrum, quite interesting sum spectra can be generated from gating on what is apparently only background.

The any coincidence results were obtained by analyzing the y-axis display

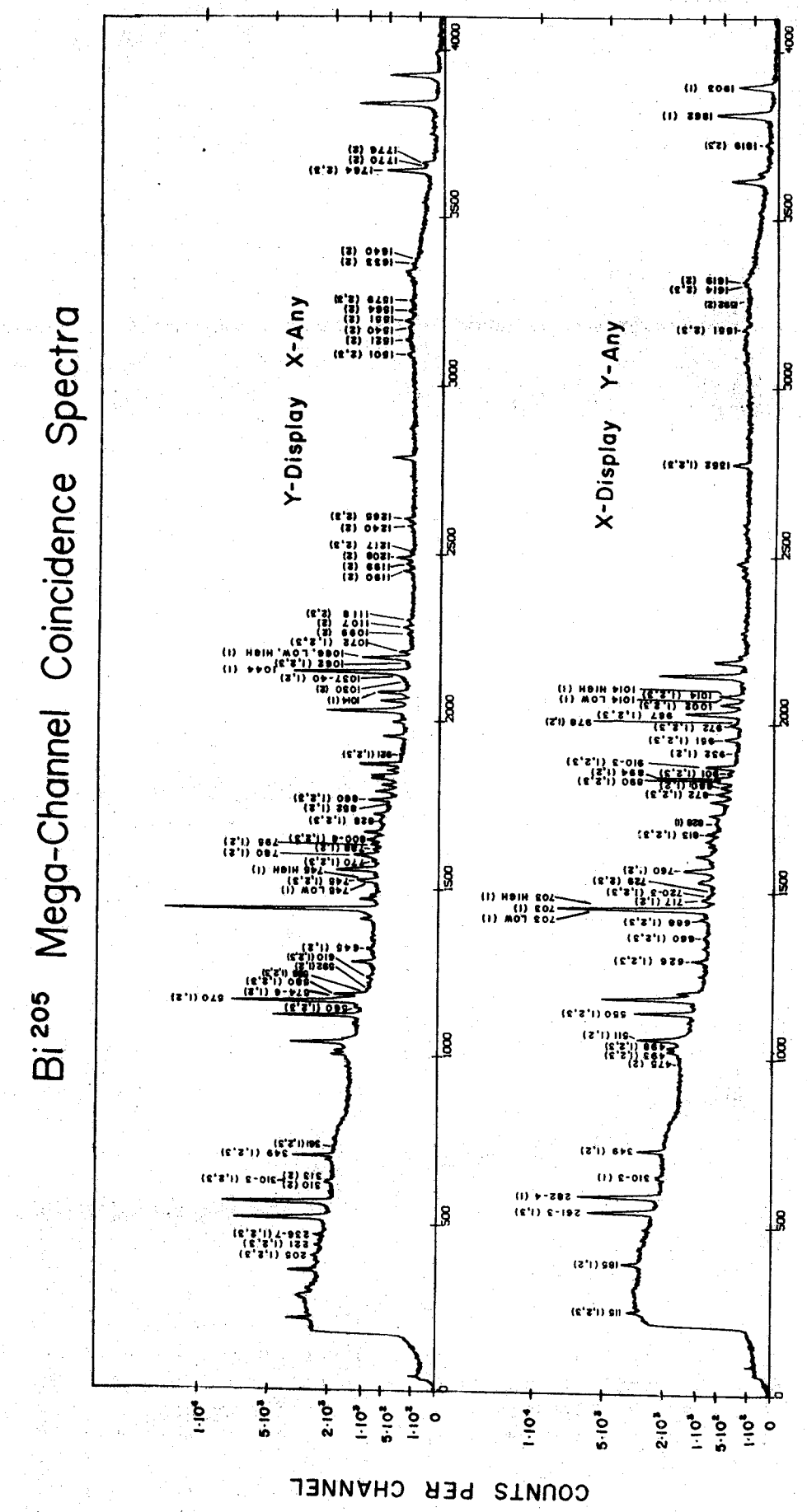

Figure 2. Gamma-gamma coincidence spectra showing x and y integral coincidence displays of the 2-dimensional data. Peaks labelled 1 correspond to gates set on peak and background. Peaks labelled 2 correspond to gates set on peak only. Peaks labelled 3 correspond to gates set on background only.

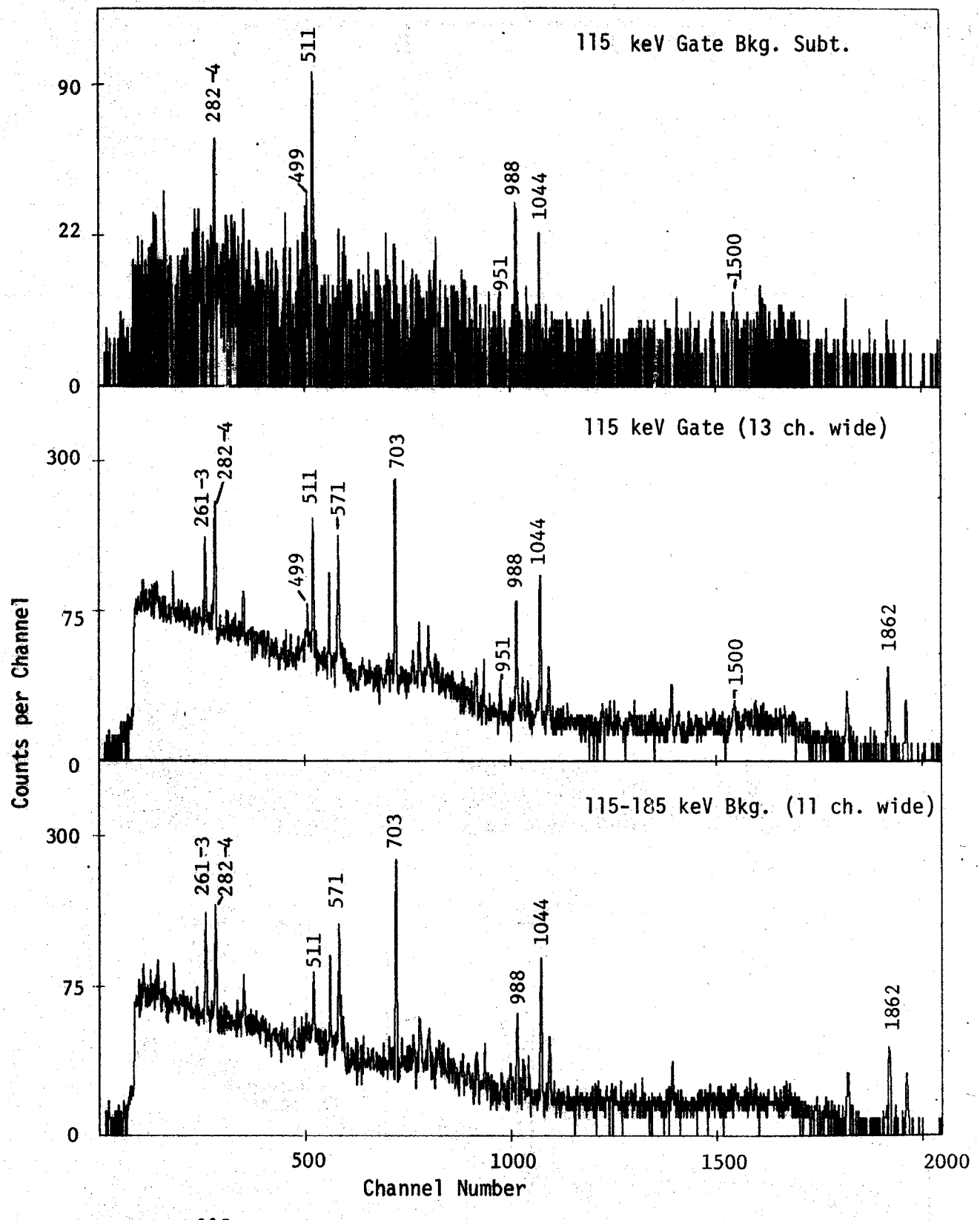

Figure 3. ^{205}Bi coincidence spectra resulting from gates set using mega-channel event recorded tapes using two Ge(Li) detectors with efficiencies of 3.6 and 2.5% relative to a 3×3 NaI(Tl) crystal. These are square root plots. A good compromise between logrithmic and linear displays of the data.

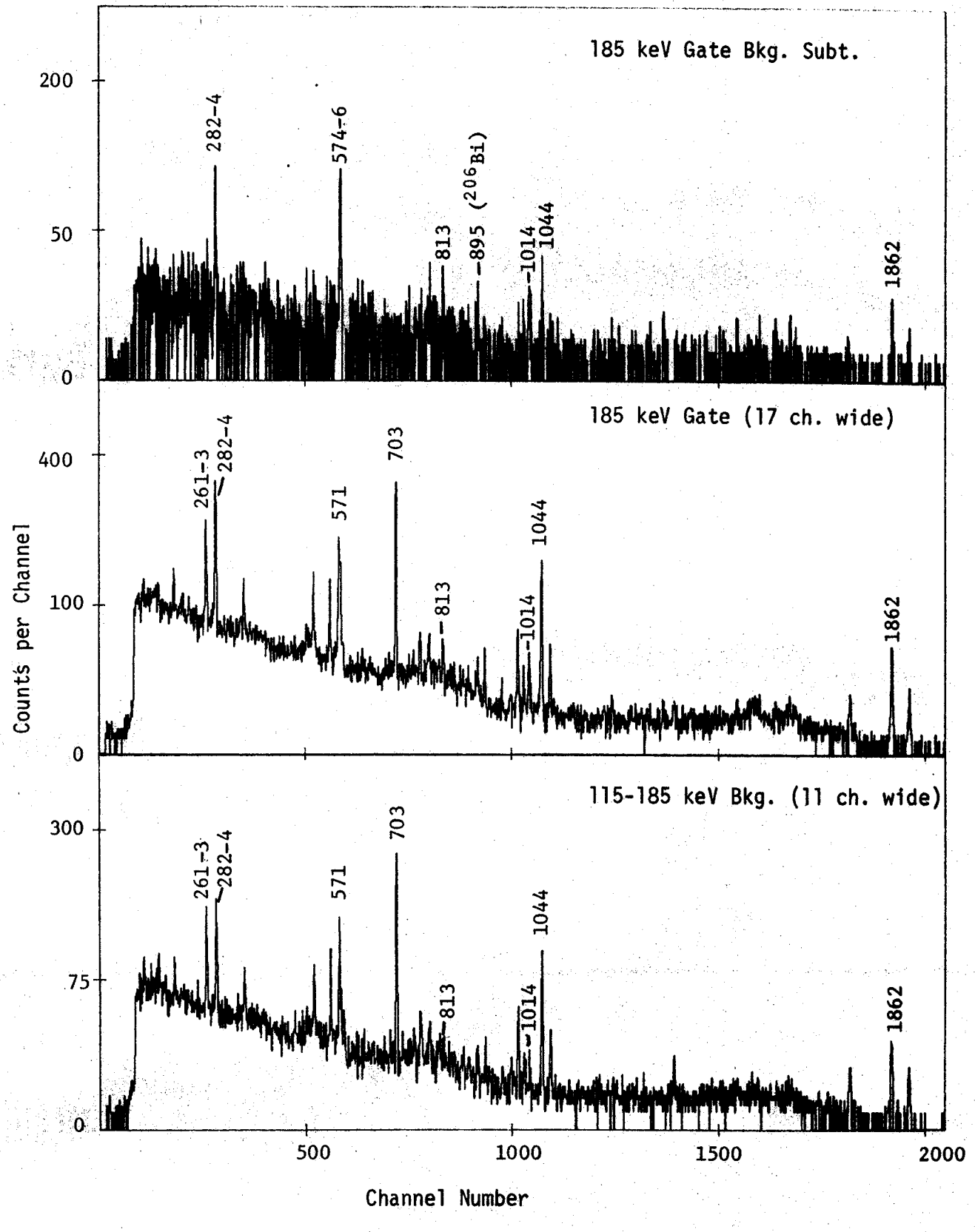

Figure 3. ^{205}Bi coincidence spectra continued.

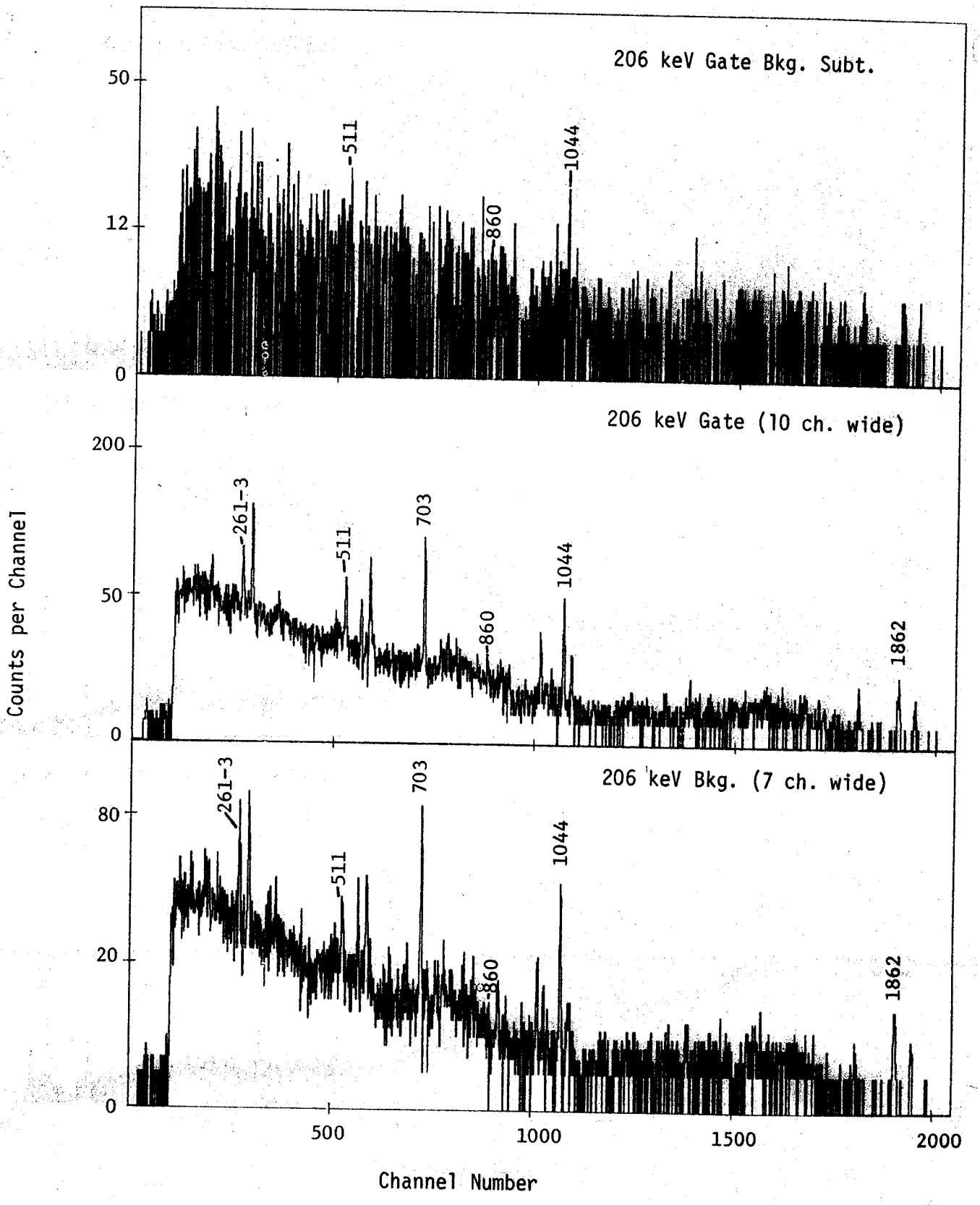

Figure 3. ^{205}Bi coincidence spectra continued.

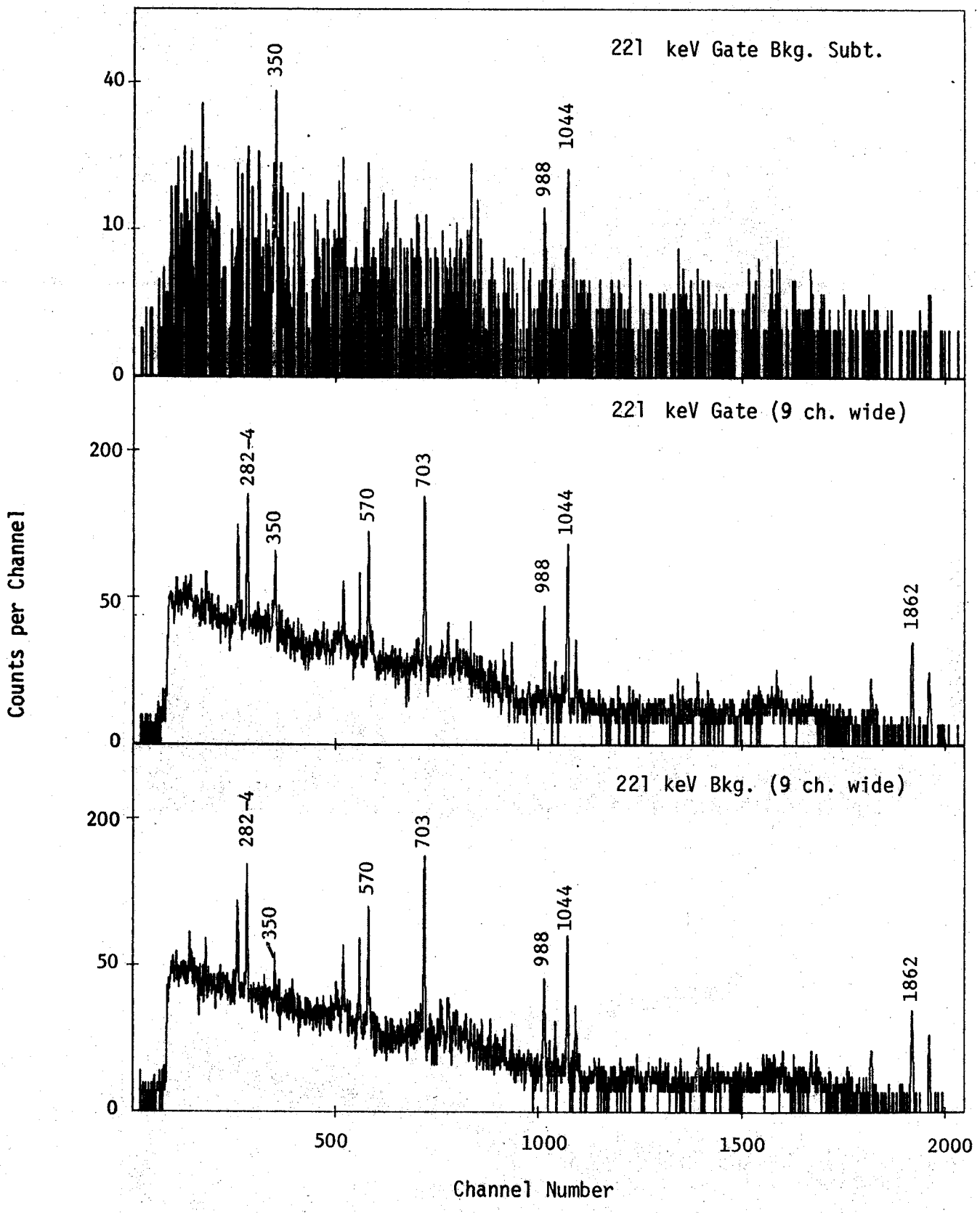

Figure 3. ^{205}Bi coincidence spectra continued.

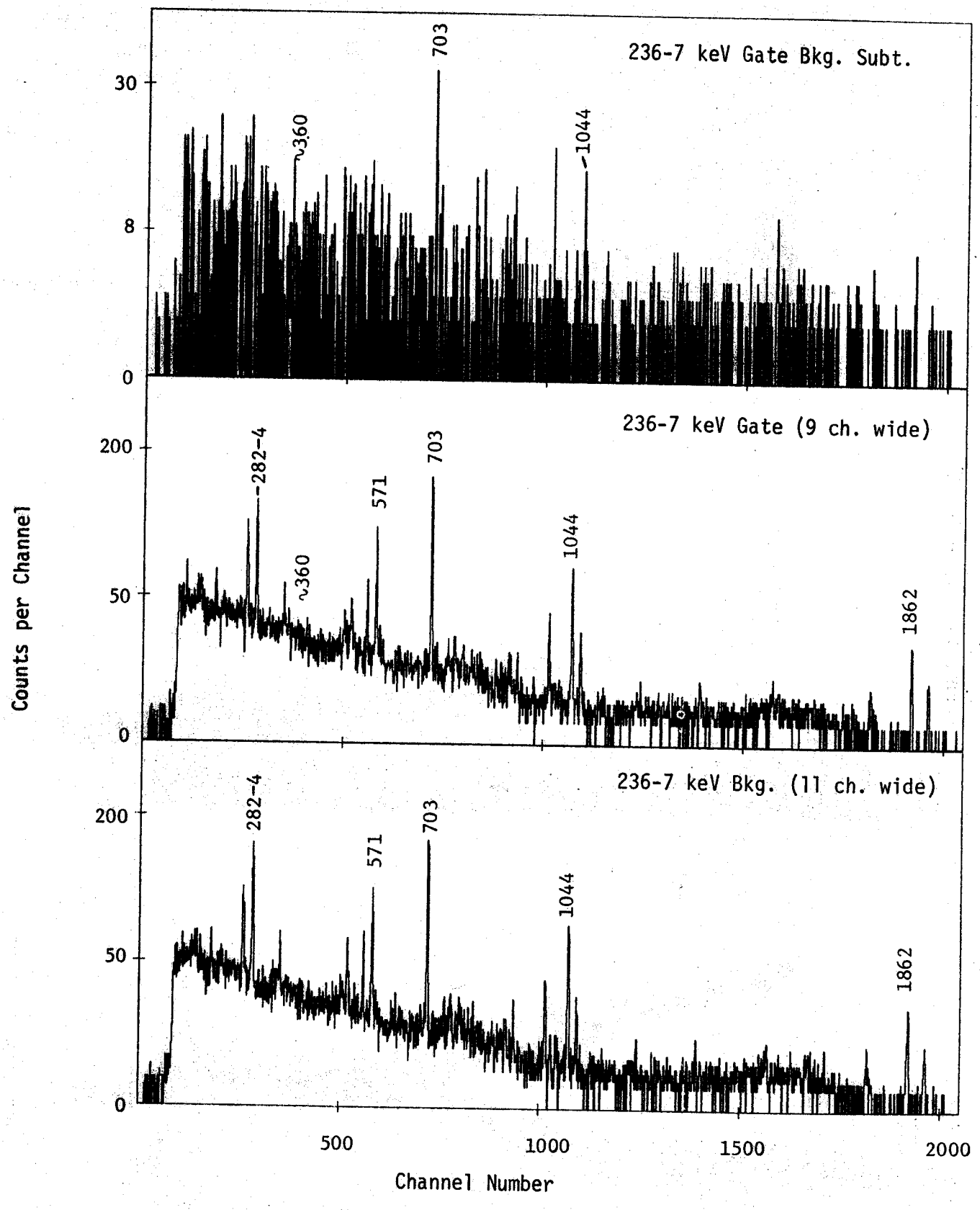

Figure 3. ^{205}Bi coincidence spectra continued.

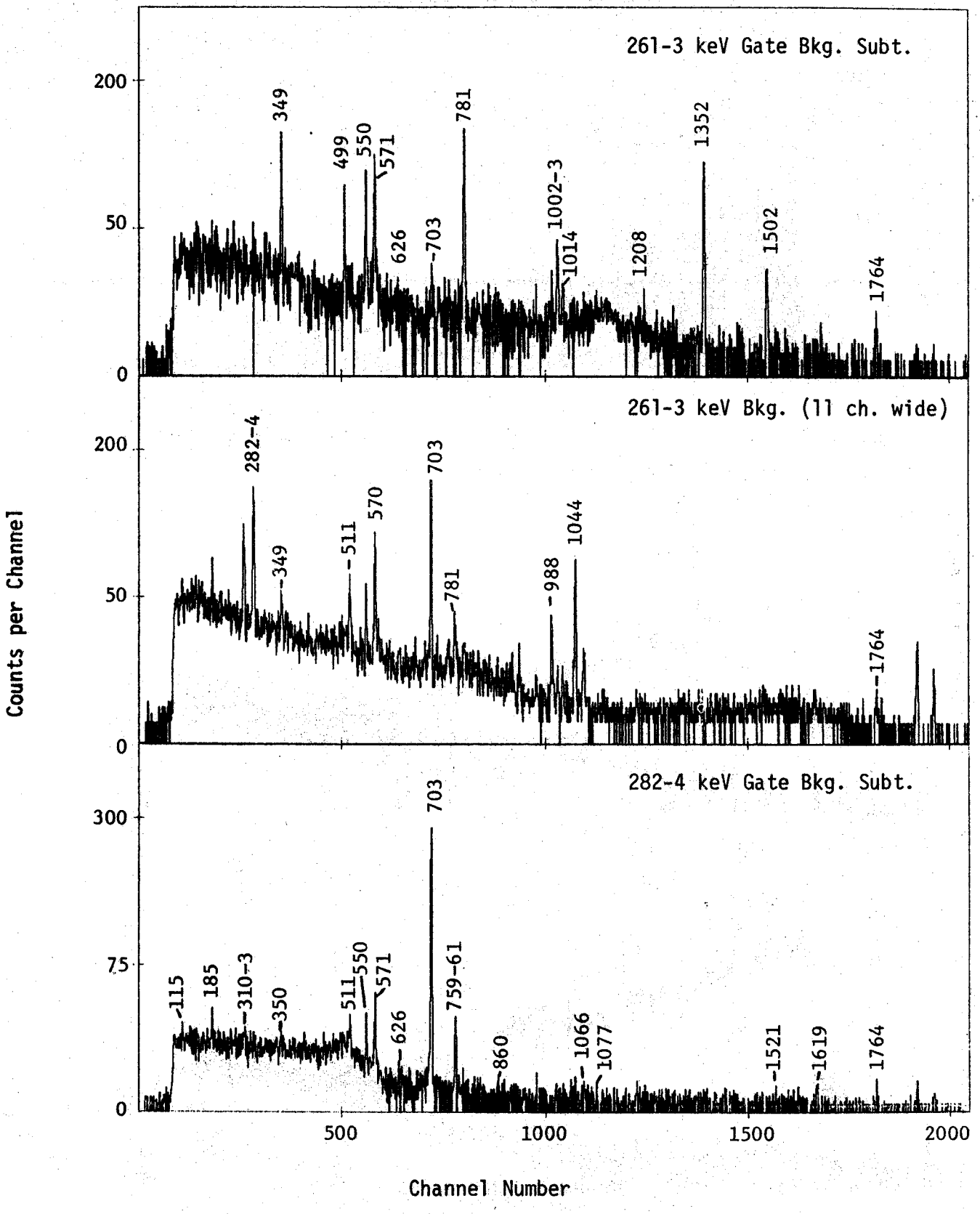

Figure 3. ^{205}Bi coincidence spectra continued.

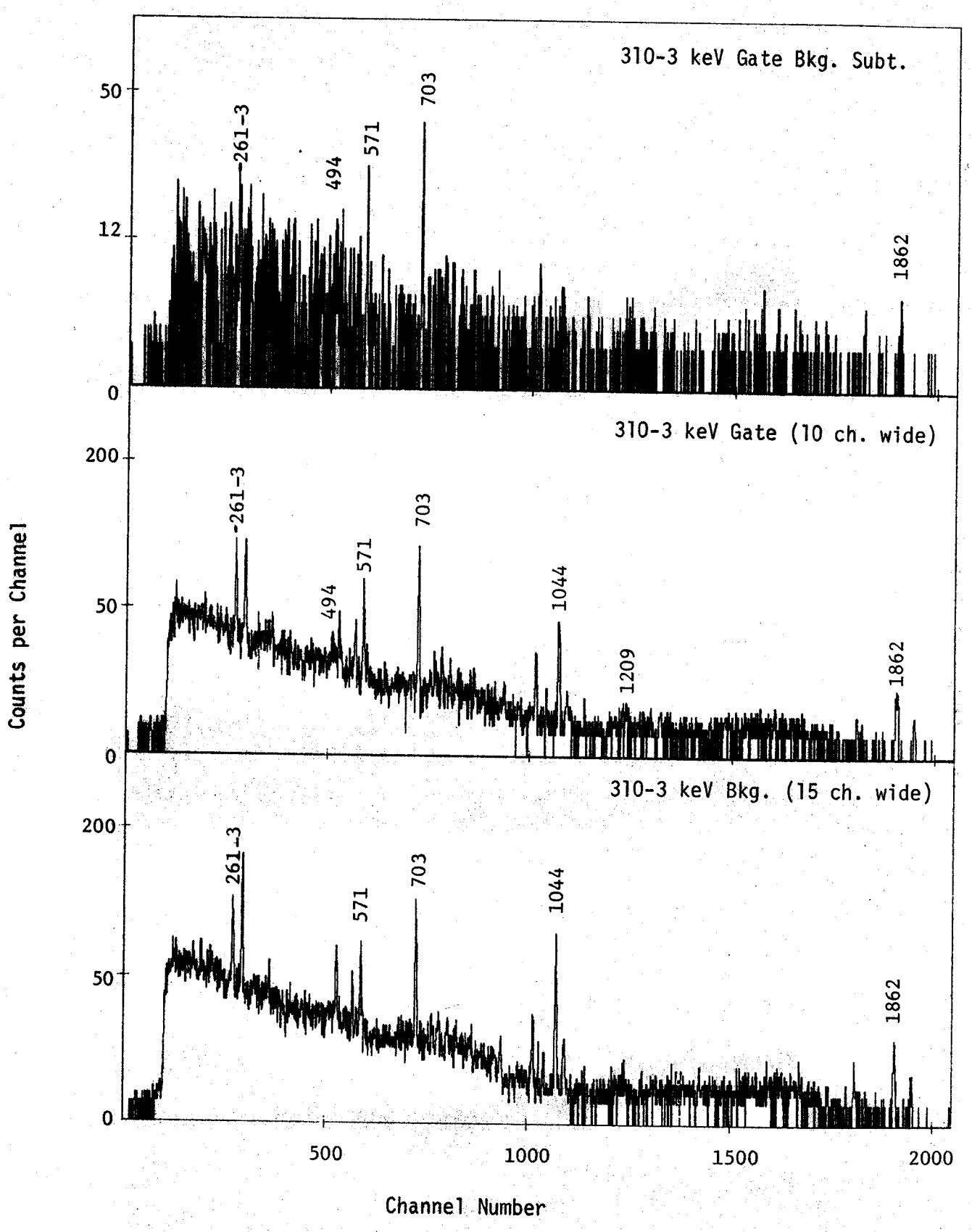

Figure 3. ^{205}Bi Coincidence Spectra continued.

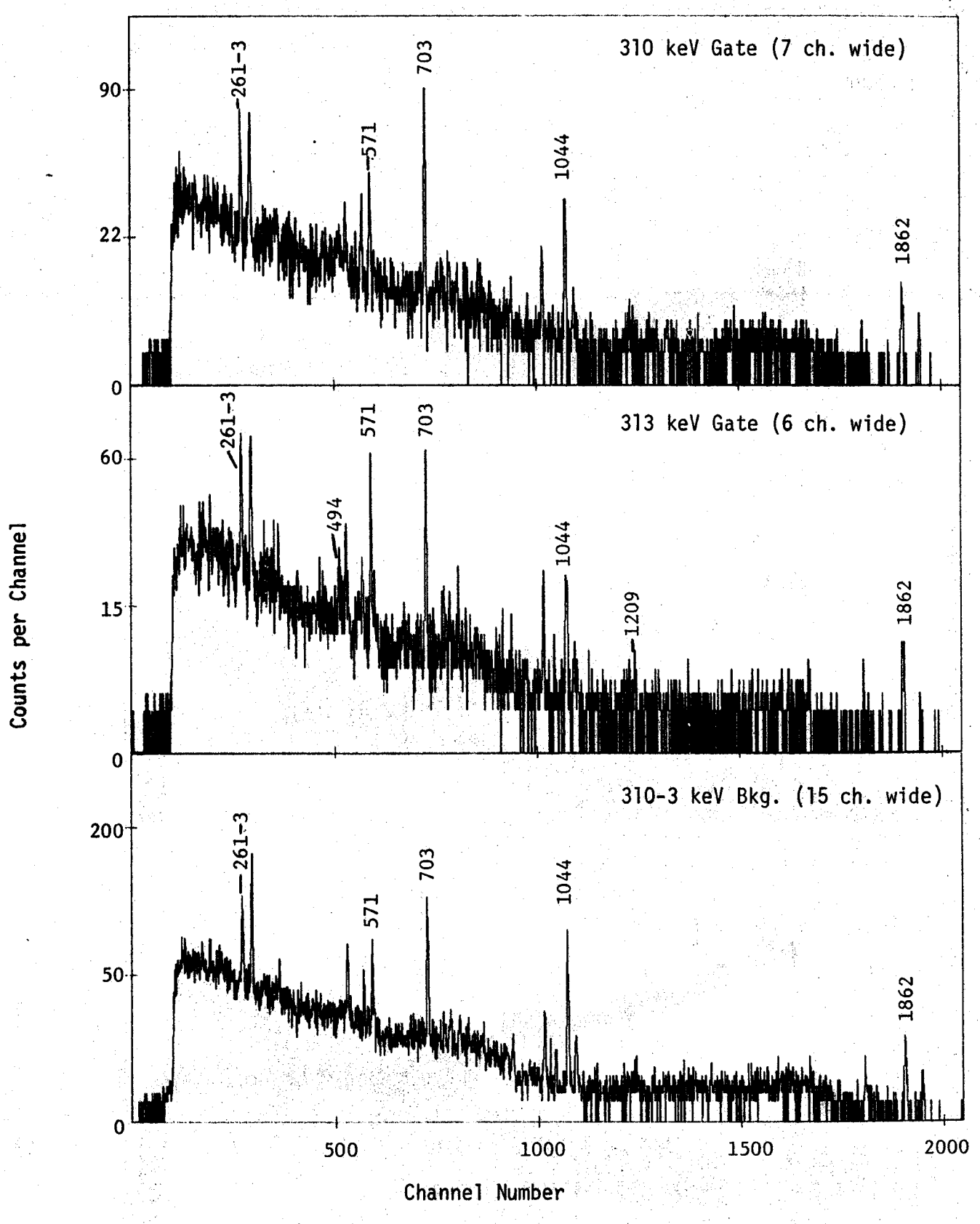

Figure 3. ^{205}Bi Coincidence spectra continued.

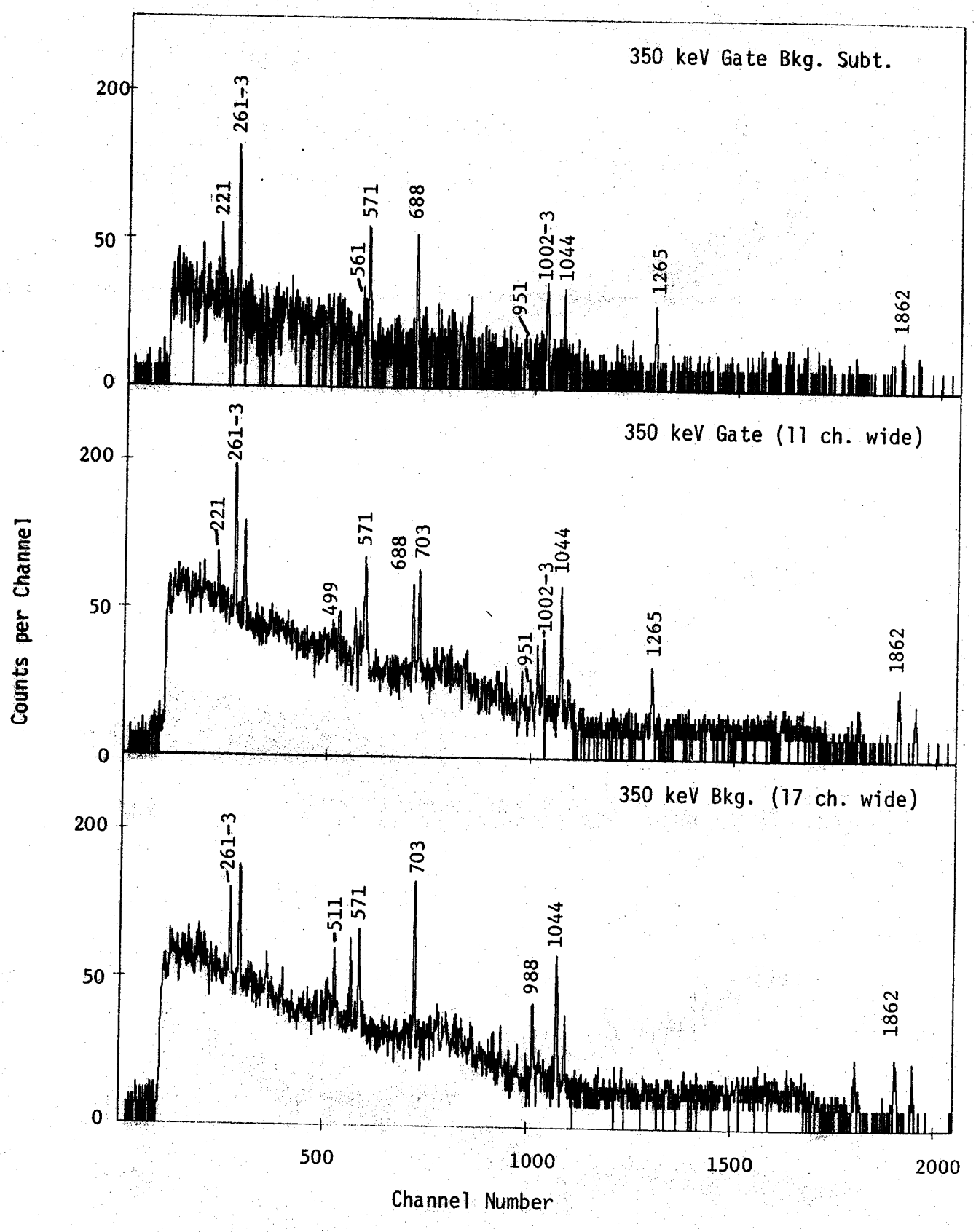

Figure 3. ^{205}Bi Coincidence spectra continued.

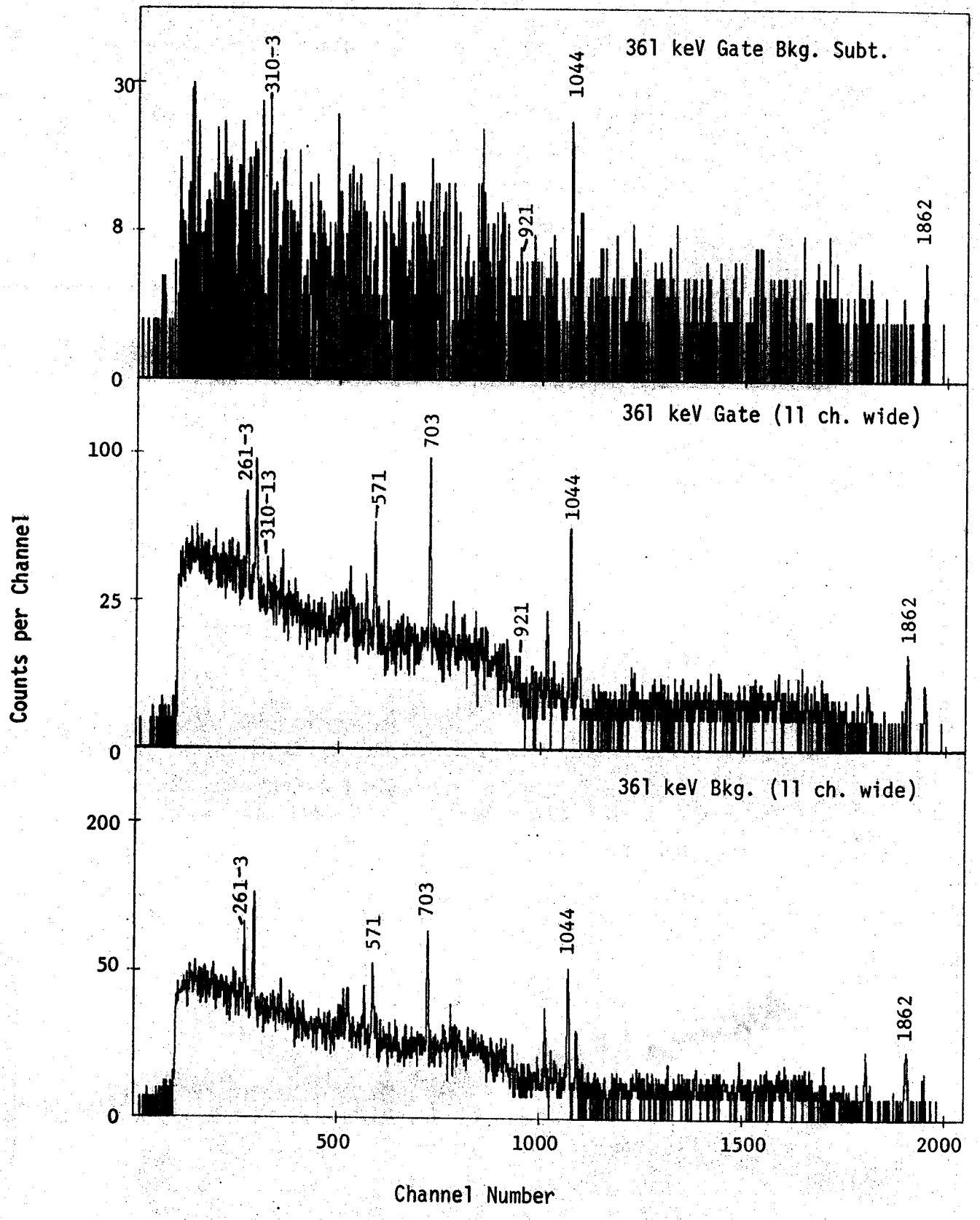

Figure 3. ^{205}Bi Coincidence spectra continued.

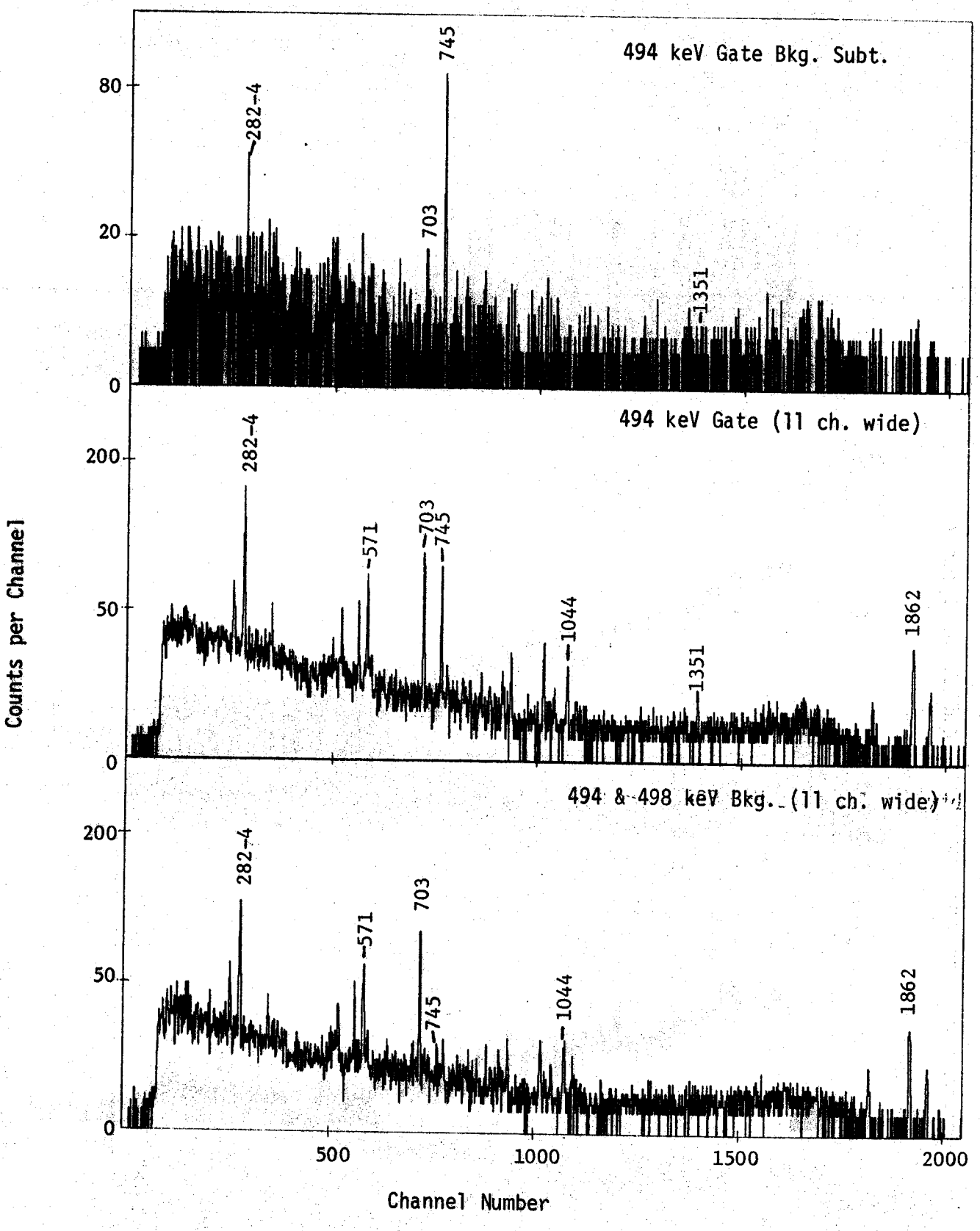

Figure 3. ^{205}Bi Coincidence spectra continued.

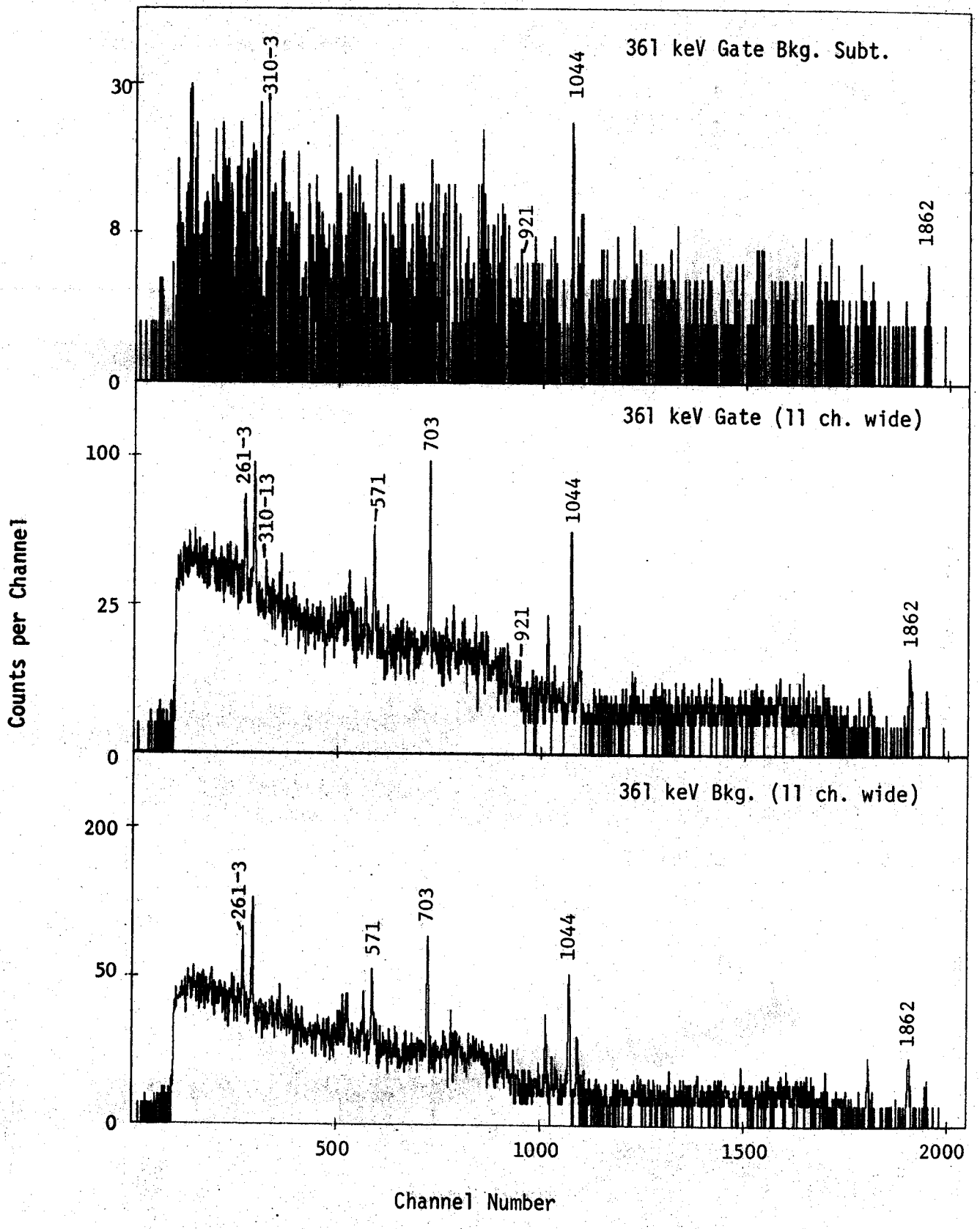

Figure 3. ^{205}Bi Coincidence spectra continued.

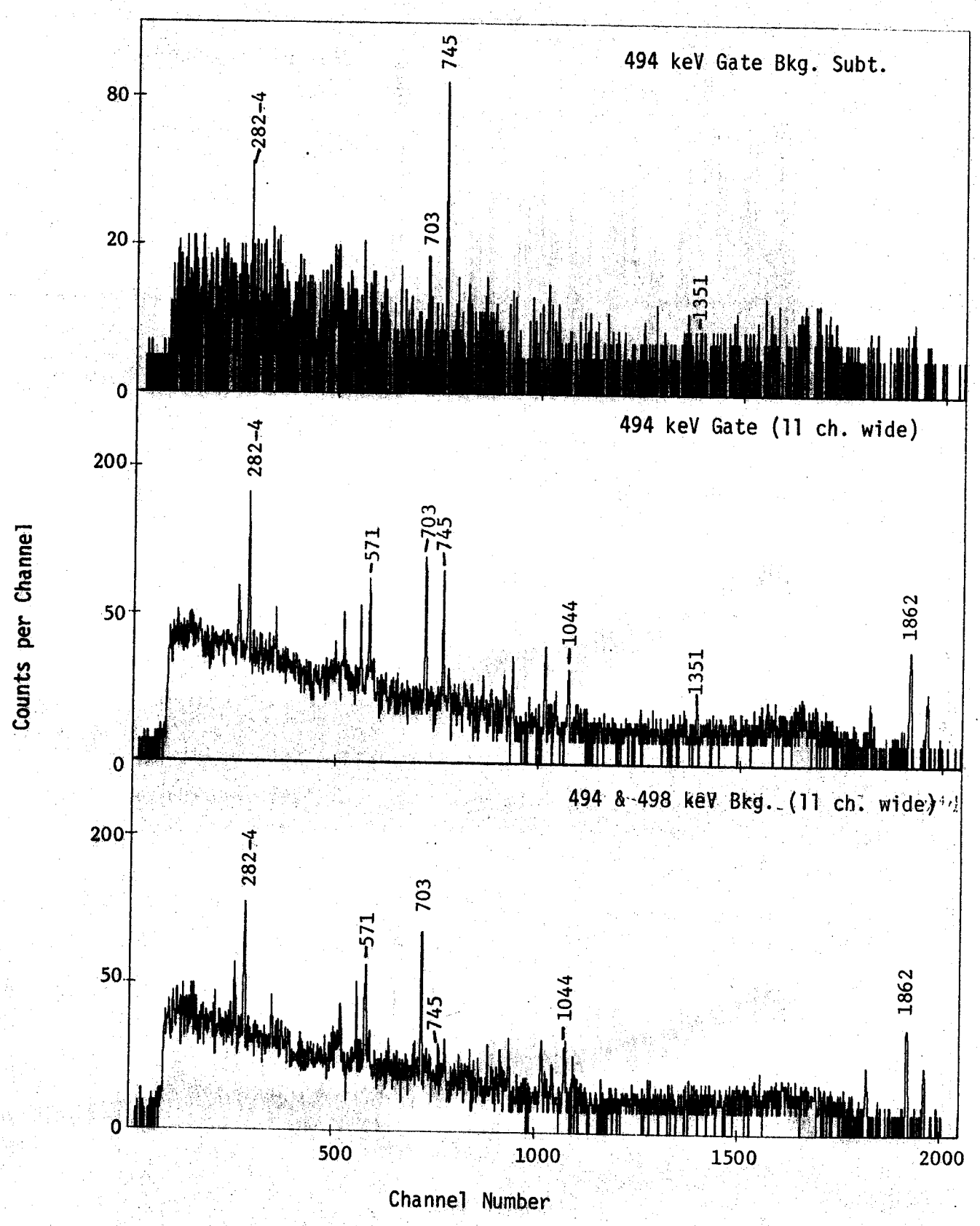

Figure 3. ^{205}Bi Coincidence spectra continued.

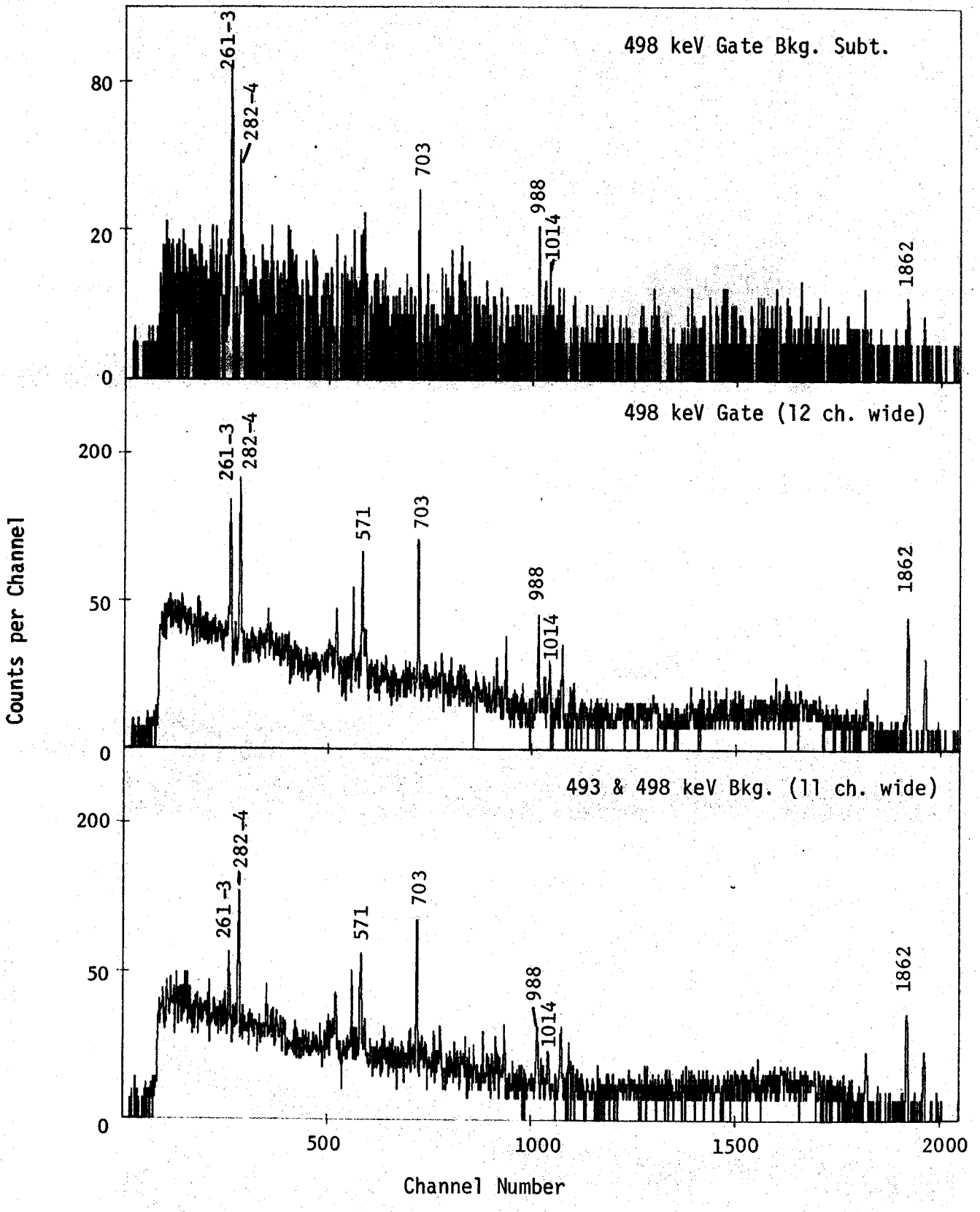

Figure 3. ^{205}Bi Coincidence spectra continued.

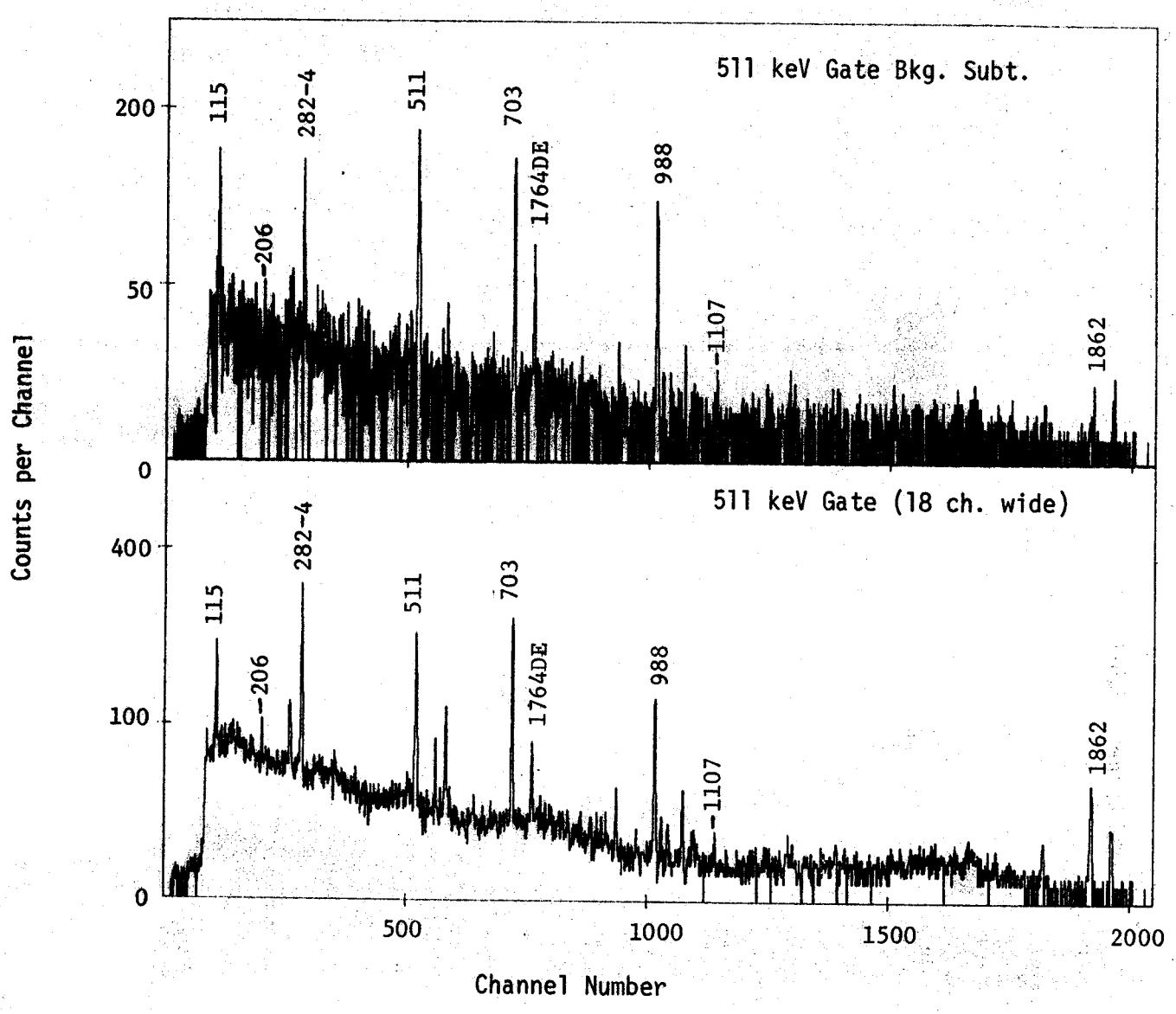

Figure 3. ^{205}Bi Coincidence spectra continued.

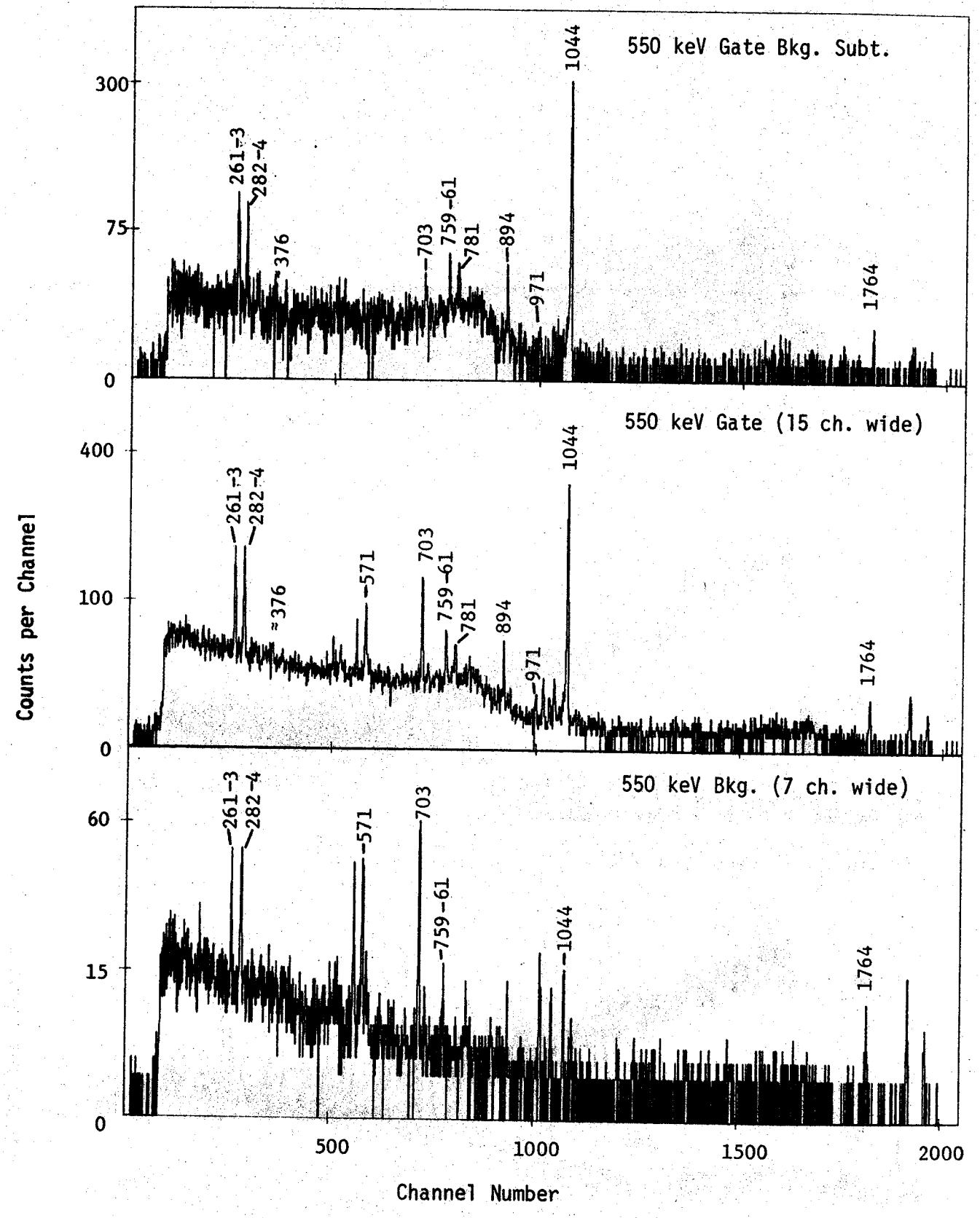

Figure 3. ^{205}Bi Coincidence spectra continued.

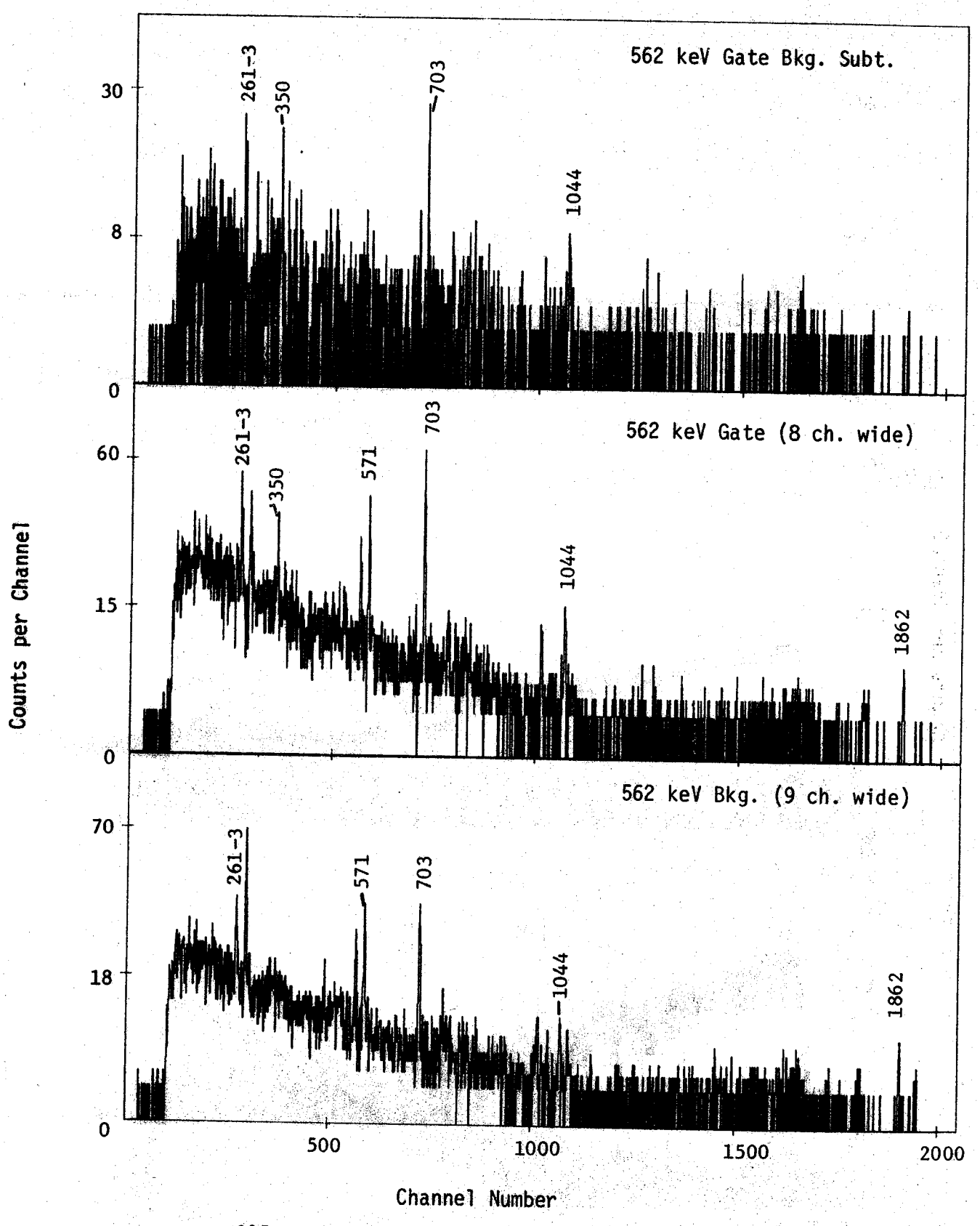

Figure 3. ^{205}Bi Coincidence spectra continued.

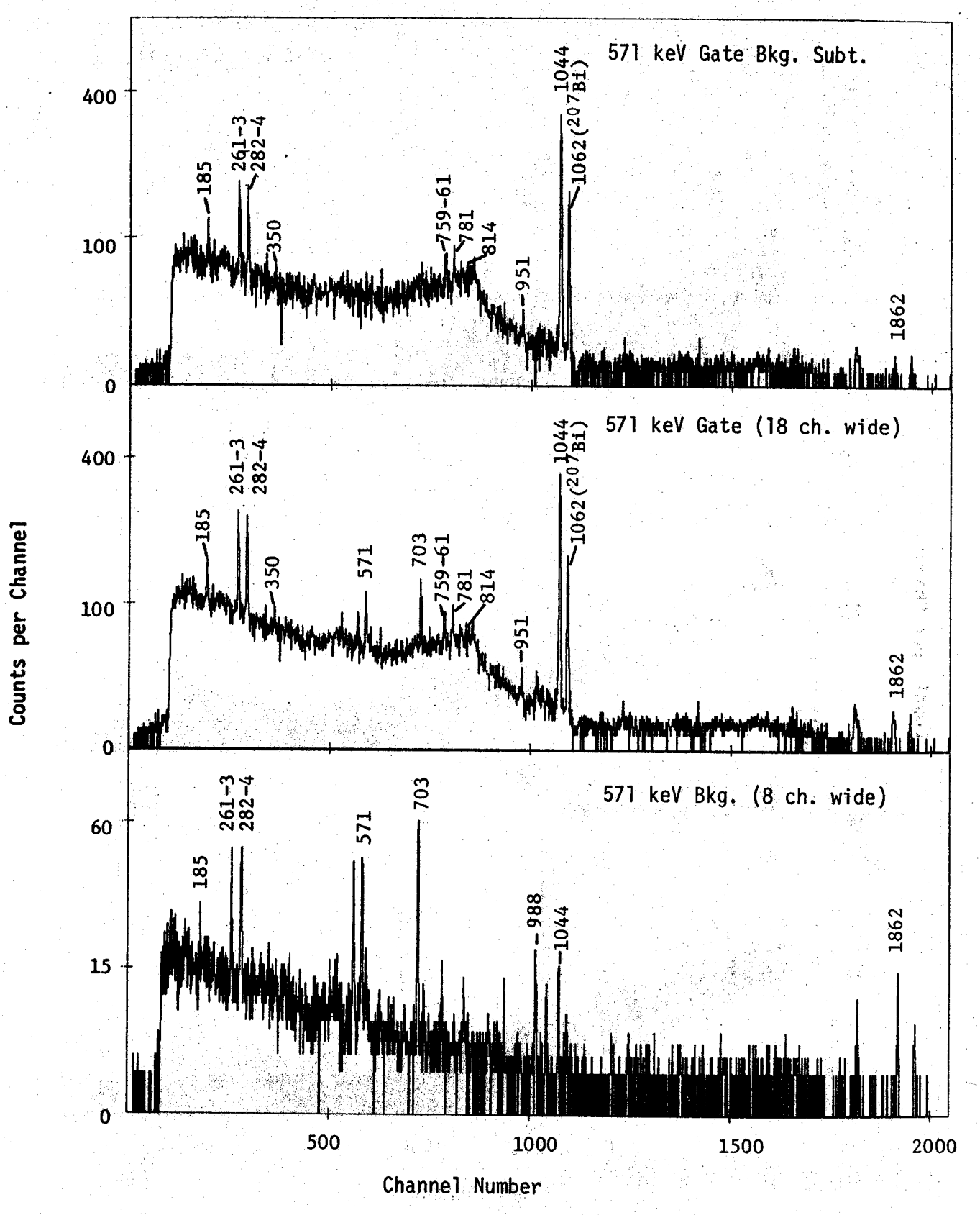

Figure 3. ^{205}Bi Coincidence spectra continued.

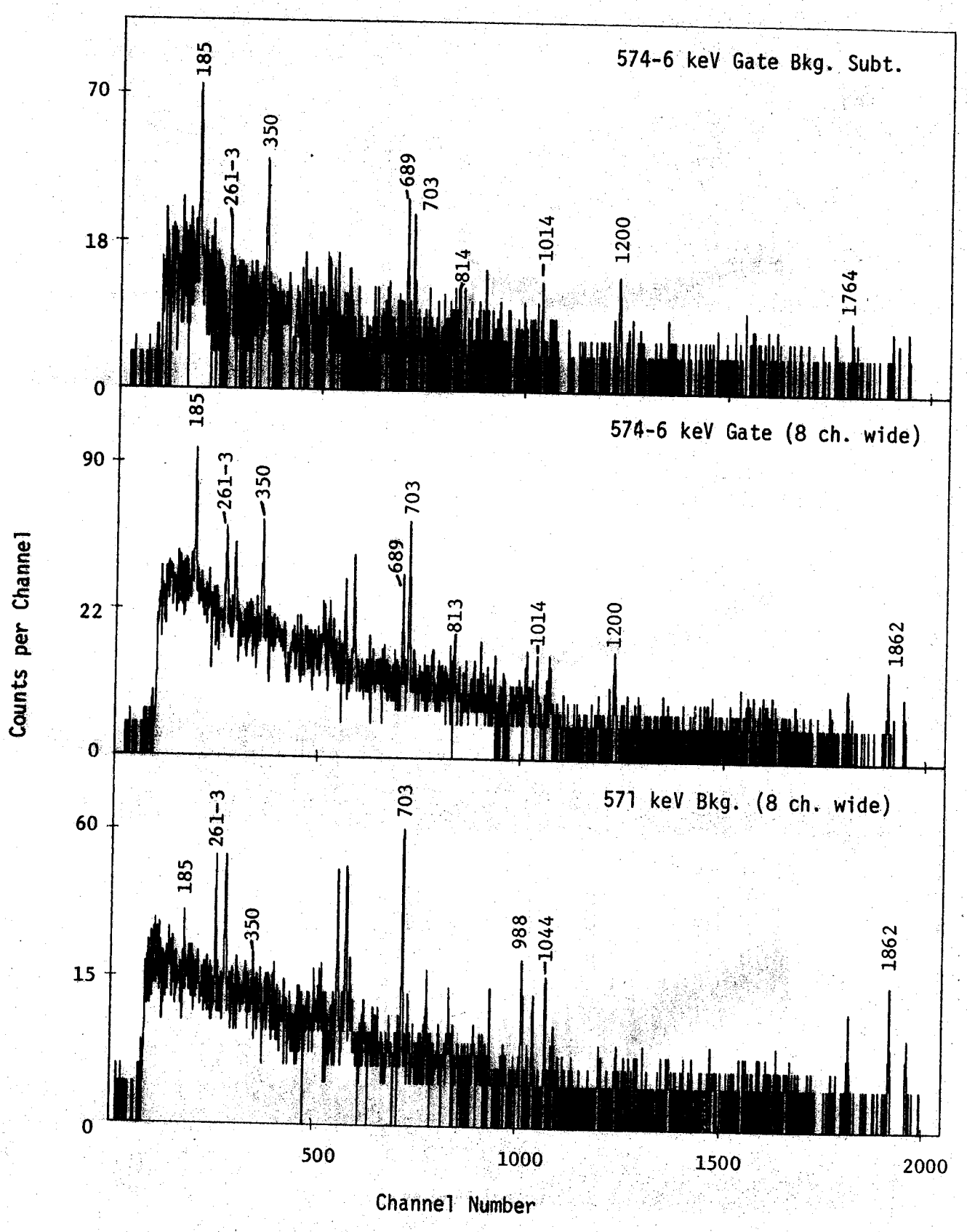

Figure 3. ^{205}Bi Coincidence spectra continued.

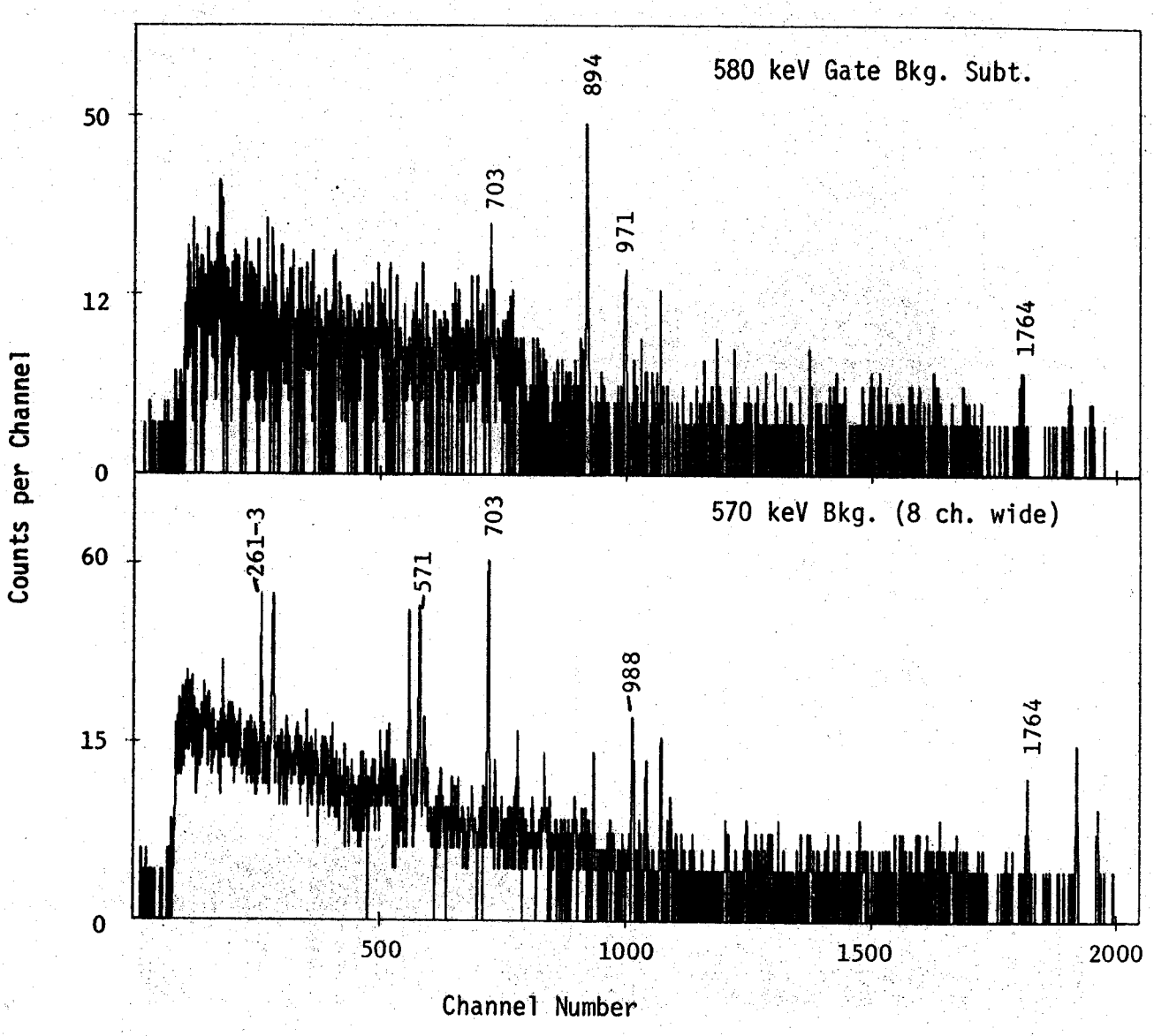

Figure 3. ^{205}Bi Coincidence spectra continued.

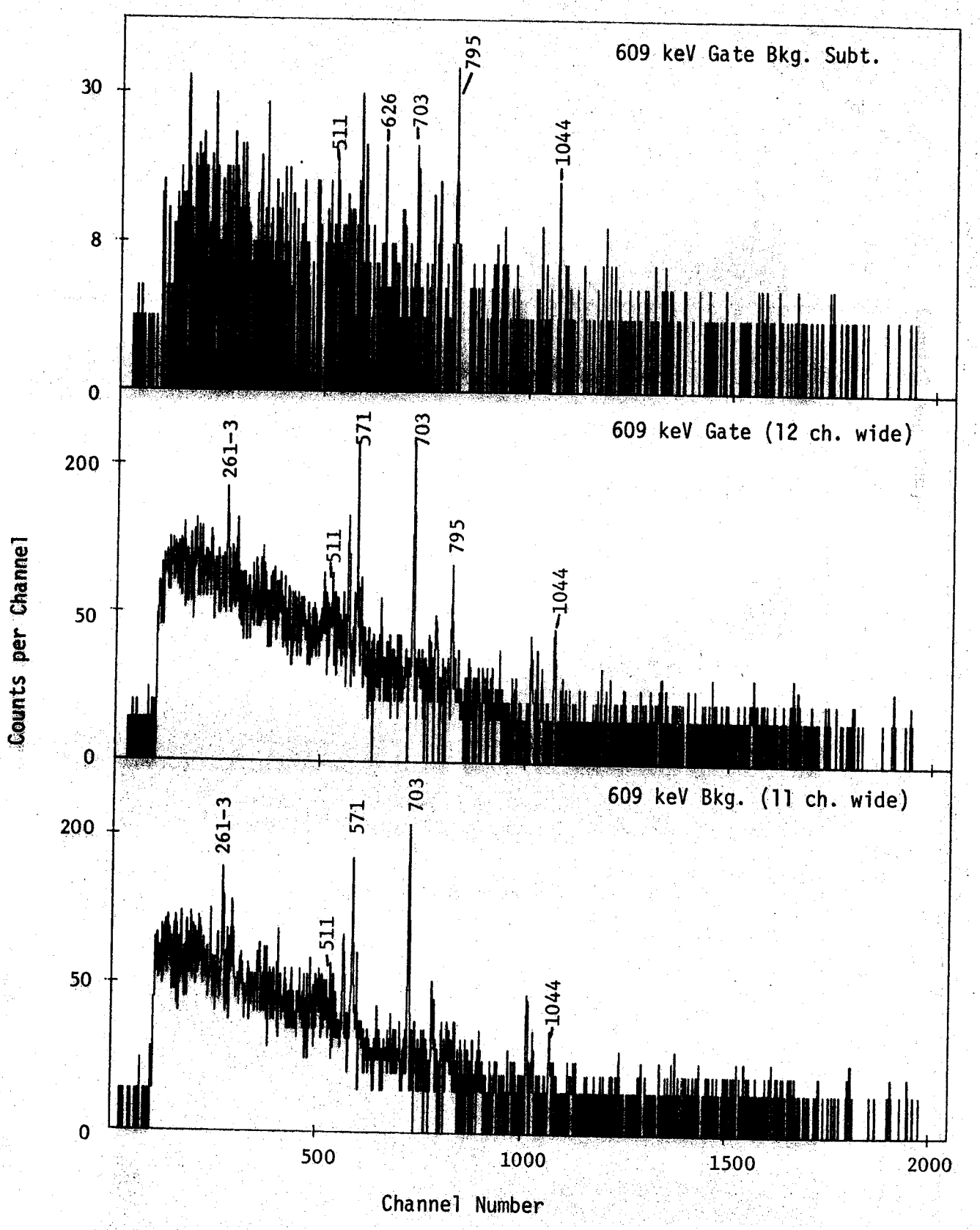

Figure 3. ^{205}Bi Coincidence spectra continued.

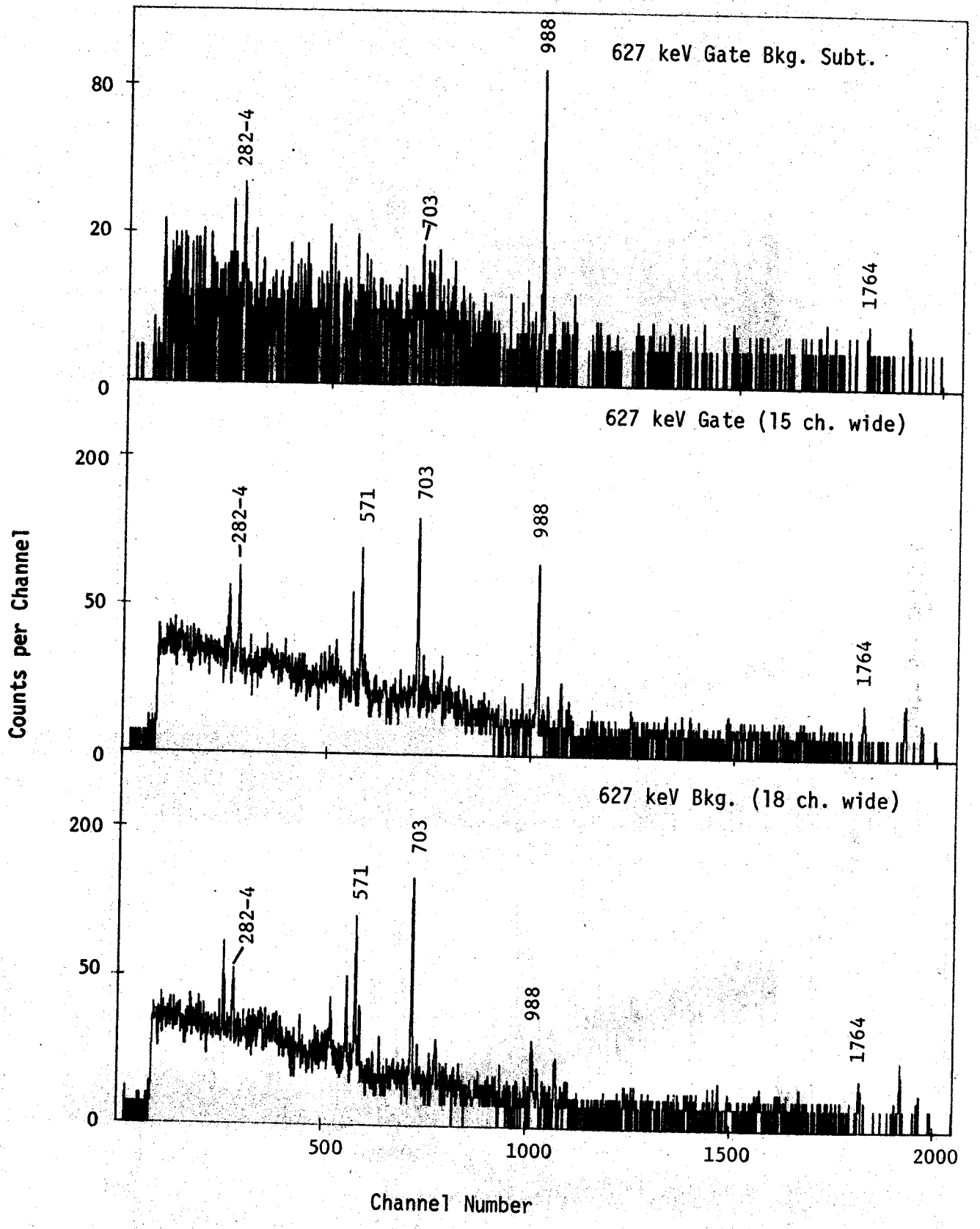

Figure 3. ^{205}Bi Coincidence spectra continued.

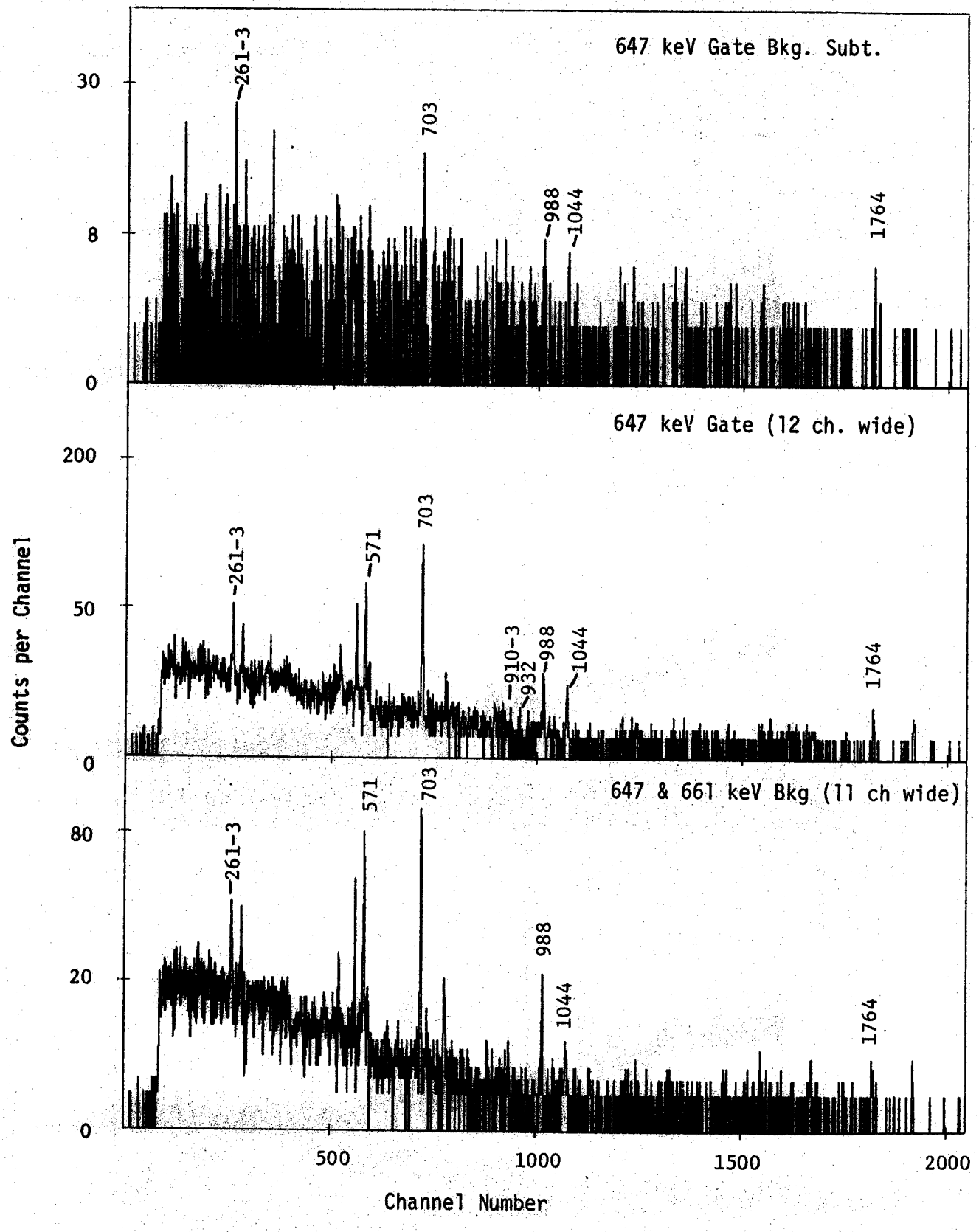

Figure 3. ^{205}Bi Coincidence spectra continued.

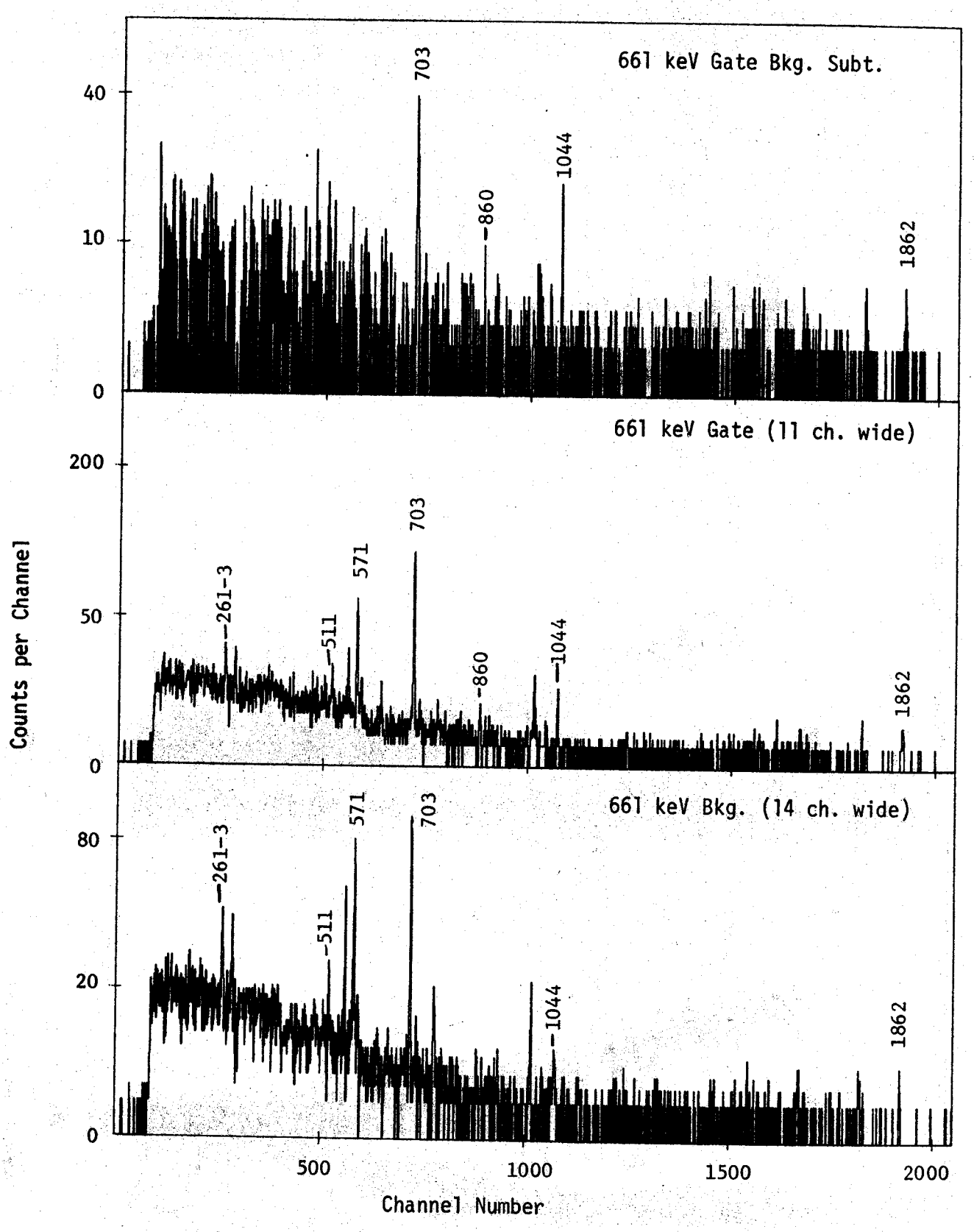

Figure 3. ^{205}Bi Coincidence spectra continued.

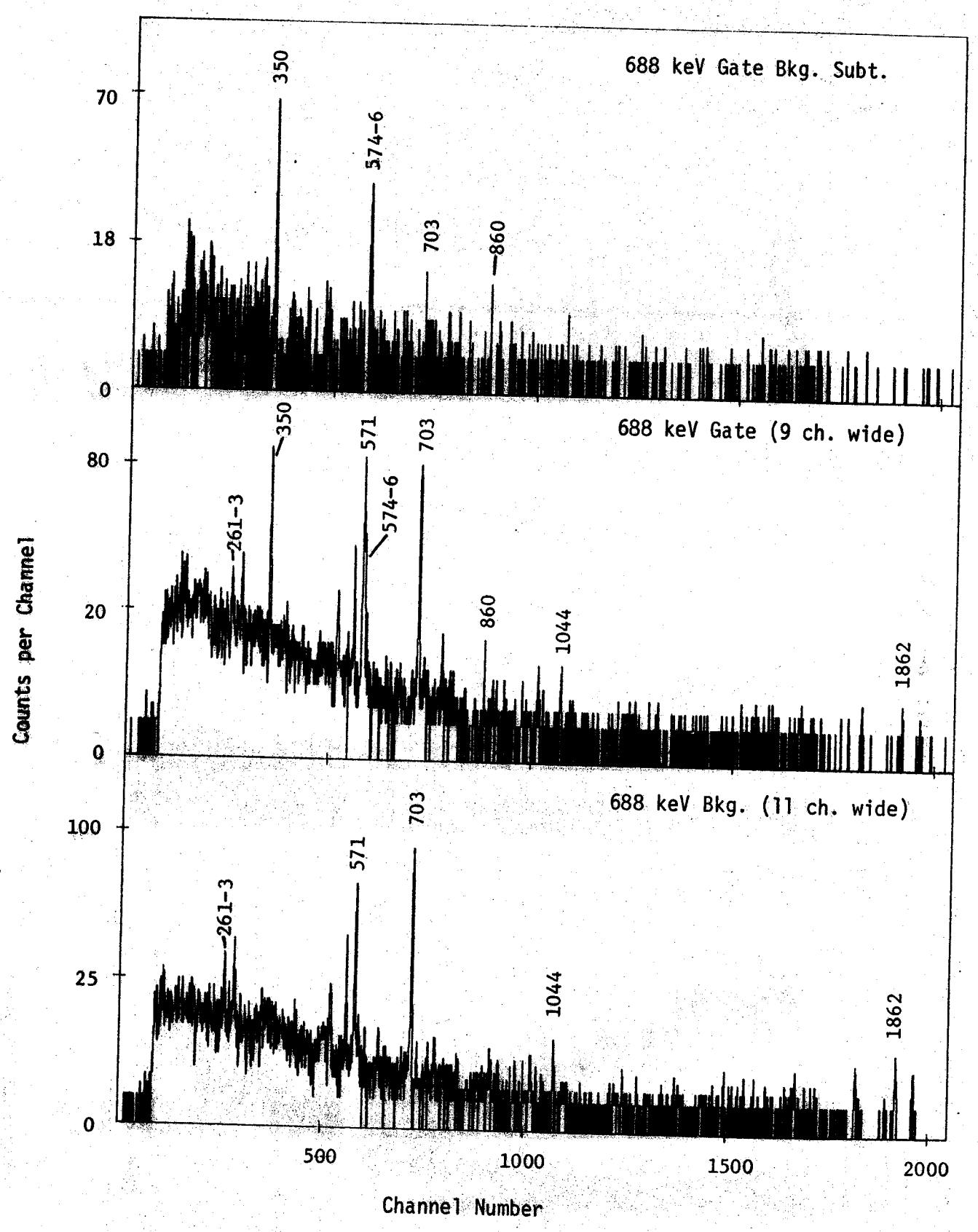

Figure 3. ^{205}Bi Coincidence spectra continued.

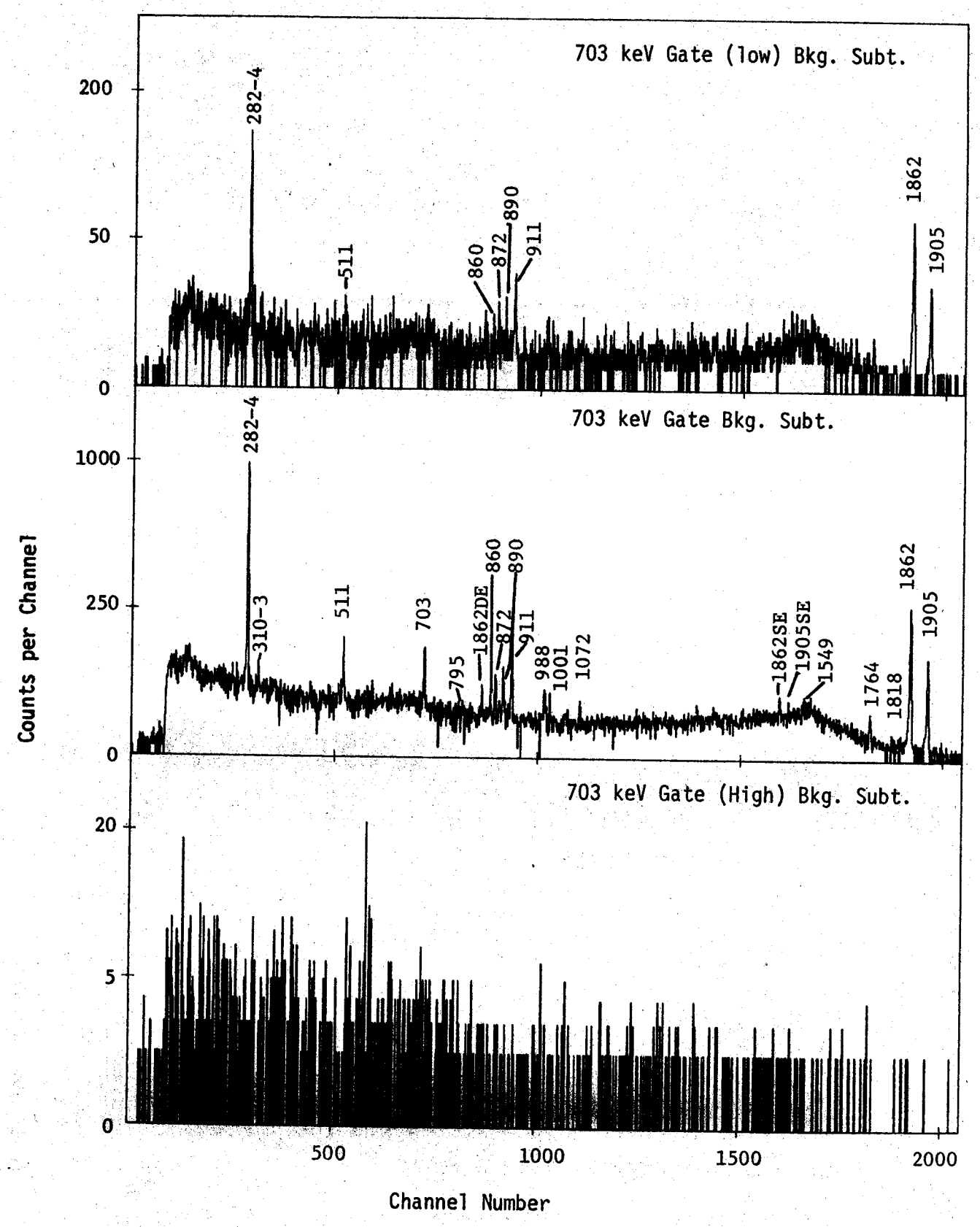

Figure 3. ^{205}Bi Coincidence spectra continued.

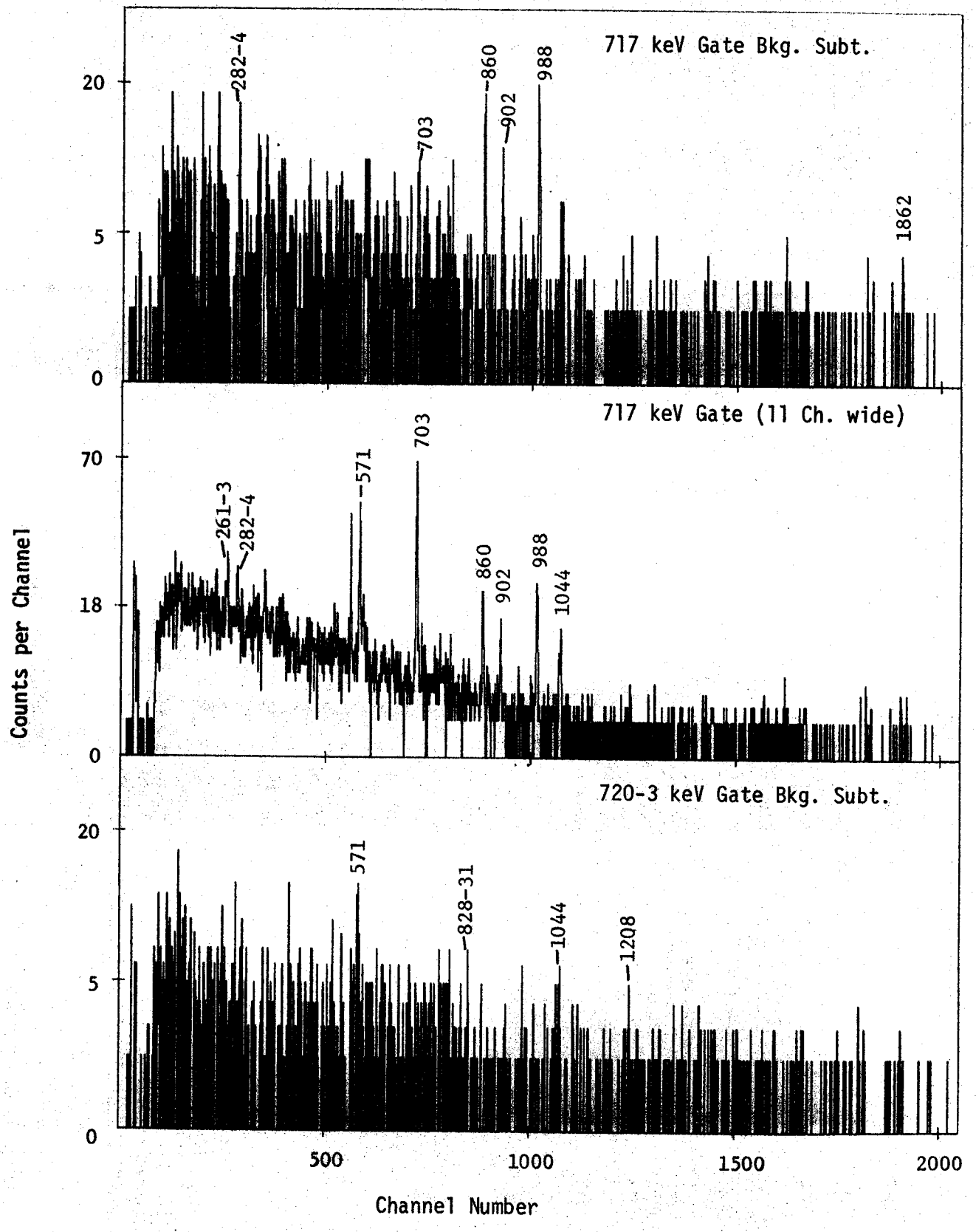

Figure 3. ^{205}Bi Coincidence spectra continued.

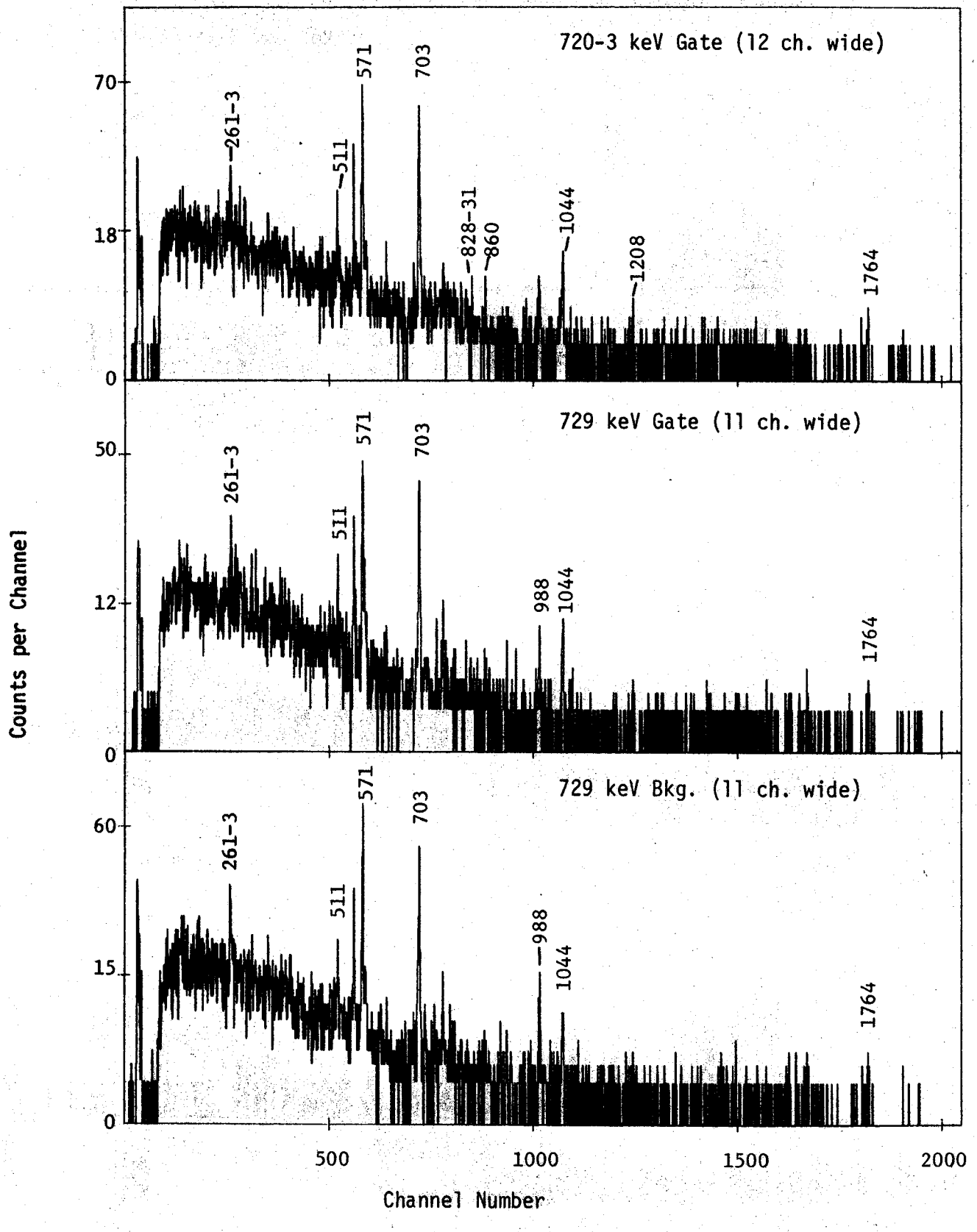

Figure 3. ^{205}Bi Coincidence spectra continued.

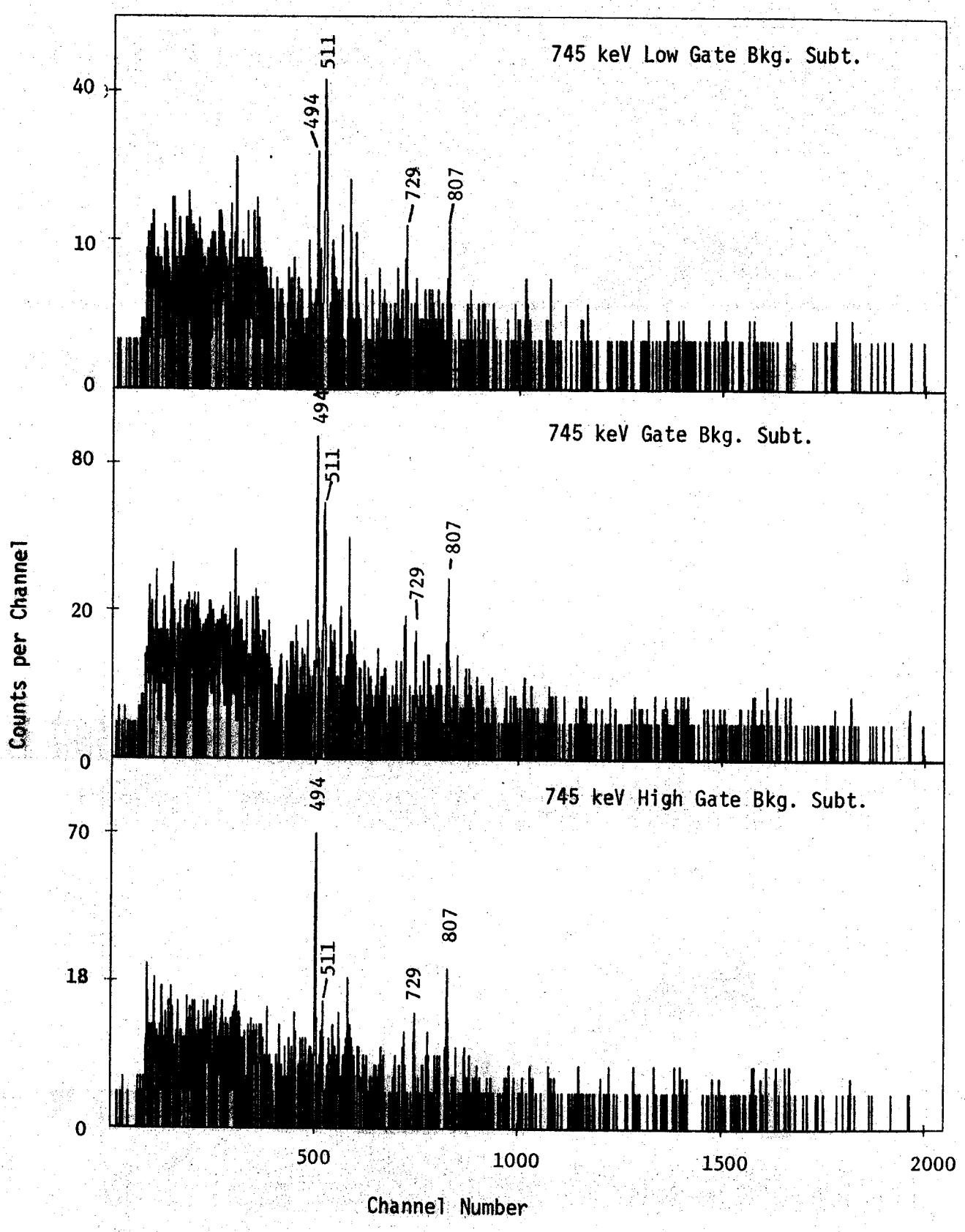

Figure 3. ^{205}Bi Coincidence spectra continued.

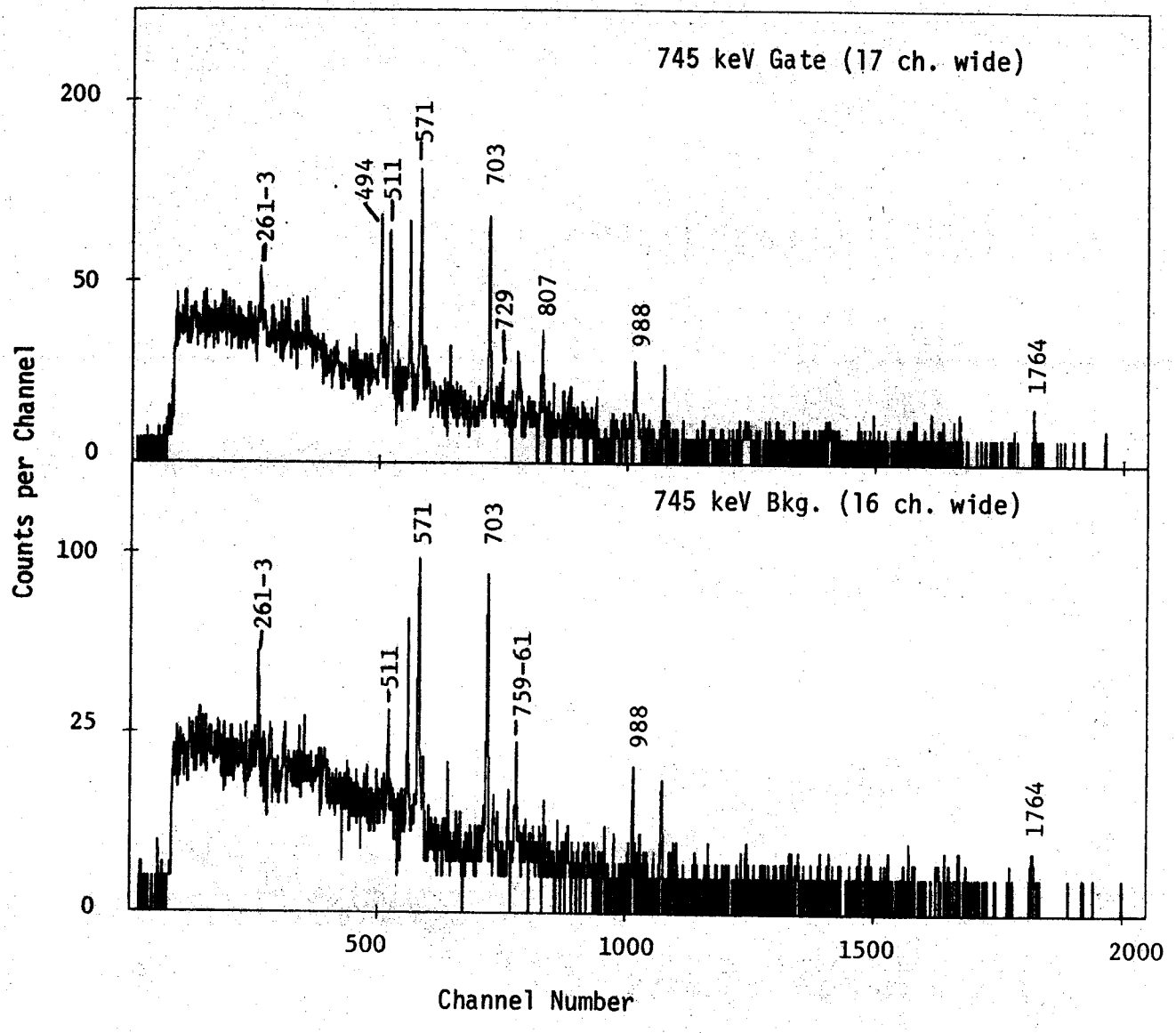

Figure 3. ^{205}Bi Coincidence spectra continued.

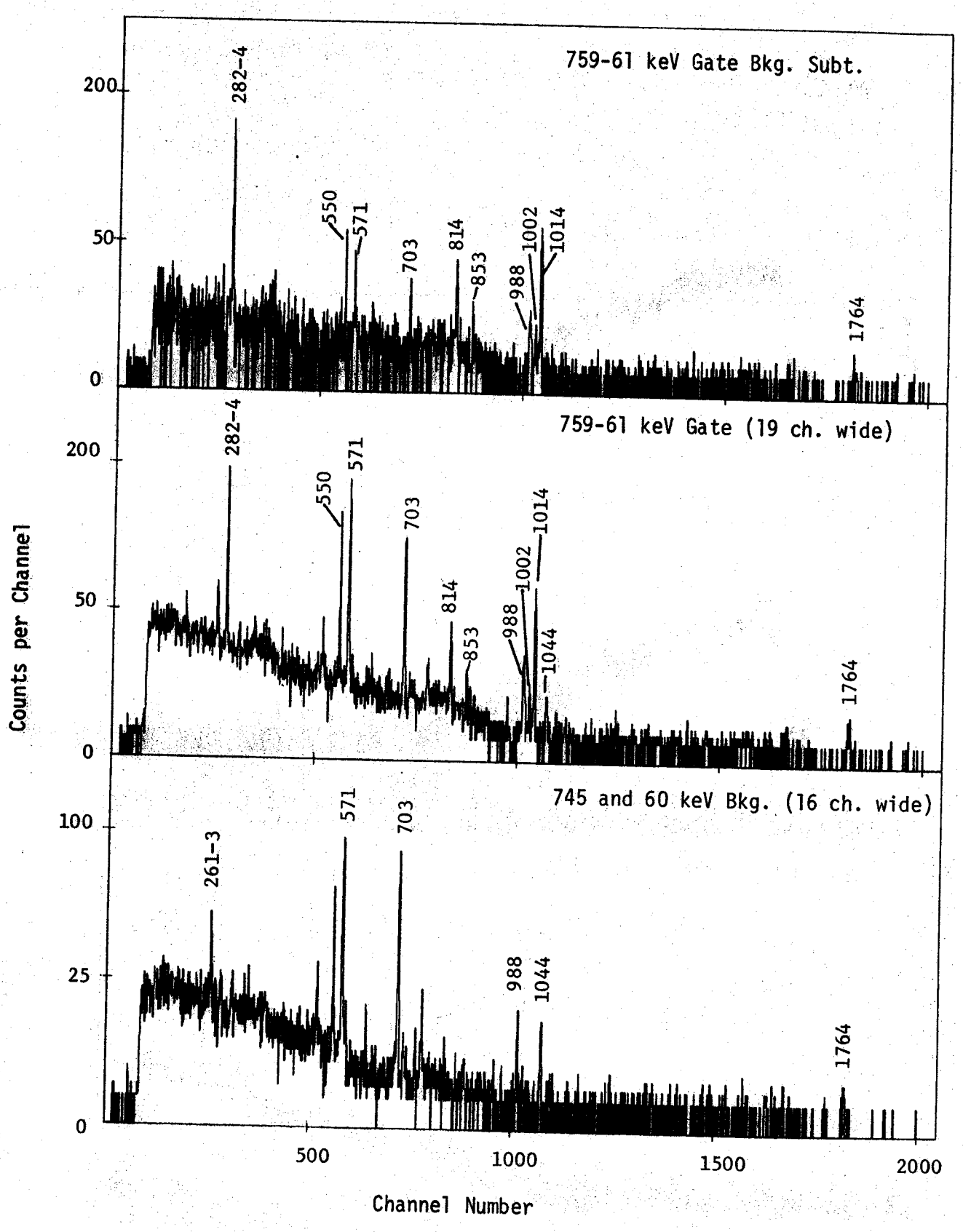

Figure 3. ^{205}Bi Coincidence spectra continued.

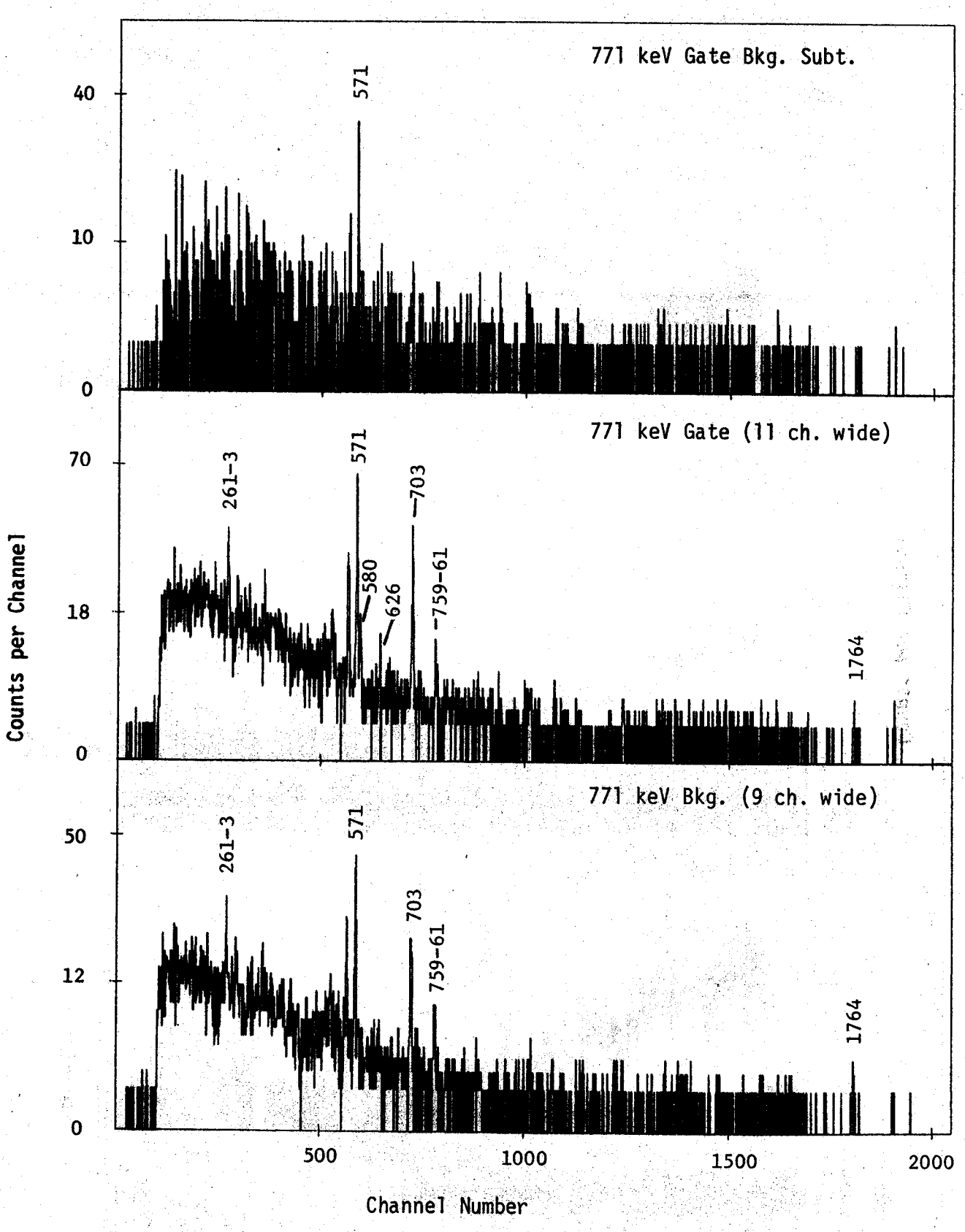

Figure 3. ^{205}Bi Coincidence spectra continued.

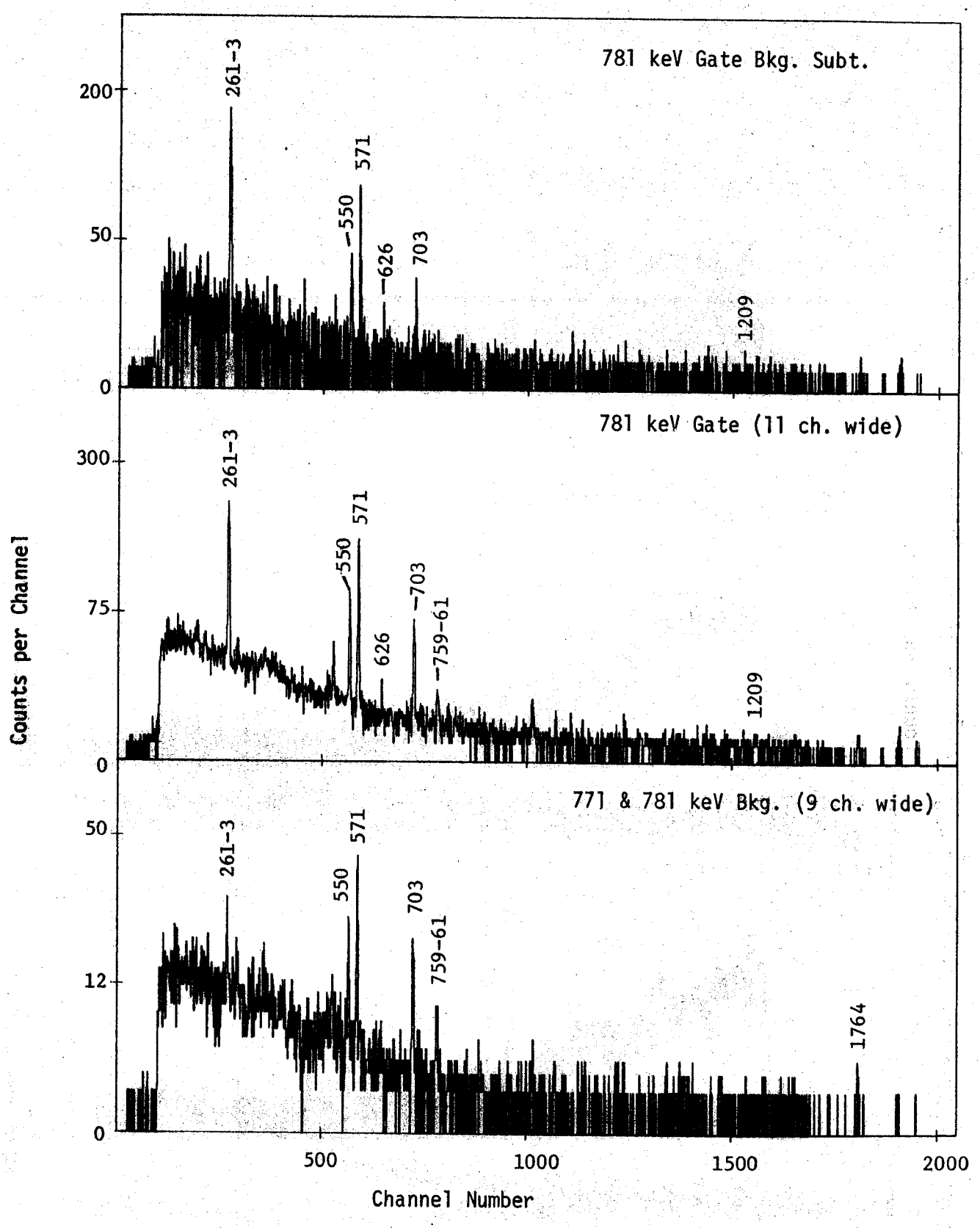

Figure 3. ^{205}Bi Coincidence spectra continued.

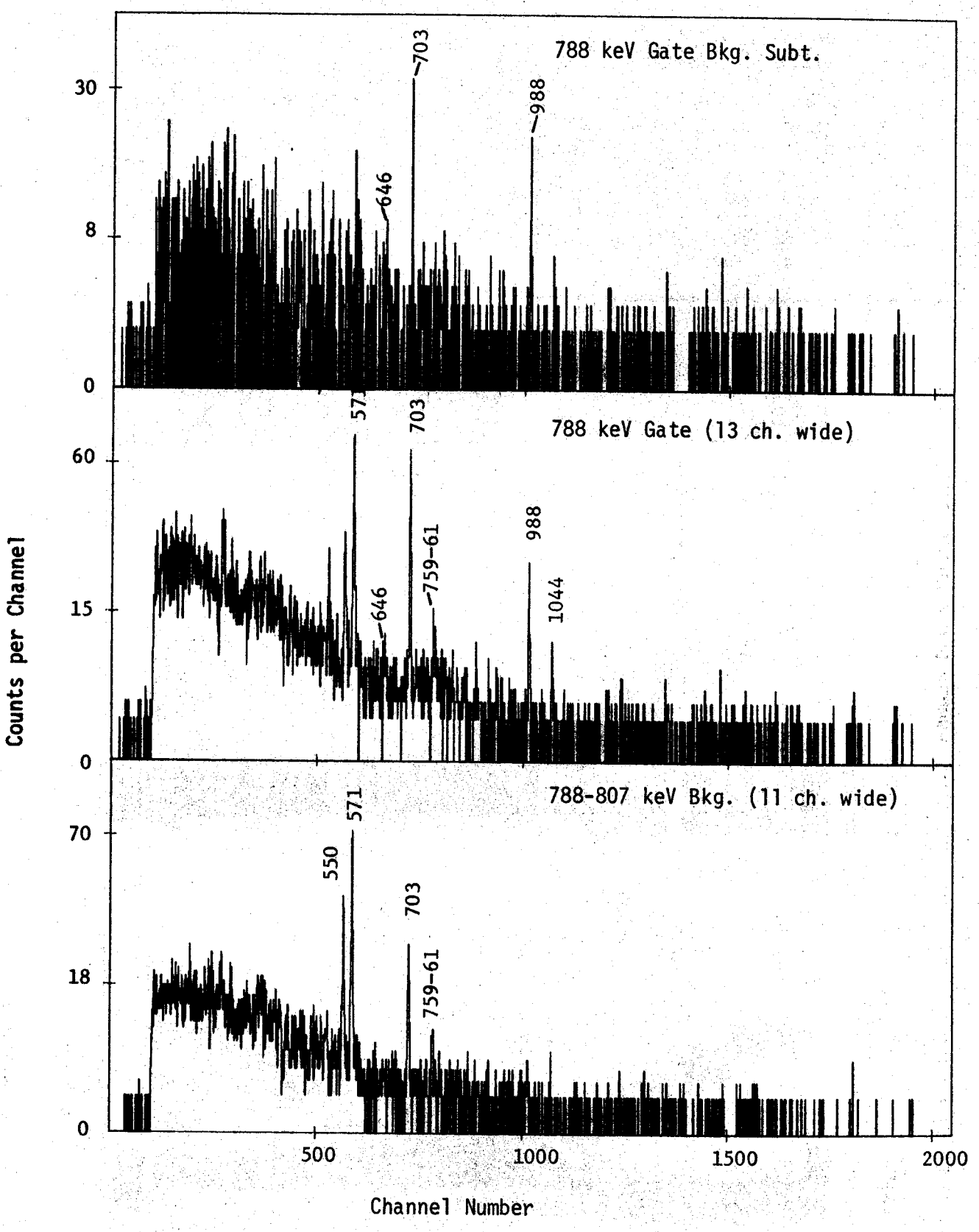

Figure 3. ^{205}Bi Coincidence Spectra continued.

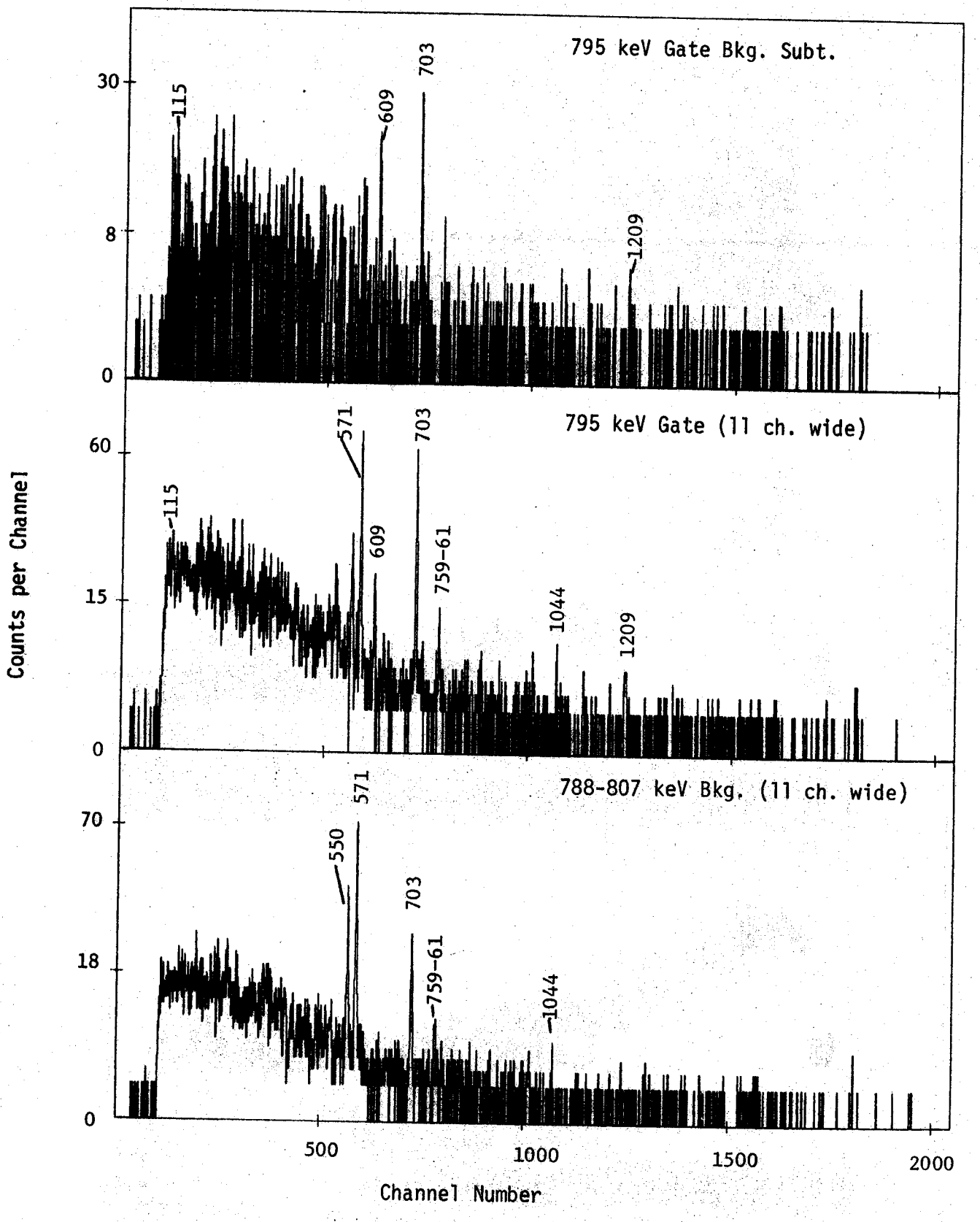

Figure 3. ^{205}Bi Coincidence spectra continued.

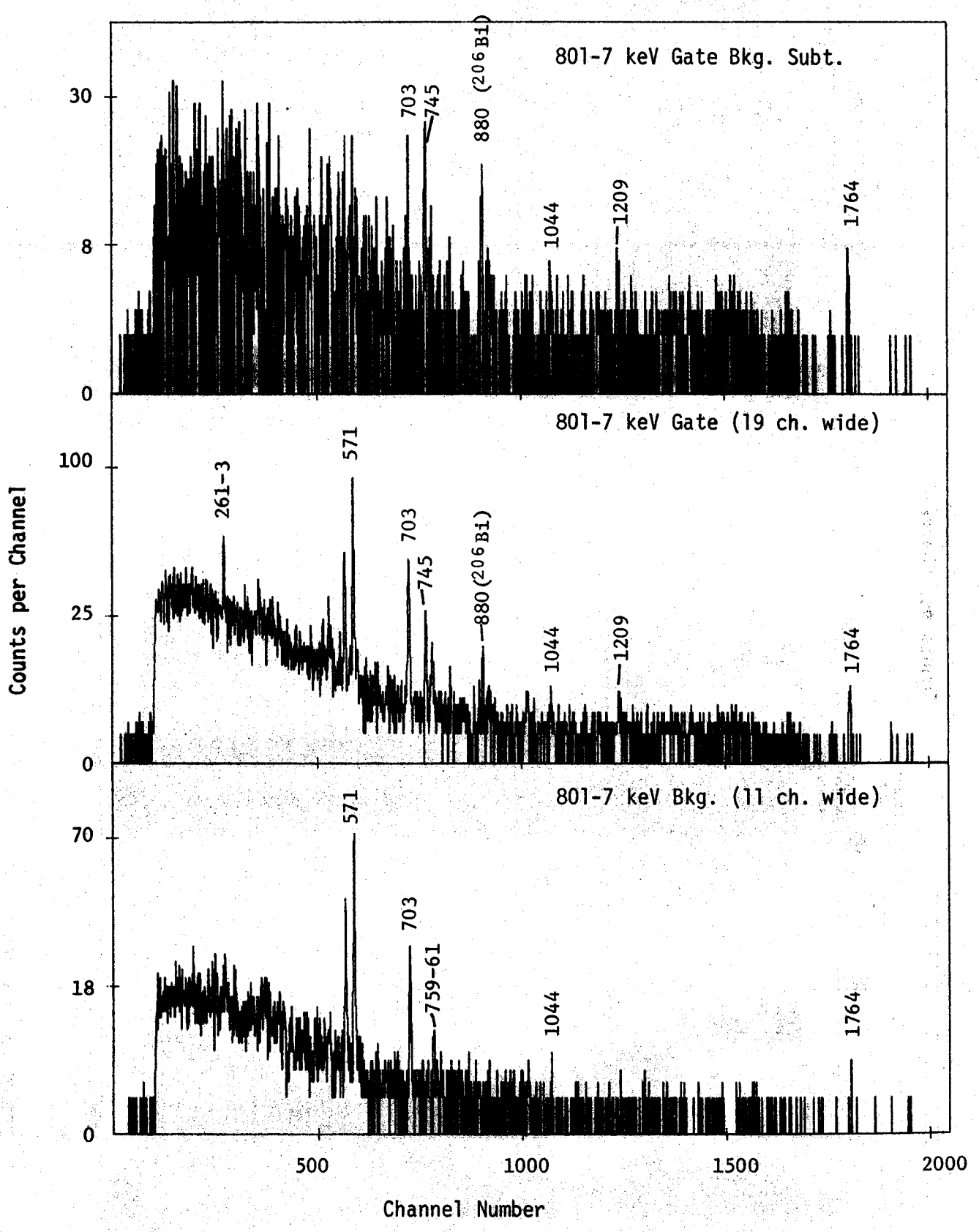

Figure 3. ^{205}Bi Coincidence spectra continued.

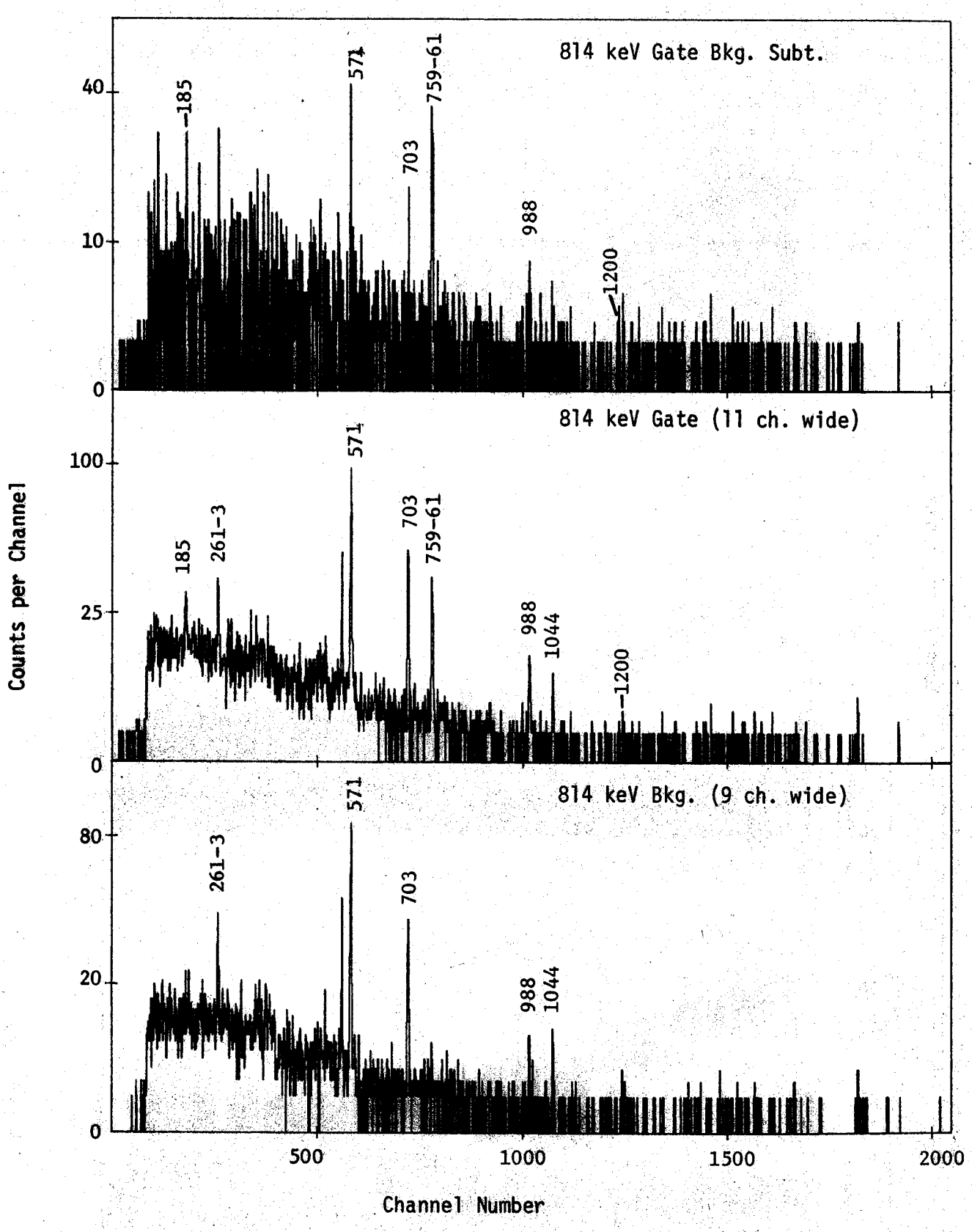

Figure 3. ^{205}Bi Coincidence spectra continued.

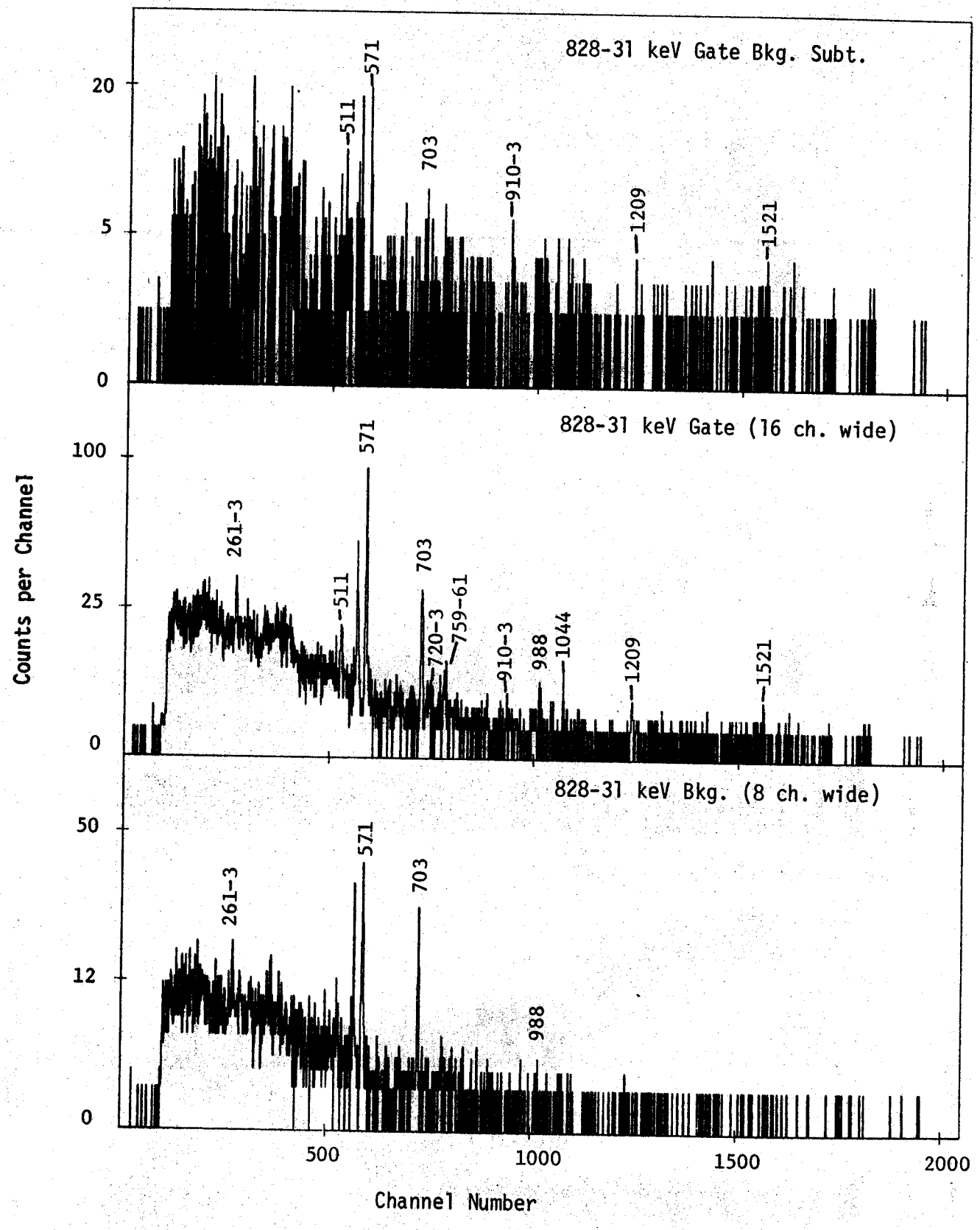

Figure 3. ^{205}Bi Coincidence spectra continued.

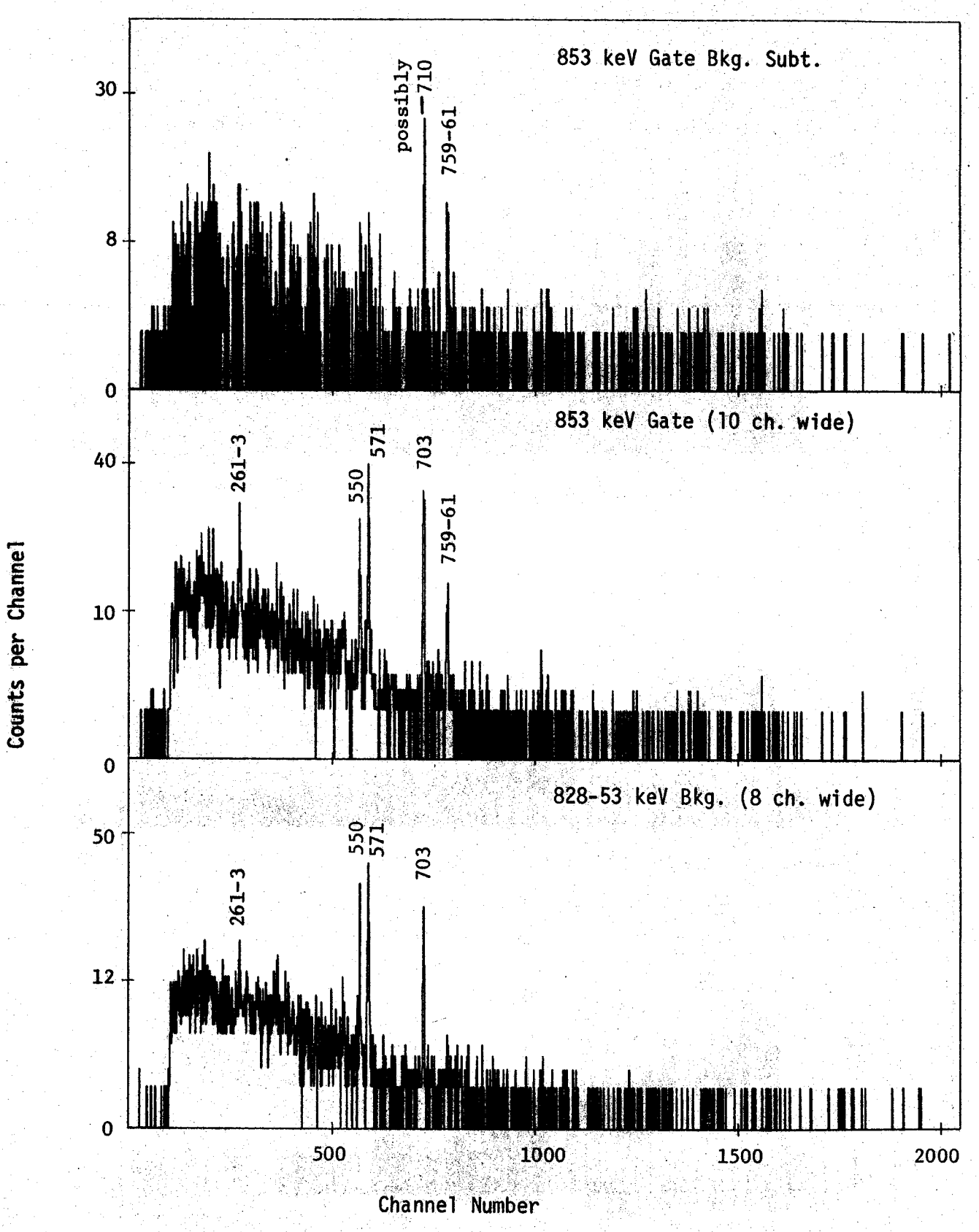

Figure 3. ^{205}Bi Coincidence spectra continued.

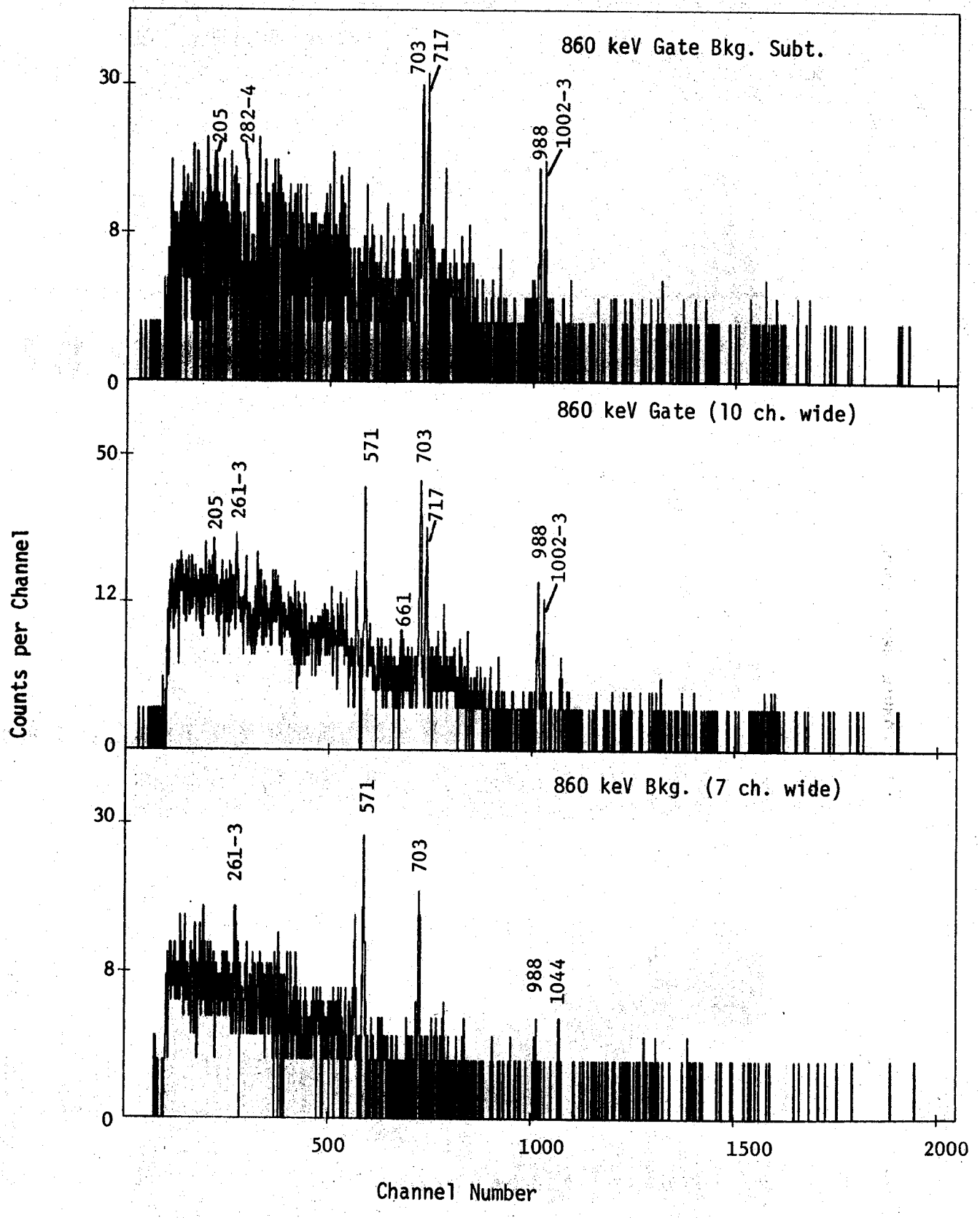

Figure 3. ^{205}Bi Coincidence spectra continued.

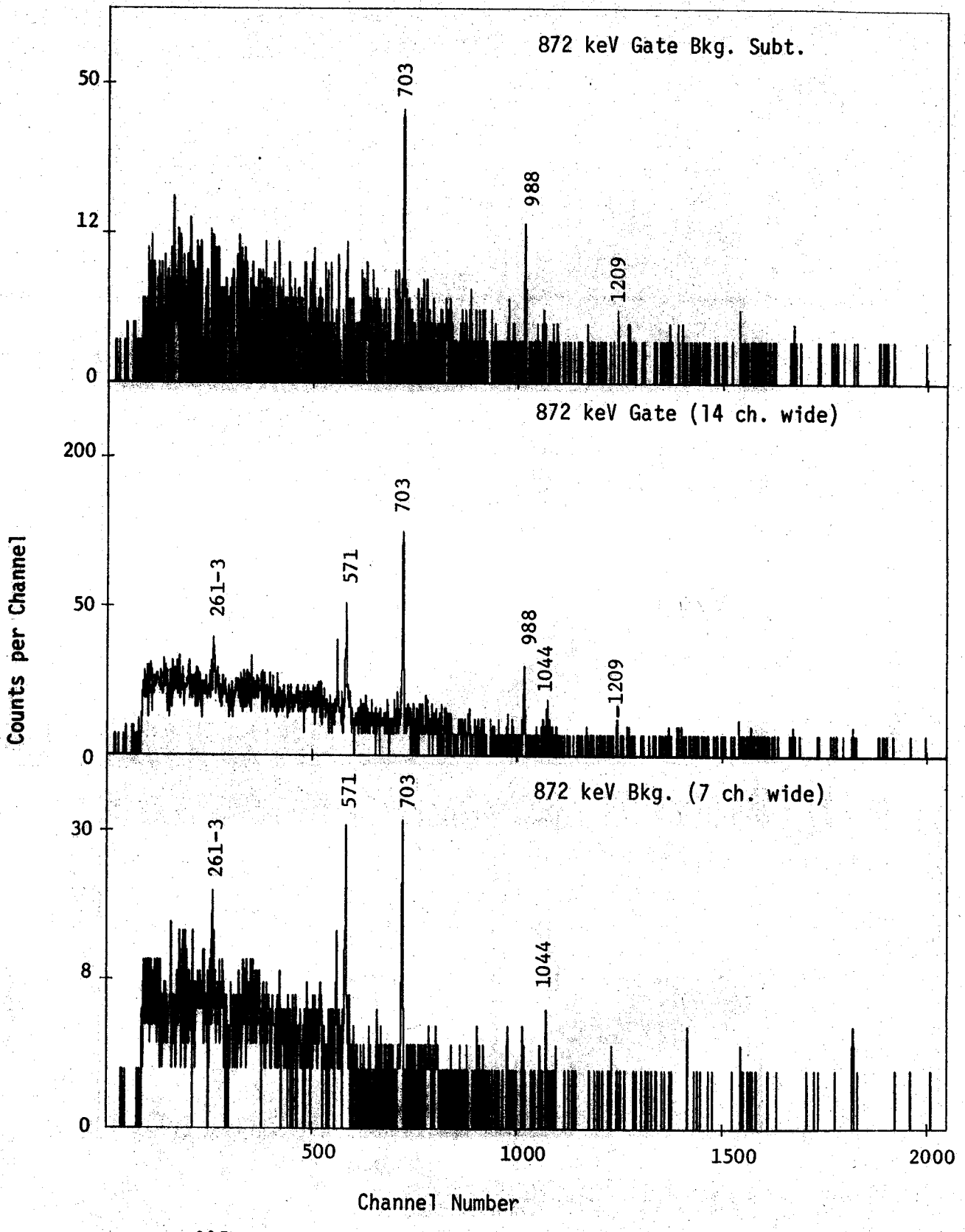

Figure 3. ^{205}Bi Coincidence spectra continued.

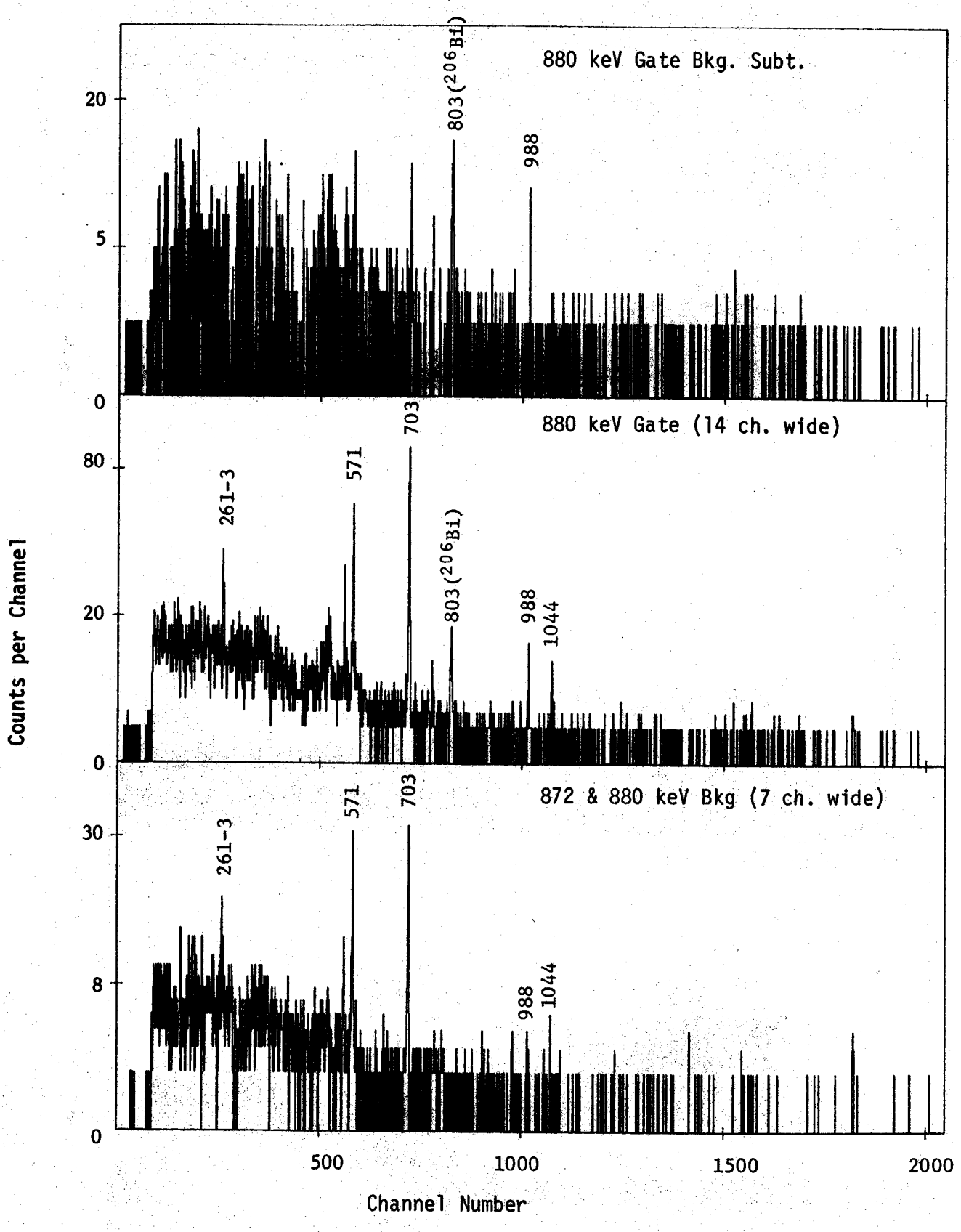

Figure 3. ^{205}Bi Coincidence spectra continued.

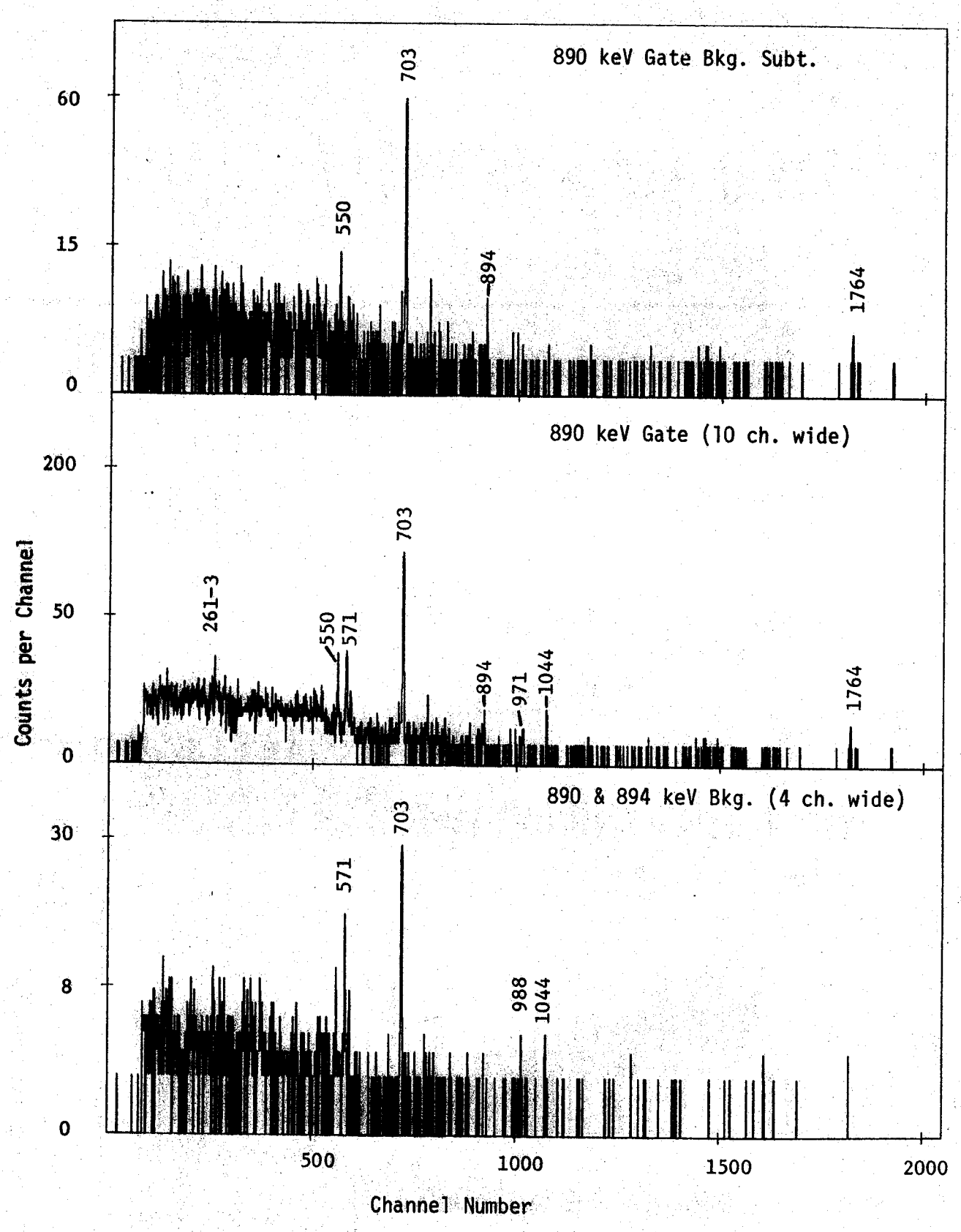

Figure 3. ^{205}Bi Coincidence spectra continued.

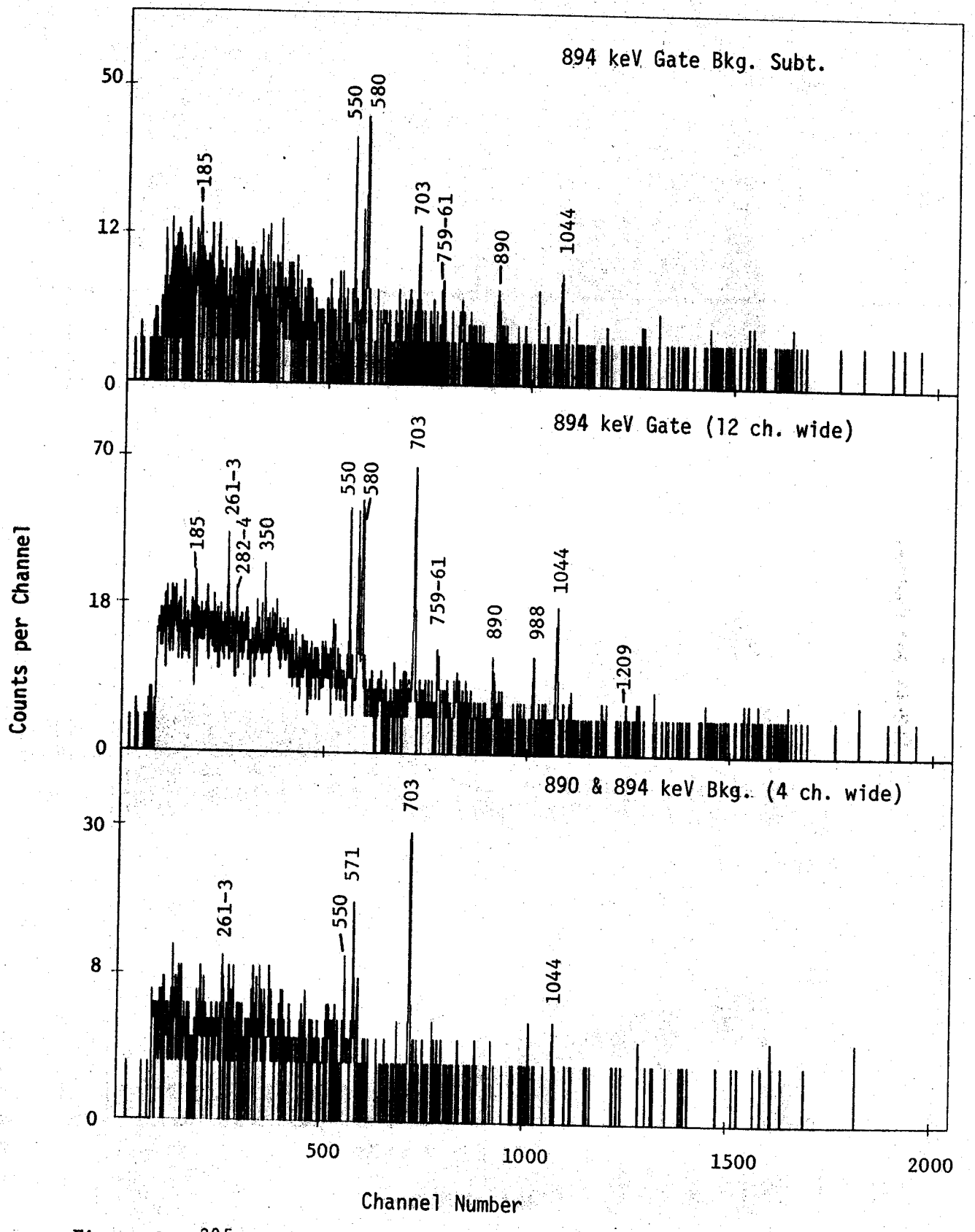

Figure 3. ^{205}Bi Coincidence spectra continued.

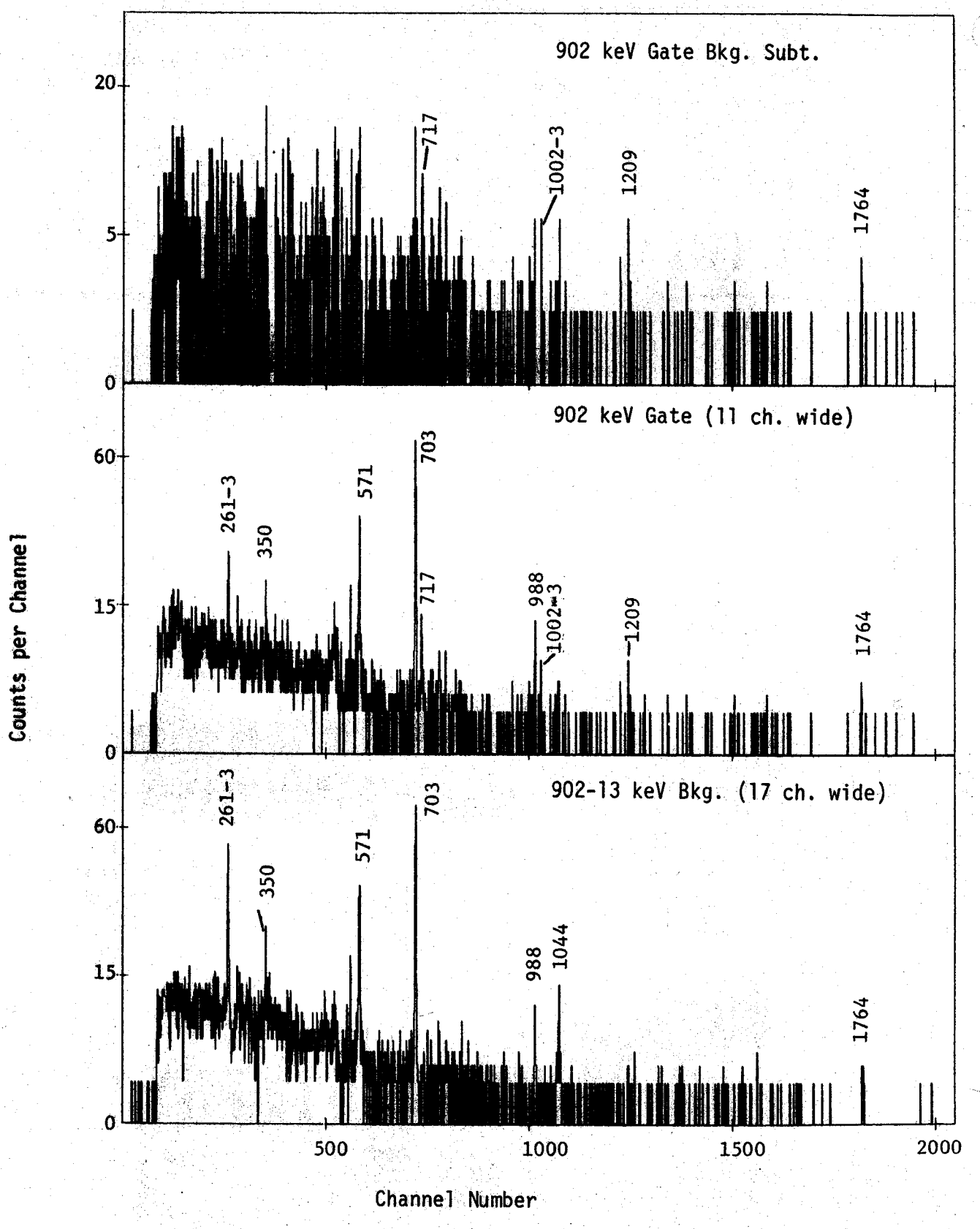

Figure 3. ^{205}Bi Coincidence spectra continued

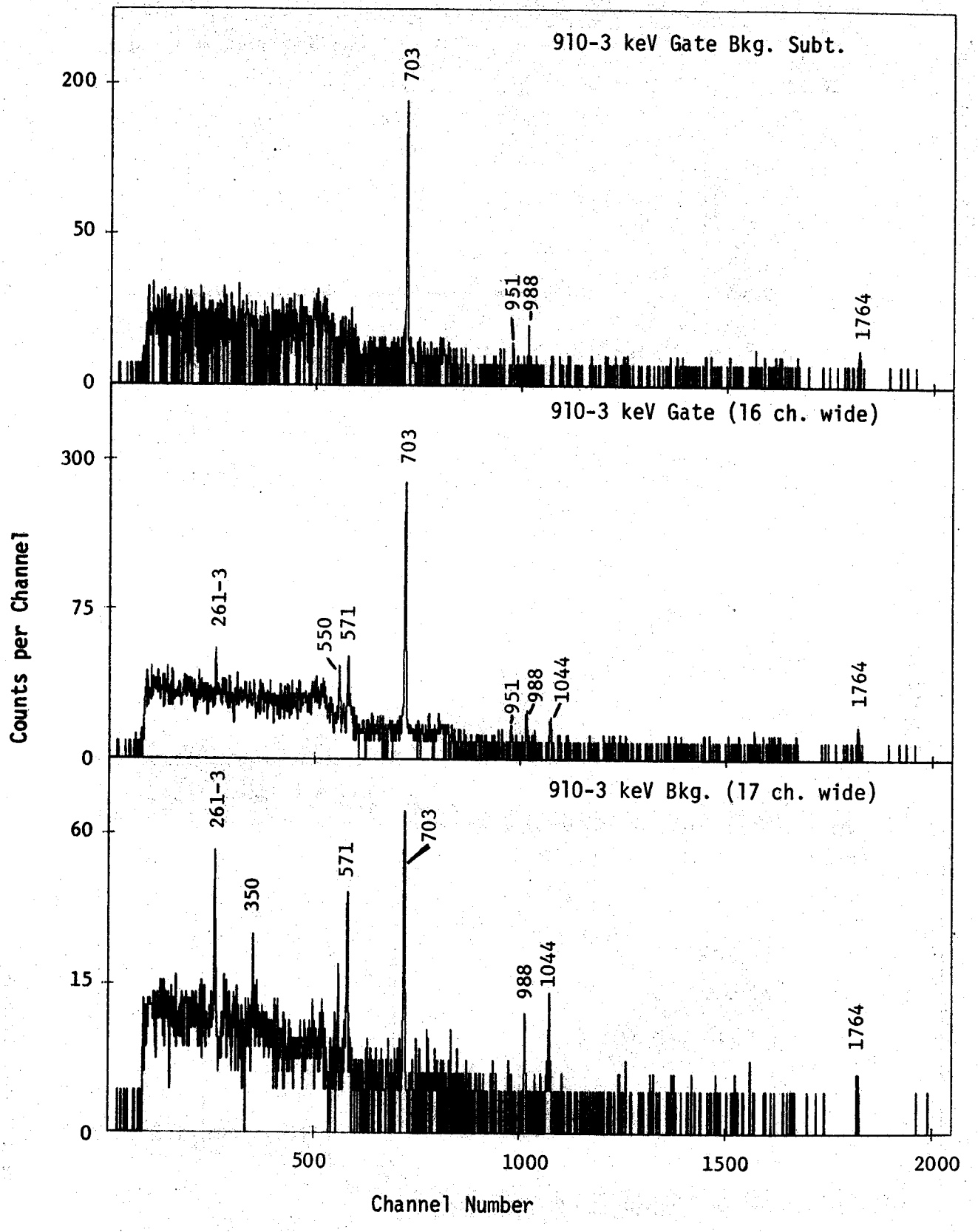

Figure 3. ^{205}Bi Coincidence spectra continued.

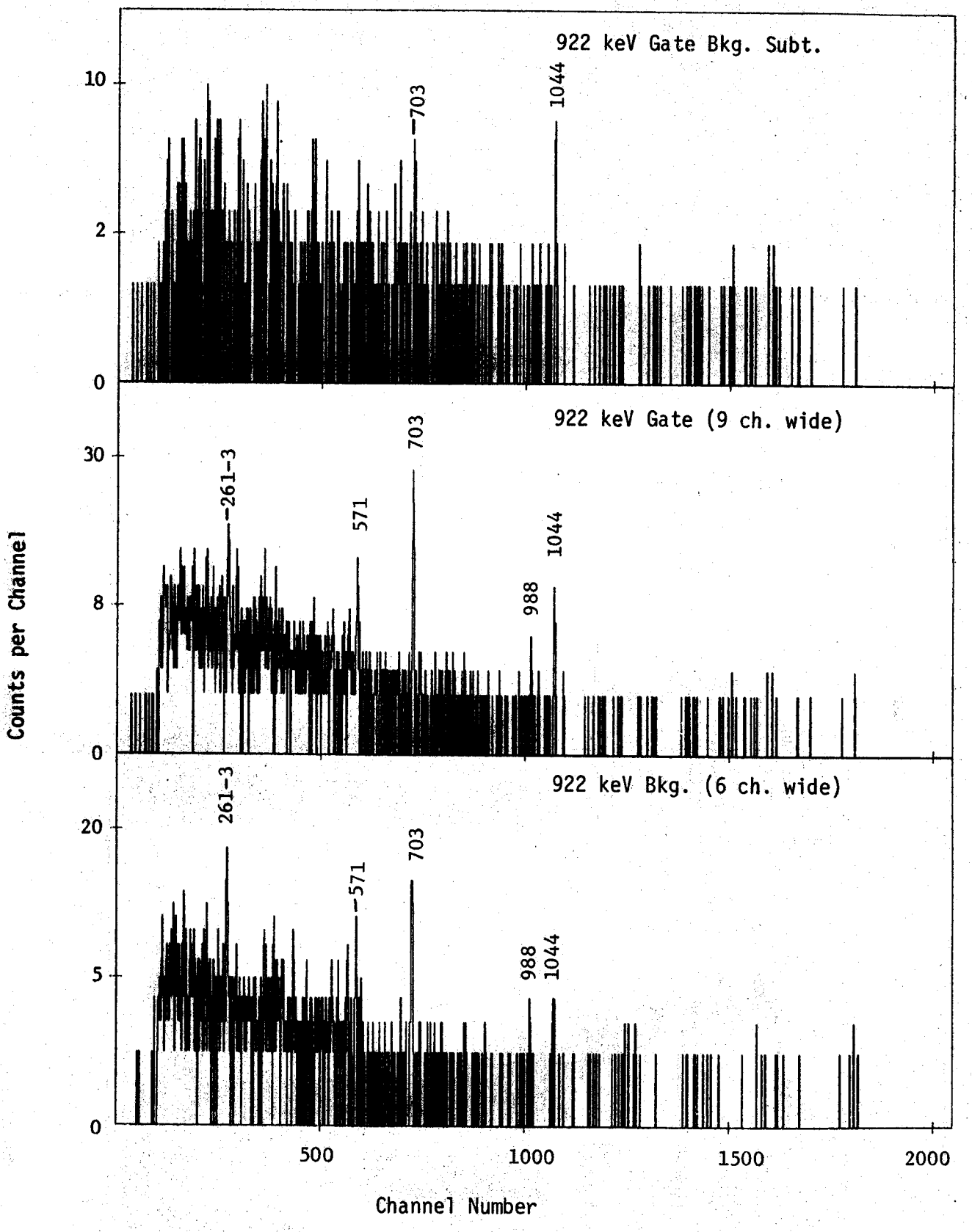

Figure 3. ^{205}Bi Coincidence spectra continued.

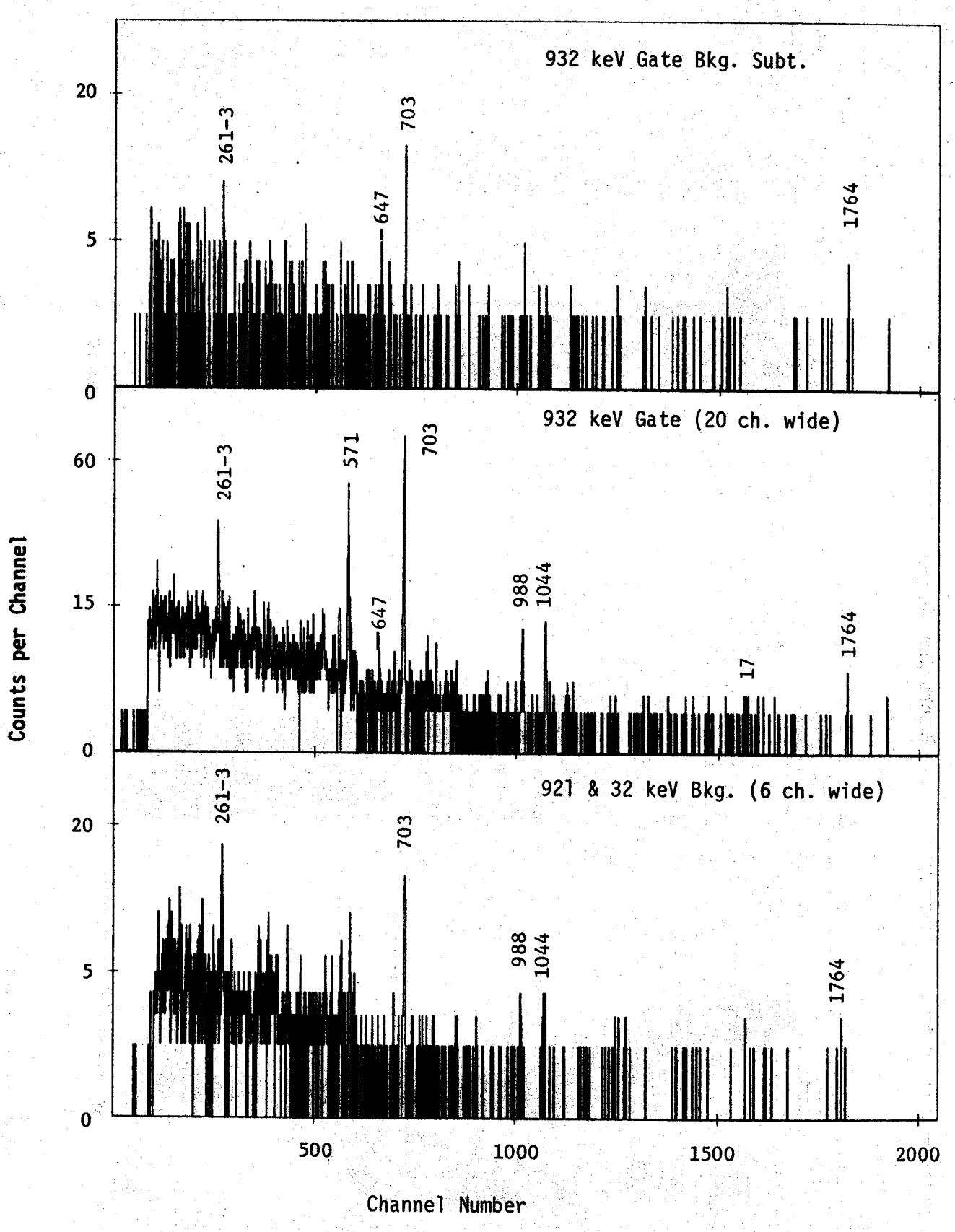

Figure 3. ^{205}Bi Coincidence spectra continued.

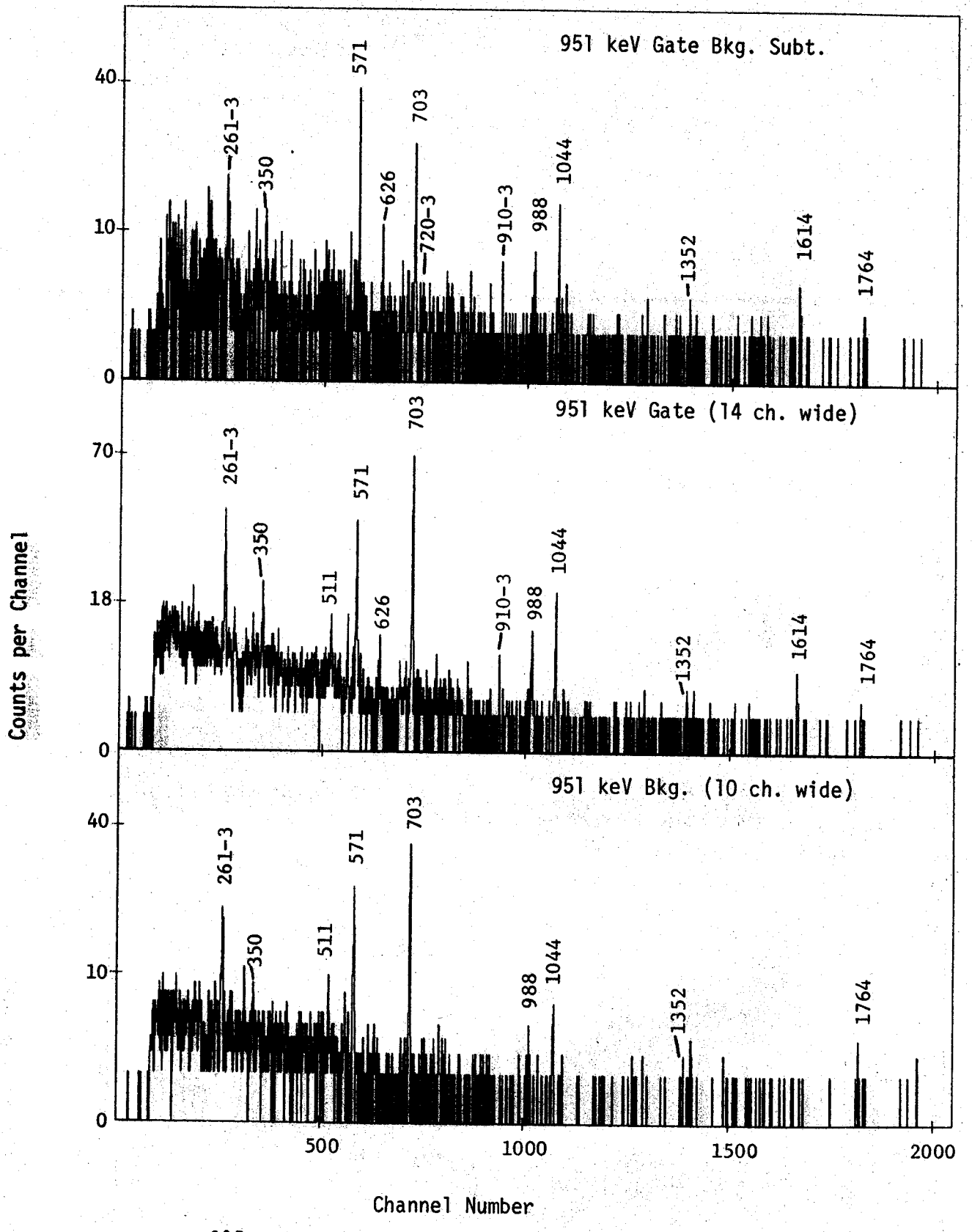

Figure 3. ^{205}Bi Coincidence spectra continued.

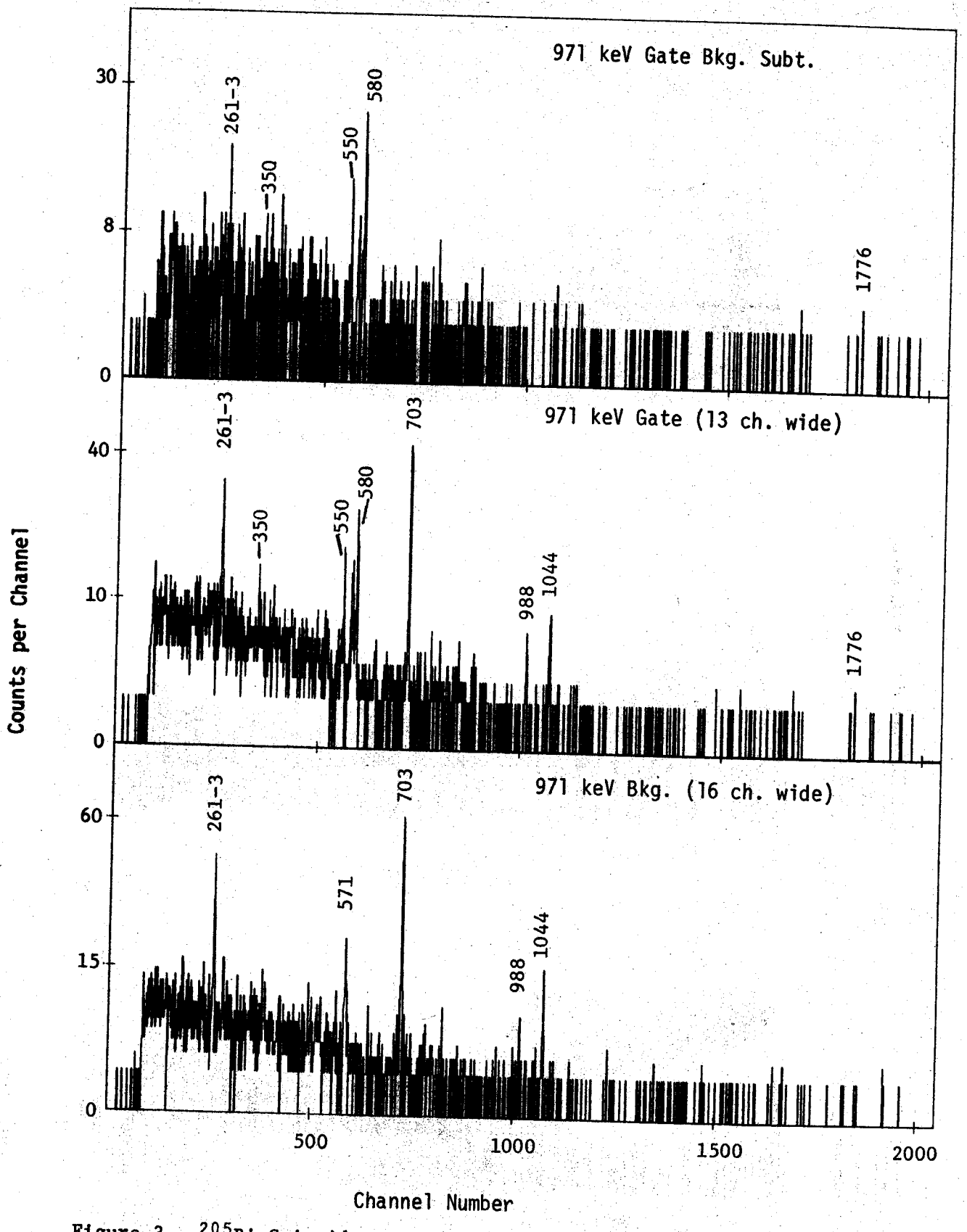

Figure 3. ^{205}Bi Coincidence spectra continued.

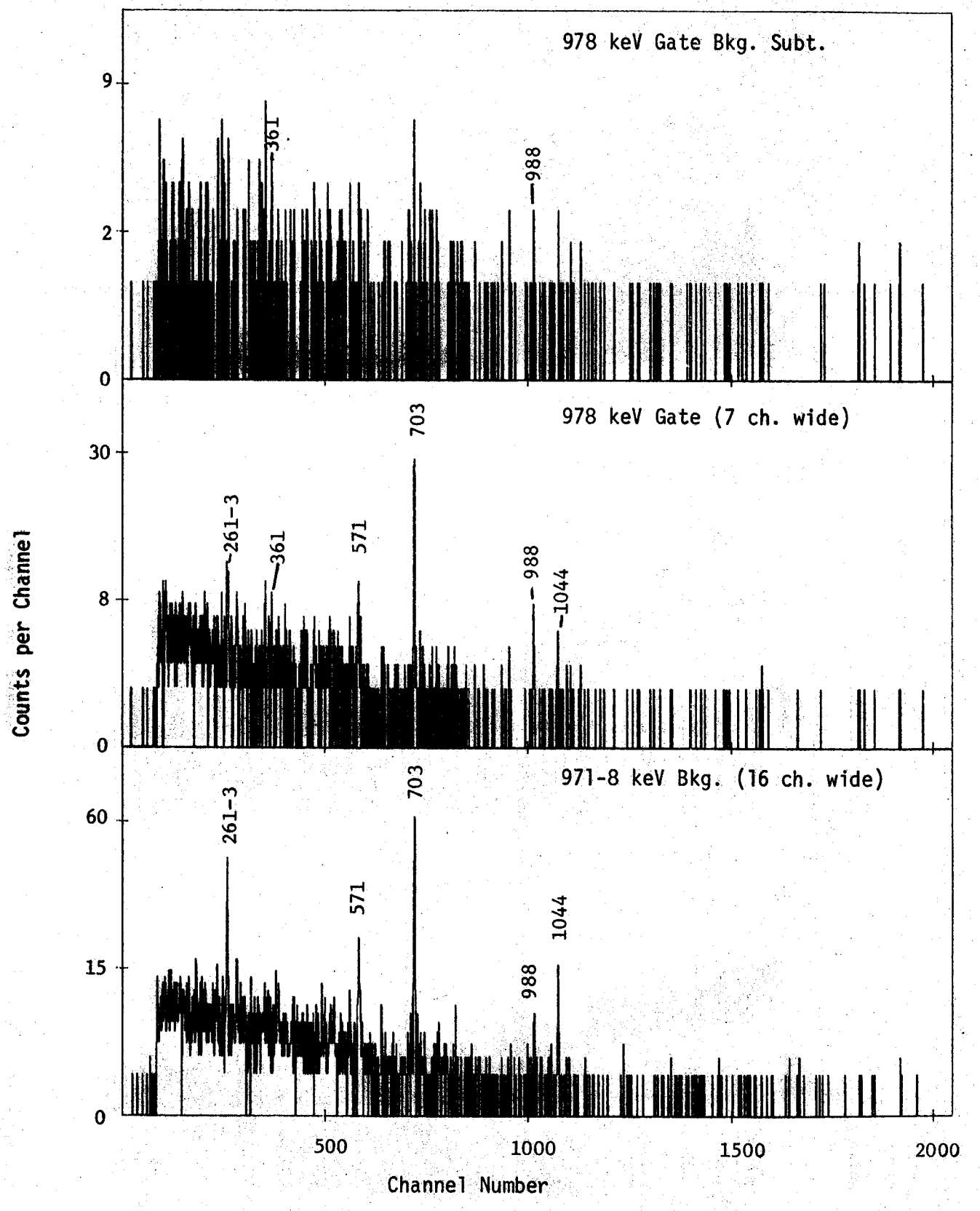

Figure 3. ^{205}Bi Coincidence spectra continued.

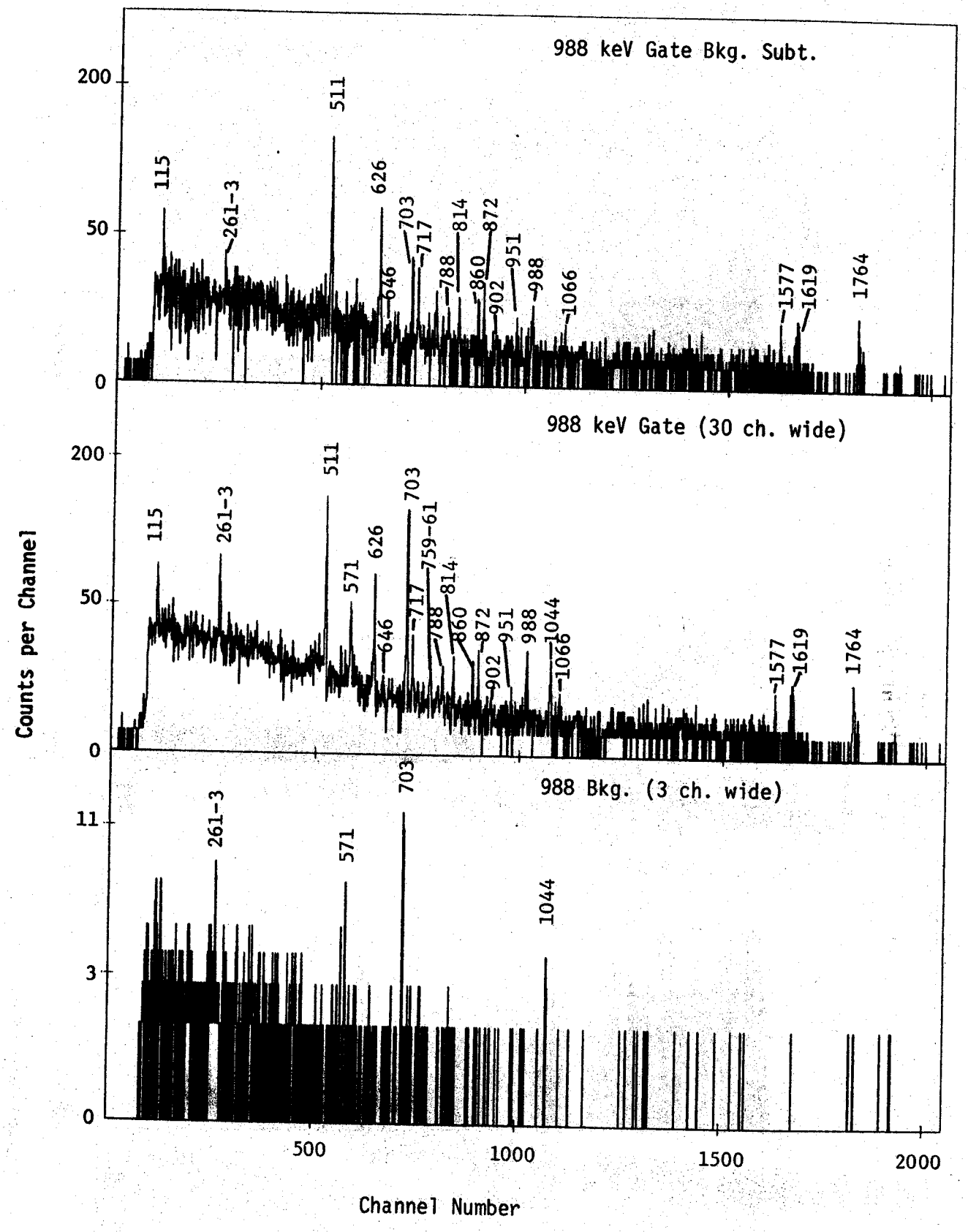

Figure 3. ^{205}Bi Coincidence spectra continued.

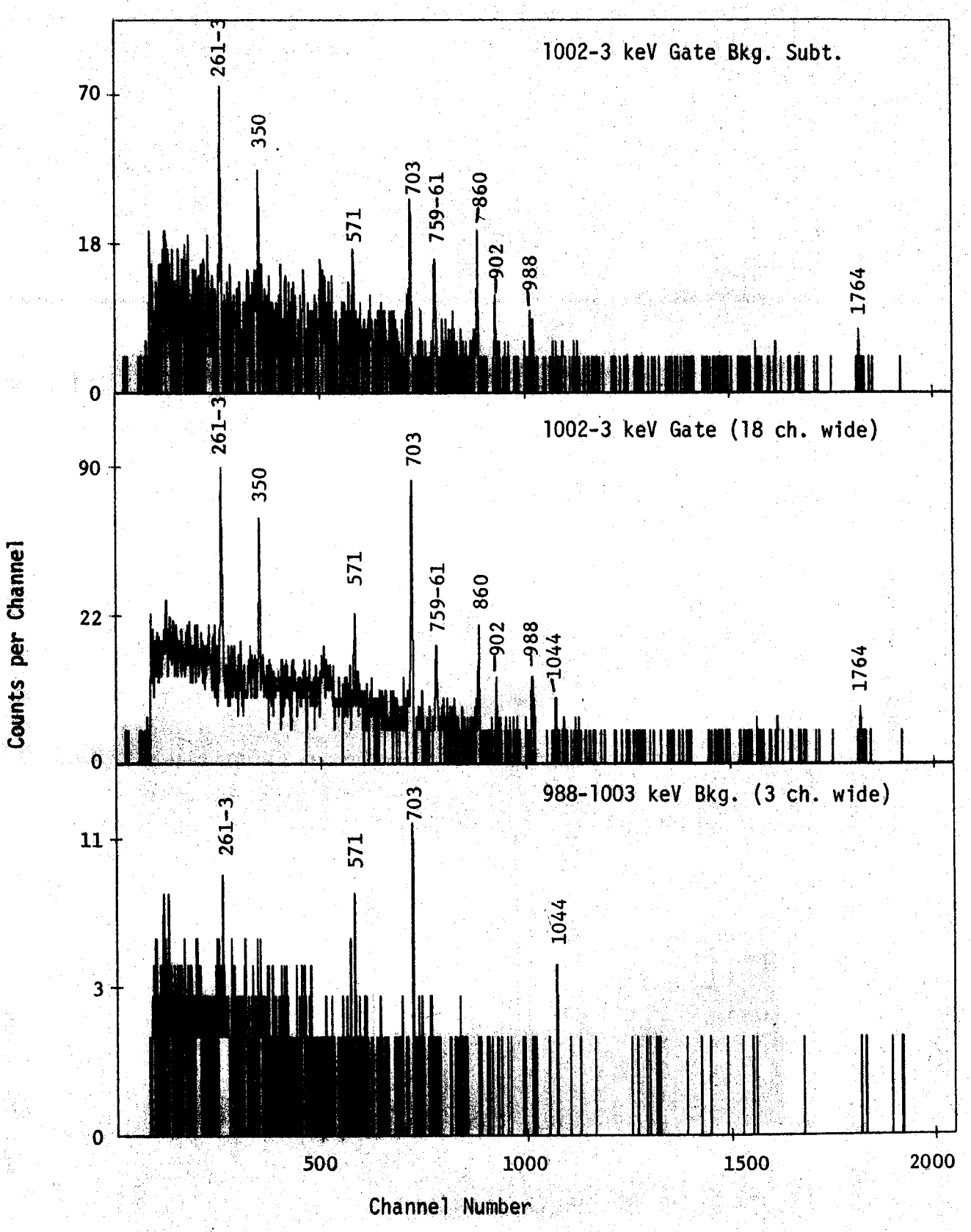

Figure 3. ^{205}Bi Coincidence spectra continued.

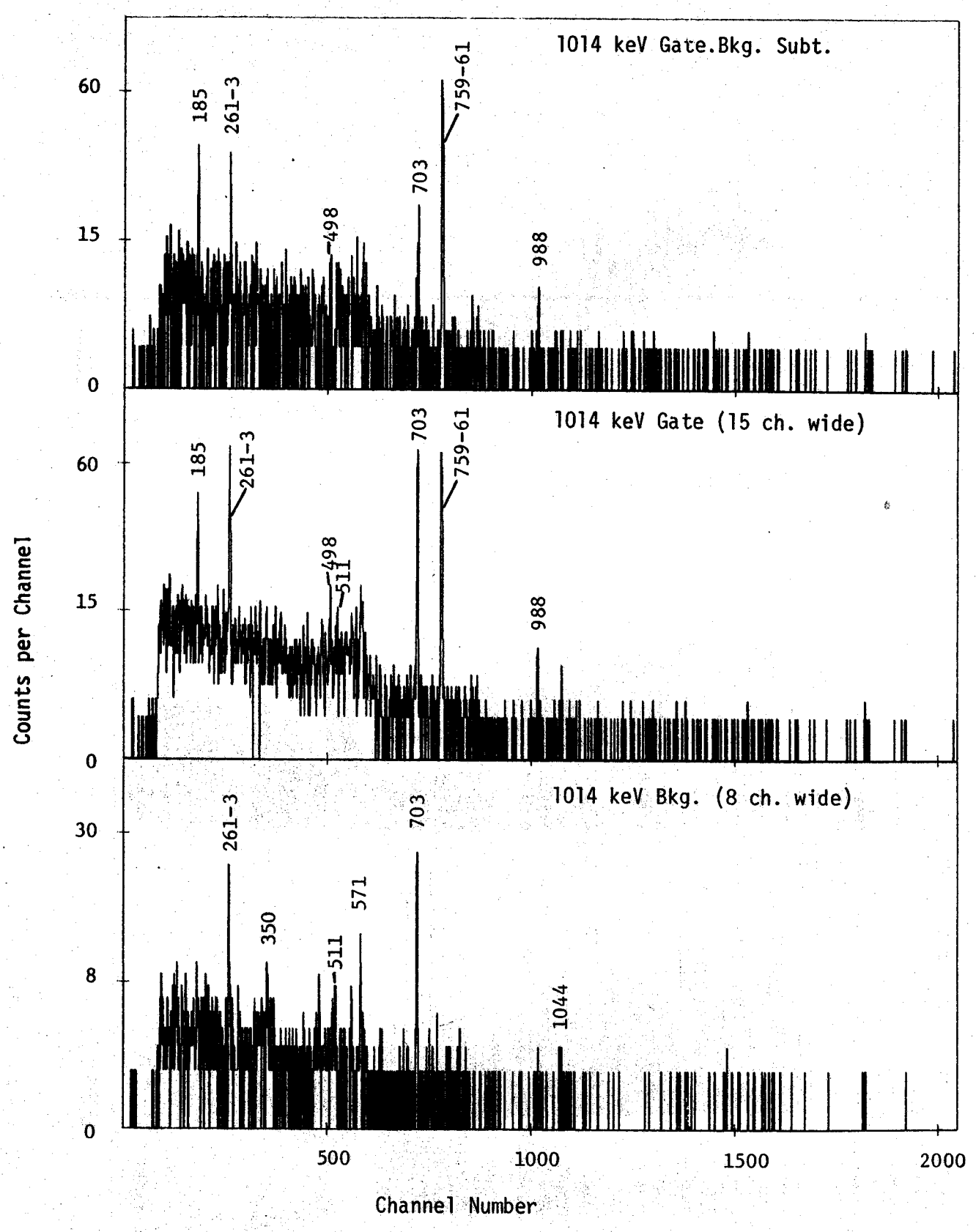

Figure 3. ^{205}Bi Coincidence spectra continued.

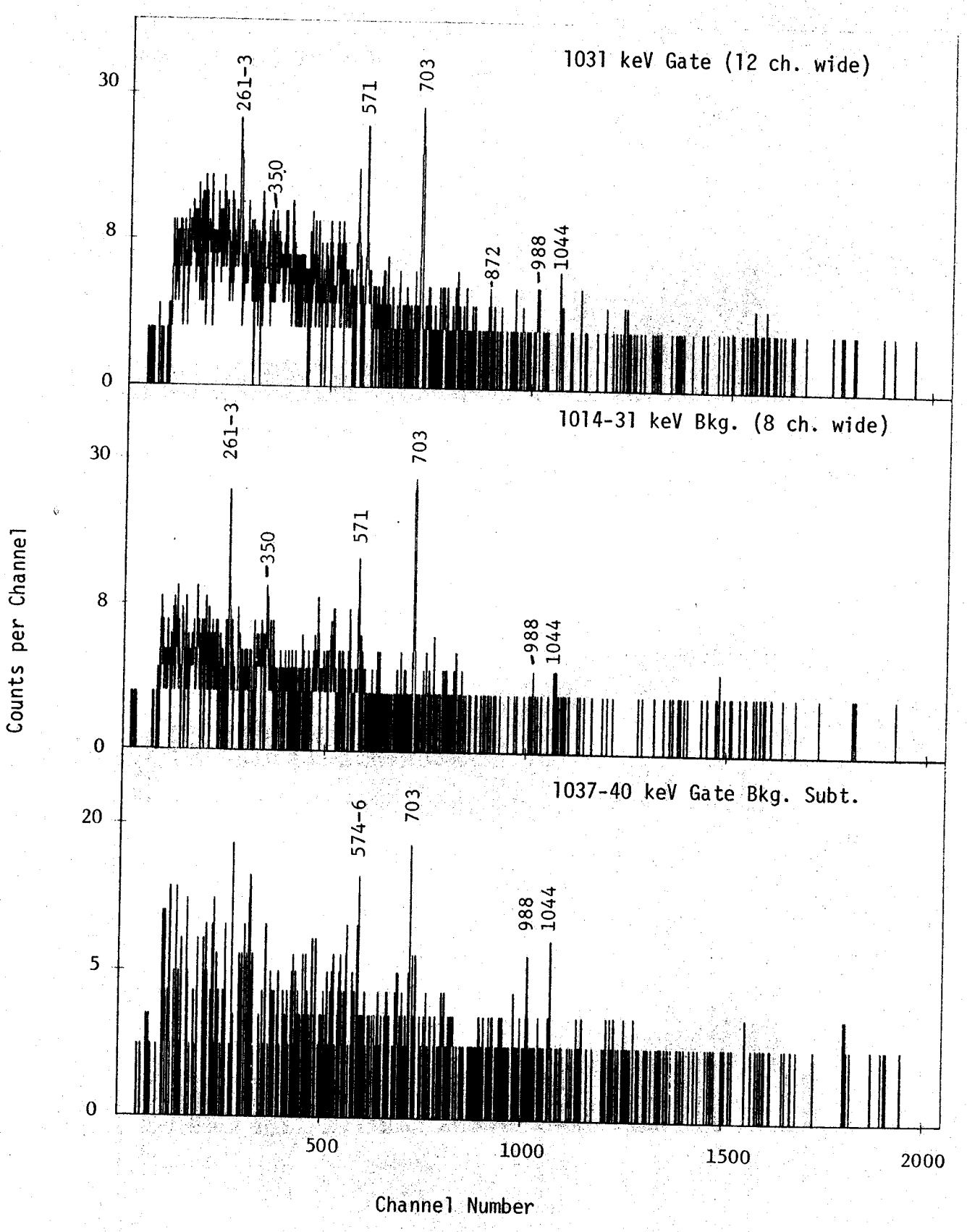

Figure 3. ^{205}Bi Coincidence spectra continued.

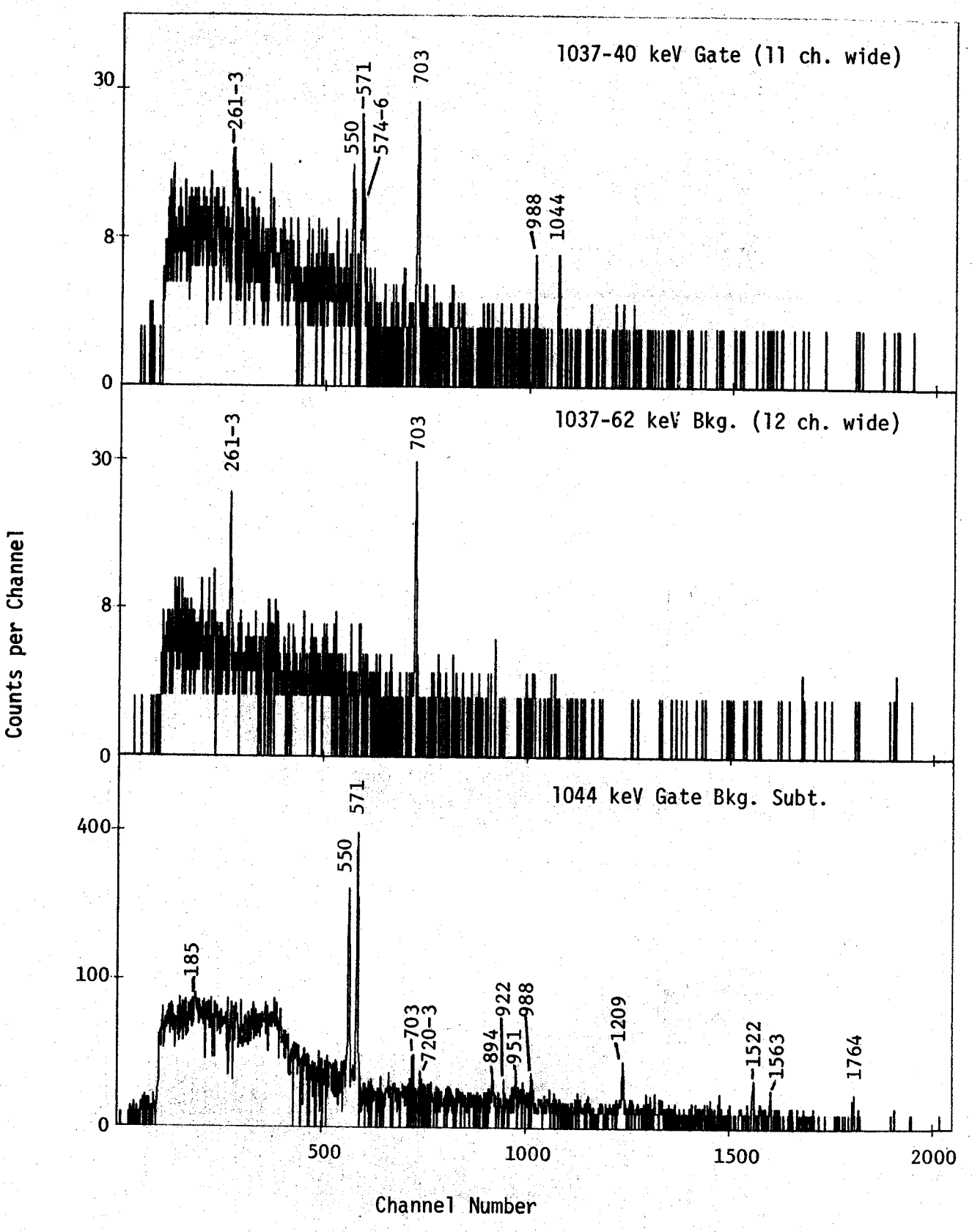

Figure 3. ^{205}Bi Coincidence spectra continued.

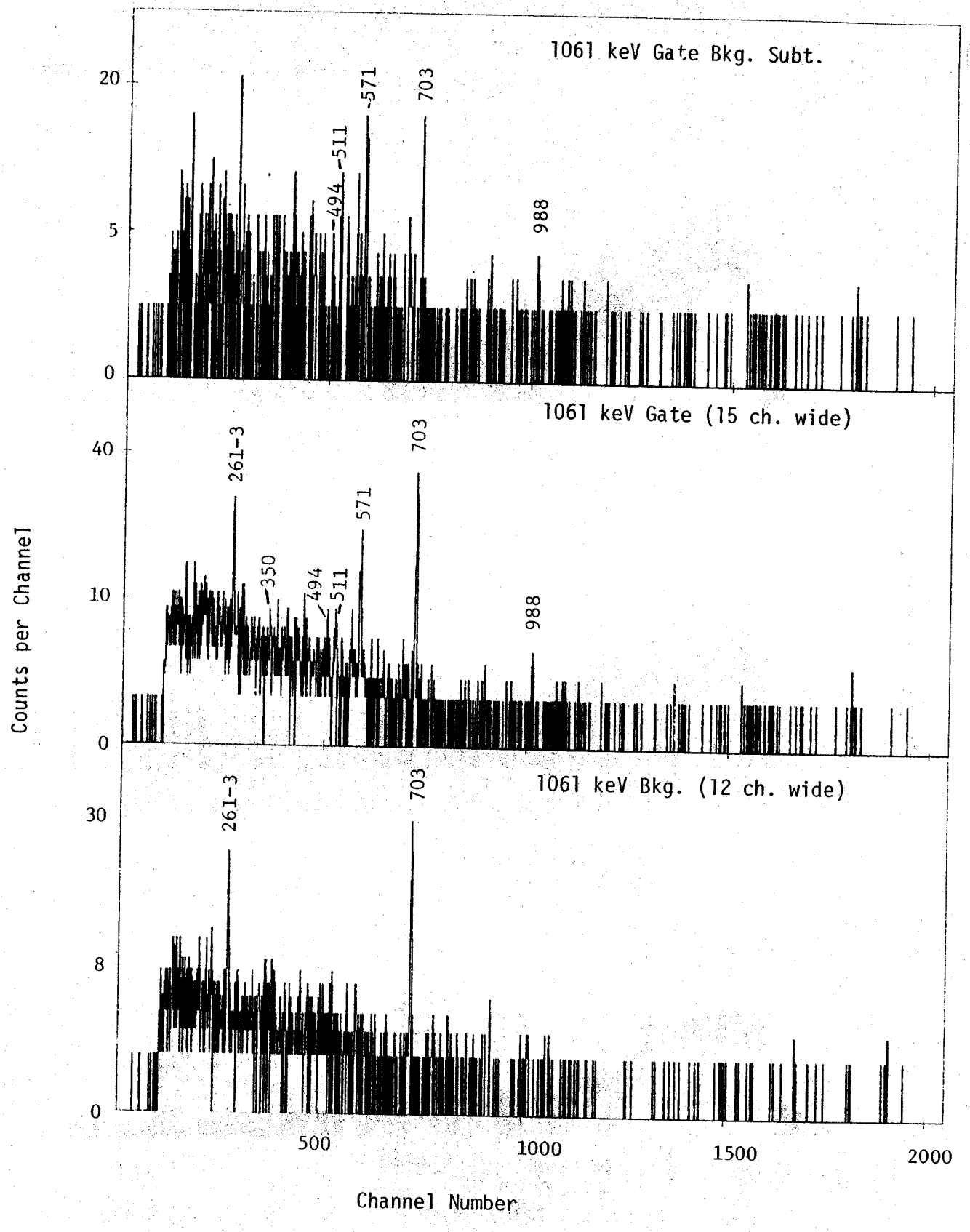

Figure 3. ^{205}Bi Coincidence spectra continued.

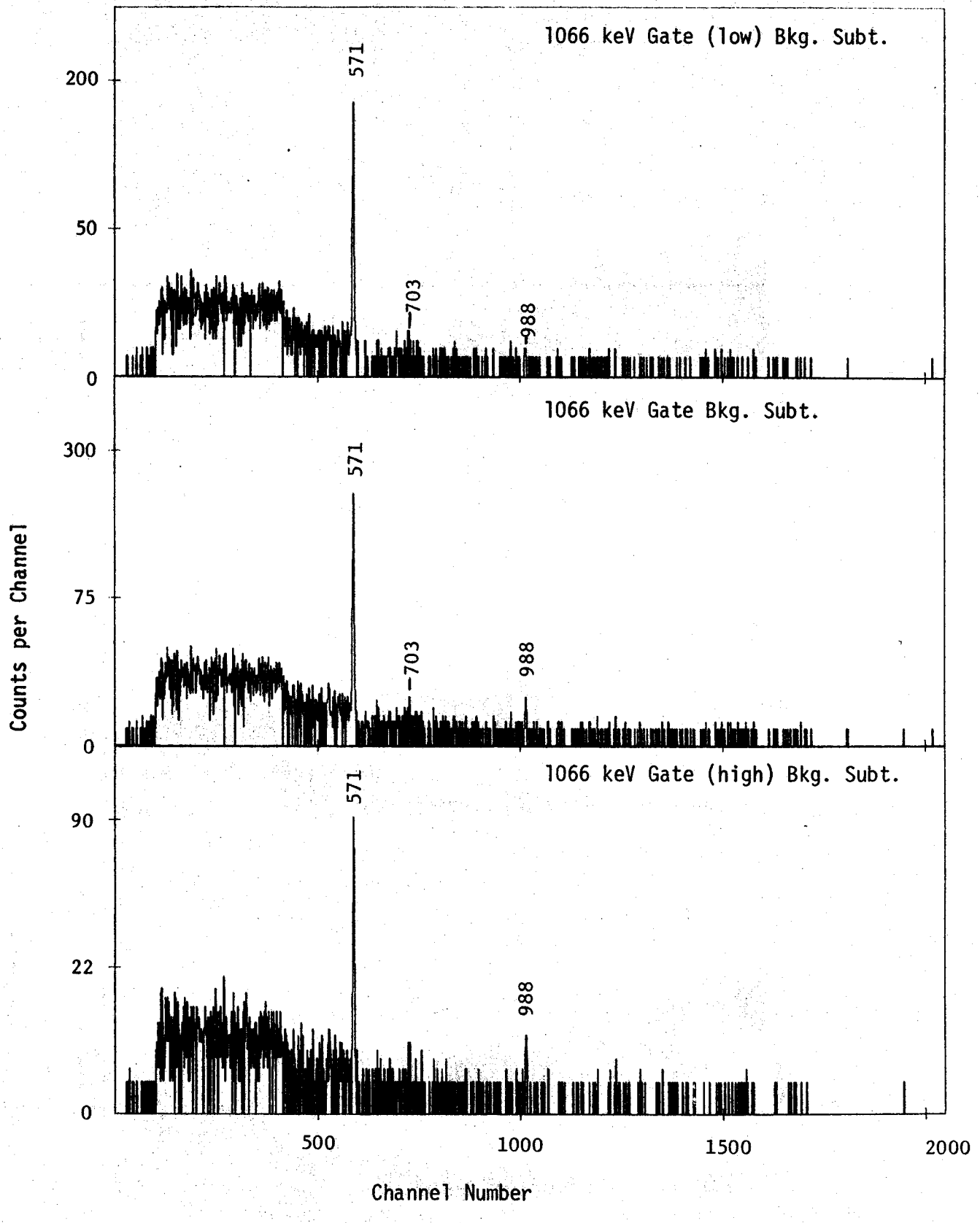

Figure 3. ^{205}Bi Coincidence spectra continued.

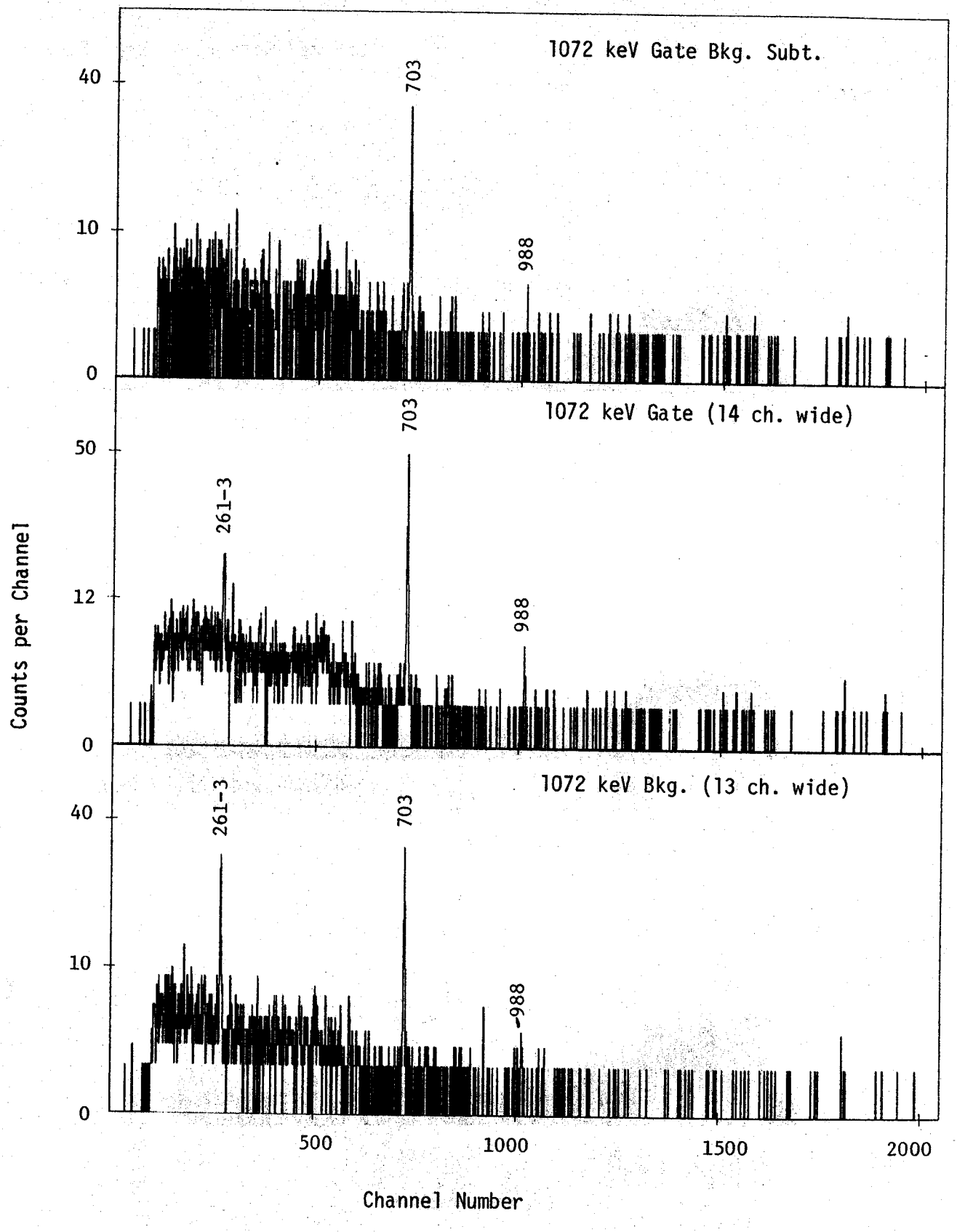

Figure 3. ^{205}Bi Coincidence spectra continued.

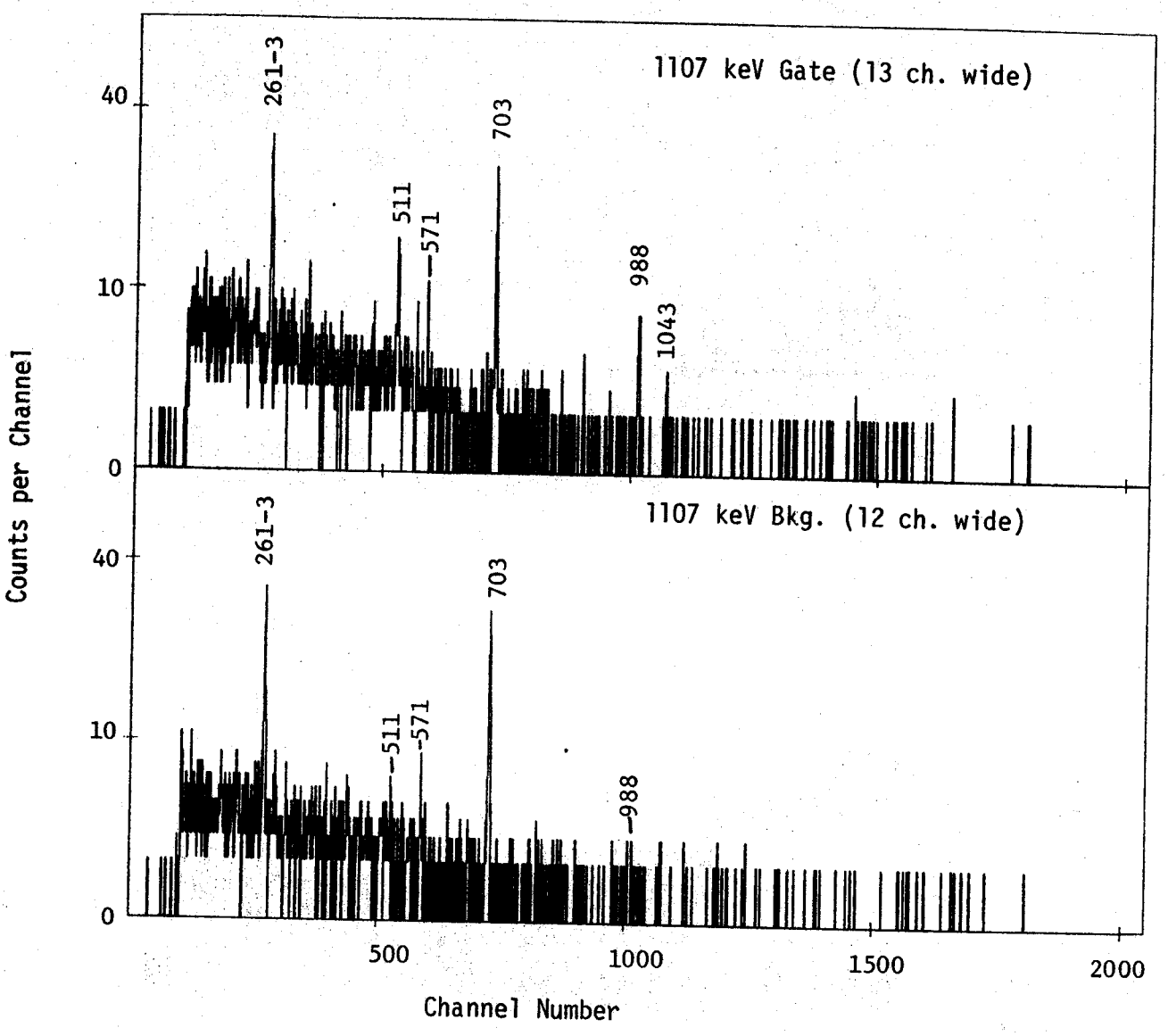

Figure 3. ^{205}Bi Coincidence spectra continued.

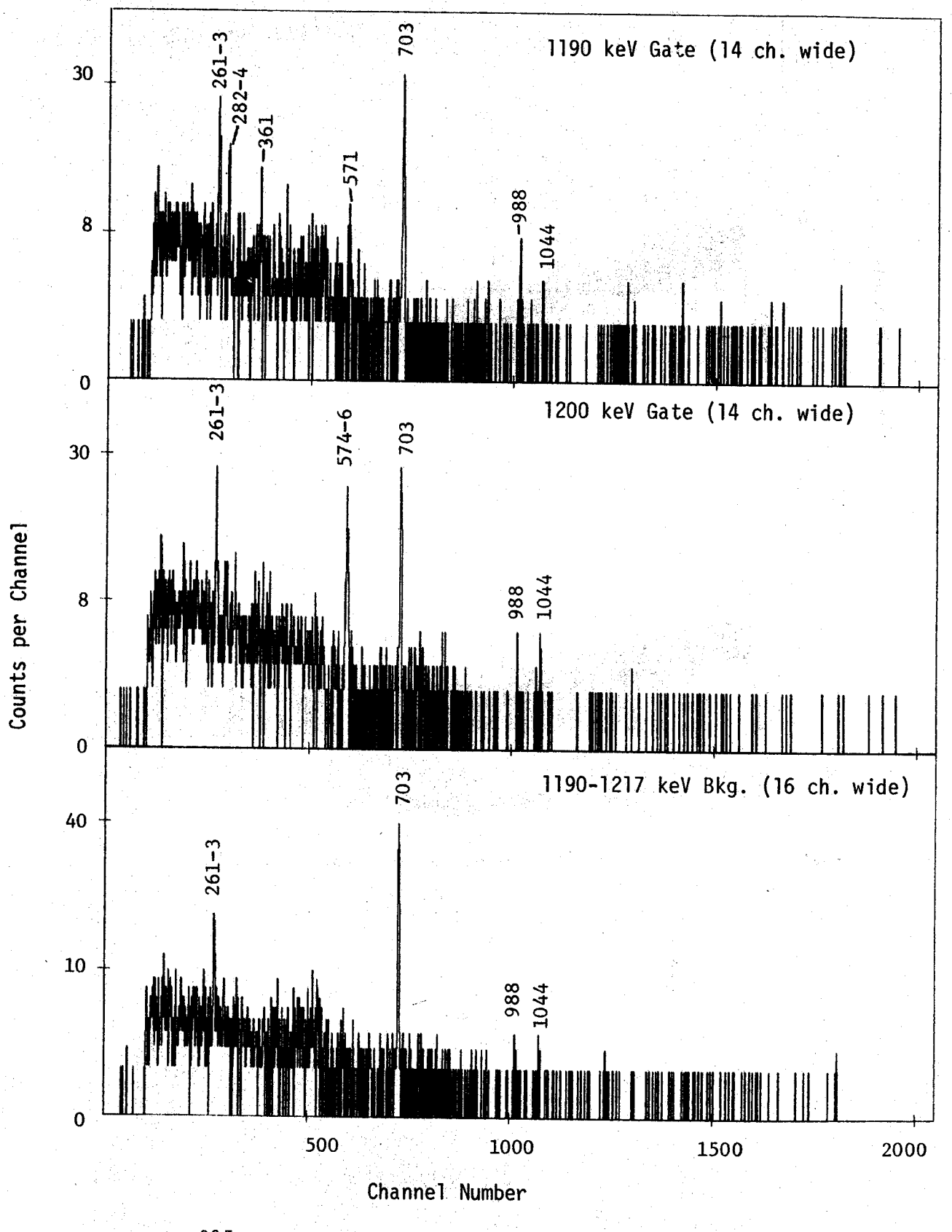

Figure 3. ^{205}Bi Coincidence spectra continued.

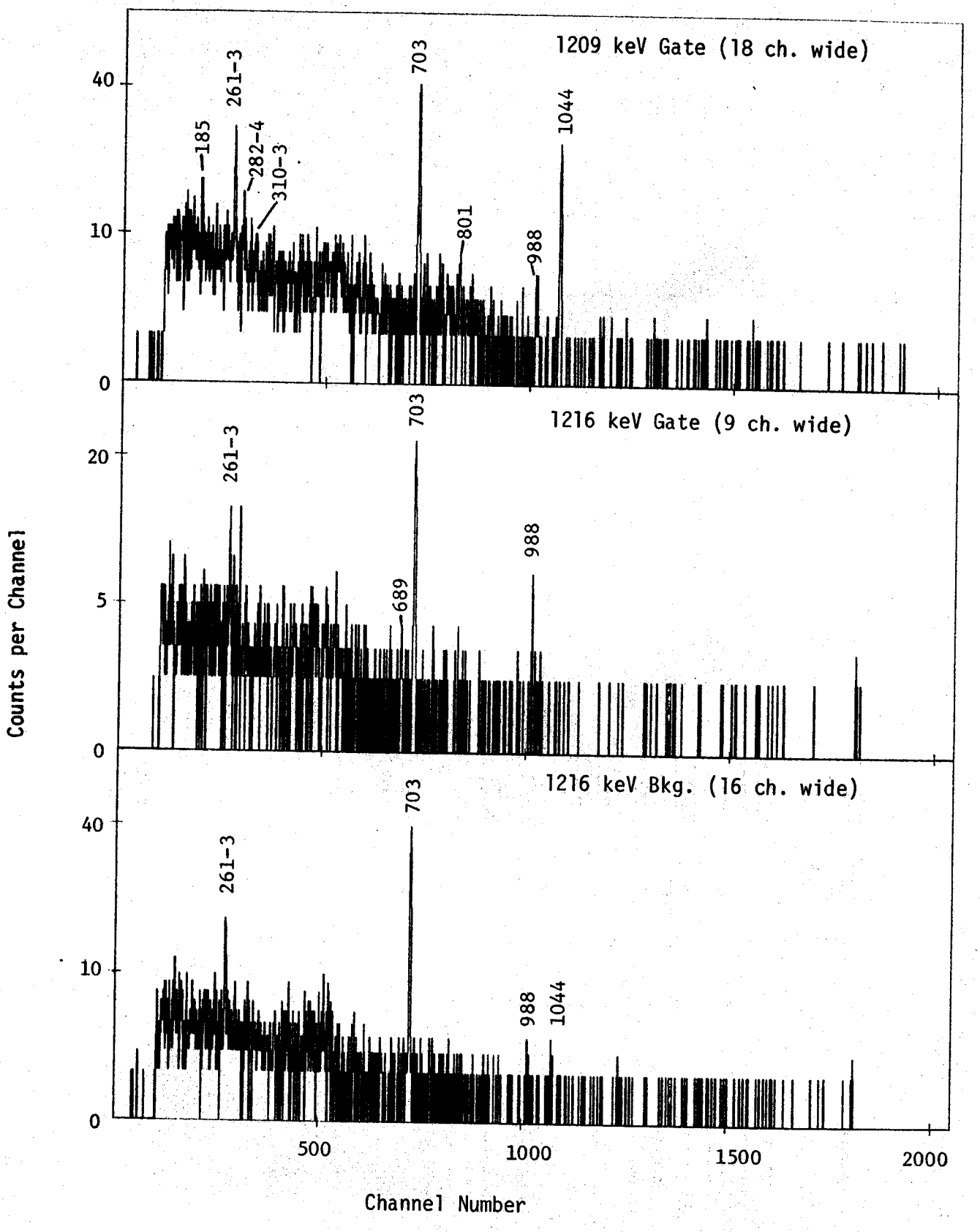

Figure 3. ^{205}Bi Coincidence spectra continued.

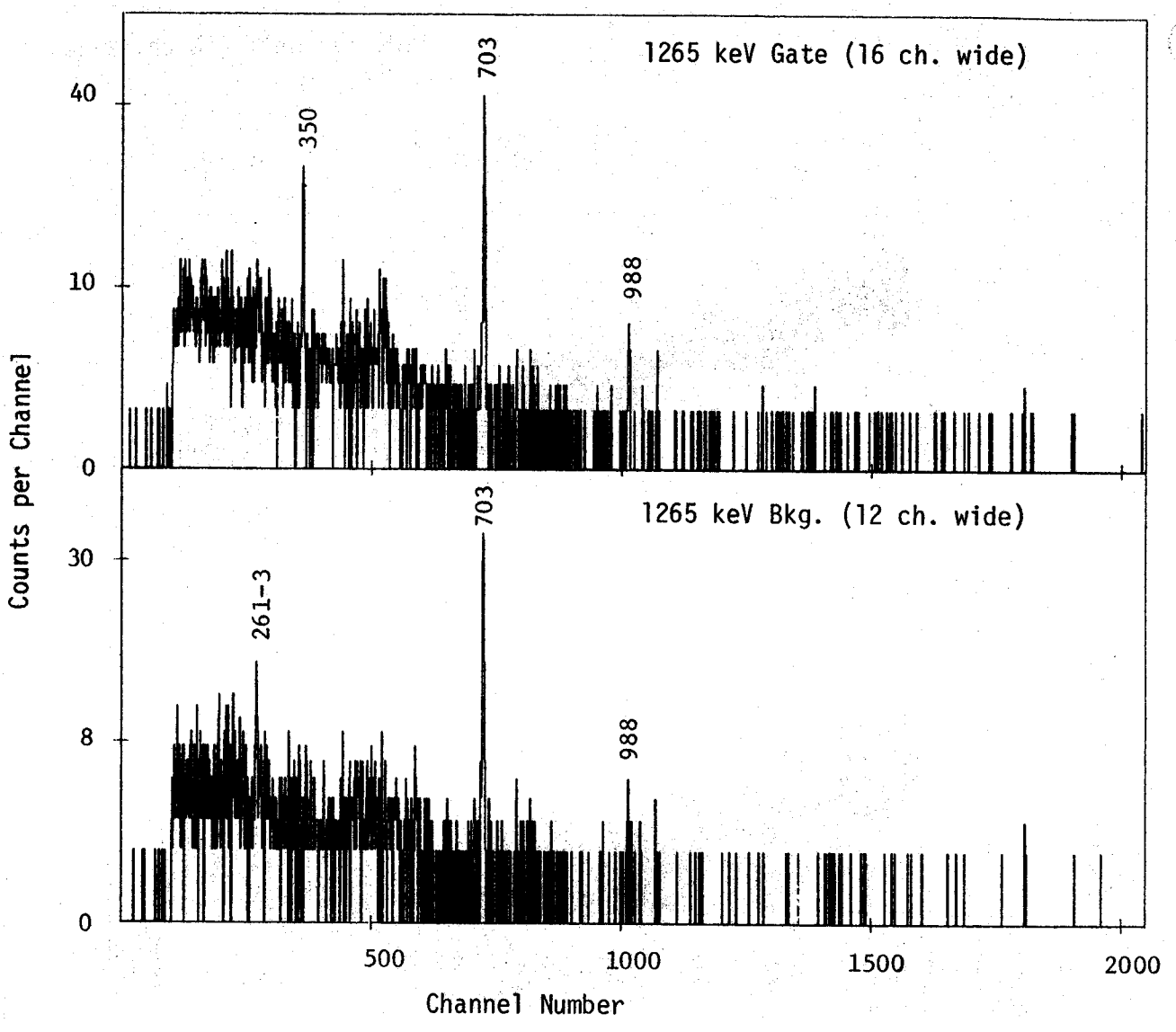

Figure 3. ^{205}Bi Coincidence spectra continued.

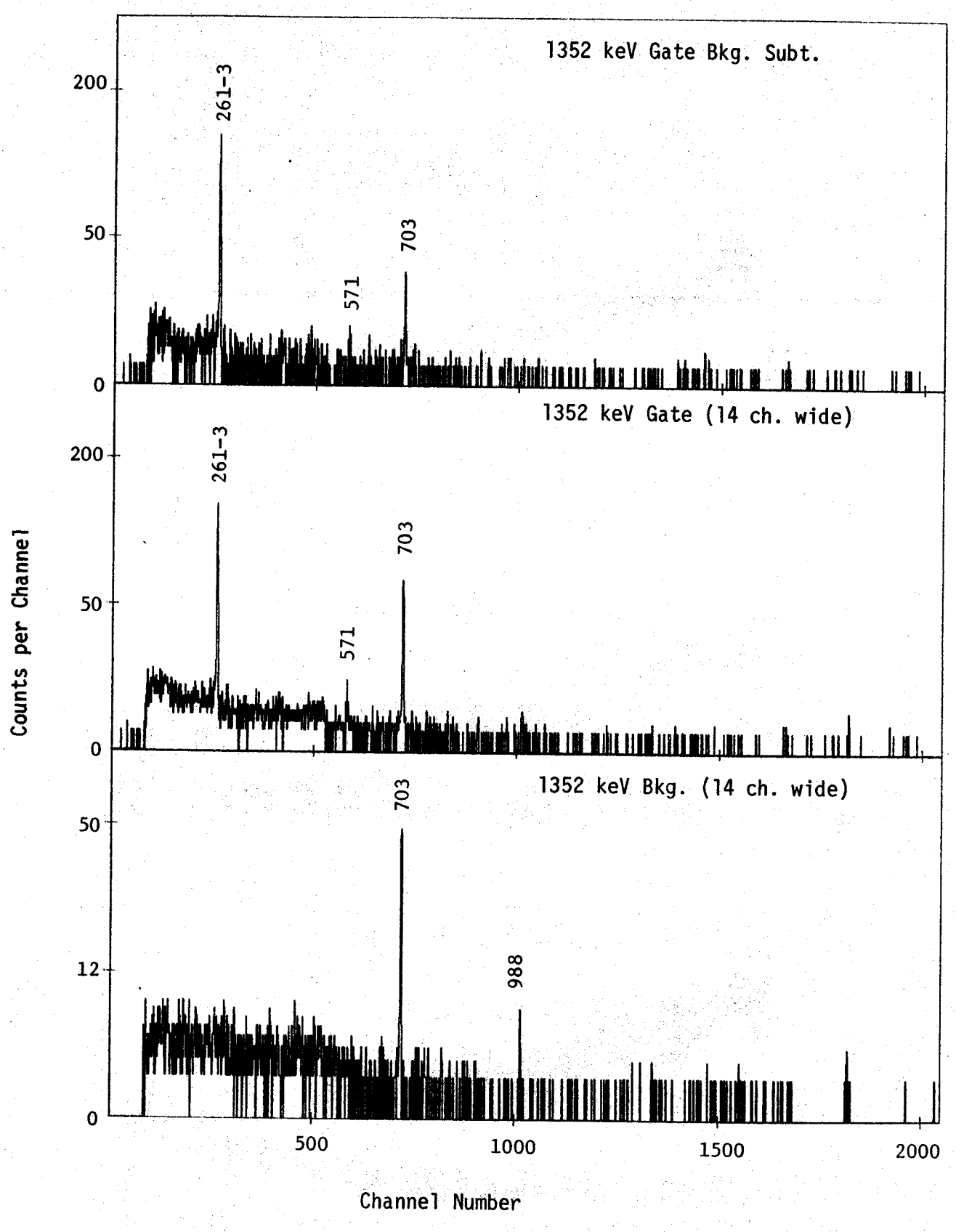

Figure 3. ^{205}Bi Coincidence spectra continued.

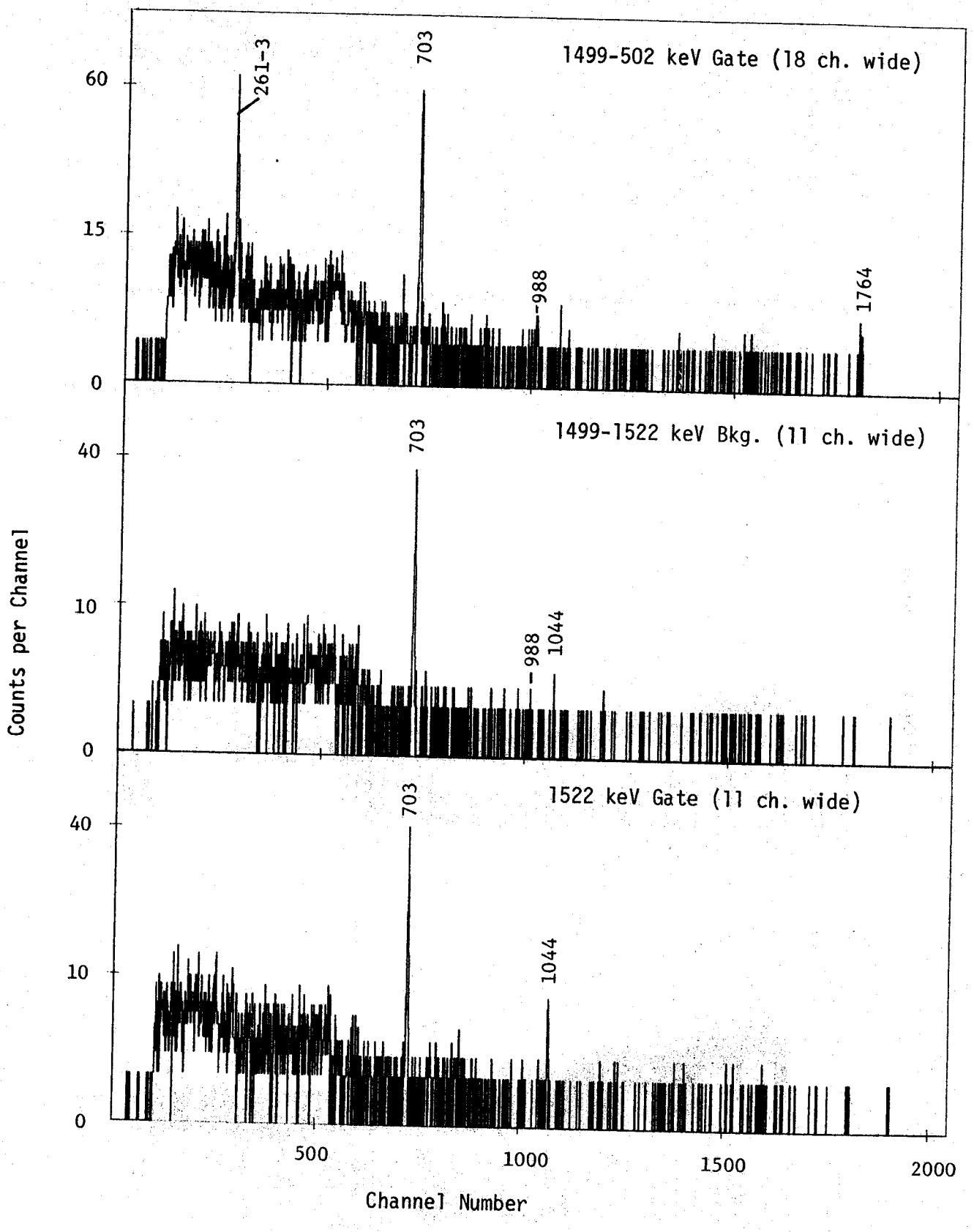

Figure 3. ^{205}Bi Coincidence spectra continued.

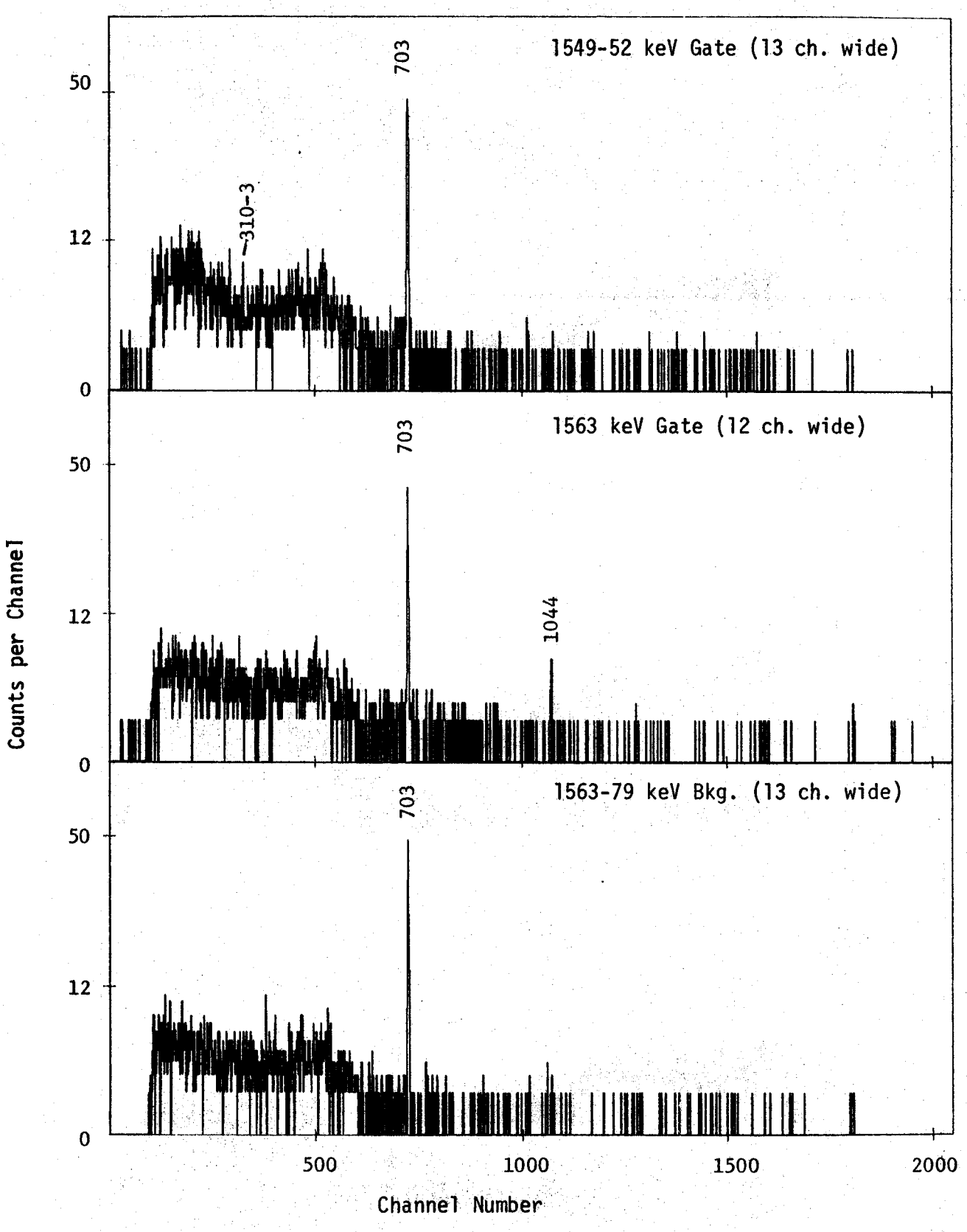

Figure 3. ^{205}Bi Coincidence spectra continued.

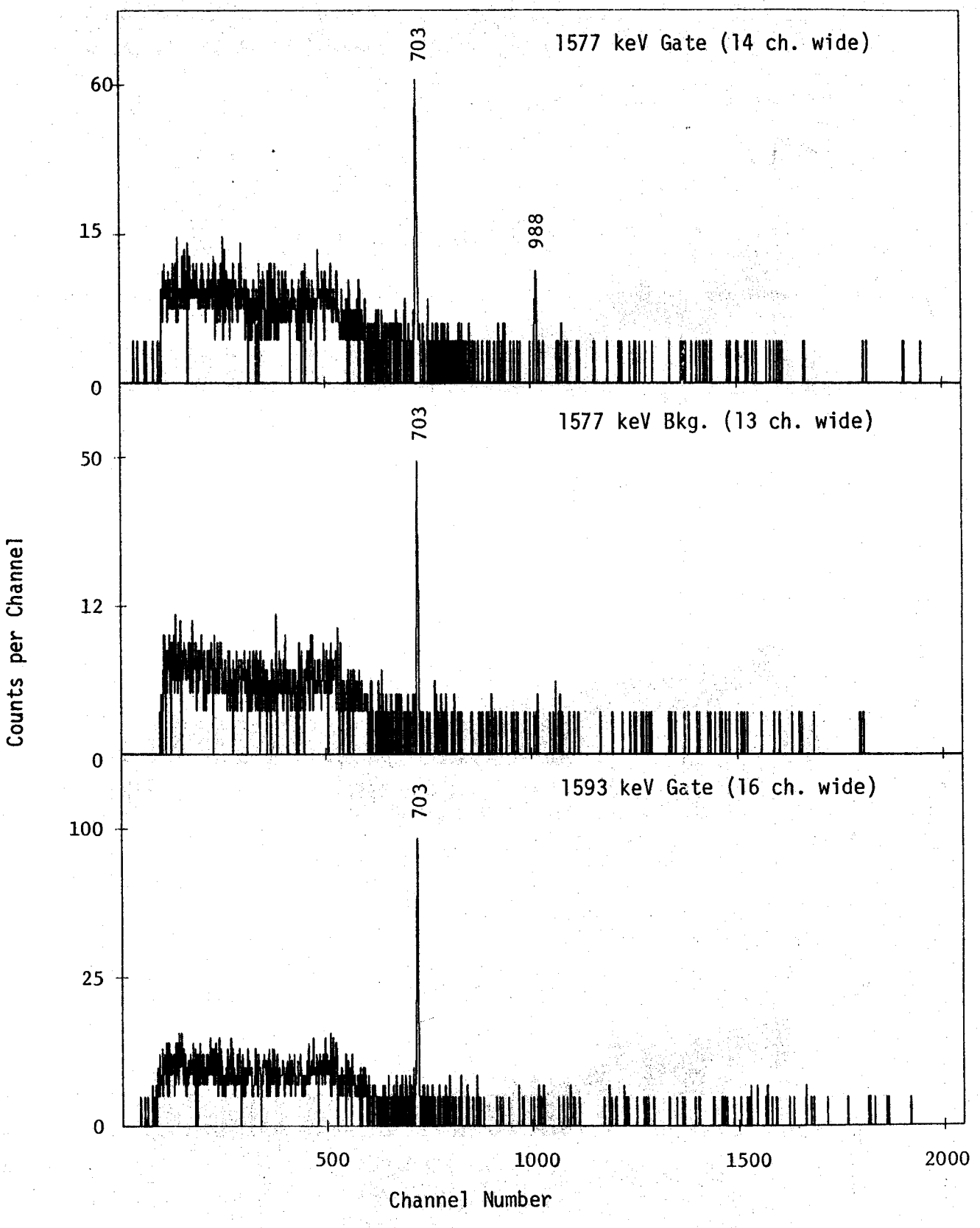

Figure 3. ^{205}Bi Coincidence spectra continued.

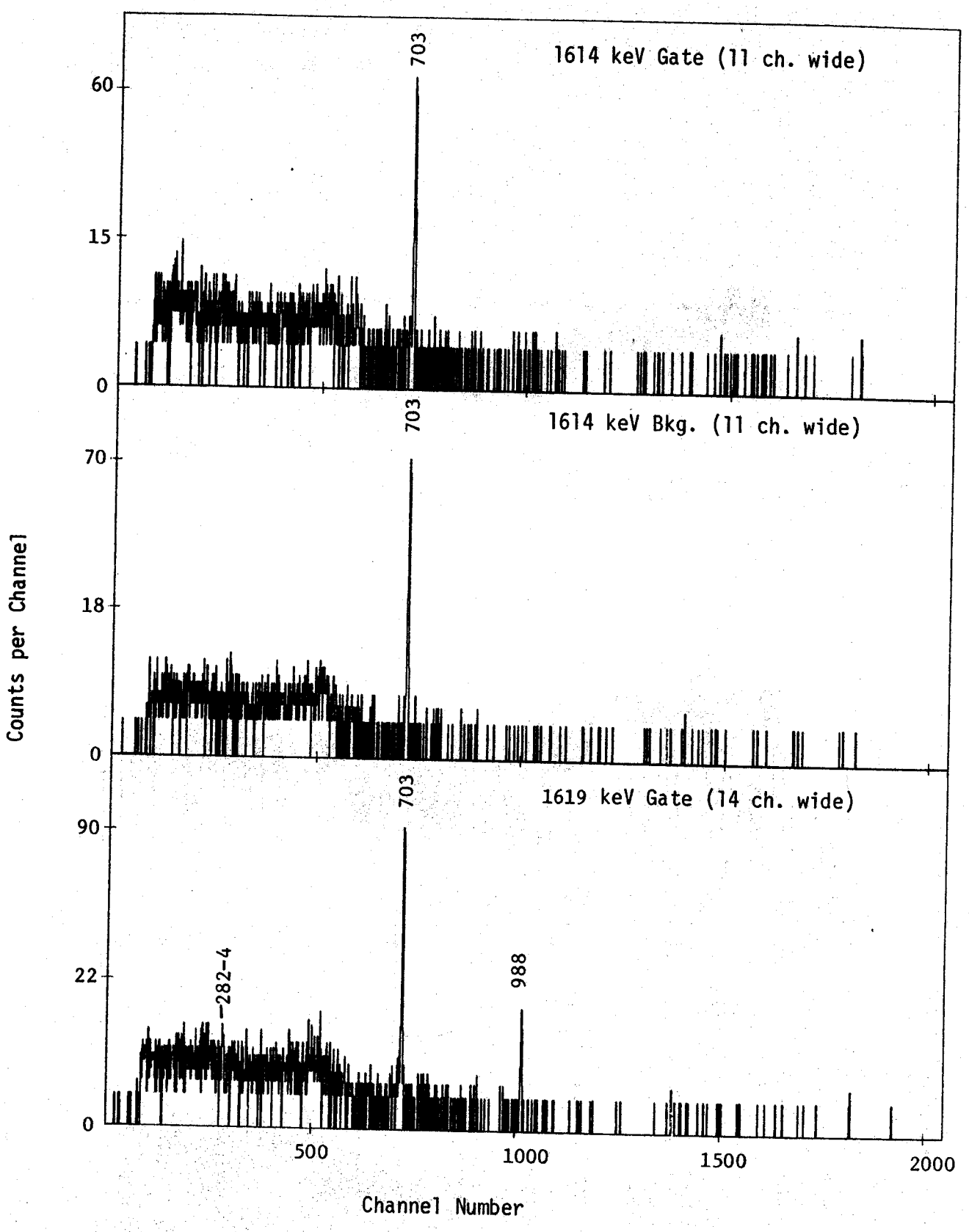

Figure 3. ^{205}Bi Coincidence spectra continued.

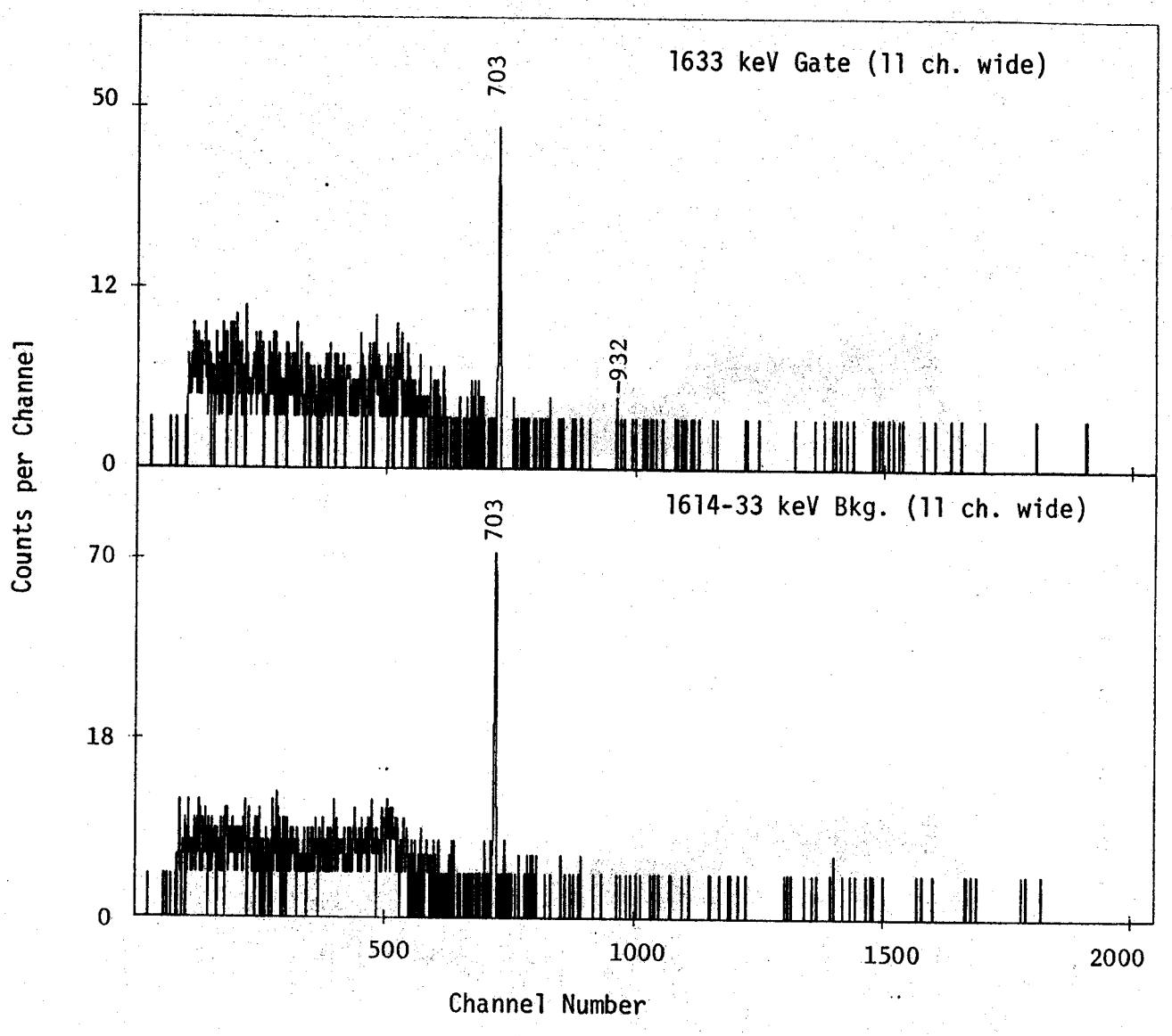

Figure 3. ^{205}Bi Coincidence spectra continued.

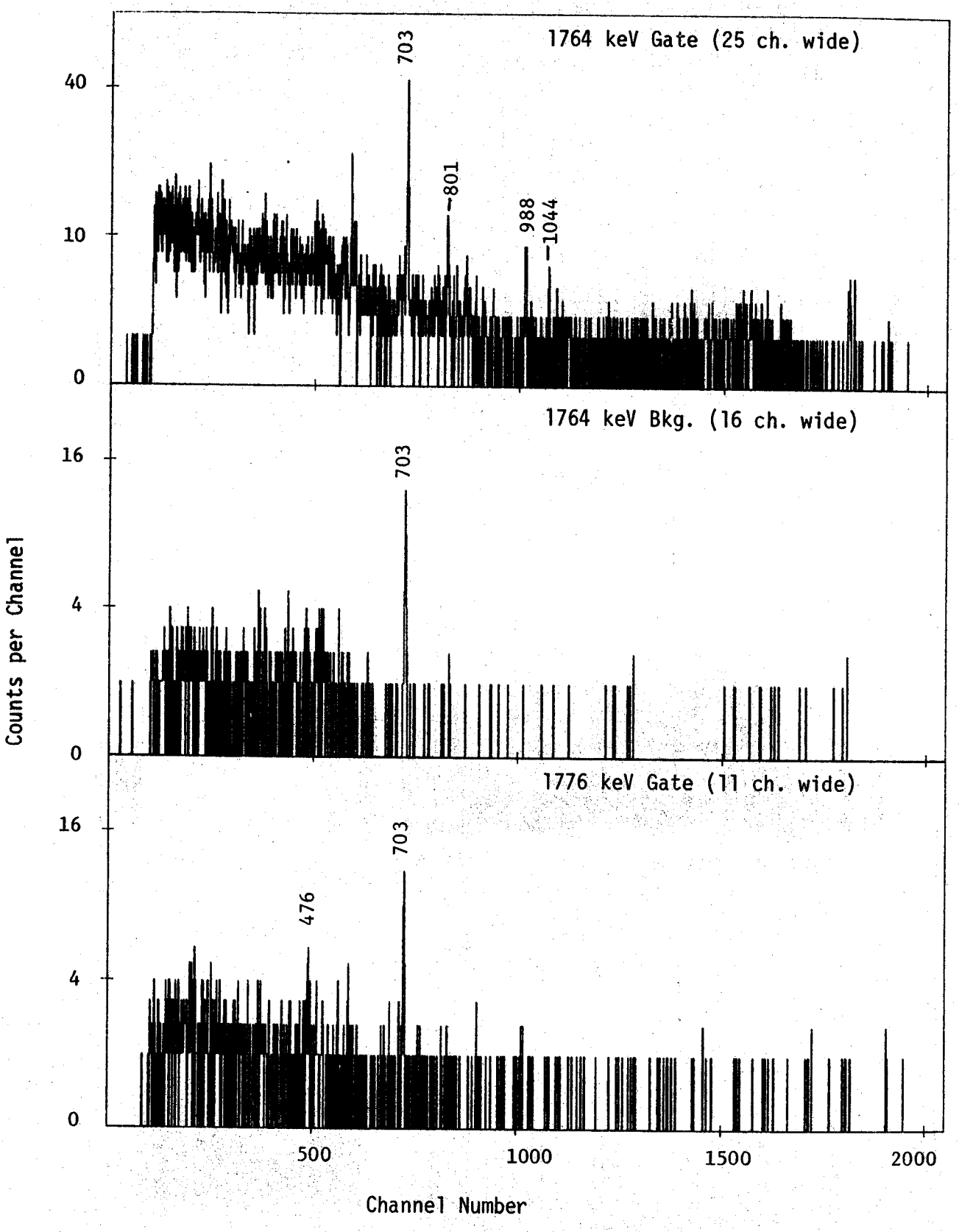

Figure 3. ^{205}Bi Coincidence spectra continued.

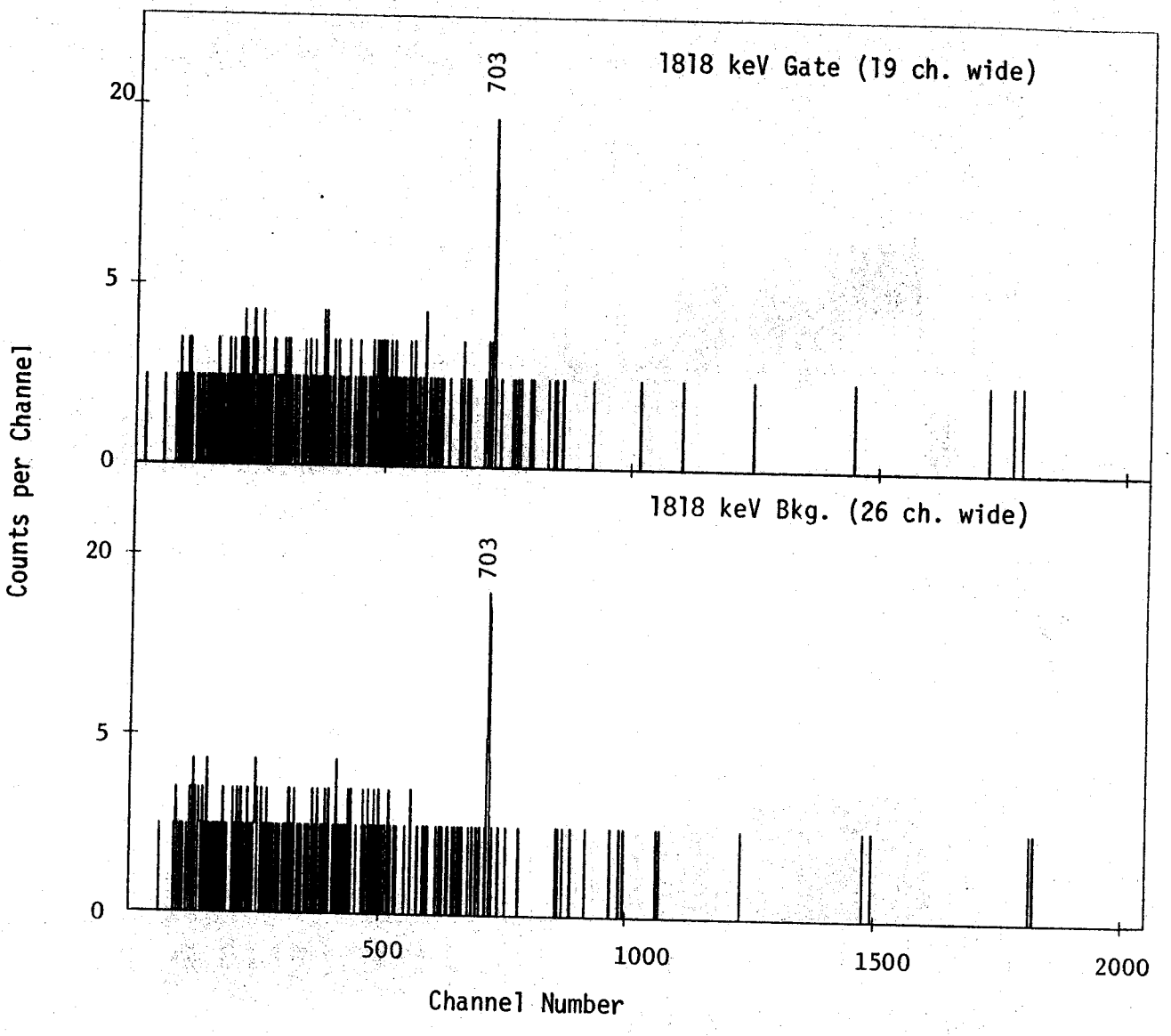

Figure 3. ^{205}Bi Coincidence spectra continued.

Table III - Summary of γ-γ Coincidence Results of ^{205}Bi Decay.

Gate Peak	Coincidence Peaks
115	282-4(P), 499(P)*, 511(D), 951(P), 988(P), 1499(D)
185	282-4(P), 574-6(D), 813(P), 1014(D), 1044(P)*
206	511(P), 860(P)
221	350(P), 1044(P)
236-7	See possible ∿360 and 703 peaks
261-3	350(D), 499(D), 550(D), 571(D), 626(P)* 781(D), 1002-3(D), 1014(P), 1209(P), 1352(D), 1502(D)
282-4	115(P), 185(D), 310-3(P), 350(P), 511(D), 550(D), 571(D), 626(P), 703(D), 759-61(D), 860(P), 1107(P), 1522(P), 1619(P)
310-3	261-3(P), 494(P), 703(P), 1209(P)
350	221(D), 261-3(D), 499(P), 562(P), 570(P)* 689(D), 951(P), 1002-3(D), 1043(D), 1265(D)
361	(See possible 310-13, 921, 978, 1043 peaks)
494	745(D), 1351(P)*
498	261-3(D), 282-4(P), 988(P)*, 1014(P) (possibly see 1717)
511	115(D), 206(P), 282-4(P), 703(P), 988(D) 1107(D)
550	261-2(D), 282-4(D), ∿376(P), 759-61(D) 781(D), 894(D), 971(P), 1044(D)
562	261-3(P)*, 350(D), 703(P)
571	185(D), 261-3(D), 282-4(D), 350(P), 759-61(D) 781(P), 814(P)*, 951(D), 1043(D)
574-6	185(D), 261-3(P)*, 350(D), 689(D), 814(P) 1014(P), 1200(D) (possibly 1717)

Gate Peak	Coincidence Peaks
580	894(D), 971(D)
609	(See definite 796 and see possible 511, 627 1043 peaks)
627	282-4(P), 703(P), 951(P), 988(D)
647	(See possible 703, 910-3, 932, 988 peaks)
661	703(P), 860(P)
689	350(D), 574-6(D), 860(P)*
703	282-4(D), 310-3(P), 511(D), 796(P), 860(P) 872(D), 890(D), 911(D), 1002-3(P), 1072(D) 1549(D), 1818(P), 1862(D), 1904(D)
717	282-4(P), 703(P), 860(D), 902(D), 988(D)
720-3	(See possible 828-31, 860, 1044, 1209 peaks)
729	745(P), 1044(P)*
745	494(D), 729(P), 807(P)
759-61	282-4(D), 550(P), 571(P), 813(D), 853(P) 1002-3(P), 1014(D)
771	626(P), 1209(P)*
781	261-3(D), 550(D), 571(D), 626(P)*, 1209(P)
788	646(P), 988(P)
796	115(P), 609(D), 703(P), 1209(P)*
801	1209(P)*, 1764(P)
807	745(P)
814	185(D), 759-61(D), 1200(P)*
828-31	(See probable 571, 720-3, 910-3, 1208, 1521 and see possible 511, 759-61, 987, 1043 peaks)
853	∿710(P), 759-61(P)

Gate Peak	Coincidence Peaks
860	205(P), 282-4(P), 661(P), 703(P), 717(D) 988(P), 1002-3(D)
872	703(D), 988(P)*, 1209(P)*
880	Only coincidence observed is with 803 from ^{206}Bi
890	703(D), 894(P), 971(P), 988(P)*
894	185(P), 282-4(P), 350(P)*, 550(D), 580(D) 759-61(P), 890(D), 1044(P), 1209(P)*
902	717(P), 1002-3(D), 1209(P)*
911	703(D), 951(P)
922	1044(D)
932	647(D), ∿420(P)
951	261-3(P), 350(D), 571(D), 626(D), 703(P) 720-3(P), 911(D), 988(P), 1044(P), 1352(D) 1614(D)
971	350(P)*, 550(D), 580(D), 1776(P)*
978	361(P), 988(P)
988	115(P), 511(D), 626(D), 646(P), 717(D) 788(P), 813(P), 860(P), 872(P)*, 902(P) 951(P), 1066(P), 1577(D), 1619(D)
1002-3	261-3(D), 350(D), 703(P), 759-61(P), 860(D) 902(D)
1014	185-(P), 261-3(P), 498(P), 574-6(P), 759-61(D)
1031	872(P)
1037-40	574-6(P)
1044	185(P)*, 550(D), 571(D), 720-3(P), 894(P) 922(P), 951(P), 1209(D), 1552(D), 1563(P)
1061	(See possible 350, 494, 511, 571 peaks)

Gate Peak	Coincidence Peaks
1066	511(P), 988(P)
1072	703(D)
1107	511(D), 988(D)
1190	282-4(P)*, 361(P)
1200	574-6(D)
1209	185(P), 282-4(P), 310-3(P), 703(P), 801(P)* 1044(D)
1216	∿680(P), 988(D)
1265	350(D)
1352	261-3(D)
1499-502	115(P), 261-3(D), 988(P)*
1522	282-4(P), 703(P), 1043(D)
1549-52	310-3(D), 703(P)
1563	1044(D)
1577	988(D)
1593	(no significant peaks)
1615	(no significant peaks)
1619	282-4(D), 703(P), 988(D)
1633	(See a possible 932 peak)
1717	(See a possible 574-6 peak)
1764	801(P)
1776	476(P)
1818	703(P)
1862	703(D)
1904	703(D)

NOTES ON TABLE:

Energies are rounded off to nearest keV.
(D) corresponds to seeing a definite coincidence.
(P) corresponds to seeing a probable coincidence (note further that peaks with strong singles intensities are generally listed as probable).

(*) corresponds to seeing a coincidence that is inconsistent with the proposed decay scheme. In many cases it is possible to explain the presence of these peaks.
(__) coincidence peaks that are underlined correspond to gates that see the present gate peak as a coincident peak.

Figure 4. Gamma-gamma sum coincidence spectra generated from mega-channel coincidence data.

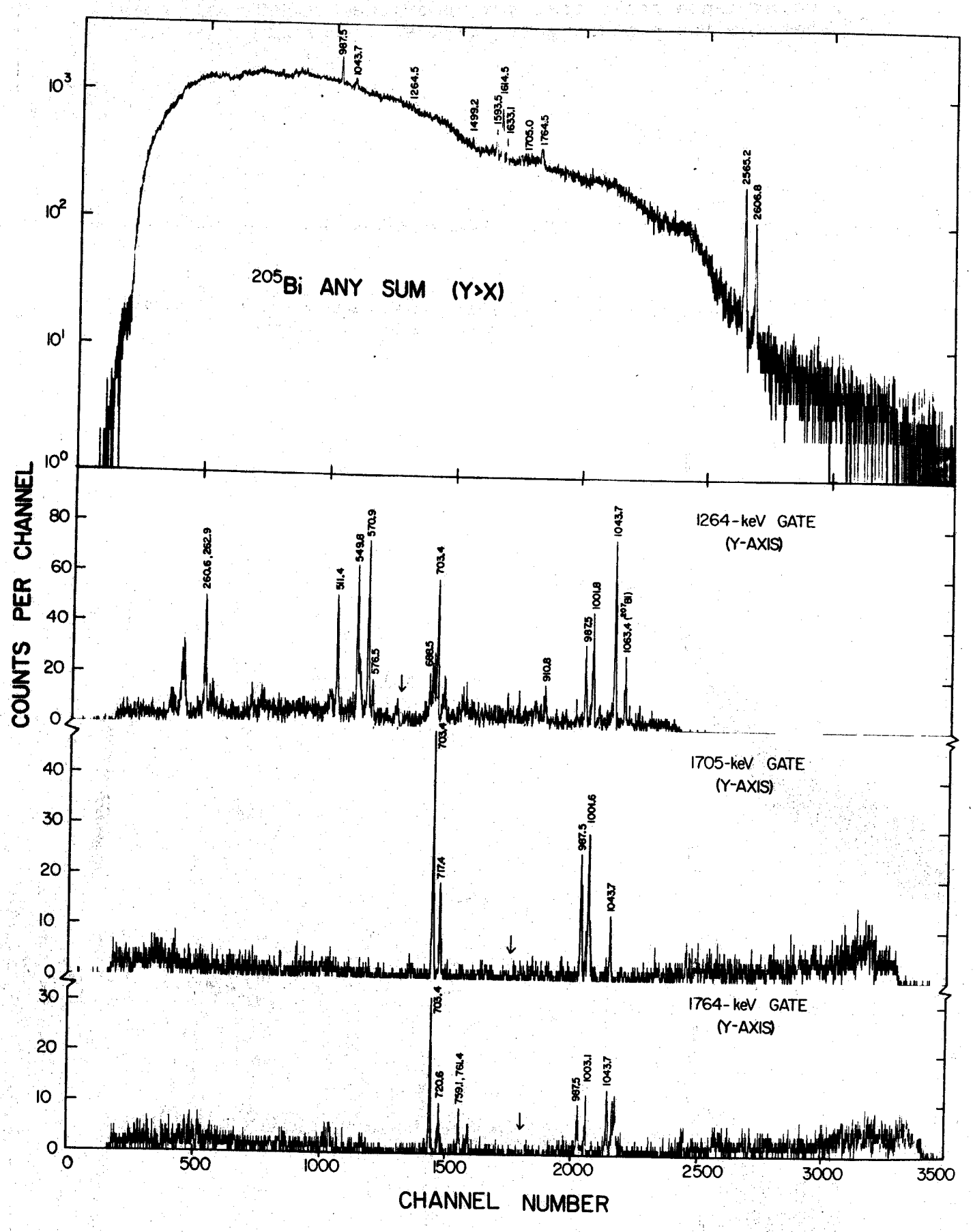

side of our megachannel coincidence experiment. Our anti-coincidence experiment used the 2.5% Ge(Li) detector in anti-coincidence mode with a 3"X3" NaI(Tl) detector and a 8"X8" NaI(Tl) split annular detector. The source was placed between the 2.5% Ge(Li) detector and the 3"X3" NaI(Tl) detector, both inside the 8"X8" NaI(Tl) annulus. The results of these runs are listed in Table IV and their primary use was to confirm assignments made in our decay scheme.

On the basis of these coincidence results we have definitely placed 80 transitions in our first confidence decay scheme (Figure [8]). Also, less conclusive coincidence data helped place 14 of the 27 additional transitions included in our second con fidence decay scheme (Figure [9]).

TABLE IV

Gamma Anticoincidence and Any coincidence Intensities

Energy (keV)	Intensity Singles	Intensity Anticoinc.	Intensity Any Coinc.
115.2	0.24	----	1.05
122.9	0.02	----	0.22
185.1	0.29	----	A
205.8	0.09	----	0.34
221.2	0.08	----	0.27
236.1	0.18	----	0.44
260.6	3.41	1.59	8.45
262.9	1.16	0.60	2.75
282.3	1.34	0.42	3.94
284.2	4.94	2.51	11.20
310.4	0.26	0.16	0.73
313.1	0.18	0.08	
349.6	1.55	0.60	4.76
361.5	0.16	0.12	0.31
488.4	0.08	0.08	----
493.6	1.12	0.60	2.59
498.6	0.53	0.20	A
511.4	3.30	1.74	12.75
549.8	8.78	5.17	19.41
561.6	0.12	----	0.89
570.9	12.92	A	A
574.0	1.87	0.81	6.54
576.5	0.73		
579.8	16.67	20.07	6.06
609.0	0.11	0.10	0.90
626.7	1.81	1.06	3.90
645.8	0.25	0.12	0.99
661.3	0.10	----	1.04
688.5	0.64	0.18	2.22
703.4	100.00	100.00	100.00
717.4	0.91	0.42	2.73

Energy (keV)	Intensity Singles	Intensity Anticoinc.	Intensity Any Coinc.
720.6	0.33	0.23	A
723.6	0.52	0.31	1.46
729.5	0.17	0.11	0.39
745.1	2.03	1.33	3.05
759.1	3.81	2.08	8.81
761.4	2.21	1.13	6.00
770.9	0.15	0.05	0.14
780.9	1.77	0.51	6.58
787.9	0.32	0.36	1.27
795.6	0.36	0.08	2.32
800.8	0.62	0.50	----
806.9	0.55	0.42	1.73
813.8	1.52	0.72	3.72
828.2	0.98	1.05	1.46
847.6	0.04	0.11	----
852.8	0.16	0.22	----
860.1	1.40	0.47	5.85
871.8	1.30	0.66	4.45
890.0	2.22	1.11	4.84
894.5	1.79	0.78	A
901.8	0.45	0.20	0.99
910.8	5.47	2.67	11.60
921.7	0.19	----	----
931.7	0.15	0.06	0.98
950.7	1.21	0.56	4.71
971.4	0.90	0.33	2.83
978.0	0.23	A	0.70
987.5	54.61	72.27	29.19
1001.6	0.83	0.67	6.16
1001.8	0.70		
1003.1	0.50		
1013.7	0.23	2.09	7.07
1014.4	3.31		
1031.2	0.16	----	1.41

Energy (keV)	Intensity Singles	Intensity Anticoinc.	Intensity Any Coinc.
1037.4	0.49	---	1.56
1043.7	25.30	11.83	54.16
1060.6	0.24	A	A
1065.8	0.34	A	A
1072.3	1.00	0.50	2.37
1107.5	0.33	0.14	1.62
1190.0	7.94	9.43	1.65
1199.8	0.65	0.27	1.42
1208.7	1.82	1.03	3.84
1216.3	0.29	0.22	0.54
1264.5	0.86	0.39	1.53
1351.6	3.50	1.95	6.85
1439.3	0.44	0.33	----
1499.7	0.56	0.55	1.69
1501.8	0.75	0.57	
1521.6	0.73	0.35	1.41
1549.6	1.05	0.35	2.99
1551.7	3.02	4.46	
1563.3	0.72	0.45	1.67
1577.4	0.50	0.45	1.54
1592.9	0.41	0.58	----
1614.5	7.92	10.33	2.20
1619.4	1.05	0.98	2.54
1764.5	121.2	141.26	19.76
1776.0	14.24	16.58	2.03
1818.2	0.20	0.12	0.81
1861.9	23.44	13.12	42.31
1903.5	9.30	5.25	16.33
1966.0	0.04	B	B
2565.2	0.18	B	B
2606.8	0.10	B	B

A = Unresolved from an interferring peak
B = Cut off end of spectra

C. Conversion Coefficients

Conversion coefficients were determined for those cases where electron data has been reported. Where possible, conversion intensities were taken from R. Stockendal's most recent studies of ^{205}Bi[ScM56, StR58, StR60, BeK64], however, conversion intensities were taken from other investigations[JoW71, FrA58, AlC70] when they were not reported by Stockendal. When there was serious disagreement between reported values, both were listed and used to calculate conversion coefficients. Conversion electron intensities were normalized to produce correct conversion coefficients for the ($1/2^+$ to $13/2^+$) 579.8-, ($5/2^-$ to $1/2^-$) 759.1-, and ($9/2^-$ to $5/2^-$) 987.5-keV transitions assuming these to be pure *E*2's. These transitions were chosen in preference to assuming the ($7/2^-$ to $5/2^-$) 703.4-keV transition to be a pure *E*2 because even a slight *M*1 admixture would shift the conversion coefficient considerably. Theoretical conversion coefficients of Hager and Seltzer[HaR68] were used for transitions below 1600 keV (the upper limit of their tables). Above 1600 keV theoretical conversion coefficients of Sliv and Band[SiK65] were used. Table V contains the transition data for ^{205}Bi along with multipolarity assignments we propose for these transitions where both photon and electron intensities were available. Transition intensities are suggested for all transitions included in our first confidence decay scheme. These intensities include an estimate of unreported *K*-, *L*-, and *M*- electron intensities. Figure 5 shows the experimental conversion coefficients superimposed over curves prepared from the theoretical conversion coefficients of Hager and Seltzer or Silv and Band.

In all cases except for the 310.4-, 1614.5, 1754.5-, 1776.0-, 2565.2-, and 2606.8-keV transitions, conversion coefficients falling near

TABLE V - ^{205}Bi Transition Data

Transition Energy (keV)	Gamma Intensity I_{703}≡100.	Electron Intensity[a] Line/intensity (ref.)	Internal Conversion Relations α_K; K:L and L ratios[b]	Multipolarity Assignment This work[c]	Ref.[d]	Others Assign.(Ref)	Transition Intensity[e] ($I_\gamma + I_{e^-}$)
2.328[f]	----	$N_{II}/3.4^{+1.1}_{-0.4}$[f] $N_{III}/4.8^{+1.5}_{-0.5}$[f]	–; N_{II}/N_{III}=0.70 ----	$E2$ ----	--- ---	$E2$[f] ----	11.45±0.71[g] ----
26.22[h]	----	L_I/17.1±1.0[i] L_{II}/0.52±0.23 L_{III}/10.6±0.7	–; $L_I/L_{II}/L_{III}$=1.6/0.05/1.0 ---- ----	$M2$ ---- ----	--- --- ---	$M2$[i] ---- ----	37.3 ±2.0 ---- ----
90.03[h]	----	L_I/0.17±0.03[i] L_{II}/0.06±0.02 L_{III}/0.09±0.02	–; $L_I/L_{II}/L_{III}$=2.0/0.7/1.0 ---- ----	$E1$ ---- ----	--- --- ---	$E1$[i] ---- ----	4.76±1.3 ---- ----
115.18	0.24±0.03	K/0.93±0.09[i] L_I/0.20±0.03 L_{II}/0.02±0.01	3.9±0.6; $K/L_I/L_{II}$=4.6/1.0/0.1 ---- ----	$M1$ ---- ----	$M1$ --- ---	$M1$[i] ---- ----	1.45±0.11 ---- ----
185.11	0.29±0.03	K/0.46±0.05[i] L_I/0.08±0.02	1.6±0.2; K/L_I=5.8 ----	$M1$ ----	$M1$ ---	$M1,E1$[i] ----	0.95±0.07 ----
205.85	0.09±0.02	----	----	----	---	----	0.21±0.05
221.17	0.08±0.02	K/0.058±0.017[j] L_I/<0.01	0.72±0.28; K/L_I >5.8 ----	$M1$ ----	$M1,E3$ ---	---- ----	0.15±0.(
236.07	0.18±0.05	K/0.09±0.02[j]	0.50±0.19; –	$M1(+E2)$	$M1,E3$	----	0.31±0.07
237.16[h]	----	K/0.01±0.003	----	----	---	----	----
260.56	3.41±0.55	K/1.84±0.17[i] L_I/0.33±0.03	0.54±0.10; K/L_I=5.5 ----	$M1$ ----	$M1$ ---	$M1$[i] ----	5.78±0.58 ----
262.89	1.16±0.12	K/0.53±0.06[i] L_I/0.10±0.02	0.46±0.06; K/L_I=5.3 ----	$M1$ ----	$M1$ ---	$M1$[i] ----	1.84±0.14 ----
282.26	1.34±0.35	K/0.58±0.06[k] K/0.38±0.04[l]	0.43±0.12; – 0.28±0.07; –	$M1$ $(M1+E2)$	$M1$ ---	$M1$[k] ----	1.97±0.36 (1.76±0.36)
284.22	4.94±0.55	K/2.18±0.22[k] K/1.33±0.13[l]	0.44±0.07; – 0.27±0.04; –	$M1$ $(M1+E2)$	$M1$ ---	$M1$[k] ----	7.29±0.59 (6.39±0.57)
310.37	0.26±0.08	K/0.050±0.012[i] L_{II}/0.070±0.007 L_{III}/0.018±0.004	0.19±0.07; $K/L_{II}/L_{III}$=2.8/3.9/1.0 ---- ----	$E3$ ---- ----	$E3$ --- ---	$E3$[i] ---- ----	0.44±0.09 ---- ----
313.06	0.18±0.05	K/0.056±0.012[i]	0.31±0.11; –	$M1$	$M1$	$M1,E1$[i]	0.24±0.05
349.56	1.55±0.16	K/0.34±0.03[k] K/0.49±0.06[q] L/0.076±0.006	0.22±0.03; – 0.32±0.05; K/L=6.4 ----	$M1$ $M1$ ----	$M1$ --- ---	not $E1$, $E2$[k] $M1$[i],$M1$[q] ----	1.96±0.16 (2.13±0.17) ----
493.65	1.12±0.11	K/0.13±0.01[k]	0.11±0.02; –	$M1$	$M1$	not $E1$, $E2$[k]	1.26±0.11
498.64	0.53±0.10	K/0.054±0.005[q]	0.10±0.02	$M1$	---	$M1$[q]	0.60±0.10
511.39	3.30±0.33	K/0.25±0.03[j] K/0.18±0.02[l]	0.076±0.011; – 0.055±0.008; –	$M1$ $(M1+E2)$	$M1$ ---	$M1$[j],$M1$[k] ----	3.59±0.33 (3.50±0.33)

549.83	8.78±0.87	K/0.073±0.007[k] K/0.091±0.012[q]	0.0084±0.0012; – 0.0104±0.0017; –	$E1$ ($E1$,$E2$)	$E1$ ---	$E1$[k] $E1$[q]	8.86±0.88 (8.88±0.88)
561.64	0.12±0.03	----	----	----	---	----	0.13±0.03
570.93	12.92±1.3	K/0.88±0.09[l] K/1.02±0.10[k]	0.068±0.010; – 0.079±0.011; –	$M1$ ($M1$)	$M1$ ---	$M1$[j],$M1$[k] ----	13.94±1.3 (14.09±1.3)
574.01	1.87±0.25	K/0.10±0.02[j]	0.054±0.13; –	$M1$	$M1$	----	1.98±0.23
576.37	0.73±0.20	----	----	----	---	----	0.77±0.20
579.80	16.67±1.7	K/≡0.28±0.03[k,a]	0.017±0.002; –	$E2$	$E2$	$E2$[j],$E2$[k]	16.92±1.7
626.71	1.81±0.18	K/0.097±0.010[q] K/0.077±0.008[j]	0.054±0.008; – 0.043±0.006; –	$M1$ ($M1$+$E2$)	--- $M1$,$E3$	$M1$[q] ----	1.92±0.18 (1.90±0.18)
688.53	0.64±0.06	K/0.012±0.001[j]	0.019±0.002; –	$E2$+$M1$	$E2$,$E3$	----	0.65±0.06
703.40	≡100.00	K/1.15±0.12 L/0.26±0.02[q]	0.012±0.001; K/L=4.2 ----	$E2$ ----	$E2$ ---	$E2$[j],$E2$[k],$E2$[q] ----	101.5 ----
717.41	0.91±0.15	K/0.023±0.005[j]	0.025±0.006; –	$M1$+$E2$	$M1$,$E3$	----	0.93±0.15
720.55	0.33±0.10	----	----	----	---	----	0.34±0.10
729.46	0.17±0.06	----	----	----	---	----	0.18±0.06
745.06	2.03±0.25	K/0.017±0.002[q] K/0.024±0.002[j]	0.0084±0.0014; – 0.012±0.002; –	$E2$ ($E2$)	--- $E2$	$E2$[q] ----	2.05±0.25 (2.06±0.25)
759.07	3.81±0.40	K/≡0.036±0.004[j,a]	0.009±0.002; –	$E2$	$E2$	----	3.85±0.40
761.37	2.21±0.40	K/0.023±0.002[j]	0.0010±0.002; –	$E2$	$E2$	----	2.23±0.40
780.90	1.77±0.18	----	----	----	---	----	1.79±0.18
795.59	0.36±0.05	----	----	----	---	----	0.37±0.05
800.81	0.62±0.10	----	----	----	---	----	0.62±0.10
806.92	0.55±0.10	----	----	----	----	----	0.56±0.10
813.84	1.52±0.15	----	----	----	----	----	1.55±0.15
852.78	0.16±0.05	----	----	----	----	----	0.16±0.05
860.10	1.40±0.15	----	----	----	----	----	1.40±0.15
871.78	1.30±0.13	----	----	----	----	----	1.34±0.13
890.04	2.22±0.22	----	----	----	----	----	2.23±0.22
894.50	1.79±0.18	----	----	----	----	----	1.81±0.18
901.84	0.45±0.05	----	----	----	----	----	0.45±0.05
910.82	5.47±0.55	K/0.096±0.009[k]	0.018±0.002; –	$M1$(+$E2$)	$M1$	$E2$[j],$E2$[k],$M1$[q]	5.58±0.55
921.74	0.19±0.03	----	----	----	----	----	0.19±0.03
950.70	1.21±0.12	----	----	----	----	----	1.21±0.12
971.35	0.90±0.09	----	----	----	----	----	0.92±0.09
987.54	54.61±5.5	K/≡0.31±0.03[k,a] K/≡0.24±0.04[l,a]	0.0059±0.0008; – 0.0044±0.0006; –	$E2$ ($E2$)	$E2$ ----	$E2$,$E1$[j],$E2$[k] ----	54.96±5.5 (54.88±5.5)
1001.6 1001.8	0.83±0.20 0.70±0.25 [m]	K/0.024±0.002[j] [m]	0.016±0.005[m]; –	$M1$ $M1$ $M1$	$M1$,$E3$		0.84±0.20 0.71±0.25

1003.1	0.50±0.15	----	----	----	----	----	0.51±0.15
1013.7	0.23±0.20	$K/0.024\pm0.003^{n}$ $L_I/0.006\pm0.001$	0.105±0.089; K/L_I=4.3 ----	$M4$ ----	---- ----	$M4^{n}$ ----	0.26±0.20 ----
1014.4	3.31±0.50	$K/0.038\pm0.004^{n}$ $L_I/0.005\pm0.001$	0.011±0.002; K/L_I=7.7 ----	$M1(+E2)$ ----	---- ----	$E1^{n},M1^{q}$ ----	3.35±0.50 ----
1043.68	25.30±2.5	$K/0.32\pm0.03^{k}$ $K/0.25\pm0.03^{l}$	0.013±0.002;– 0.010±0.002; –	$M1$ $(M1+E2)$	$M1$ ----	$M1^{j},M1^{k}$ ----	25.67±2.5 (25.59±2.5)
1065.81	0.34±0.04	----	----	----	----	----	0.34±0.04
1072.30	1.00±0.10	----	----	----	----	----	1.01±0.10
1107.50	0.33±0.03	----	----	----	----	----	0.33±0.03
1189.96	7.97±0.79	$K/0.087\pm0.009^{j}$ $K/0.074\pm0.007^{q}$ $L/0.017\pm0.002$	0.011±0.002; – 0.0093±0.0013; K/L=4.4	$(M1)$ $M1$	$M1$ ----	$M4,M3,E2^{j}$ $M1^{q}$	(8.04±0.79) 8.03±0.79
1199.76	0.65±0.06	----	----	----	----	----	----
1208.66	1.82±0.18	----	----	----	----	----	0.65±0.06
1216.34	0.29±0.04	----	----	----	----	----	1.85±0.20
1264.51	0.86±0.09	----	----	----	----	----	0.29±0.04
1351.56	3.50±0.35	$K/0.010\pm0.001^{q}$ $L/0.0018\pm0.0004$	0.0029±0.0004; K/L=5.6 ----	----	----	----	0.87±0.09
1499.71	0.56±0.14 [o]	---- [o]	----	$E2$ ----	---- ----	$E2^{q}$ ----	3.51±0.35 ----
1501.79	0.75±0.20 [o]	$K/0.005\pm0.001^{j}$ [o]	0.004±0.002	$M1(E2,E2)^{o}$	----	$E2^{q}$	0.56±0.14
1521.60	0.73±0.07	----	----	$E2(M1,E3)^{o}$	$M1,E2,E3$	$E2^{q}$	0.75±0.20
1549.60 1551.71	1.05±0.11 [p] 3.02±0.30 [p]	---- $K/0.009\pm0.001^{j}$ [p]	---- 0.002±0.001; –	----	----	----	0.73±0.07
1563.29	0.72±0.12	----	----	$E1^{p}$ $E2^{p}$	---- $M1,E2,E3$	---- ----	1.06±0.12 3.03±0.30
1577.35	0.50±0.05	----	----	----	----	----	0.72±0.12
1592.9	0.41±0.10	----	----	----	----	----	0.50±0.05
1614.52	7.92±0.79	$K/0.036\pm0.004^{j}$	0.0045±0.006; –	----	----	----	0.41±0.10
1619.38	1.05±0.11	----	----	$M1^{c}$	----	----	7.96±0.79
1764.46	121.2±12.	$K/0.39\pm0.04^{k}$	0.0032±0.0005; –	----	----	----	1.05±0.11
1775.96	14.24±1.4	$K/0.046\pm0.05^{k}$	0.0032±0.0005; –	$M1^{c}$	$M1,E3$	$E2^{j},M1^{k}$	121.6±12.
1818.22	0.20±0.02	----	----	$M1^{c}$	$M1,E3$	$M1^{k}$	14.29±1.4
1861.91	23.44±2.3	$K/0.015\pm0.002^{k}$ $L/0.0017\pm0.0004^{q}$	0.0064±0.0009; K/L=8.8 ----	----	----	----	0.20±0.02
1903.46	9.30±0.93	$K/0.005\pm0.001^{k}$	0.00054±0.00013; –	$E1$ ----	$E1$ ----	$E1^{j},E1^{k}$ ----	23.46±2.3 ----
1966.01	0.04±0.01	----	----	$E1$	$E1$	$E1^{k}$	9.30±0.93
2565.19	0.18±0.04	$K/0.00033\pm0.0001^{k}$	0.0018±0.0008; –	----	----	----	0.04±0.01
2606.75	0.10±0.02	$K/0.00018\pm0.0001^{k}$	0.0018±0.0012; –	$E3,M2,E2^{c}$	$E3,M2,E2$	----	0.18±0.04
				$E3,M2,E2^{c}$	$E3,M2,E2$	----	0.10±0.02

Footnotes to Table V:

[a] Electron intensities are normalized to give correct conversion coefficients for a collection of definite *E*2 transitions (579.8-, 759.1- and 987.5-keV transitions)(see text). Where possible, values have been chosen from R. Stockendal's most recent work; if there is a disagreement with other reported results, all are listed.

[b] Error limits for the *K*/*L* ratios should be inferred from electron uncertainties.

[c] In all cases except for the 310.4-, 1614.5-, 1764.5-, 1776.0-, 2565.2- and 2606.8-keV transitions conversion, coefficients falling near those for *E*3 transition are reported as *M*1+*E*2, a more likely situation and is consistent with our decay scheme. See text for discussion of 310.4-, 1614.5-, 1614.5-, 1764.5-, 1776.0-, 2565.2- and 2606.8-keV multipolarity assignments.

[d] Ref. RupT71.

[e] Transition intensities include unseen *L* and *M* conversion intensities. In cases where multipolarity assignments were not made, electron intensities were estimated using multipolarities inferred from the decay scheme.

[f] Ref. JohW71.

[g] Transition intensity determined by the sum of the 260.6-, 574.0- and 759.1-keV transition intensities.

[h] Energy value taken from VegS63.

[i] Ref. StoR60.

[j] Ref. SchM56. Electron intensity uncertainties not given by author. We have assigned uncertainties of ±10%.

[k] Ref. StoR58. Electron intensity uncertainties not given by author. We have assigned uncertainties of ±10%.

[l] Ref. FriA58. Electron intensity uncertainties not given by author. We have assigned uncertainties of ±10%.

[m] Electron intensities for 1001.6- and 1001.8-keV doublet apparently reported as singlet at 1002.7-keV.

[n] Ref. BerK64.

[o] Reported electron intensity for 1501.8-keV transition probably incorporates the 1499.7-keV transition.

[p] Reported electron intensity for 1551.7-keV transition probably incorporates the 1549.7-keV transition and the most consistent assignment is *E*1 and *E*2 for the 1549.7- and 1551.7-keV transitions, respectively.

[q] Ref. AllC71.

Figure 5. Experimental conversion coefficients superimposed over theoretical conversion coefficient curves.

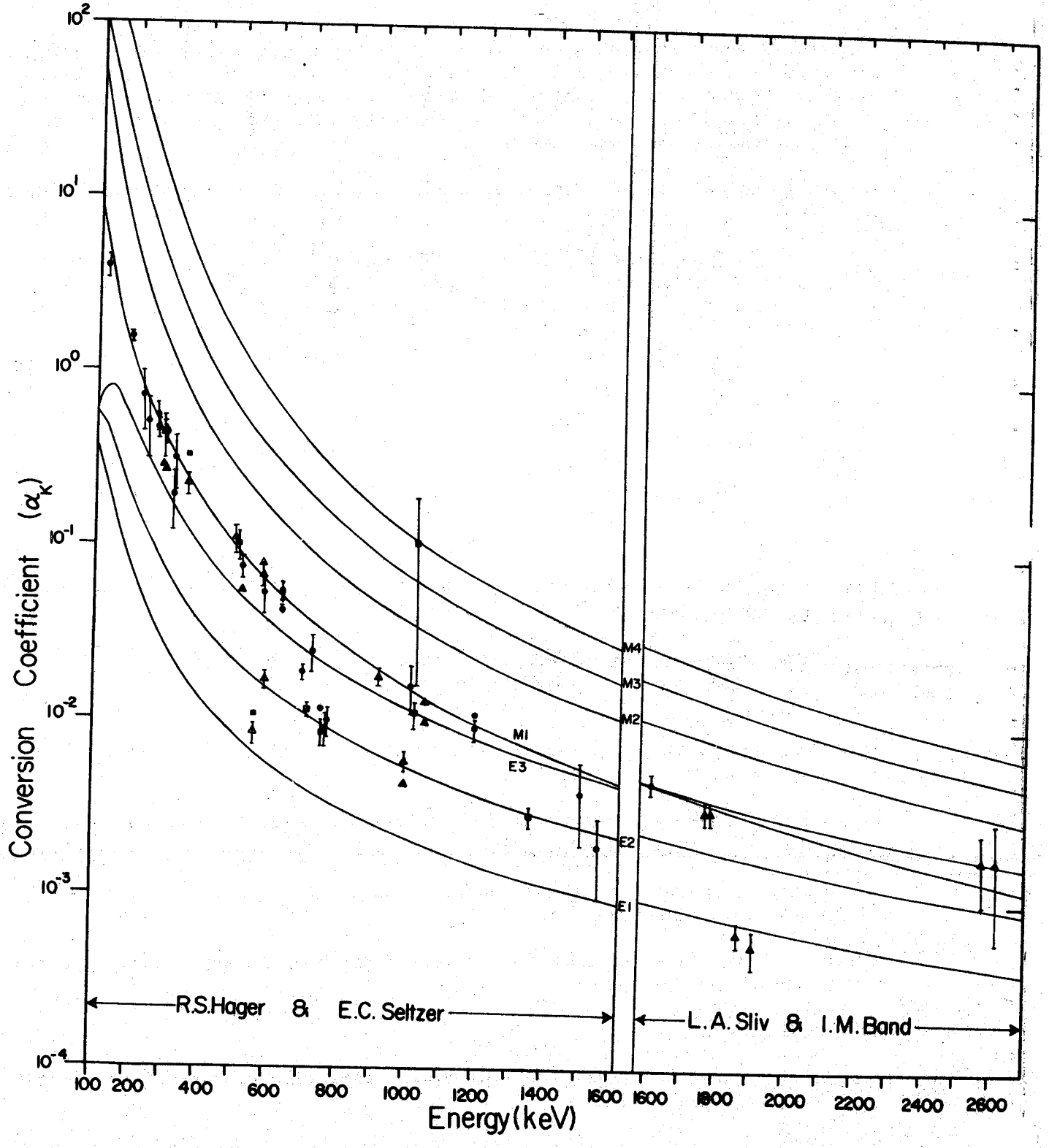

those for $E3$ transitions are reported as $M1+E2$, a more likely situation and consistent with the proposed decay scheme. On the basis of conversion ratios the 310.4-keV transition has been conclusively shown to be an $E3$ transition[StR60]. The 1614.5-, 1764.5-, and 1776.0-keV transitions fall where $M1$ and $E3$ conversion coefficients are nearly equal. While it is not possible to rule out an $E3$ assignments, our assignment of $M1$ is more likely and consistent with our prepared decay scheme. Near 2600 keV the conversion coefficients for $M1$, $M2$, $E2$, and $E3$ all lie quite close and uncertainties for the 2565.2- and 2606.8-keV transitions are quite large. On the basis of our calculated logft's for the feeding to these levels, only the $M1$ possibility can be eliminated.

Electron intensities for three high-energy multiplets were apparently reported as singlets. If we assume that the electron intensity for the 1001.6- and 1001.8-keV doublet was reported as a singlet and treat the γ intensity similarly, the conversion coefficient is that for an $M1$ transition. It is more likely and consistent with the decay scheme that there are both $M1$ transitions than that they are a combination of $M2$ and $E2$ or $M3$ and $E1$ transitions. If the 1003.1-keV γ intensity is included, the situation is less clear cut but then an assignment of $M1+E2$ seems most likely for the collection. If the electron intensity reported for the 1501.8-keV transition includes that for the 1499.7-keV transition, then assignments of $M1$ and $E2$ respectively seem likely and are consistent with their placement in our decay scheme. However, a completely safe assignment would be $M1$, $E2$, $E3$ for both transitions. Similarly for the 1549.6- and 1551.7-keV transition the only combination of assignments consistent with the γ intensities is $E1$ and $E2$ respectively.

In all cases where conversion ratios were available, they were considered in making multipolarity assignments.

D. % β Feedings and Logft[15] Values

Total β feeding percentages were determined for those levels involved in our first confidence decay scheme (Fig. 8) using transition intensities listed in Table V. These transition intensities include experimental K and L conversion intensities where available and estimates of unseen K, L, and M conversion intensities where reported experimental values are incomplete. Position feedings to levels in ^{205}Pb were determined experimentally (see Section III.F.), and are reported in Table VII. The electron capture feedings are reported in Fig. 8 and are just total β feedings minus β^+ feedings.

Beta feeding to the $5/2^-$ ground state would be a second forbidden decay and would then be quite small. An estimate of the feeding to the ground state could have been made using the K x-ray intensity and the K fluorescence yield; however, the uncertainties involved would make this estimate meaningless.

Logft values listed in Fig. 8 were calculated with the assistance of the computer code "Decay Scheme" [BeD69] which is essentially the equivalent to the use of the graphs found in the *Table of Isotopes* [LeC67].

E. Low Energy Conversion*

The MSU $\pi\sqrt{2}$, iron-free, double focusing β-ray spectrometer[VeL64] was used to record very low energy portions of the electron spectra resulting from the decay of ^{205}Bi and ^{206}Bi. A post-focusing acceleration technique was used to extend the useful urge of the spectrometer down to less than 1 keV[VeL64]. The energy resolution, which was limited by the source size and quality, was determined to be 0.3% for the L_I line from the 26.22-keV transition in ^{205}Pb. As source thickness became more critical at the lower energies, the line width increased to as much as 0.6% at 1 keV with a substantial tail as well. The energy calibration and instrumental transmission were monitored throughout the experiments by periodically running over the L_{III}-$M_{IV}M_V$, L_{III}-M_VM_V Auger doublet in addition to the L_I conversion line from the 26.22-keV transition.

During the counting periods of three or more half-lives, a number of passes were made over the low-energy region of interest and these were compared for consistency. In the end, all of the data for each source were corrected for half-life and a point-by-point weighted average and three-point smoothing were carried out. In Fig. 6 a comparison of the ^{205}Bi and ^{206}Bi spectra is shown. The gross features of these spectra are much what is expected - a rather intense Auger background with very broad peaks corresponding to many predicted unresolved *M* Auger lines. Since ^{206}Bi has no low-energy transitions, its spectrum appears to consist solely of Auger lines; however, in the ^{205}Bi spectrum the N_{II} and N_{III} (but not the N_I) conversion lines from the 2.33-keV transition are present and quite discernable. The higher energy conversion lines fall on top of strong Auger lines and are not unambiguously resolved from them.

---

* Work conducted in conjunction with Bill J. [JoW71].

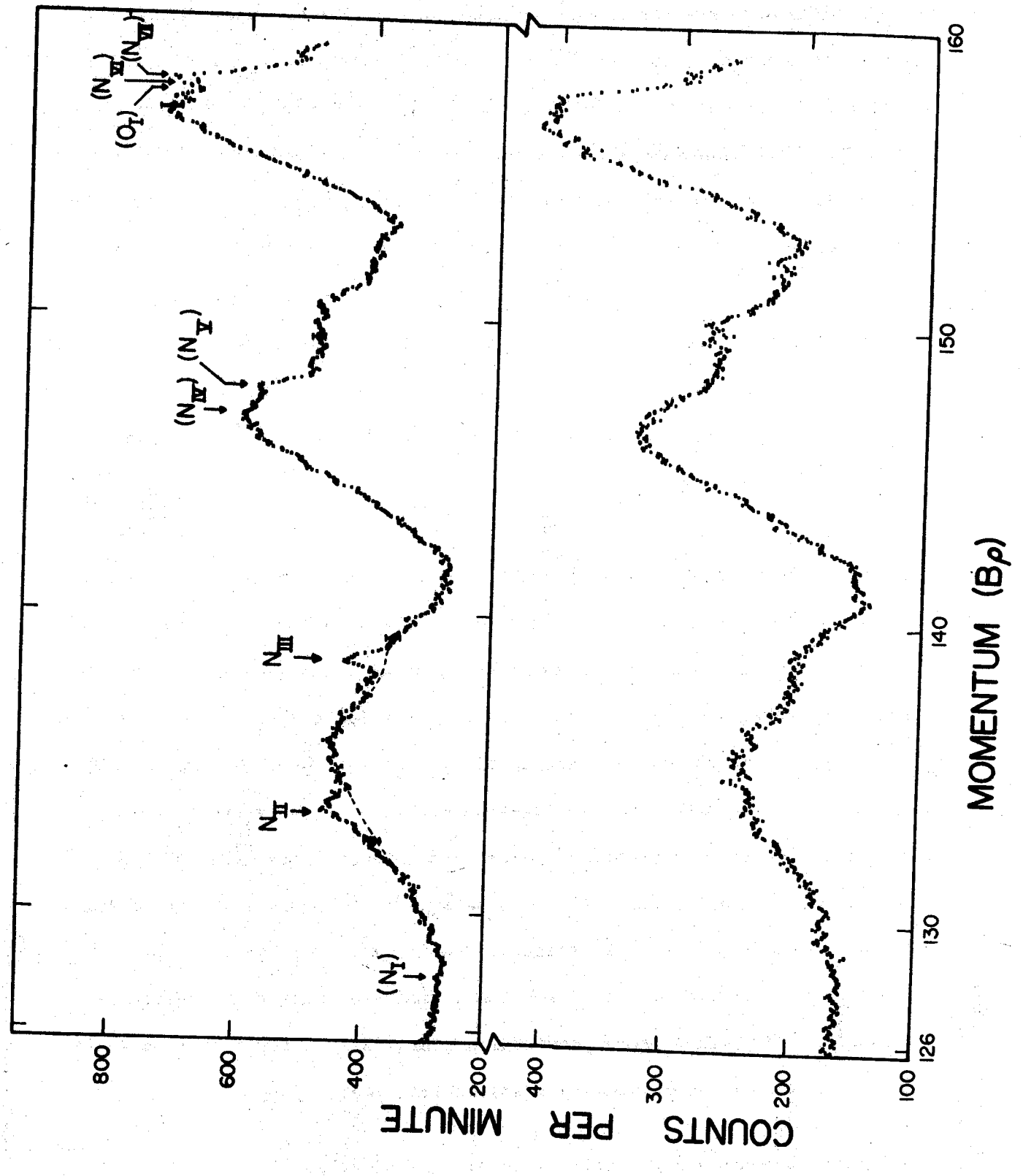
COUNTS PER MINUTE
MOMENTUM (Bρ)
(N_I)
N_II
N_III
(N_II)
(N_I)
(N_III)
(O_I)
800
600
400
200
400
300
200
100
126
130
140
150
160

Caption to Figure 6:

(Top) The N-conversion spectrum of the 2.328-keV transition in ^{205}Pb resulting from the ε decay of ^{205}Bi. The N_{II} and N_{III} lines are clearly visible above the M-Auger background and have energies of 1.564±0.007 and 1.684±0.007 keV, respectively. The positions where other conversion lines would fall are indicated in parentheses. The dashed line represents the experimental Auger background under the N_{II} and N_{III} peaks.

(Bottom) The ^{206}Bi spectrum, which contains no low-energy conversion electrons is shown for comparison. This spectrum was used to remove the Auger background from the ^{205}Bi spectrum.

To subtract the Auger background the ^{206}Bi spectrum was normalized to the ^{205}Bi spectrum and a point-by-point subtraction carried out. It should be pointed out that this tacitly assumes that the Auger components are the same for the two spectra. This should be a fair approximation, although M_I and M_{III} conversion of the 26.22-keV transition in ^{205}Pb does cause some different M primary vacancy distributions, each in turn cause slight variations in the Auger spectra. Despite this and the statistical fluctuations, the N_{II} and N_{III} lines still stood out clearly. The line shapes and areas, including low-energy tails, were determined by demanding that the two lines have identical shapes and that the background (^{205}Bi -const. X ^{206}Bi) have no maxima or minima under the lines.

Basing the energy calibration on the L_I line of the 26.22±0.001 keV transition[StR60], the energy of the 2.33 keV transition was measured to be 2.328±0.007 keV. This compares with 2.33±0.03 keV determined in the γ-ray study by stripping the 260.6-, 262.9, and the 759.1-761.4 keV doublets in several spectra with our best resolution.

A summary of the electron intensity data is given in Table VI. The fact that the assumed baseline, affecting especially the low-energy tails, is more likely to be high than low accounts for the asymmetrical errors on the intensity ratios. The measured N_{II}/N_{III} ratio of 0.70±0.25 is in excellent agreement with the prediction of Dragoun, Pauli, and Schmutzler [DrO69]. These are the first experimental data that have been available to test these predictions.

The total intensity of the 2.328-keV transition relative to the 703.4-keV transition can be obtained from the $(N_{II} + N_{III})/L_{I_{26.22}}$ ratio by the following relation:

Table VI. Conversion Intensity Data for the 2.328-keV Transition in ^{205}Pb

	This work	Other experiments	Theoretical[a]
$\alpha_{N_{III}}$	fiducial line ($\equiv 2.03\times10^{7}$)	---	2.03×10^{7}[b]
N_I/N_{III}	$<5\times10^{-2}$	---	5.8×10^{-3}[b]
N_{II}/N_{III}	0.70 ± 0.25	---	0.74[b]
N_{IV}/N_{III}	$<5\times10^{-2}$	---	1.7×10^{-2}[b]
N_V/N_{III}	$<5\times10^{-2}$	---	1.5×10^{-2}[b]
O_{II}/N_{III}	O_{II} present	---	$1.4\pm0.3\times10^{-1}$[c]
O_{III}/N_{III}	O_{III} present	---	$2.1\pm0.4\times10^{-1}$[c]
P_{II}/N_{III}	$<5\times10^{-2}$	---	1.0×10^{-2}[c]
P_{III}/N_{III}	$<5\times10^{-2}$	---	1.5×10^{-2}[c]
$\frac{N_{II}+N_{III}}{L_{I_{26.22}}}$	$0.48^{+0.15}_{-0.05}$	---	---
$\frac{\Sigma 2.328^{d}}{L_{I_{26.22}}}$	$0.59^{+0.21}_{-0.07}$	---	---
$\frac{\Sigma 2.328^{e}}{\Sigma 703.3}$	$0.10^{+0.04}_{-0.02}$	0.106 ± 0.008[f] 0.112 ± 0.008[g]	---

Footnotes to Table VI:

[a] All other conversion coefficients are at least a factor of 3 smaller than those listed.

[b] Graphical and numerical interpolation of Ref. [Dr069].

[c] Linear extrapolation on log-log paper of Ref. 11 from 10 keV. Errors represent extrapolation uncertainties.

[d] $(N_{II}+N_{III})/L_I$ multiplied by (total conversion)/$(N_{II}+N_{III})$ from the 1st column.

[e] I.e., the ratio of the total transition intensities; see text for method of calculation.

[f] Ref. 2 with 26.22-keV conversion data from Ref. [StR60] and 703.4-keV conversion data from Ref. [StR59].

[g] Ref. 3 with 26.22-keV conversion data from Ref. [StR60] and 703.4-keV conversion data from Ref. [StR59].

$$\frac{I_{2.328}}{I_{703.4}} = \frac{N_{II} + N_{III}}{L_{I_{26.22}}} \quad \frac{\alpha_{2.328}}{\alpha_{N_{II}} + \alpha_{N_{III}}} \quad \frac{L_{I_{26.22}}}{K_{703.4}} \quad \frac{\alpha_{K_{703.4}}}{1 + \alpha_{703.4}} \quad ,$$

where the second, third, and fourth terms on the right have respective values of 1.24±0.05 (from the last column of Table VI, 14.9 [StR60], and 0.011±0.001 [StR59]. As shown in Table VI, this ratio has a value of $0.10^{+0.04}_{-0.02}$, which agrees well with the sum of the intensities of the γ rays plus conversion electrons of the transitions feeding the 2.328-keV state. Assuming that the decay scheme is correct, this result then suggests that the predicted[Dr069] ratio, $\alpha_{2.328}/(\alpha_{N_{II}} + \alpha_{N_{III}})$, also agrees with experiment.

Only the N_{II} and N_{III} conversion lines were measured quantitatively in this work. There appears to be appreciable intensity at the momenta corresponding to the O_{II} and O_{III} lines, however, the fluctuations in the difference curves mask the much weaker transitions.

F. β^+ Feeding

The β^+ feeding was determined using the 2.5% Ge(Li) detector and an 8X8-in. split NaI(Tl) annulus with ≤10% resolution. The detectors were set up with the Ge(Li) detector just outside the active volume of the annulus. The source was encapsulated in 10 mils of lead to cause the positrons to annihilate in the central region of the annulus, thereby increasing the β^+ feeding detection effeciency by improving the geometry. The counting requirement was a triple coincidence between the halves of the annulus and the Ge(Li) detector, with the halves of the annulus gated on the 511±45-keV region to detect the 511-keV annihilation photons at 180° to each other and the Ge(Li) detector having just a baseline set to discriminate against x-rays. The resolving times were 50-50-100 nsec. for the halves of the annulus and Ge(Li) detectors respectively, which led to an overall resolving time, $2\tau \approx 50$ nsec. This resulted in a timing triple chance count rate of less than one count per 10 minutes. The resulting self-gated singles (SGS) and triple coincidence spectra (3-C) are shown in Figure 7.

A second pair of spectra were collected using ^{22}Na as the source with as nearly as possible the same geometry. The ratio ε_K/β^+ for feeding the 1274.6-keV transition in ^{22}Na is 1.104, which corresponds to 90.6% β^+ feeding. The percent β^+ feeding to levels in ^{205}Bi could then be determined using the relative 3-C/SGS counting ratios.

Transitions showing up in the ^{205}Bi triple coincidence run have their origins as one of the following: a transition from a level that is β^+ fed, a transition in a cascade from a level that is β^+ fed, a transition in a cascade from a transition that pair produces in the central geometry of the annulus, or a transition in coincidence with transition falling into or summing into the 511-511-keV gates.

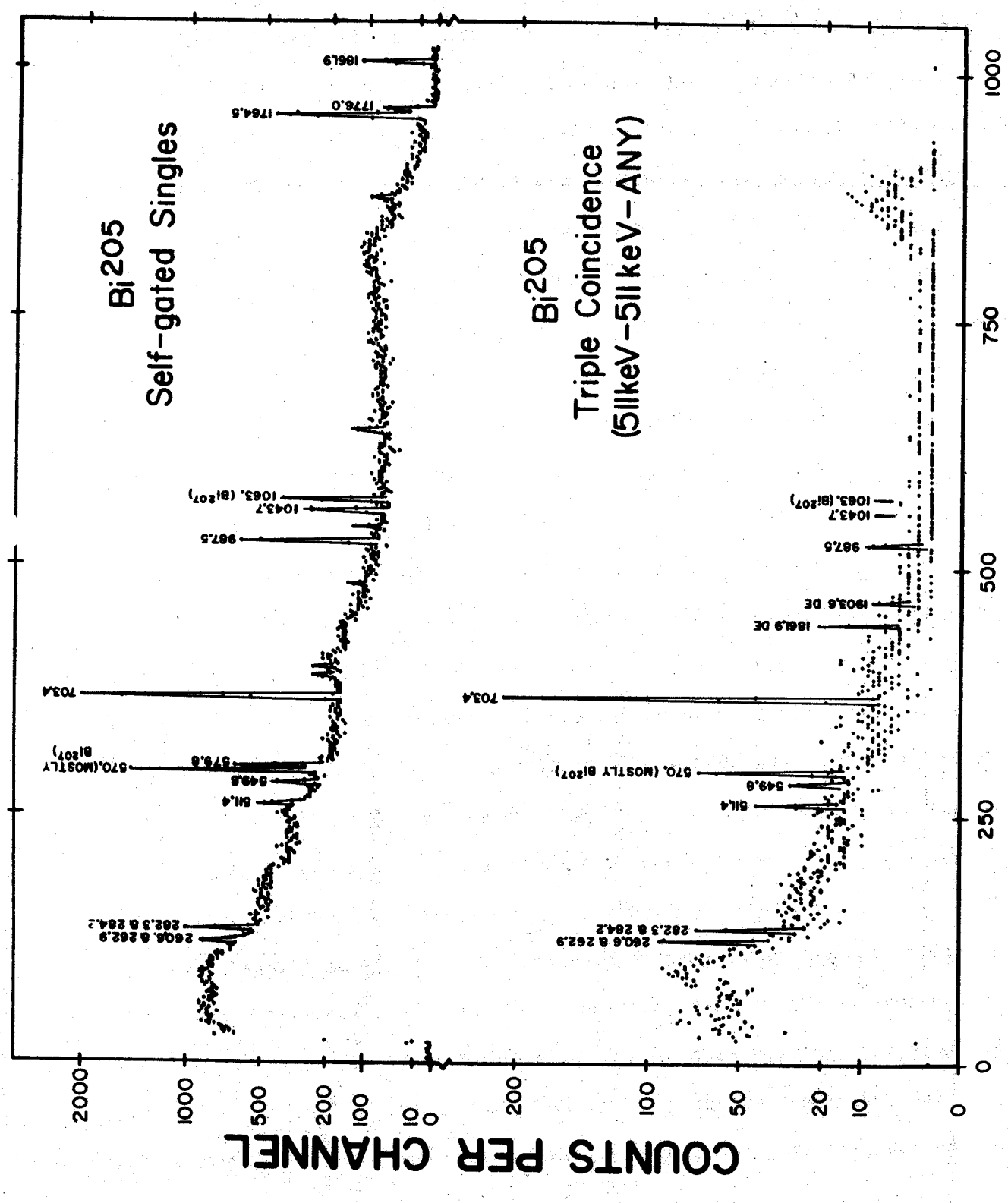

Figure 7. Gamma self gated singles and triple coincidence spectra to determine β^+ feedings

The 1043.7-keV level is fed by 549.8- (8.9% relative intensity) and 570.9-keV (13.9%) transitions which fall in or partially in the 511±45-keV gates and by 1208.7- (1.8%), 1521.6- (0.73%), and 1563.3-keV (0.72%) transitions capable of pair production in the source or in the Pb foil (see decay scheme Fig. 8). The 987.5 keV level is fed by a 511.4-keV (3.6%) transition and by 1577.4- (0.50%) and 1619.4-keV (1.1%) transitions. While β^+ feeding is possible for either of these levels (see Table I), it is apparent the 1043.7-keV level is fed extremely weakly if at all (see Fig. 7). Accordingly, the contributions to the 987.5-keV peak due to coincidences with a γ-ray's falling in the 511-keV gate and due to coincidences with γ's giving rise to pair production should be less than the intensity of the 1043.7-keV peak in the 3-C spectrum. This sets as a limit that the 987.5-keV peak results from >67% true β^+ originated triple coincidences.

The source was chosen to contain a rather large fraction of ^{207}Bi with its 569.9-1063.4-keV coincidence. It is not energetically possibly to have β^+ feeding to the 1633.1-keV metastable level; further, even if it were, the decay is delayed and could not give rise to true triple coincidences. Thus, the 1063.4-keV transition is weakly present only because of its coincidence with the 569.6-keV transition falling partially in the 511±45 keV gates. After correcting for intensity, the contribution to the 987.5-keV peak because of the 549.8- and 570.9-keV γ's falling partially in the 511±45-keV gates must be more than the normalized intensity of the 1063.4-keV peak in the 3-C spectrum. This sets as a limit that the 987.5-keV peak results from <98% true β^+ originated triple coincidences.

The reported β^+ feeding to the 987.5-keV level in Table I is the average of the results using the limits determined above and has been given a range

of uncertainty equal to approximately twice the difference between the above limits.

It was felt that our data would only allow placing an upper limit on the possible β^+ feeding to the 1043.7 keV level. We used the full intensity of the 1043.7-keV peak to set this limit.

The 703.4-keV level is fed by a 284.20keV (7.3%) transition from the 987.5-keV level, also by a 1861.9- (23.5%) and a 1903.6-keV (9.3%) transition, plus others of less consequence. Accordingly, it is necessary to correct the 703.4-keV feeding for being part of a cascade from the β^+-fed 987.5-keV level and for pair production of the 1861.9- and 1903.6-keV transitions. The correction for feeding from the 987.5-keV level was made directly and that for the pair production was made using the ^{207}Bi present in the sample. In this instance the presence of the 569.6-keV peak from ^{207}Bi can only result from its being fed by pair producing 1769.7 keV transition. Thus, after accounting for differences in pair production determined from double escape peak intensities and detector efficiencies, it was also possible to correct the 703.4-keV feeding for pair production, see Table VII.

Table VII. β^+ Feeding in the Decay of ^{205}Bi

Energy of Level	Predicted ε_K/β^+ →	% β^+ Feeding	This Work	Ref. PerC62
703.4	80[a] →	0.17	0.095±.02	0.058±.01
987.5	300[a] →	0.014	0.006±.002	
1043.7	500[a] →	0.001	<0.002	

[a] Predicted ε_K/β^+ ratios were determined using graphs reproduced in Table of Isotopes, Lederer, Hollander, and Perlman, 6th Ed. (1968).

IV. Decay Scheme

A. γ Considerations

The peak at ≈1002 keV has been considered to be a singlet depopulating the 1264.7-keV level in recent investigations. However, this assignment was not completely consistent with our coincidence results. The 1002-keV gate did indicate coincidences with the 260.6-262.9-keV doublet and the 349.6-keV transition (see Table III and Figures 3 and 8), as it should to depopulate the 1264.7-keV level. The additional coincidences (703.4-, 759.1-761.4- 860.1-, and 901.8-keV), observed and confirmed by gating on them to observe a ≈1002-keV peak, could not be explained without introducing even more radical inconsistencies. These observed coincidences could be explained if the ≈1002-keV peak were indeed a triplet depopulating a new level at 1705.0 keV and the 1764.5-keV level in addition to the 1265.7-keV level. As an initial check on this hypothesis, the centroids of the ≈1002-keV transition were determined when gating on those peaks in coincidence with it. These results are listed in Table VIII and can be seen to fall into the three groups predicted. As a further check on the triplet hypothesis, sum coincidence gates were set at 1265-, 1705-, and 1764-keV (see Figure 4). In each case the ≈1002-keV and 263-, 703-, or 761-keV transitions, respectively, were seen as sum coincidences. Thus, the 1002-keV peak has been conclusively shown to be a triplet with the placements indicated in our first confidence decay scheme (see Fig. 8). The peak at ≈312 keV has previously been considered a doublet depopulating the metastable level at 1013.7 keV and the level at 576.4 keV. Our observed 703.4-keV coincidence evidence supported the assignment for the 310.4-keV transition depopulating the isomeric level (see Figs. 3 and 8, and Table III. However, coincidences with the 1208.7- and 493.6-keV

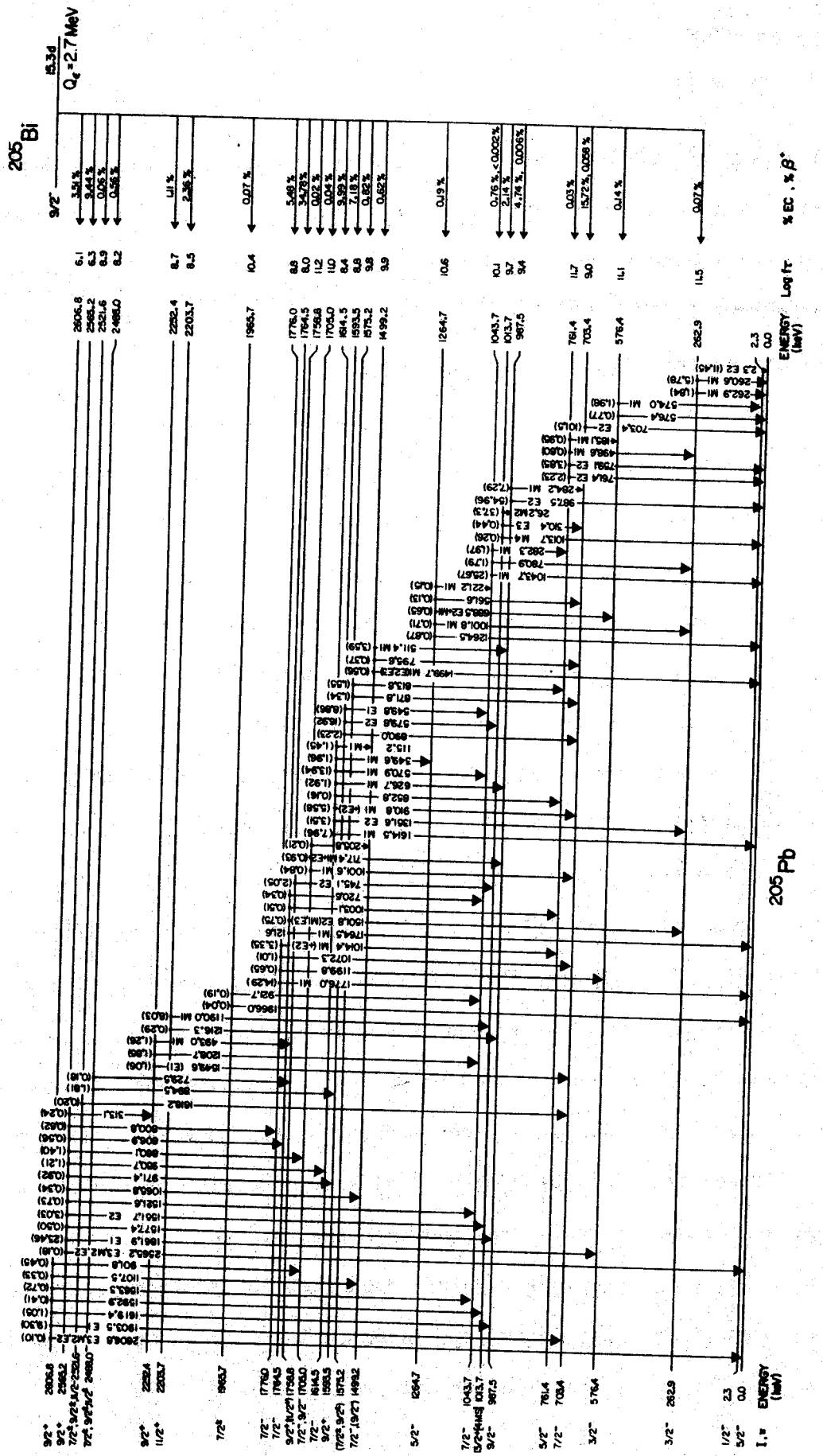

Figure 8. ^{205}Bi First confidence decay scheme containing only those transitions for which there is an abundance of coincidence data.

Table VIII. Centroids for 1002 Peak(s)

	1001.6	1002.0	1003.1
860.1	1030.00		
703.4	1030.18		
901.8	1030.24		
901.8[a]	1030.25		
262.9		1030.47	
349.6[a]		1030.67	
349.6		1030.74	
761.4			1031.22

[a] Centroids found on the x-display axis and normalized for comparison with the other centroids which were found on the y-display axis.

transition require an assignment for the 313.1-keV transition as depopulating the 2565.2-keV level. Further, the probable presence of a 262.9-, 260.6-keV coincident transition lends support to the assignment for a 313.6-keV transition depopulating the 576.6-keV level. Applying the same analysis of centroids and sum-coincidences as to the 1002-keV multiplet, we could not obtain conclusive evidence that the 312-keV multiplet was also a triplet. On the basis of the evidence that was collected, a transition of 313.6-keV depopulating the 576.5-keV level was included in the second confidence decay scheme, (see Fig. 9).

Doublets at 1500 and 1550 keV were initially observed because of their broadness. Energies and intensities for these transitions were obtained by stripping and were confirmed as doublets through a study of our coincidence results. Recent investigations [a, b] had assigned the 1500-keV peak feeding the level at 262.9-keV. The observed strong coincidence between the 1500-keV peak and the 262.9- and 260.6-keV doublet confirms this assignment for a 1501.6-keV transition. The additional probable coincidence between the 1500-keV peak and the 115.2-keV transition suggests the further assignment of a second component of the 1500-keV peak depopulating the level at 1499.2 keV. From stripping this multiplet peak, the resulting energies are 1501.8 and 1499.7 keV. This is a fair agreement for the 1501.8-keV transition, but the agreement for the 1499.7-keV transition is something less. There is possible coincidence evidence for a weak coincidence between one component of the 1500-keV peak and the 987.5-keV transition, which would represent a depopulating of the 2488.0-keV level by a 1500.5-keV transition and could be the source of the problem in the energy determination of the 1499.2-keV transition. However, it was not felt that there was enough evidence for this transition and its assignment

to include it in the decay scheme or list of observed transitions. Similarly, recent investigations had assigned the 1550-keV peak as feeding the 4msec. level at 1013.7 keV. This was confirmed by the increase in its intensity in the anticoincidence experiment and a decrease in the combined 1551.7-, 1549.6-keV transition intensity in the anticoincidence results from the megachannel coincidence experiment, (see Table IV). The 1549.6-keV component of the doublet was assigned on the basis of its coincidence with the 703.4-keV transition and a member of the 312-keV multiplet (statistics were such that we could not definitely identify the components of the 312-keV multiplet, see Fig. 3). The only consistent assignment for the 1549.6-keV transition is from the 2252.4- to the 703.4-keV levels.

Two additional weak peaks were observed in the low energy tail of the 1043.7-keV transition, at 1037.4 and 1040.1 keV. There is weak coincidence evidence that the 1037.4-keV transition is feeding the level at 576.4 keV (see Fig. 4 and Table III). However, it was felt that the evidence for this assignment was not conclusive enough for it to be included in our first confidence decay scheme.

It was thought that the $5/2^-$ level at 1264.7 might give rise to a ground state ($5/2^-$), first excited state ($1/2^-$) doublet separated by 2.3 keV similar to the doublet depopulating the $5/2^-$ level at 761.4 keV. A search for the second component of this doublet was complicated by the presence of the single-escape peak of the 1776.0-keV transition. It was only possible to place an upper limit on the 1262.4-keV transition intensity and that is <0.40%.

The peak at 1593 keV was checked to see if in addition to the 1592.9-keV transition feeding the isomerical level at 1013.7 keV, a transition

depopulating the 1593.5-keV level could be found.

This search was complicated by a 1596-keV transition occurring in ^{206}Bi and the double-escape peak from a 2614.5-keV transition from ^{208}Tl occurring in the room background. The results of this search are such that to say any more than that the 1593.5-keV transition is not a major component of the 1593-keV peak would be presumptuous.

One final multiplet should be considered, that lying at 720-keV. The 717.4-keV transition was assigned depopulating the 1705.0-keV level on the basis of its definite coincidences with 860.1-, 901.8-, and 989.5-keV transitions, in addition to probable coincidences with 282.3- or 284.2- and 703.4-keV transitions (see Figures 3 and 8 and Table III). However, the coincidence results for the 720.6- and 723.6-keV members of the group are inconclusive, giving only possible coincidences with 828.3- or 831.1-, 860.1-, 1043.7-, and 1208.7-keV transitions. On the basis of this evidence alone, no assignment could be made with confidence. When examining the 1764-keV sum-coincidence gate the 720.6- and 1043.7-keV transitions were observed, thus indicating the 720.6-keV transition was depopulating the 1764.5-keV level, (see Figures 4 and 8). On the basis of the possible 723.6- and 828.2-keV coincidences and their energy sum, the 723.6-keV transition was assigned depopulating the 2565.2-keV level in our second confidence decay scheme.

B. ^{205}Pb First Confidence Levels

The basic framework of the ^{205}Pb level scheme consisting of levels at 0.0 [$5/2^-$], 2.3 [$1/2^-$], 262.9 [$3/2^-$], 576.4 [$3/2^-$], 703.4 [$7/2^-$], 761.4 [$5/2^-$], 987.5 [$9/2^-$], 1013.7 [$13/2^+$], 1043.7 [$7/2^-$], 1264.7 [$5/2^-$], 1499.2 [$7/2^-(9/2^-)$], 1614.5 [$7/2^-$], 1764.5 [$7/2^-$], 2565.2 [$9/2^+$], and 2606.8 [$9/2^+$] keV has been established in recent investigations[VeS64, VeS71] and are only reconfirmed by this study with some slightly differing energies and several changes in spin assignments. Thus, with the exception of mentioning the differing spin assignments, these levels will not be discussed further.

The spin of the 1043.7-keV level was established as $7/2^-$ on the basis of an *M*1 transition to or from levels at 0.0 [$5/2^-$], 761.4 [$5/2^-$], 1264.7 [$5/2^-$], and 1614.5 [$7/2^-$] keV and an *E*1 transition from the level at 1593.5 [$9/2^+$] keV. We have listed the spin of the 1499.2-keV level as $7/2^-(9/2^-)$. There are *M*1 transitions to and from levels at 987.5 [$9/2^-$] and 1614.5 [$7/2^-$] keV respectively, narrowing the spin to $7/2^-$ or $9/2^-$. A probable *M*1 transition to the ground state [$5/2^-$] then restricts the spin to $7/2^-$. Further, on the basis of its log*ft* of 9.9, a spin assignment of $7/2^-$ seems slightly preferred over the $9/2^-$ assignment made in earlier investigations[VeS64, VeS71] on the basis of a theoretically predicted $9/2^-$ level at about 1600-keV.

Arguments supporting the existence of and assignments for each of the remaining first confidence levels at 1575.2 [$5/2^+$, $7/2^\pm$, $9/2^-$], 1593.5 [$9/2^+$], 1705.0 [$7/2^-$, $9/2^-$], 1758.8 [$9/2^+$, $(11/2^+)$]. 1776.0 [$7/2^-$], 1965.7 [$7/2^\pm$], 2203.7 [$11/2^+$], 2252.4 [$9/2^+$], 2488.0 [$7/2^\pm$, $9/2^\pm$, $11/2^\pm$], and 2521.6 [$7/2^\pm$, $9/2^\pm$, $11/2^-$] will be presented in detail.

The 1575.2-keV level was identified by the strong coincidences between the 871.8- and 703.4-keV transitions and the 813.8- transition and the transitions depopulating the 761.4-keV level (See Fig. 3 and Table III). The 703.4- and 761.4-keV levels are firmly established and no additional strong coincidences were observed in the 813- or 871-keV gates, so a level at 1575.2-keV is the only consistent possibility. If it is assumed that the transitions to the 761.4- [$5/2^-$] and 703.4-keV [$7/2^-$] levels are either *M*1, *E*1, or *E*2 and the reported log*ft* of 9.8 is indicative of an allowed or first-forbidden β decay, then the possible spins for the 1575.2-keV level are $5/2^+$, $7/2^\pm$, or $9/2^-$. This is also consistent with the observation of a transition from the 2606.8-keV $9/2^+$ level in a second confidence decay scheme. As in the case of the 1499.2-keV level, we do not feel justified in narrowing our spin assignment on the basis of theoretically predicted levels.

Strong coincidences between the 890.0-keV transition and the 703.4- and 894.5-keV transition indicates a cascade between these transitions. The level at 703.4 keV is firmly established; thus the 703.4-keV transition is the final element of the cascade. Further, a level at 2488.0-keV is indicated by the absence of any additional strong coincidences (this level is discussed further later in this section). γ intensities for the 890.0-keV (2.2%) and 894.5-keV (1.8%) transitions suggest an intermediate level at 1593.5 keV as more probable. This placement is supported by strong coincidences between the 894.5-keV transition and the 579.8- and 549.8-keV transition, which correspond to transitions between the 1593.5-keV level and the well-established levels at 1013.7 and 1043.7 keV. Final confirmation is added by the observed strong coincidence between the 971.4-keV transition and the 579.8- and 549.8-keV transitions. Here the 971.4-keV transition is

between the well established level at 2565.2 keV and the 1593.5-keV level. The spin assignment for the 1593.5-keV level is determined to be $9/2^+$ on the basis of an *E*2 transition to the 1013.7-keV [$13/2^+$] level and an *E*1 transition to the 1043.7-keV [$7/2^-$] level.

The 1705.0-keV level was identified on the bases of strong sum coincidences of the 1001.6+703.4-keV transitions and the 717.4+987.5-keV transitions (see Fig. 4). Confirmation was added by the observation of strong coincidences between the transitions feeding, 860.1- and 901.8-keV, and those depopulating the level (see Fig. 3 and 8 and Table 3). The 1001.6-keV 1 transition to the 703.4-keV [$7/2^-$] level and the 717.4-keV 1+ 2 transition to the 987.5-keV [$9/2^-$] level require that the spin and parity of the 1705.0-keV level be $7/2^-$ or $9/2^-$. Consideration of the other transitions, with no multipolarity assignments, to and from the 1705.0-keV level does not allow a further reduction of the possible assignments. The log *ft* value of 11.0 tends to favor the $7/2^-$ assignment; however, log *ft*'s can be high for many reasons and high log *ft*'s are considerably less conclusive than low log *ft*'s. In addition, the log *ft*'s for ^{205}Bi are all quite high. For these reasons, we feel that no preference between the assignments of $7/2^-$ and $9/2^-$ can be made.

A level at 1758.8 keV is established on the basis of strong coincidences between the 745.1-keV transition and the 806.9-, 729.5 and 493.0-keV transitions from the well established levels at 2488.0 and 2252.4 keV, respectively (the 2565.2-keV and the levels at 2488.0 and 2252.4 keV are discussed in detail later in this section). The spin assignment for the 1758.8-keV level was made on the basis

of the 745.1-keV *E*2 transition to the 1013.7-keV [$13/2^+$] level. While the *E*2 transition does not rule out the possibility of spins $15/2^+$, $13/2^+$, or $11/2^+$, it does seem these should have some *M*1 character. The log *ft* of 11.2 eliminates $17/2^+$, which would be a 3rd forbidden β decay to this level. Accordingly, the assignment for this level is $9/2^+(11/2^+)$. This is consistent with the assumption that the 806.9-keV transition from the 2565.2-keV [$7/2^+$] level is *M*1, *E*1, or *E*2.

The lack of definite coincidences observed for the moderately intense 1776.0-keV [14.3%] transition suggests a level at 1776.0 keV. This is confirmed by coincidences between the 1199.8-keV transition and those depopulating the 576.4-keV level, the 1072.3-keV transition and the 703.4-keV transition, and the 1014.4-keV transition and those depopulating the 761.4-keV level. The *M*1 character of the 1776.0-keV transition limits the spin of the 1776.0-keV level to $3/2^-$, $5/2^-$, or $7/2^-$. The log *ft* of 8.8 eliminates all but $7/2^-$ for the spin assignment.

The level at 1965.7 keV was established primarily on the basis of the observed coincidence between the 921.7-keV transition and the 1043.7-keV transition to the ground state. This was supported by the observation of a possible coincidence between the 978.0-keV transition and the 987.5-keV transition to the ground state in addition to the presence of a 1966.0-keV transition in the γ-singles spectrum. On the assumption that the 1966.0- and 921.7-keV transitions are *M*1, *E*1, or *E*2, and further that the log *ft* of 10.4 suggests an allowed $7/2^{\pm}$. The lack of any definite coincidences for the moderately intense 1190.0-keV [8.0%] transition, coupled with the intensity of the transitions being up in the anticoincidence study and down in the any coincidence study (see Table IV), suggests either the 1190.0-keV transition feeds

the isomeric level at 1013.7 keV from a level at 2203.7 keV. The possibility for a level at 2203.7 keV is confirmed by the observation of coincidences between the 1216.3- and 987.5-keV transitions. The *M*1 character of the 1190.0-keV transition to the 1013.7-keV [$13/2^+$] level limits the spin assignment for the 2203.7-keV level to $11/2^+$, $13/2^+$ or $15/2^+$. The final assignment of $11/2^+$ was made on the assumption that the 1216.3-keV transition to the 987.5-keV $9/2^-$ level was *M*1, *E*1, or *E*2. This assignment is consistent with the observed log *ft* of 8.5 for this level.

Coincidences between the 1549.6-keV transition and the 313.1- and 703.4-keV transitions suggests a cascade from the 2565.2-keV level to the ground state. The new level was placed at 2252.4 keV on the basis of the observed coincidences between the 1208.7-keV transition and the depopulating the 1043.7-keV level, also between the 493.0-keV transition and those depopulating the 1758.8-keV level. The *M*1 character of the 493.0-keV transition to the 1758.8-keV [$9/2^+(11/2^+)$] level limits the spin assignment for the 2252.4-keV level to $7/2^+$, $9/2^+$, $11/2^+$, or $(13/2^+)$. The determination of the probable *E*1 nature of the 1549.6-keV transition to the 703.4-keV [$7/2^-$] level further limits the spin assignment to $7/2^+$ or $9/2^+$. This is consistent with the observed log *ft* of 8.7.

The level at 2488.0 keV was identified on the basis of observed coincidence between the 894.5-keV transition and those depopulating the level at 1593.5 keV and between the 729.5-keV transition and those depopulating the level at 1758.8 keV. Assuming the 894.5- and 729.5-keV transition to be *M*1, *E*1, or *E*2 only limits the possible spin of the 2488.0-keV level to $5/2^+$, $7/2^{\pm}$, $9/2^{\pm}$, $11/2^{\pm}$, or $13/2^+$, any of which is consistent with the determined log ft of *8.2* for this level. The level at 2521.6 keV

was identified only on the basis of an observed coincidence between the 1818.2- and 703.4-keV transitions. The assumption that this transition is *M*1, *E*1, or *E*2 coupled with the log *ft* of 8.9 only limits the possible spin of the level to $5/2^+$, $7/2^+$, $9/2^+$ or $11/2^-$.

C. Second Confidence ^{205}Pb levels

Additional levels at 1633.5 [7/2, $9/2^-$], 1737.2 [$9/2^+$, $11/2^-$], 2108.2, 2327.4, and 2421.4 keV are included in a second confidence decay scheme. Transitions included in the second confidence decay scheme were placed on the basis of weak or inconclusive coincidence information and/or on the basis of energy sums. These transitions that appear as dashed lines are most uncertain.

A cascade between the 2565.2-keV level and the 987.5-keV level is suggested by the presence of the 645.8-keV transition when gating on the 931.7- and 987.5-keV transitions (see Figs. 3 and 9 and Table III). This new level was placed at 1633.5 keV on the basis of a probable coincidence between the 787.9-keV transition depopulating a level at 2421.4-keV and the 645.8-keV transition. Further, when a coincidence gate was set on a possible 1633.5-keV transition, a possible coincidence with the 645.8-keV transition was observed. On the assumption that each of the γ's observed are *M*1, *E*1, or *E*2, the 931.7-keV transition from the 2565.2-keV [$9/2^+$] level and the 645.8-keV transitions to the 987.5-keV [$9/2^-$] level limit the possible spin assignment to $7/2^{\pm}$, $9/2^{\pm}$, or $11/2^{\pm}$. The 1633.5-keV transition to the $5/2^-$ ground state further limits the possible spin assignment to $7/2^{\pm}$ or $9/2^-$.

The observation of a probable coincidence between the 122.9-keV transition and the 349.6-keV transition depopulating the 1614.5-keV level suggest the possibility of a level at 1737.2 keV. Support for this level is added with the observation of a probable coincidence between one member of the 720-723-keV doublet and one member of the 282-831-keV doublet. Again, if the assumption is made that the 122.9-keV

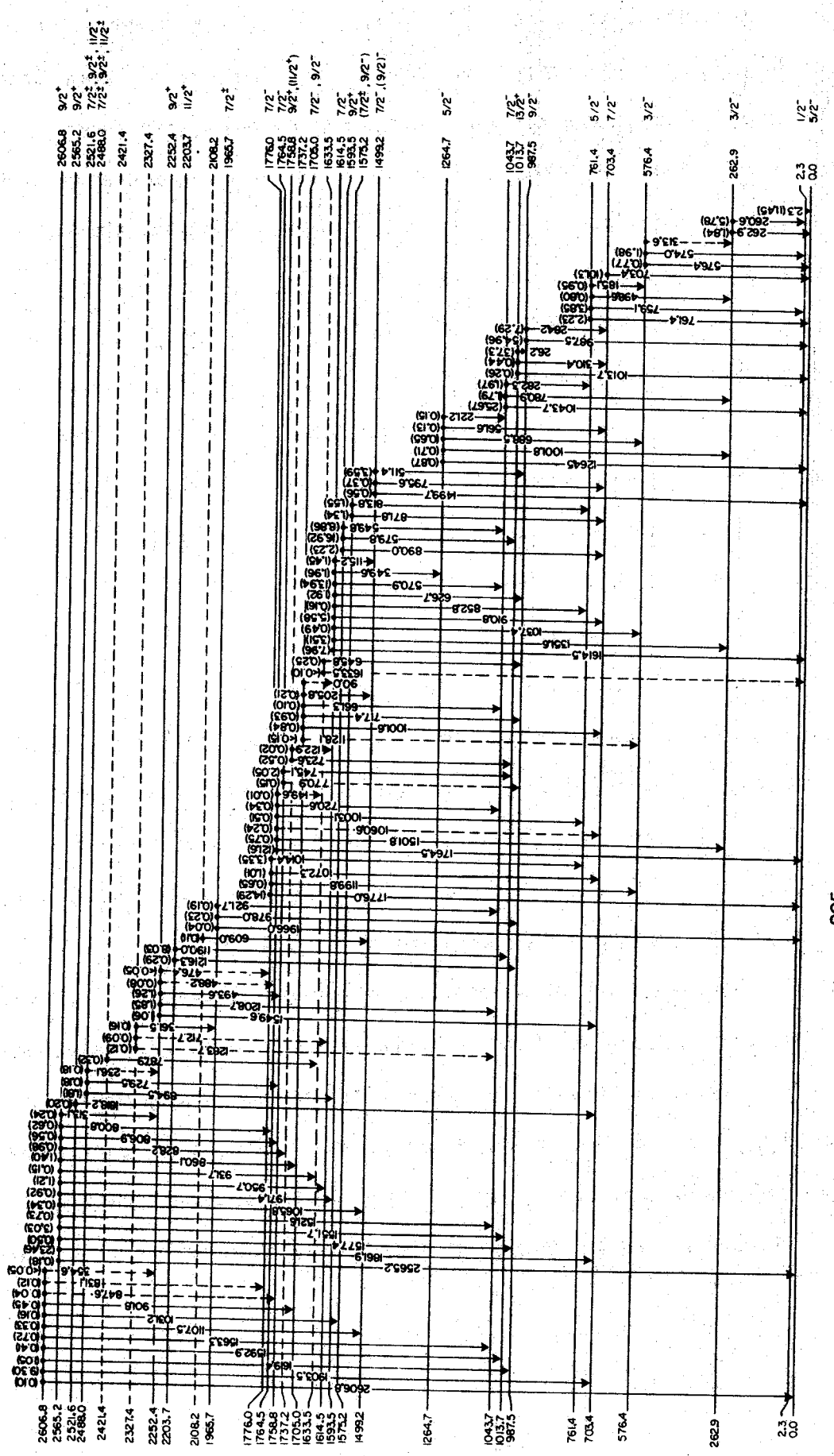

Figure 9. $^{205}_{Bi}$ Second confidence decay scheme

transition to the 1614.5-keV $7/2^-$ level and the 723.6-keV transition to the 1013.7-keV $13/2^+$ level are each *M*1, *E*1, or *E*2, the possible spin assignment is limited to $9/2^+$ or $11/2^-$. The level at 2108.2 keV is suggested on the basis of the probable coincidence between the 609.0-keV transition and those depopulating the 1499.2-keV [$7/2^-$, ($9/2^-$)] level, primarily the 795.6-keV transition. It is felt that no meaningful spin and parity assignment could be made on the basis of this one transition.

The level at 2327.4 keV is suggested on the basis of the possible coincidence between the 361.5-keV transition and the 978.0-keV transition depopulating the 1965.7-keV level. In addition, two transitions are added depopulating this level on the basis of energy differences. The transitions are a 712.7-keV transition to the 1614.5-keV [$7/2^-$] level and a 1283.7-keV transition to the 1043.7-keV [$7/2^-$] level. It is felt that no meaningful spin and parity assignment could be made for this level.

The level at 2421.4-keV is suggested by the probable coincidence between the 789.9-keV transition and the 645.8-keV transition depopulating the second confidence level at 1633.5 keV. On the basis of this one transition it is felt that no meaningful assignment for the spin and parity of this level can be made.

Many additional second confidence transitions between first confidence levels are included in the second confidence decay scheme. However, it is possible to narrow further only one of the spin assignments of the existing first confidence levels. That is for the 1705.0-keV level. The 1128.1-keV transition to a $3/2^-$ state reduces the spin possibility to $7/2^-$.

Because of the tentative nature of many of the second confidence transitions, percent feedings, and log ft values were not recalculated for the levels.

V. Discussion

It is intended that the theoretical discussion presented in this paper of the level scheme deduced for ^{205}Pb be quite limited in scope and depth. We have recently completed studies of the decay of ^{204}Bi and ^{203}Bi in this laboratory [CrJ68] which will be published shortly and envision a paper following these discussing in more detail the theoretical implications of this large collection of work on the neutron-deficient region. The discussion that is presented here is limited to those levels lying below about 1500 keV.

The nucleus ^{205}Pb is 3 neutron holes away from the doubly-magic ^{208}Pb nucleus and should be quite rigid with respect to vibrations. Thus, its level scheme should be amenable to explanation through rather straightforward shell-model calculations. Early theoretical calculations, such as the semi-quantitative calculations of Pryce [PrM56] in 1956, attempted to account for the level scheme of ^{205}Pb below 2.5 MeV by considering only the various couplings of the 3 neutron holes in the N=5 oscillator shell with an estimate of the effects of configuration mixing. Above about 2.5 MeV it should be possible to excite a proton or neutron to the next higher oscillator shell and the situation becomes more complicated. Pryce extracted parameters for the level spining in ^{205}Pb from those in ^{207}Bi. The ordering of the neutron levels is $h_{9/2}$,$f_{7/2}$,$i_{13/2}$,$p_{3/2}$,$f_{5/2}$, and $p_{1/2}$ thus the ground state would have the configuration $(\nu p_{1/2}^{-2})(\nu f_{5/2})^{-1}$ giving rise to the spin and parity of $5/2^-$. The configurations $(\nu p_{1/2})^{-2}$ $(\nu p_{3/2})^{-1}$, $(\nu p_{1/2})^{-1}$ $(\nu f_{5/2})^{-2}$, $(\nu p_{1/2})^{-1}(\nu g_{5/2})^{-1}(\nu p_{3/2})^{-1}$, and

$(\nu p_{3/2})^{-2}(\nu i_{1/2})^{-1}$ can then account for all the observed levels below about 1.5 MeV. However, the energy fit is not very good at all and even the ordering of all but the lowest levels does not agree with experiment.

Similarly, it is possible to account for all low-lying observed ^{205}Pb levels observed by simply assuming that paired neutrons couple to 0 with the remaining single particle/hole coupling to a quadrupole vibration fo the ^{204}Pb/^{206}Pb core. The center of gravity of the vibrational levels built on the ground state would be expected to occur at about 900/800 keV, and would give spins $1/2^-$ to $9/2^-$, inclusively. Indeed, when True [TrW61] included weak coupling of the particle to the collective notion of the core, an improved fit with experiment was the result.

At first glance the *E*2 character of the 703.4-keV ($7/2^-$, $5/2^-$) and 761.4-keV ($5/2^-5/2^-$) transitions seems to be in support of the vibrational nature of these states with the transitions corresponding to $(\nu f_{5/2})^{-1}(2^+) \longrightarrow (\nu f_{5/2})^{-1}(0^+)$. However, if these states were different couplings of the 3-neutron-hole configurations $(\nu p_{1/2})^{-2}$ $(\nu p_{5/2})^{-1}$ also would not be facilitated by an *M*1 transition.

If we consider the collection of states involved to be the $2.3(1/2^-)^-$, $576.4(3/2^-)^-$, $761.4(5/2^-)^-$, $703.4(7/2^-)^-$ and $987.5(9/2^-)$keV states, then their center of gravity is 746 keV. This compares about equally favorably with the single particle/hole coupled to the ^{204}Pb/^{206}Pb core at 899/803 or with the zero-order energy predicted by Pryce for the $(\nu p_{1/2})^{-1}(\nu g_{5/2})^{-2}$ configuration. If it were possible to measure lifetimes of the *E*2 transitions involved, it should be possible to decide on the dominant character of these states. Collective

enhancement of the $E2$ transitions should result if they result primarily from coupling to a vibrational state of the core.

The more recent calculations of Miranda [MiA67] using a potential with a weak spin dependence and weak non-localities present an improved fit with the experimentally determined levels. In Figure 10 we present a comparison with our levels.

Figure 10. Comparison of experimentally determined levels in ^{205}Bi with those theoretically calculated by [PrM56] —> P, [TrW61] —> T and [MiA67] —> M.

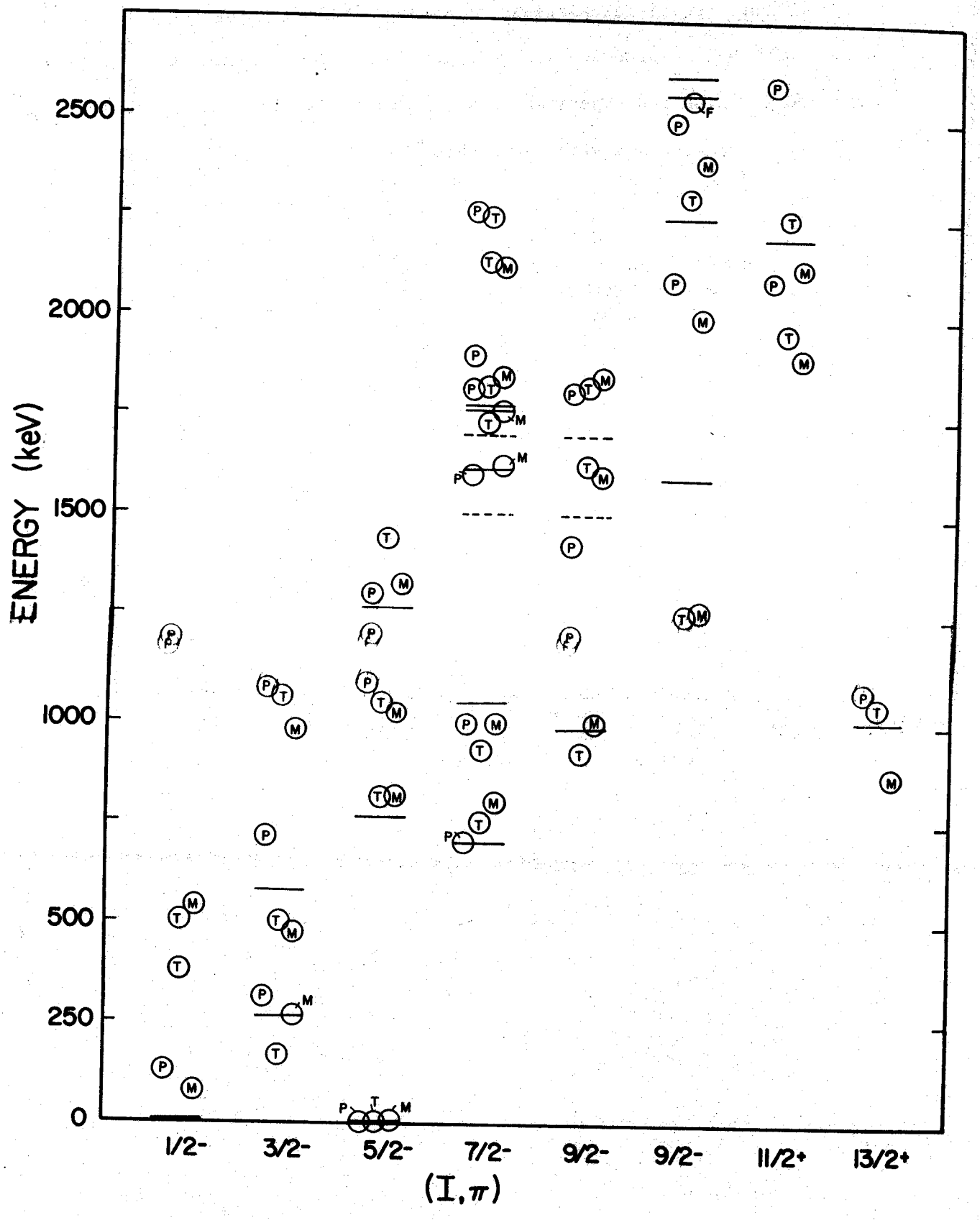

REFERENCES

[AlC 70] Colin Allan, private communication.

[AlC 71] C. J. Allan, Can. J. Phys. 49, 157 (1971).

[AlD 60] D. E. Alburger, Phys. Rev. 118, 1076 (1960).

[BeD 69] D. B. Berry, Ph.D. Thesis, Mich. State Univ. (1969).

[BeK 64] K. E. Bergkuist and R. Stockendal, Ark. Fys. 27, 339 (1964).

[CrJ 68] J. Cross, Ph.D. Thesis, Mich. State Univ. (1968).

[DoR 68] R. E. Doebler, Mich. State Univ., Nuclear Chem. Annual Report 1968.

[DoR 70] R. E. Doebler, Ph.D. Thesis, Mich. State Univ. (1970).

[DrO 67] O. Dragoun, H. C. Pauli, F. Schmutzler, Nuclear Data, Sect. A6, 235 (1969).

[DrO 69] O. Dragoun, H. C. Pauli, and F. Schmutzler, Nuclear Data Sheet, Sect. A6, 236 (1969).

[FrA 58] A. R. Fritsch and J. M. Hollander, J. Inorg. Nucl. Chem. 6, 165 (1958).

[GuJ 70] J. Guile, Mich. State Univ. Nuclear Chem. Annual Report 1970.

[HaR 68] R. S. Hager and E. C. Seltzer, Nuclear Data 4A, 1 (1968).

[HeC 61] C. J. Herrlander, Ark, Fys. 20, 71 (1961).

[JoW 71] W. C. Johnston, W. H. Kelly, S. K. Haynes, K. L. Kosanke, Wm. C. McHarris, Phys. Rev. Letters, 26, 1043 (1971).

[LeC 67] C. M. Lederer, J. M. Hollander, and I. Perlman, *Table of Isotopes* 6th ed., John Wiley & Sons (1967), New York.

[MiA 67] A. Miranda, Nuclear Phys. 92, 386 (1967).

[PeC 61] C. F. Pedrisat, H. J. Leisi, and J. H. Brunner, Nuclear Phys. 31, 157 (1961).

[PrM 56] M. H. L. Pryce, Nuclear Phys. 2, 226 (1956).

[RoJ 69] J. T. Routi and S. G. Prussin, Nuclear Inst. Methods, 72, 125 (1969).

[RuT 71] T. D. Rupp and S. H. Vegors, to be published.

References (Contd.)

[StK 65] *Alpha-, Beta-, and Gamma-Ray Spectroscopy*, Vol. 2, ed. by Kai Siegbahn, North Holland Publishing Co. (Amsterdam) 1965.

[StR 58] R. Stockendal and S. Hultburg, Ark. Fys. 15, 33 (1958).

[StR 59] R. Stockendal and S. Hultberg, Ark. Fys. 15, 33 (1959).

[StR 60] R. Stockendal, Ark. Fys. 17, 553 (1960).

[ScM 56] M. Schmorak, R. Stockendal, J. A. McDonell, and T. R. Gerholm, Nuclear Phys. 2, 194 (1956).

[TrW 61] W. W. True, Nuclear Phys. 25, 155 (1961).

[VeL 64] L. J. Velinsky, Ph.D. Thesis, Mich. State Univ., (1964).

[VeS 60] S. Vegors and R. L. Heath, Phys. Rev. 118, 547 (1960).

[VeS 64] S. H. Vegors, Nuclear Phys. 48, 230 (1964).